Development & Upscaling of 3D Printed Chromatography Columns for Virus Purification

A thesis submitted in partial fulfilment of the requirements for the degree of

Doctor of Philosophy in Chemical and Process Engineering
University of Canterbury

Written by

Sean Ashley Feast

February 2021

Department of Chemical and Process Engineering
Te Whare Wānanga o Waitaha, University of Canterbury
Ōtautahi, Christchurch
Aotearoa, New Zealand

Foreword and Acknowledgements

The following thesis is the summation of three years of research and study that could not have been made possible without the following people. Firstly, my supervisors Professor Conan Fee and Dr. Tim Huber who have provided me with experienced guidance, support, and direction. To my parents, Raewyn and Gary, who have not only encouraged me with my studies but have always pushed me to pursue my interests. To Creighton Dawson, Hannah Parlane, and Simone Woodford, collectively known as part of the "Festie four," for helping me through the stressful days and long weekends. To Courtney Crozier, Gaby Rutherford, Kathryn van Emple, Joe Kearns, Joe Stanley, and Jesse Bryan, thank you for your friendship and support. Also, my flatmates for listening to the day's troubles and providing a great place to work during the lockdown.

A special thanks to the people and organizations I have had the pleasure of collaborating with. To Dr. Cristina Peixoto, Mafalda Moleirinho, and Sofia Moreira from iBET, for hosting me in Lisbon and providing both adenovirus and lentivirus for our work. To Professor Steven Cramer and Akshat Mullerpatan from Rensselaer Polytechnic Institute, for hosting me in Troy as well as helping test the first set of columns I had produced. To Associate Professor Steven Gray for providing the adeno-associate virus samples and insight into commercial gene therapy production.

To the helpful team in the chemical and process engineering department at the University of Canterbury, including Michael Sandridge and Glenn Wilson for helping me with all of the lab resources used for this work. Leigh Richardson, Graham Mitchell, and Paul Tolson for their expertise in fabricating the custom rigs used throughout this project. To Rayleen Fredericks who taught me nearly every lab technique, culturing, and quantification method she knew. Without your help, I would not have been able to accomplish half of the experiments I managed. Your experience was invaluable and patience is incredible.

Abstract

The work presented in this thesis has demonstrated the purification of a range of viruses from both clarified lysate and cell culture using 3D-printed chromatography columns. Previous research and development of 3D-printed columns suggested they would benefit the recovery of virus and virus-like particles used for biopharmaceutical applications such as vaccines and gene therapies. The columns' ability to passage solids while effectively bind and elute a target biological allowed the combination of multiple steps (clarification, filtration, and capture chromatography) in the downstream processing of viruses. This reduction in processing steps and production time should minimize costs for virus production, especially for expensive gene therapies.

A triply periodic minimal surface known as the Schoen gyroid formed the cellulose hydrogel-based columns' channel structure. These monolithic-style columns had 300 μm hydraulic diameter channels allowing the passage of solids. Anion exchange (Q or DEAE) or multimodal (hydroxyapatite) ligands were attached to the structure's walls and pores to bind and elute a range of viruses. Both DEAE (229 μeq/mL & 85 mg/mL) and Q (346 μeq/mL & 138 mg/mL) functionalities have comparable ligand densities and BSA static binding capacities compared to bead-based media. Recovery of oncolytic adenovirus (69 ± 6%) and lentivirus (57%) from DEAE columns is high compared with traditional media. Purification of M13 bacteriophage directly from cell culture under comparable conditions to an expanded bed chromatography process showed a high recovery (87.7% ± 5% for 1.49×10^{11} pfu/mL). Additionally, it was completed three times faster without the difficulties associated with a fluidized bed.

This work also acknowledged and examined how this technology could scale from the lab to pilot-size columns capable of processing larger volumes of feedstock. Development of a 'segmentation method' alongside commercially available printer advancement led to a single part size increase of 1500%. Fabrication of pilot-sized column (30 cm long by 5 cm diameter, 500 μm channel diameter) is estimated to take 20 hours.

Contents

List of Publications

1. Moleirinho, Mafalda G., Feast, Sean, Moreira, Ana S., J. S. Silva, Ricardo, Alves, Paula M., J. T. Carrondo, Manuel, . . . Peixoto, Cristina. (2021). 3D-printed ordered bed structures for chromatographic purification of enveloped and non-enveloped viral particles. Separation and Purification Technology, 117681. doi:https://doi.org/10.1016/j.seppur.2020.117681.

2. Huber, T., Zadeh, H. N., Feast, S., Roughan, T., & Fee, C. (2020). 3D printing of gelled and cross-linked cellulose solutions, an exploration of printing parameters and gel behaviour. Bioengineering, 7(2). doi:10.3390/bioengineering7020030.

3. Huber, Tim, Feast, Sean, Dimartino, Simone, Cen, Wanwen, & Fee, Conan. (2019). Analysis of the Effect of Processing Conditions on Physical Properties of Thermally Set Cellulose Hydrogels. Materials, 12(7), 1066.

List of Figures

List of Tables

Abbreviations

AAV	Adeno-Associated virus
Ad	Adenovirus
AIDS	Auto Immune Deficiency
BSA	Bovine Serum Albumin
CAD	Computer Aided-Design
CAR	Coxsackievirus and Adenovirus Receptor
CIP	Clean-In-Place
CLSM	Confocal Laser Scanning Microscopy
CV	Column Volume
DBC	Dynamic Binding Capacity
DEAE	Diethylaminoethyl
DI	Deionized
DMF	Dimethylformamide
DNA	Deoxyribonucleic acid
DTT	Dithiothreitol
EBA	Expanded Bed Adsorption
ECH	Epichlorohydrin
EDS	Energy Dispersive Spectroscopy
EDTA	Ethylenediaminetetraacetic Acid
ELISA	Enzyme-Linked Immunosorbent Assay
FDA	Food and Drug Administration
FDM	Fused Deposition Modelling
FE-SEM	Field Emission Scanning Electron Microscope
FPLC	Fast Protein Liquid Chromatography
FT-IR	Fourier Transform - Infrared Spectroscopy
GMAC	Glycidyl Trimethylammonium Chloride
HA	Hydroxyapatite
HCP	Host Cell Proteins
HEK293	Human Embryonic Kidney Cells
HELA	Henrietta Lack Cells

HETP	Theoretical Plate Height
HIC	Hydrophobic Interactions Chromatography
HIS	Histidine
HIV	Human Immunodeficiency
HSPG	Heparan Sulfate Proteoglycan
IDA	Iminodiacetic Acid
IMAC	Immobilized Metal Affinity Chromatography
IPA	Isopropyl Alcohol
LDS	Lithium Dodecyl Sulfate
NHS	N-Hydroxysuccinimide
NTA	Nanoparticle Tracking Analysis
OCP	Octacalcium Phosphate
PEG	Polyethylene Glycol
pfu	plaque forming units
Q	Quaternary amine
qPCR	quantitative Polymerase Chain Reaction
RNA	Ribonucleic acid
RPI	Rensselaer Polytechnic Institute
SBF	Simulated Body Fluid
SCID	Severe Combined Immunodeficiency
SDS-PAGE	Sodium Dodecyl Sulfate–Polyacrylamide Gel Electrophoresis
SEC	Size Exclusion Chromatography
STL	Standard Triangle Language
TEM	Transmission Electron Microscope
TLC	Thin Layer Chromatography
TPMS	Triply Periodic Minimal Surface
TU	Transducing Units
VG	Viral Genomes
VLP	Virus-Like Particles
XRD	X-Ray Diffraction

Symbols

As	Asymmetry
HETP	Theoretical plate height
a	Right side of a peak
b	Left side of a peak
hmin	Reduced plate height
Dp	Particle diameter
V_r	Retention volume
W_h	Peak width at half peak height
l	Unit cell length
s	Surface area of a unit cell
ε	Porosity
d	Hydraulic diameter
a	Specific surface area
C0	Feed concentration
$V_{b,10\%}$	Break through volume at 10% of feed concentration
V_0	Void volume
CV	Column Volume
$DBC_{10\%}$	Dynamic binding capacity at 10%
Qmax	Static binding capacity

1 Introduction

1.1 Background

Current advances in biopharmaceutical medicine have explored the use of viruses as delivery mechanisms to insert modifications genes to a patient's cells as a cure to genetic diseases (Figure 1-1) [1]. This technology, termed gene therapy, has grown steadily in the past 5 years with the approval of two therapies (Luxturna and Glybera) for sale [2, 3]. The pipeline for US Food and Drug Administration (FDA) approval sees hundreds of these therapies currently undergoing various stages of clinical trials [4]. Gene therapies are a lifeline for patients whose condition was previously a potential death sentence. As with the advancement in the use of these modified viruses, efforts are being made to optimize the production (upstream) and purification (downstream) processes to produce them.

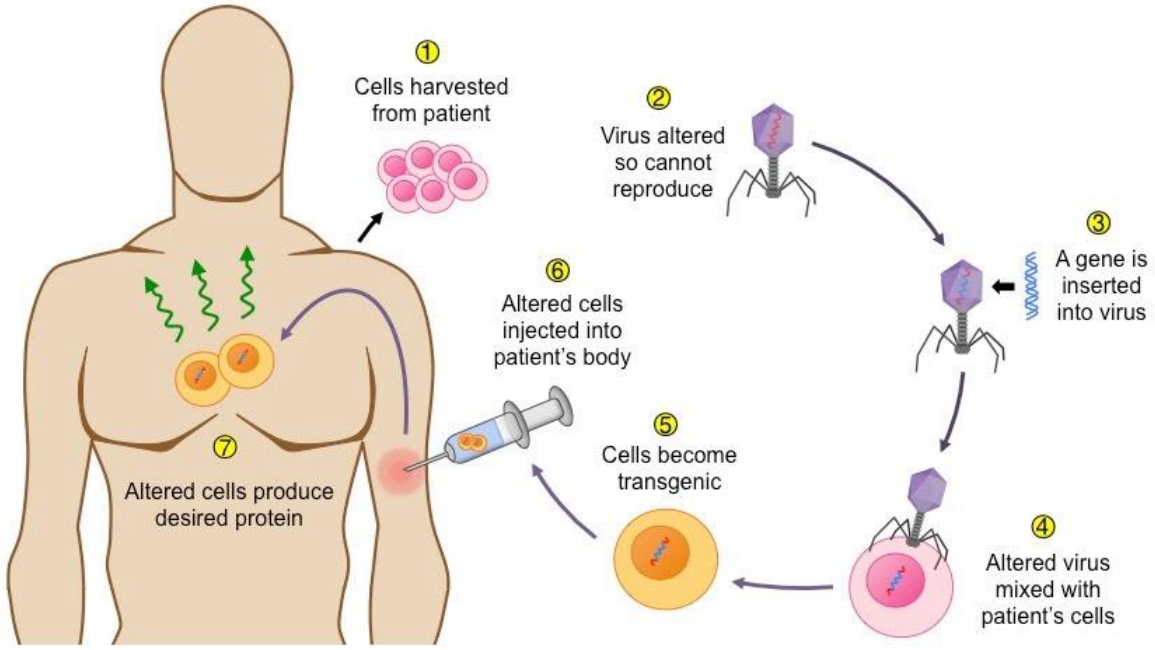

Figure 1-1: Diagram showing a method for administering virus based gene therapies [5].

Upstream processing involves culturing the virus inside a host cell used as a biological factory for replication. Host cells and culturing methods are specific to each type of virus and even differ between serotypes of the same virus. Downstream processing involves separating the newly replicated viral particles away from contaminants such as host cells, proteins, DNA,

and endotoxins. There are multiple steps in a purification strategy, including cell lysis, clarification, capture chromatography, intermediate purification, polishing, and formulation (Figure 1-2). Current purification strategies use previously optimized technologies for proteins and adapted for use with viruses. Of these, the most common, packed bed chromatography columns used in the capture, intermediate, and polishing steps have low recoveries and capacities for virus and virus-like particles [6]. Technologies such as monoliths and membranes have emerged specifically designed to purify viruses [7-9]. Although promising, both require clarified feedstreams, and monoliths suffer from issues in scalability [10].

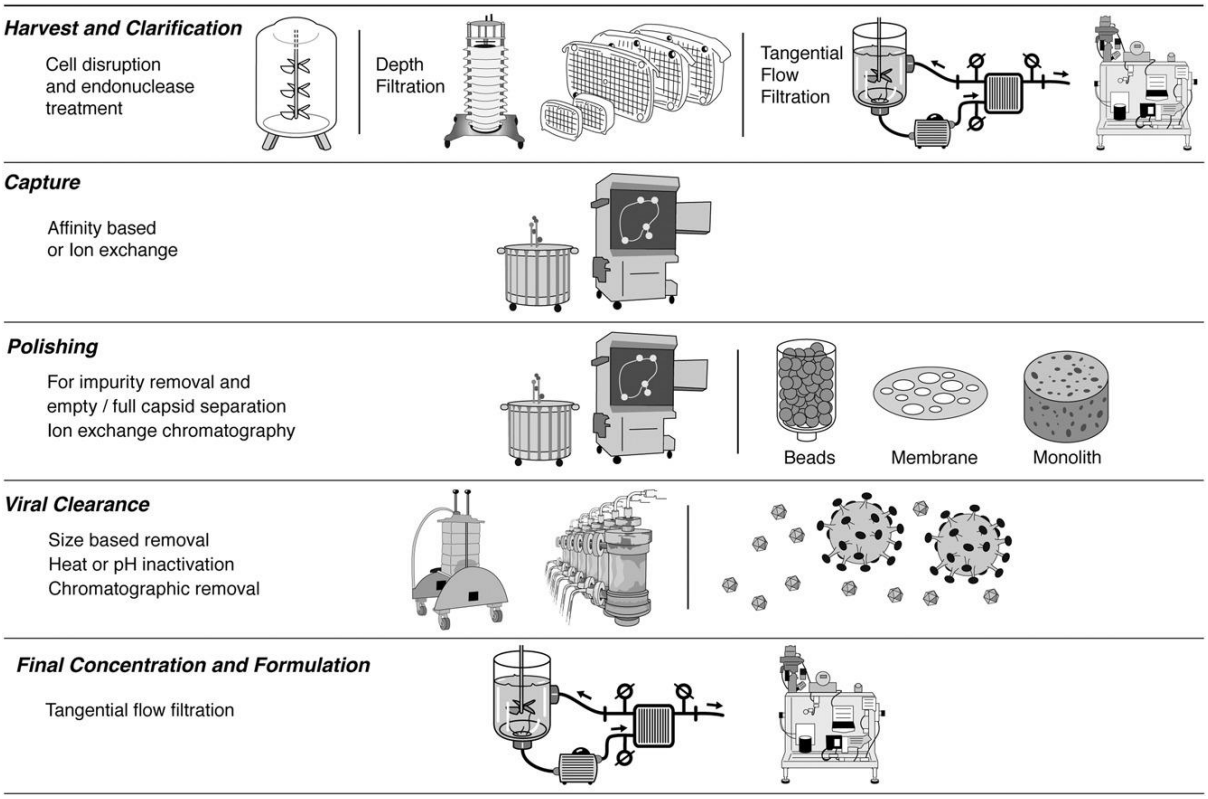

Figure 1-2: Overview of the steps for the industrial purification of adeno-associated virus [11].

Expanded bed adsorption (EBA) chromatography can purify target biologicals such as proteins or viruses directly from cell culture or lysate. A bed of chromatography beads is fluidized by an upwards flow of buffer, expanding the bed to between two and three times its original height. This fluidization allows for the passage of solids through the bed while allowing the chromatography beads to contact the feedstream and bind the target biological [12]. EBA was a revolution in bioprocessing; however, the industry did not widely adopt it

because of issues related to the fluidized bed, such as channeling, fouling, need for specialized equipment, and bed collapse [13, 14].

Additive manufacturing, or the more commonly termed 3D printing, involves the layer-by-layer production of a 3D object. Computer-Aided-Design (CAD) software combined with 3D printing can produce complicated items not possible with other manufacturing techniques. Many industries now use 3D printing with a wide range of materials such as plastics, metals, and waxes. 3D printing in chromatography is an emerging field with the ability to design ordered flow channels within a given structure. Large ordered channels within a cylindrical agarose-based hydrogel can passage solids such as cells, while functional groups on the walls and internal pores can bind and elute protein. Proteins have been separated from a simulated cell broth directly similar to an expanded bed process using 3D-printed chromatography columns (Figure 1-3) [15]. This technology could purify viruses directly from crude cell lysate more effectively than traditional media [16].

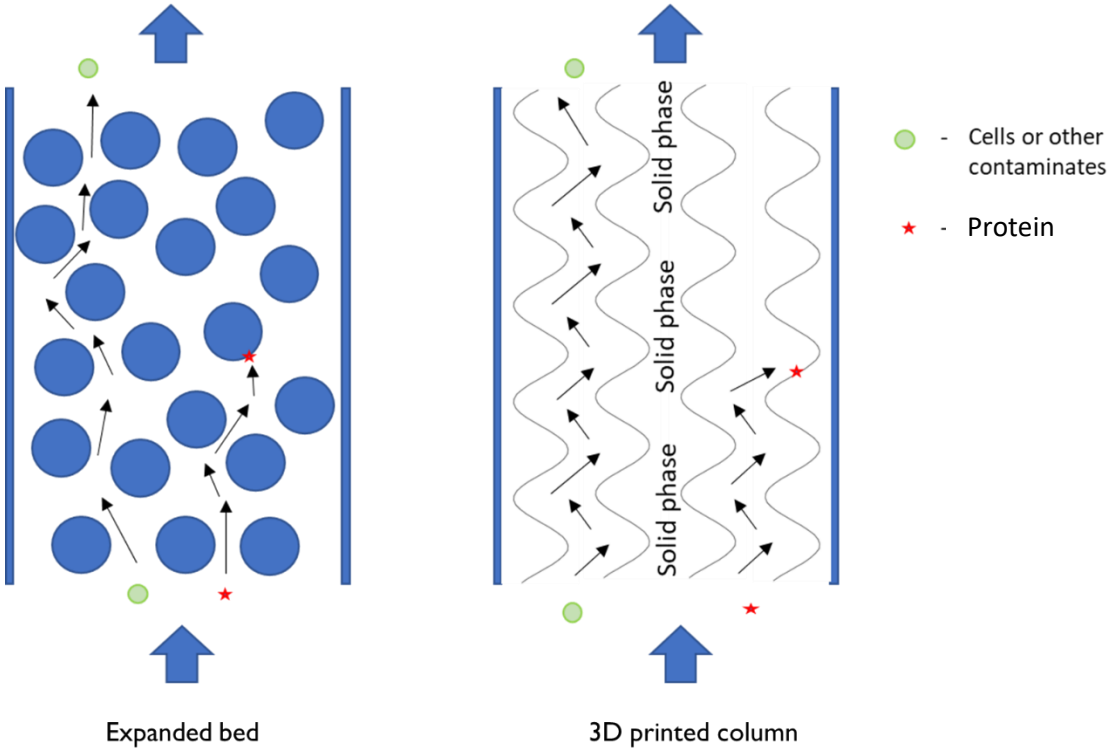

Figure 1-3: Comparison between how expanded bed chromatography and 3D-printed columns passage solids. Unseen are the channels that also extend radially through the 3D-printed column.

The previous research using 3D-printed chromatography media has shown its potential as an alternative to expanded bed chromatography. This thesis describes work carried out to investigate optimizing 3D-printed chromatography columns to be a platform for the purification of viruses. A unique cellulose hydrogel is investigated as a potential chromatography stationary phase. Various chemical and mineral functionalities of the cellulose hydrogel are used to bind and elute a range of viruses. Purification directly from cell culture is compared between 3D-printed columns and an expanded bed adsorption process. The scalability of this technology has also been investigated using the currently available commercial 3D printers. Scalability and practicality of production are important if this technology is to be adopted by the industry at any level.

1.2 Objectives

This work aims to evaluate the purification of virus or virus-like particles directly from cell culture or lysate using 3D-printed chromatography columns. More specifically, the objectives are as follows:

- To evaluate a novel cellulose hydrogel to be the stationary phase of the 3D-printed chromatography columns.

- Expand on and optimize the current range of functional ligands useable with the 3D-printed chromatography columns.

- To determine the column's performance purifying a range of viruses from both clarified and unclarified feed streams. Including evaluating the resulting purity of separated viruses.

- To understand and optimize factors that affect the column's performance to maximize recovery and minimize processing time.

- To compare the 3D-printed column purification process against an established expanded bed chromatography purification.

- Evaluate scale-up of this technology, including determining current 3D printing constraints.

1.3 Organization of thesis

Chapter 2 details literature around the downstream processing of gene therapies, focusing on the current state of the art and new and emerging technologies such as monoliths and membranes. The recovery at each step in the downstream processing of viruses is examined. Chromatography performance indicators are explained and used in experimental chapters to compare different chromatography media. Various 3D printing methods are examined, with a focus put on those currently used in chromatography. The literature on 3D printing in chromatography is limited; however, more researchers are investigating its potential as the field grows.

Chapter 3 outlines all of the materials and equipment used throughout this project. It also contains the standard methods used for most of the work except those used in Chapter 6. The final experimental chapter contains its methods section to be standalone detailing upscaling methods and results. The chapter contains details of construction, functionalization, stationary phase analysis, and viral purification testing of 3D-printed columns.

The following three chapters detail the results and discussion of these experiments in a logical order. The first chapter investigates the cellulose stationary phase proposed for these columns and its appropriateness for viral purification. The second chapter details using these optimized columns to purify a range of viruses from clarified and unclarified feed streams. Finally, the last experimental chapter explains a potential upscaling method of 3D-printed chromatography columns with current technology. Recommendations based on the results of this research are made in the conclusive chapter of this thesis.

2 Literature review

The following is a review of downstream purification looking at viral vectors used in gene therapies. Attention is also focused on alternatives to current strategies, specifically 3D-printed chromatography columns. These columns are the primary focus of this work as an alternative to current technology for viral purification.

2.1 Gene therapies

Cystic fibrosis, Huntington's disease and, Duchene muscular dystrophy are genetic diseases, which up until the discovery of gene therapies have been incurable and, in some cases, death sentences. Previously, doctors could only minimize the symptoms and treat the side effects of these diseases. However, gene therapies have provided a possible pathway to develop cures by using viruses as vehicles to deliver corrected or modified genes directly to a patient's cells. Recombinant viruses or virus-like particles can have specific genes inserted into their genetic code. Upon infection with these modified viruses, the inserted gene is transferred into the host cell's genome. It is possible to control what type of cells will be infected depending on the virus's morphology. For example, Duchene muscular dystrophy results from a mutation in a gene that encodes the muscle protein dystrophin. Sufferers slowly lose muscle function due to not being able to produce this protein, with treatments aimed at mitigating this loss with steroids. It was proposed that a corrected version of the gene could be inserted into a patient's DNA via a modified adeno-associate virus (AAV) [17]. The corrected gene could, in theory, allow that patient to produce dystrophin, effectively curing the disease. Multiple pharmaceutical companies are working on AAV-based therapies for Duchene muscular dystrophy, most of which are in phase 1 or 2 clinical trials [18, 19]. Extensive testing is required for these therapies as genetic code modification can have unforeseen results causing cancerous cells or extensive immune responses by the host cells. Most notably, a gene therapy used to treat X-linked severe combined immunodeficiency (SCID) resulted in four patients from a clinical trial developing T cell leukemia 31 to 68 months after treatment [20].

Gene therapy has rapidly grown in the past 20 years, expanding to encompasses a range of potential viral vectors and targeted diseases [21]. Challenges in this field are a limited understanding of genetics, virus life cycles, human biological pathways, and the production

and commercialization of these treatments. The development of therapies through clinical trials and commercialization means the production of these viruses and resulting therapies is crucial to their success. Minimizing cost and production time is also essential to make these therapies more readily available to those who need them. The following is a review of the downstream processing of such therapies and viruses.

2.1.1 Range of viruses for gene therapy

There is a large range of viruses currently being used for gene therapy research and undergoing clinical trials. Of these, the three most used are adenovirus, AAV, and retrovirus [22]. They make up nearly 50% of all clinical gene therapy trials [1]. Each of these viruses undergoes its purification strategy specific to the vector, serotype, and upstream processing. Figures 2-1 to 2-3 have been taken from the review paper "Gene therapy clinical trials worldwide to 2017: An update" by Edelstein *et al*. [4]. Figure 2-1 shows the increase in the number of new gene therapies in clinical trials since 1989. The number of therapies in clinical trials has steadily increased over the past 25 years.

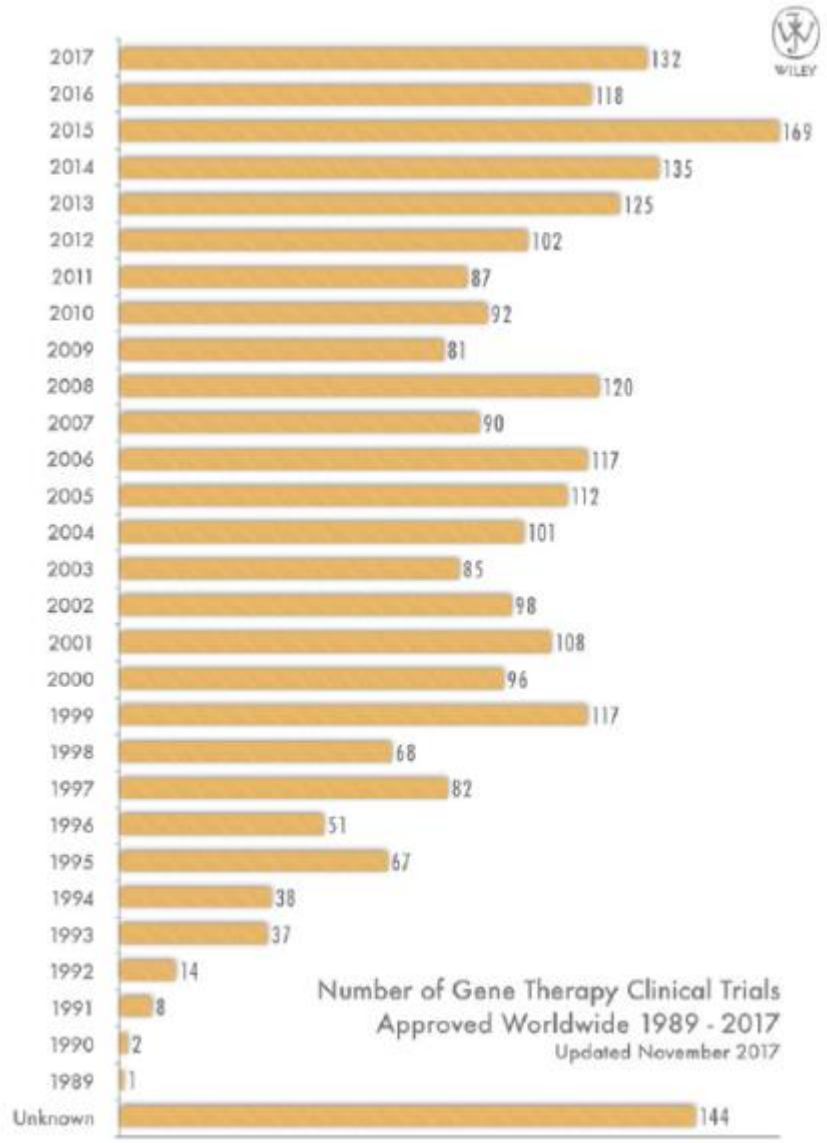

Figure 2-1: Number of new gene therapy clinical trials approved worldwide 1989-2017 [4].

Figure 2-2 shows which diseases are the main focus of the current clinical trials. Cancer treatments are the main research area for gene therapy research (65% of clinical trials) as they target the largest number of patients. Many genetic diseases are rare, affecting only a small percentage of the population.

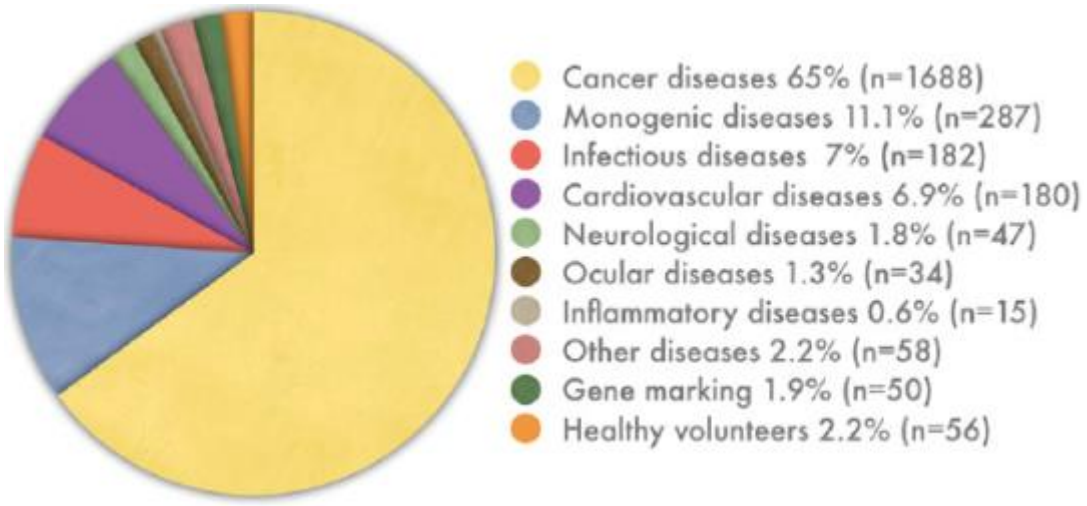

Figure 2-2: Break down of gene therapies to treat different diseases worldwide 1989-2017 [4].

The viral vector required for a specific gene therapy is chosen depending on where the gene needs to be inserted, its size, the target cell type, and other biological conditions. Figure 2-3 shows how the current clinical trials are broken down based on the viral vector used. Adenovirus, retrovirus, and AAV are the most commonly used and studied in this field. There is the potential for other viral vectors to emerge and become predominant in this field; however, based on current clinical trials, the three previously mentioned viruses will focus on this work. Viruses that infect bacterial cells are also of interest for proof of concept experiments. They have similar morphologies while being inexpensive and lower safety risks than human viruses or gene therapies.

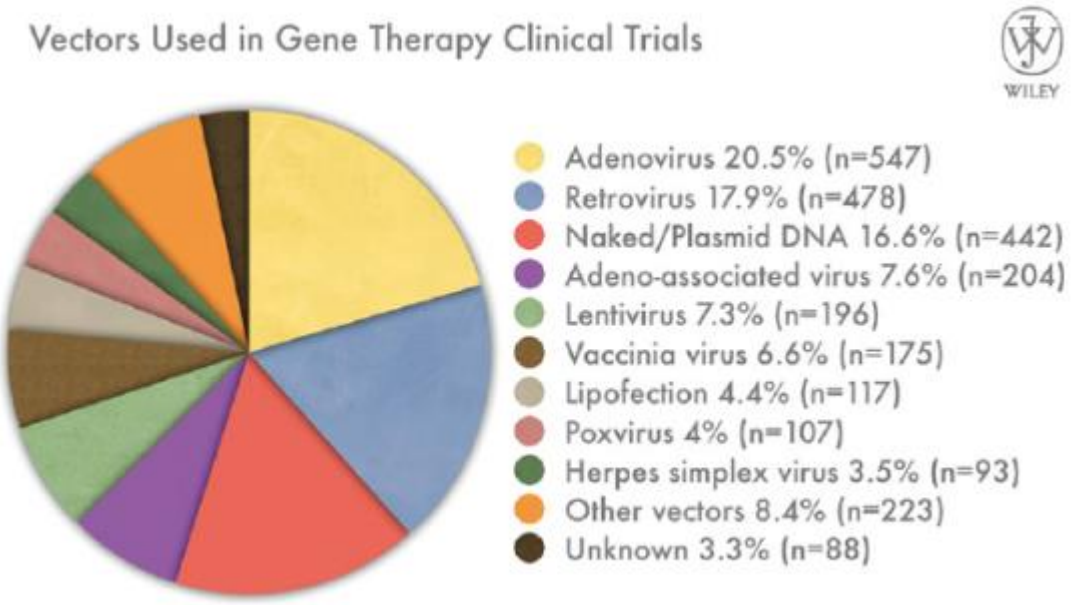

Figure 2-3: Break down of viruses used in current gene therapy clinical trials worldwide 1989-2017 [4].

2.1.2 Adenovirus

The adenovirus has a nonenveloped capsid, made up of hexon and penton proteins with an overall 70 to 100 nm diameter [23]. Figure 2-4 shows the overall structure, which has a protein fiber extending from each hexon base topped with a distal knob that interacts with the cell receptor CAR (Coxsackievirus and Adenovirus Receptor) [24]. The capsid has an overall negative charge which is often exploited to purify the virus [25-27].

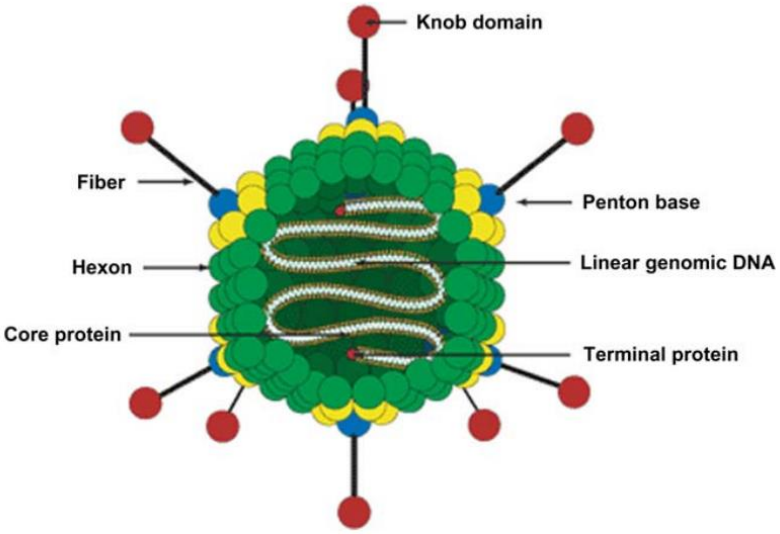

Figure 2-4: Depiction of the structure of an adenovirus [28].

The adenovirus's genetic material is not incorporated into its host's genome during infection, and it is left free inside the host's nucleus [29]. Therefore, as cells divide and replicate, new cells will not contain the virus's DNA. Therapies using adenoviral vectors are short-term and may require follow-up treatments. The replicated virus is contained inside the host cell till cell death is triggered [30]. Therefore, cell lysis is required to release the virus into the solution before downstream processing. The adenovirus is the cause of the common cold and is easily identified by the body's immune response system [31]. This immunogenic response can limit the virus's effectiveness for use as a gene therapy [32]. Deletions in the adenovirus plasmid can allow for a recombinant gene size of up to 7.5 kb [23]. Deletions are in the E1 region, which renders the virus unable to replicate without help from a packaging cell line or helper virus, and E3, which codes for immunogenic evasion not associated with virus replication [33]. Replication of recombinant adenovirus is performed in transformed HEK293 (human embryonic kidney cells with E1 plasmid) to replicate and packaging adenovirus [34]. The focus of adenovirus gene therapies is for cancer treatments to destroy tumor cells. The focus of adenovirus gene therapies is for cancer treatments to destroy tumor cells. However, other researched diseases are Duchene muscular dystrophy, cystic fibrosis, and glaucoma [35-39]. Several of which are in various stages of clinical trials [40]. Oncolytic therapies target cancer cells, causing lysis and inflammation, which in turn activates the host's immune response to target these cells [41]. Other anti-cancer therapies use the gene P-53, the gene that regulates

cell apoptosis, to reduce the size of cancerous tumors [37, 42]. Adenovirus is also used for vaccines, where the virus stimulates an immunogenic response by replicating a surface protein from a targeted virus, most recently for COVID-19 [43].

2.1.3 Adeno-associated virus

The AAV also has a nonenveloped capsid relatively smaller than the adenovirus, 20 to 30 nm in diameter [44]. It comprises three capsid proteins VP1, VP2, and VP3 expressed in the ratio of 1:1:10, respectively [45]. These surface proteins can differ between serotypes resulting in variations in the type of cells they can infect [46]. They also affect the various purification methods because of changes in binding affinity, hydrophobicity, and isoelectric point [47-50]. It is helper virus dependent, requiring coinfection with either adenovirus or herpes simplex virus to replicate [51]. Although very prevalent in the human population, the virus has not been associated with any specific disease and has a minimal immunogenic response [52]. AAV has a single strand of DNA, approximately 4.7 kb long, coding for structural and packaging proteins. Removal of these genes allows for an insertion up to 4.5 kb with the deleted genes provided in trans either by a packing cell line (HEK293) or by helper adenovirus [51]. AAV infects dividing and non-dividing cells and integrates into the host's genome site specifically [53]. This results in long-term genome alteration, with the gene being inserted into chromosome 19 nearly 100% of the time. AAV is produced in the cytoplasm and can either follow a lytic or lysogenic reproductive pathway [54, 55]. Glybera by Amsterdam Molecular Therapeutics was an AAV serotype 1 therapy approved by the European Union to treat lipoprotein lipase deficiency, although heavily criticized [3]. Only one person has ever received the drug because of how rare the disease is and the expensive one million dollar price [56]. Its approval from the European Union was not reapplied for in 2017 and is currently no longer on the market. The first-ever FDA approved in vivo gene therapy was Luxturna by Spark Therapeutics, a recombinant AAV serotype 2 used to treat Leber's congenital amaurosis retinal disease [57]. It too costs nearly one million dollars; however, it has had more success with multiple patients receiving the drug with varying degrees of success in restoring vision [57]. There are currently 204 clinical trials of various AAV taking place in 2017 compared with 547 adenovirus and 478 retrovirus trials [4].

2.1.4 Retrovirus

The retrovirus is an enveloped virus larger than both the adenovirus and AAV up to 200 nm in diameter. It contains a genome of 130 to 280 kb of which transgenes greater than 10 kb can be included [58]. The retrovirus does not contain DNA. Its genetic material is RNA, which must be transcribed into DNA before insertion into the host genome. The integrase enzyme can insert the genetic material into any arbitrary position in the host's genome, which in some cases can lead to oncogenesis [20]. Site-specific integration requires targeted retrovirus transduction by localizing the virus's delivery and addition of insulators to prevent unintended positional effects causing oncogene activation [59]. Most enveloped viruses do not require cell lysis before purification. The virus is secreted by the host cell into the culture medium through a process called budding. Lentivirus is a genus of retrovirus commonly known to cause human immunodeficiency (HIV), which can cause Auto Immune Deficiency (AIDS). Targets for lentivirus gene therapies are mostly cancer treatments and extended to ocular gene delivery, cystic fibrosis, and other genetic diseases [60-62]. Production of lentivirus can be difficult compared with nonenveloped viruses because of rapid inactivity of the virus at room temperature. Lentivirus has a narrow survivability range of pH, salt concentration, and titer, which cause rapid inactivity if exceeded [63, 64]. Lab-based culturing techniques produce low titers of these viruses, which hinders the scale-up of potential retro and lentivirus therapies [65, 66].

2.1.5 Bacteriophage

Viruses that infect bacterial cells are known as bacteriophages (prokaryotic viruses). These phages act similarly to mammalian viruses infecting a host cell and hijacking its bio-molecular machinery to replicate itself [67]. Two different replication methods can occur during bacteriophage infection, the lytic cycle or the lysogenic cycle [68]. The first involves the injection of the bacteriophage's plasmid into the cell's cytoplasm. The plasmid's genes are expressed, replicating the virus's DNA and protein coat followed by assembly and lysis of the cell. The second involves the incorporation of the phage's plasmid into the host cell's genetic material. When the host cell replicates, it copies the bacteriophage's DNA and incorporates it into the newly divided cells. Typically, at a later stage, after multiple divisions, the bacteriophages plasmid will be removed from the host's DNA and revert to the lytic cycle.

Like eukaryote viruses, bacteriophages come in various strains and serotypes that depend on different bacterial hosts to replicate. There are 13 different bacteriophage families, with 96% having tails while the other 4% are filamentous or icosahedral [69]. Typical examples of these variations in shape are M13 (Filamentous), T4 (head-tail), and cystovirus (icosahedral) [70-72]. Bacteriophages have been used as an alternative to antibiotics as they only infect and kill only bacterial cells, specifically for antibiotic-resistant infections [73]. Another more common use for them is phage display to study protein-protein, protein-peptide, and protein-DNA interactions. Common purification methods used for bacteriophages are polyethylene glycol (PEG) precipitation of aqueous two-phase systems (ATPS) [74, 75]. Purification of various phages using chromatography has given mixed results [76, 77].

2.2 Current viral downstream processing

2.2.1 Lab-scale methods

Current lab-scale viral purification methods commonly use density gradients, either with CsCl or iodixanol, for high purity separation. CsCl is toxic, and trace amounts remain in the solution after purification. Therefore, it is avoided by researchers preparing doses for clinical trials. This method is also time-consuming and produces low overall yields [78]. A benefit of this type of separation is removing empty capsids (protein coats not containing genetic material) from infectious viruses resulting in high full to empty capsid ratios [79].

2.2.2 Clinical/manufacturing scale methods

Figure 2-5 outlines the major manufacturing steps for clinical trial grade viral vectors. However, the order of some of these steps can vary depending on the vector. Before chromatography, there are multiple steps to remove solids, such as cell debris, organelles, and DNA. Smaller contaminants such as host proteins, endotoxins, and digested DNA can then be removed using packed bed chromatography. Final polishing and formulation removes any remaining impurities and changes the solution into the desired buffer for storage/delivery.

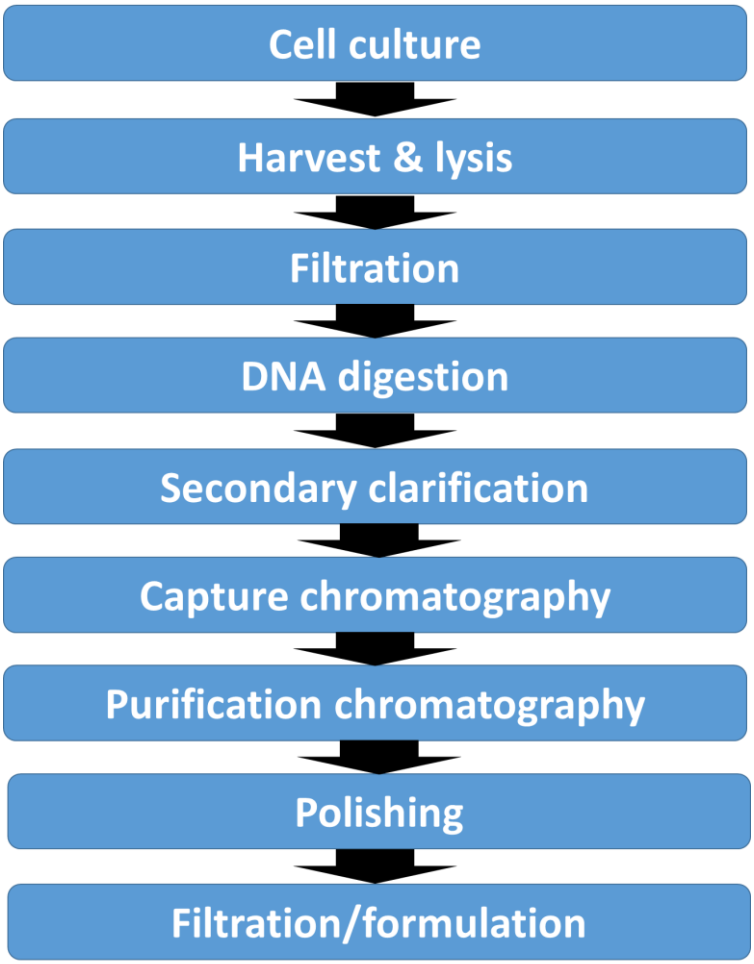

Figure 2-5: Outline of the major steps in downstream processing of virus and virus-like particles.

2.2.2.1 Cell incubation and virus replication

Developed cell lines contain plasmids for viral replication and packaging, such as HEK293 [80]. The cells contain plasmids for deleted E1 genes that are associated with the replication of adenovirus and AAV. These cells have been used for many viral host cells (lentivirus – HEK293 E or T) but mostly adenovirus and AAV [66]. Other cell lines, such as Henrietta Lack (HELA) cells, have previously been used but have been phased out because of HEK293 producer cell lines [81]. Retrovirus has been produced by trans-infection with a helper virus into HELA cells, but a packaging cell line (PSI-2) is now used for helper virus-free production [82]. Cells can be grown in a variety of ways depending on the quantity required. Cell factories, shaker flasks, and roller bottles are all used for small-scale, while perfusion and bioreactors are more common for larger scale. Transfection of the cells occurs when the required cell density is reached, typically after 48 to 72 hours of seeding growth. Cell harvest

occurs 72 and 96 hours after incubation. These growth conditions, media used, and protocols are different for each individual, cell line, virus, serotype, gene insert, and end application [46, 77, 83-85].

2.2.2.2 Virus harvest

Techniques used for cell collection and concentration vary based on host cells' growth conditions and the replicated virus. Cells grown on supports are detached before cell death by the addition of trypsin [86]. Suspended cell cultures are centrifugated or filtrated to form a cell pellet or paste, and the culture medium discarded. The discarded culture medium can contain up to 47% of the total viral production After collection, cells are lysed to mediate the release of the replicated virus into the solution. There are many different techniques for cell lysis characterized into mechanical or chemical lysis. A 3 cycle freeze-thaw method is used for lab-scale but does not scale up effectively [87]. Mechanical lysis uses shear forces or mechanical disruption to break open cell walls, for example, homogenization, bead mill, or tangential flow filtration [88, 89]. Multiple passes through a homogenizer or a fine bead mill can reduce the size of cell debris from lysis [90]. Typically, a lysis buffer such as triton X-100 is used in conjunction with an increase in agitation speed for manufacturing scale lysis [91]. The addition of other ionic detergents followed by incubation is also an effective lysis method, but removing additives downstream can be an issue. However, as of 2021, triton X-100 will no longer be used in clinical-grade gene therapies [92]. New surfactants are being developed and tested for improving gene therapy recovery rates, such as polysorbate 20 used for lysis and recovery of oncolytic viruses [93].

2.2.2.3 Clarification

The lysate from the cells contains large amounts of unwanted cell debris, organelles, lipids, and DNA that need to be removed before most chromatography forms can occur to prevent column blocking, low capacity, and fouling [94]. The initial step is to remove these larger particles (solids) by short centrifugation or lysate filtration. Centrifugation at high speed or extended periods can lead to losses in the titer of infectivity because of aggregation of the virus or sedimentation [95]. Filtration can remove cell debris, typically using membranes or depth filters with cut-off sizes (0.2 to 0.3 μm) large enough to allow the virus to pass through

[96]. Recovery rates from these sorts of filters can be upwards of 90% [85, 97]. Normal flow filtration using depth filters can also remove DNA and host cell proteins by adsorption in the membrane [98]. However, these devices' capacity is low and entirely dependent on cell culture conditions and lysate composition [99]. Filtration devices can be single-use to simplify cleaning and validation controls required by goods and manufacturing practices [97, 100]. Benzonase is used to digest leftover DNA after removing cell debris to reduce solution viscosity [101]. This digestion is also required to meet FDA regulations for host DNA levels below 10 ng/mL, no bigger than 200 bp [102]. Benzonase is an expensive nuclease enzyme that adds a considerable cost to gene therapy production. Recently, Oxford Biomedica has released a new product SecNunc™, in which nucleases are produced either within the host cell or in a helper cell-cultured alongside [103]. Then during lysis, the enzyme is released from the cells directly into the lysate.

2.2.2.4 Concentration

After primary and secondary clarification (if required), a concentration step is used to reduce volume before chromatography-based purification. Typically, ultrafiltration is employed to concentrate lysate. This reduction of volume reduces processing time and overall cost [104].

2.2.2.5 Capture and Purification

Fast protein liquid chromatography (FPLC) is currently the preferred method for the purification of viral particles. FPLC uses cylindrical columns (known as packed beds) filled with small beads (40-120 μm diameter) functionalized to adsorb target biologicals. The random nature of the packing leaves small gaps between beads allowing liquid flow. The clarified lysate is passed through said column allowing components of the lysate to be bound. After a washing step to flush through contaminates and weakly bound particles, the virus is eluted from the column by introducing counter ion or competitive species that preferentially bind to adsorption sites. Binding and elution from the column can exploit different aspects of the virus's physical characteristics [105]. Characteristics are typically isoelectric point, hydrophobicity, particle size, or cell receptor binding sites. Commonly, between two and four steps are required, the first one to two steps being the capture and intermediate purification followed by purification and polishing steps. Packed bed chromatography has been the classic

method for purifying proteins, monoclonal antibodies, DNA, and viruses. New technologies such as membranes and monoliths are also explored later in this review.

2.2.2.6 Ion exchange

Ion exchange is an effective purification method because of its high bind capacity and resolution [106]. Ion exchangers can be used as the capture step or the purification step, or in some cases, both [107]. It relies on the electrostatic charge of the capsid or envelope of the virus. The stationary phase's functional ligands will either have a positive or negative charge to bind the opposite charge. Anion exchange purification of adenovirus, AAV, and lentivirus is possible because of their negative charge at pH 7 because of an overall acidic isoelectric point [108, 109]. Purification using cation exchange requires biologicals with a basic isoelectric point. Cation exchange purification of AAV requires specific pH conditions that limit its use [110]. Cation and anion exchange work for binding viruses because of the large size of the virus's capsid or envelope containing both positive and negative patches of their surfaces, even though the overall charge may be negative.

The binding of viral vectors occurs at higher conductivities than that of proteins and endotoxins, allowing them to be separated effectively. DNA is highly negatively charged and will elute off at a greater salt concentration after the virus has been eluted, providing separation [95]. Anion exchange can also separate infectious viruses from empty capsids. Empty capsids are unwanted by-products of viral therapies as they will stimulate an immune response without infecting the host cell with the gene of interest. Full and empty capsid have slight differences in isoelectric point, allowing for elution at different conductivities from an anion exchange column [48, 111, 112].

Recently, membrane and monolithic supports for anion exchangers have shown larger capacities for binding [113]. Lentivirus vectors have been purified by anion exchange chromatography while maintaining high gene expression levels and recovery from the column of 68% [114]. Anion exchange methods have also been described for pseudotyped HIV-1 based lentivirus vectors for purification and concentration up to 10^{10} transforming units per mL (TU/mL) [115]. Adenovirus was purified using a range of anion exchange resins with a recovery of 75% for dynamic binding capacities of 1.2×10^{10} plaque forming units per mL

(pfu/mL) [26]. Anion exchange has been used extensively for AAV purification over a range of serotypes; The purification of clinical-grade AAV serotype 8 achieved a recovery of 41% and a 90% purity [116]. The purification of AAV serotypes 1, 2, and 5 by anion exchange has produced 99% pure stocks with titters of 1×10^{12} to 1×10^{13} vector genomes/ml (VG/mL) [117]. Work on AAV serotypes 2, 8, and 9 for human gene therapies have provided similar results [118]. Purification of M13 bacteriophage with anion exchange managed a recovery of 74% [76]. A cation exchange packed bed column was used to purify AAV serotype 2 gene therapy encoding cystic fibrosis transmembrane chloride regulator [119].

2.2.2.7 Size exclusion chromatography (SEC)

SEC for purification of viruses and virus-like particles does not involve adsorption to the column; instead, it relies on the proteins and smaller molecules being slowed in pores while the comparatively larger virus is eluted in the flow-through or just thereafter [79]. This effect is caused by these resin beads' pore size, which is large enough for proteins to diffuse into but exclude the larger viral particles. As size-exclusion relies on smaller particles' diffusion into pores, it is very slow compared with other chromatography methods. The resolution also deteriorates if sample volume exceeds 4-5% of the bed volume [95]. However, it is still a useful technique used across all viral purifications, often as a polishing or purification step [120]. Taking advantage of convective transport instead of diffusion can enchant SEC. Monoliths and membranes for size exclusion typically can operate at a flow rate 10 to 20 times faster while offering better resolution than packed beds [44]. Viral particles leave the column in the equilibrium buffer allowing reformulation of the solution. SEC is an attractive polishing step for viral purification.

GE has designed Capto Core 700 to polish adenovirus serotype 5 to meet new regulatory requirements for DNA and host cell protein (HCP) levels [121]. Purification of adenovirus serotype 5 by SEC in a two-column open-loop system gave a recovery rate of 86% [122, 123]. DNA and HCP clearance was found to be 90% and 89%, respectively. DNA and HCP clearance was to be 90% and 89%, respectively. Running two SEC columns in the loop type series system increases recovery up from 45% and increases load capacity and reduces purification time.

SEC is predominantly a polishing step used for lentivirus and AAV of various serotypes [64, 66, 117, 118, 124-126].

2.2.2.8 Affinity

Affinity chromatography involves binding viral particles to highly selective ligands attached to a solid phase support media. Porous media dominate this field, typically optimized for proteins, resulting in pore sizes between 60 to 100 nm. Viral particles are too big to diffuse into these pores at standard flow rates. This limits interactions of the virus with the support media's surface, reducing the binding capacity of columns However, highly selective binding can still be effective at viral separation using heparin affinity for some AVV serotypes and lentivirus [51, 127]. Heparan sulfate proteoglycan (HSPG) is a cellular receptor that binds AAV used for affinity chromatography. It is not used widely at clinical or commercial scale because of column leaking and the toxicity of HSPG [128]. Newly developed AVB affinity resin and POROS AAV CaptureSelect for AAV purification make use of single-domain antibody fragment to bind and elute a range of AAV serotypes. These resins have shown a great affinity for AAV particles with recoveries between 70 - 90% [129-131]. However, as an affinity resin, ligand leaking is still an issue with the need for detection kits to measure how much of the camelid antibody fragment has leached into the eluent [132, 133].

2.2.2.9 Immobilized Metal Affinity Chromatography (IMAC)

IMAC is a variation on affinity chromatography taking advantage of specific interactions between proteins and metal ions. Metal ions are bound to a support media in a complex with a chelating ligand. Subsequently, bound viral vectors can be then eluted with a change in pH or the addition of competitors such as Ethylenediaminetetraacetic Acid (EDTA) or imidazole [95]. The most common is the purification of histidine-tagged (HIS-tagged) proteins by Nickel (II) affinity [134, 135]. Purification of adenovirus is possible using the interaction between the virus and Zn^{2+}or Cu^{2+} ions. IMAC has successfully purified AAV by the addition of a HIS-tag into the viral capsid. This modified AAV serotype 8 achieved a recovery of 90% in one step [136]. Herpes simplex virus type 1 has also been purified by IMAC chromatography using an immobilized cobalt column with a recovery of 90% [137]. This technique also suffers from

leaching similar to affinity chromatography. Metal ions can become detached from the support material and be found in the purified solution.

2.2.2.10 Hydrophobic interactions (HIC)

This method of purification employs a hydrophobic stationary phase and an aqueous mobile phase. Binding relies on hydrophobic interactions between the viral vector and the stationary phase. Higher conductivities allow the virus to bind to the stationary phase; usually, ammonium salts are used with butyl or phenyl ligands for the stationary phase. Deformation of proteins can be common in HIC, but proteins tend to refold when eluted as such viral particles may suffer the same fate but be unable to configure themselves back to their original structure[79, 95]. HIC purifications are ignored for purifying infectious particles but are still used for some quantitative analysis.

2.2.2.11 Multimodal chromatography

Multimodal chromatography uses two or more discrete mechanisms to bind and elute specific target proteins or viruses. These types of media provide a unique and selective binding at the cost of complexity. The most commonly used for viral purification is hydroxyapatite (HA), a mineral of calcium and phosphate. The phosphate group acts as a strong cation exchanger, while the calcium group provides metal coordination binding sites [138, 139]. Elution with a phosphate salt gradient causes the conductivity increase to elute the cation exchanger component while the phosphate ion competes for the calcium affinity sites [140]. Sodium chloride elution gradients are also possible where the increased conductivity elutes the cation exchange part of the media, but the chloride ions do not elute off the calcium affinity component. This variation in elution buffers allows a completely different set of selectivities. Enveloped viruses show strong binding to HA's calcium component through exposed phosphate groups. This suggests phosphate gradients may be better suited for enveloped viruses such as retrovirus and lentivirus, while sodium chloride gradients may work better on non-enveloped such as adenovirus and AAV [79]. Many AAV and adenovirus purifications have been commercialized and patented using an HA step in the process [141-145]. Most notably, purification of AAV serotype 2 using HA in conjunction with an anion exchange step to yield a 90% purity [146]. A two-step purification of poliovirus used both

ceramic HA and fluorapatite, removing 99% of host cell proteins and double-stranded DNA [147]. HA has not been as prolific for the purification of lentivirus. Elution conditions required by hydroxyapatite purifications can cause viral inactivation because of the narrow range of pH and salt concentration the virus can survive in.

Other forms of multimodal functionalities combine ion exchange and SEC by covering ion exchange beads in a layer of inert porous material. This outer layer excludes larger molecules from reaching the ion exchange binding sites. Multimodal anion-SEC for the polishing step of viral purification has shown promise with the range of Capto™Core resins. Notably, purification using this type of multimodal resin includes yellow fever virus for inactivated vaccine manufacturing and the separation of enveloped virus-like particles from extracellular vesicles [148, 149]. Combinations of hydrophobic interactions and anion exchange are also available but have not been used for virus purification [150].

2.2.2.12 Polishing

After intermediate purification, smaller trace contaminants remain, which need to be removed by a final purification step. Polishing requires high-resolution chromatography, typically anion exchange or SEC (gel filtration). Contaminants could be traces of DNA, endotoxins, helper virus, or empty viral capsids [151]. SEC or gel filtration is the most common polishing step next to anion exchange [107, 152]. The final steps after polishing of the viral particles are correct buffer formulation for storage and FDA approval

2.2.3 Lysate particle size distribution

Crude cell lysate is a soup-like mixture containing proteins, lipids, organelles, DNA, and various biological components. Table 2-1 outlines the size distribution of some potential contaminants and varying viruses found in cell lysates.

Table 2-1: Size of particles in potential cell lysate [44, 153-156]

Particle	Diameter nm
AAV	20-26
Minute virus of mouse	25
Rhinovirus	30
Hepatitis B	42
Adenovirus	59-67
Epstein-Bar virus	80-100
HIV	100-120
Herpes simplex virus	110-200
Murine leukemia virus	120-150
HEK293 cells	13000
Mitochondria	200-700
HELA	20000
Nucleus	8000-10000
Cell debris (bacteria)	200-500
Cell debris (mammalian)	<5000~
Cell debris (CHO)	<7000~
Cell debris (mammalian, homogenized, 5 passes)	1000~
HELA median HCP size	3-8

As previously mentioned, cell lysate needs to be clarified to remove larger solid particles before loading onto chromatography columns to prevent fouling. Cell lysate can contain many particles with varying sizes depending on the cell lysis techniques employed. Multiple passes through a homogenizer can minimize cell debris to around 1000 nm [90]. However, more passes through the homogenizer could increase the risk of losing infectious viruses by

shear forces. It is important to know what contaminants are present and their size distribution for SEC purification.

In current manufacturing, clarification (the removal of solids such as cell debris and large molecular weight molecules) occurs using centrifugation or filtration [95]. The large weight and size difference provides a simple method for debris removal but can result in losses in infectious particles. There has not been adequate research detailing cell lysates' particle size distribution or the effects cell lysis conditions have on cell debris size. Digestion of DNA by Benzonase can reduce the size of DNA can be reduced down to below 10 base pairs and reduce solution viscosity [101]. Digestion is an essential step in any chromatography-based purification of viruses, as the reduction in viscosity is needed to allow flow through the column to avoid high back pressures.

2.2.4 Column loading potential

Chromatography media was originally designed for protein purification with pore sizes between 50 to 100 nm. The same beads are used for viral purification and have significantly lower binding capacities than those observed for proteins [157]. This lower capacity is because of the virus not being able to penetrate the beads' pores, limiting the virus to the chromatography beads' surface. Pore sizes over 4× larger than the viral vector still exhibited monolayer binding on the surface. This monolayer is because of the strong binding of the virus at the pores' entrance, resulting in pore blockage or steric hindrance [158]. Therefore, the pore size may need to be an order of magnitude larger for the viral particles to penetrate the pores and increase potential binding capacity.

The dynamic binding capacity (DBC) of adenovirus serotype 5 on an anion exchange resin was $1.2 \times 10^{10}\ VP/mL$ from clarified cell lysate [26]. This DBC is the benchmark for viral binding capacity for current anion exchange chromatography media. This purification used clarified lysate, where cell debris and host DNA are considerably less than crude lysate. Therefore, the binding capacity may be much lower for crude lysate because of biomass contending for binding positions on the chromatography media. However, purification of adenovirus serotype 5 by expanded bed chromatography from crude lysate gave a DBC of

$1.1 \times 10^{10}\ VP/mL$. This capacity is only slightly less than what was found for purification from clarified lysate [159].

The volume of lysate loaded depends on the concentration of viral particles, which may vary depending on upstream processing and virus production. Many papers only start taking note of viral concentration after initial filtration and clarification; however infectious particles may be lost during these steps [95]. Purification of adenovirus by continuous two-column quasi-continuous SEC allowed for the increase of loading volumes from the recommended 1 to 5% of column volume to 20.7% [152]. It also increased virus recovery and reduced processing time significantly. Optimization of ligand density for anion exchanger hydrogel membranes showed a medium-density (2.2μmol/cm²) provided the best recovery rate for adenovirus [8].

2.2.5 Chromatography performance

Various identifiers can be examined to determine a chromatography column's performance and used for comparisons. The main three examined in this work are asymmetry, theoretical plate height (HETP), and binding capacity (dynamic and static). Both asymmetry (A_s) and HETP can be determined from residence time distribution data from a pulse test (tracer experiment). An example peak can be seen in Figure 2-6, taken from a GE Healthcare pamphlet on column efficiency [160]. A_s is a measure of how symmetrical an elution peak from a column is. It is defined by the ratio of the length of one side of the peak (b) (at 10% of the peak height) to the other side (a). Typical values for As in packed bed columns are between 0.8 and 1.8. It can also be an indicator of column channeling, blocking, or poor packing.

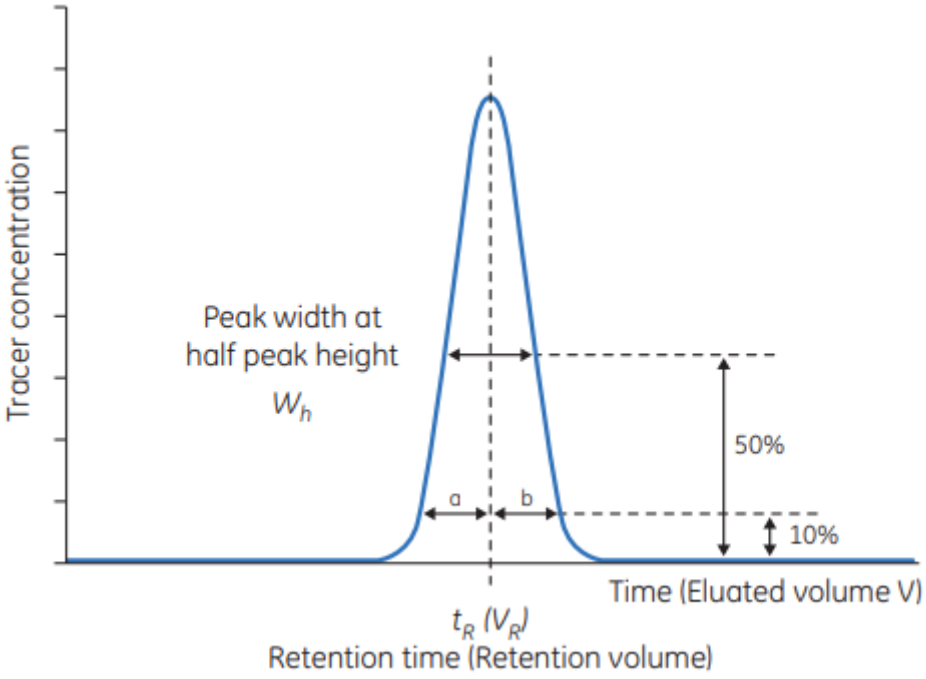

Figure 2-6: Example of a tracer elution peak from a packed bed chromatography column [160].

HETP is a measure of column resolution, identified by how narrow and tall a peak elution is in addition to the column's bed height. HETP can be calculated from the following equation 2-2, where L is the length of the column:

$$HETP = \frac{5.54}{L} \times \left(\frac{v_r}{W_h}\right)^2, \quad (2\text{-}1)$$

The lower the value of HETP the better resolution you should expect from the column. The reduced plate height (h_{min}) can then be calculated from the HETP by dividing it by the beads' particle diameter (D_p).

$$h_{min} = HETP/D_p, \quad (2\text{-}2)$$

The reduced plate height can be used to compare between columns of varying bed height and particle size. For traditional packed beds, for optimal column performance, h_{min} value is suggested to be below 3.

Multiple pulse tests are carried out over a range of flow rates to compared theoretical plate height values to determine the best operating flow rate. A plot of HETP by flow rate is a Van Deemter plot, as shown below in Figure 2-7. The Van Deemter plot curve shows the best operating flow rate, which occurs at the minima. The Equation shown in Figure 2-7 describes the coefficients (A, B, and C) that give rise to the graph's tick shape. A is a constant value that describes random eddy diffusion within the system regardless of fluid velocity (u). B describes the longitudinal molecular diffusion through the column, which is minimized at higher flow rates. C represents the mass transfer limitations of the system, which rise with an increase in flow rate. Additionally, determining the slope to the right of the minima provides information regarding maximum operating flow rates. The more gradual the slope, the larger the operating range of flow rates possible near peak system performance. Higher flow rates are more desirable to minimize processing times for chromatography steps.

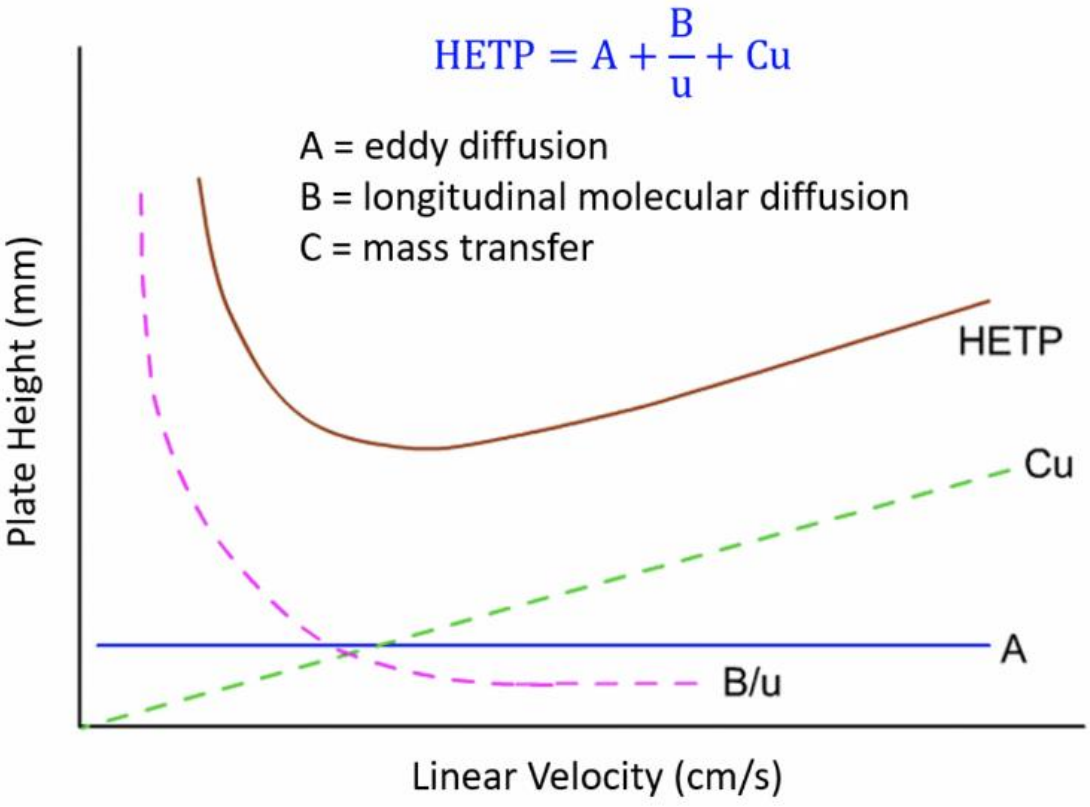

Figure 2-7: Example of a Van Deemter plot [161].

A reduction in particle diameter can minimize the HETP for a packed bed chromatography system [162]. However, this will increase the pressure drop across the column. Optimization of flow rates, particle size, and pressure drop are required to maximize column production while maintaining efficiency.

2.3 Alternative purification techniques

2.3.1 EBA chromatography

EBA chromatography can separate proteins from crude lysate material without the need for a prior clarification or filtration step. It can be a combination of clarification, concentration, and an initial purification capture step. Unlike packed bed chromatography, the crude lysate is pumped to flow up through a fluidized bed of porous beads where the target protein or virus can interact and bind with the chromatography media while all the unwanted contaminants pass through (cell debris, cell culture medium, and cell DNA) [163-165]. After a long wash step, the protein is eluted off the column by changing pH or conductivity. The benefit of expanded bed chromatography over a packed bed is its ability to passage solids because of the fluidized bed. EBA allows for purification directly from crude cell lysates or culture fluids. EBA can suffer from a variety of issues resulting from the column's load material and bed fluidization. Figure 2-8 shows a comparison between a packed bed and an expanded bed system.

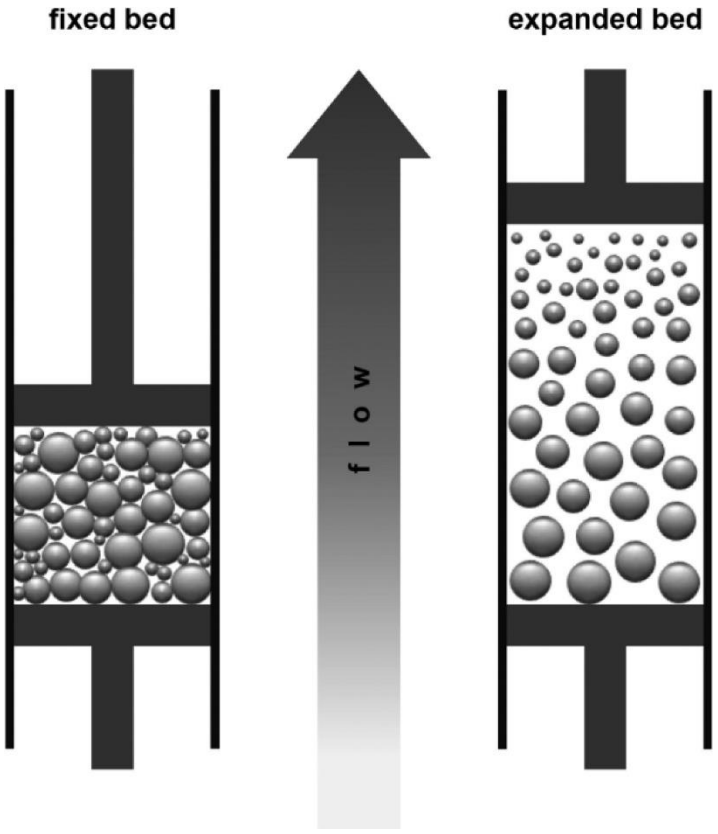

Figure 2-8: Comparison between a packed (fixed) bed chromatography column and an expanded bed column [166].

Crude lysate contains significant amounts of biomass, non-targeted proteins, lipids, and other unwanted particles. These unwanted particles can deposit themselves onto the chromatography media, reducing available binding sites and disrupting column flow [167]. Excessive biomass significantly affects anion exchange media as cell membranes, DNA, and proteins from host cells are typically negatively charged. Biomass fouling is less common in cation and affinity adsorbents than anion exchange resins because of their specific binding requirements or negative charge [168]. In attempts to reduce bio adhesion during loading of EBA columns, higher conductivities resulting in reducing unwanted particles' zeta potential have proven effective [169]. However, this is only effective to a point, as conductivity plays a crucial part in binding targeted proteins, so an upper limit to this effect is quickly reached. Reducing cell debris size has been correlated with reducing zeta potential, resulting in less bio adhesion of unwanted particles [90]. However, breaking down the cell into smaller pieces requires higher shear forces resulting in protein degradation and activity loss. Therefore, potential viral capsid damage could also occur when trying to reduce cell debris size. The expanded bed flow rate is also limited and must remain constant once set to maintain the bed expansion to around two to three times its packed size.

Specifically, for EBA chromatography, coating the resin beads with a high molecular weight polymer has been found to stop biomass deposition on the resins' surface. A highly negatively charged polymer like PAA (Poly(acrylic acid)) has been used to reduce the binding of cells to anion exchanger resin's surface during purification [170]. If the coating is too dense, the polymer can affect the resin's binding capacity, blocking the entrance of the pores for proteins to diffuse into. A cross-linked coating of agarose reduced bio deposition for E. coli cells and cell debris during purification [171]. Agarose provided a more stable coating than PAA, which suffered from leaking into the solution at higher conductivities.

A one-step anion exchange EBA purification of adenovirus gave a recovery of 32% infectious viral particles and a concentration factor of 5 using a quaternary amine (Q) resin [159]. Additionally, the VP: IU (viral particles to infectious units ratio) was 13:1, within the FDA's 30:1 range [172]. The crude cell lysate was loaded onto the expanded bed without the need for

centrifugation or filtration, allowing for the binding of viral particles present in the culture medium because of early cell lysis [173].

Anion exchange EBA purification of M13 bacteriophage gave a recovery of 82% [174]. This bacteriophage is a good candidate for expanded bed purification as the particles are secreted out of the cell without requiring lysis. Without the need for cell lysis, there is significantly less DNA and other negatively charged contaminants in the solution to compete with the M13 particles for binding.

2.3.2 Monoliths

Monoliths are a single piece stationary phase (column) used as an alternative to packed bed chromatography. They contain a random interconnected porous structure that acts as flow channels through the column. Monoliths are one interconnected piece capable of higher fluid flow rates and back pressures than conventional packed beds [175]. The main difference between packed beds and monoliths is how solutes are transported to and from the surface. Where packed beds rely on diffusion, monoliths use convection imposed by the mobile phase's pressure [44]. Convective transport occurs faster than diffusion, which tends to limit larger molecules such as viruses, as it is relative to the velocity of the mobile phase not the size of the particle. Because of the monolith's porous nature, a larger number of binding sites are available, resulting in monoliths having higher capacities than packed beds. Monoliths exhibit clogging/fouling of pores, especially when high host cell DNA is present in lysate, but it has been suggested increasing pore size up to 6 nm could solve this issue [176]. Monoliths can be functionalized with ligands for ion exchange (cation and anion), affinity, IMAC, or hydrophobic interactions.

Monoliths are an emerging technology for protein and virus purification. researchers used a monolith composed of chitosan and poly(vinyl) alcohol (50:50) was used to recover adenovirus serotype 5 by anion exchange [7]. Development of a streptavidin derivatized macro-porous monolith enabled a single-step capture of chemically biotinylated Moloney Murine Leukaemia virus by affinity chromatography [177]. Although only 8% of recoveries were achieved, it was a proof of concept for monolithic purification from crude load material.

More effective capture of proteins from crude lysate has been performed with a super macro-porous monolith with pore sizes ranging from 10 to 100 μm [178]. However, monolith fouling is an issue with caking forming on the column's top or at the inlet. Lipid fouling from clarified supernatant reduces binding capacity and increase back pressure [179]. In an attempt to prevent fouling, another epoxy monolith was used to first remove lipids from the supernatant, essentially adding in a clarification step [180].

Purification using a CIM® QA monolith was employed for influenza A virus for vaccines yielding 98% recovery and 52% reduction of host cell DNA and HCP, respectively [181]. Icosahedral bacteriophage PRD1 was purified using Q and dimethylamine (DEAE) anion exchange monoliths with yields of infectious particles up to 80%. Purified particles were eluted in high concentrations of approximately 5 mg/ml [182]. A range of monoliths made from biomaterials has also been tested and characterized for the purification of adenovirus. Variations of chitosan, dextran, agarose, and polyvinyl alcohol created various porous structures from freeze-drying. The resulting structures functionalized with Q anion exchange ligands gave recoveries between 33 to 70% [183].

2.3.3 Membranes

Membranes are microporous sheets typically made of polymers wrapped into spherical rolls to maximize surface area per volume. They allow for higher flow rates as most of the mass transfer occurs by convection like monoliths; however, unlike monoliths, membranes do not suffer from high-pressure drops. As with advances in monoliths, membranes are also seeing increasing use for viral purification. Porous membranes functionalized with ligands for affinity and ion-exchange chromatography have purified adenovirus, AAV, and influenza virus [184, 185]. Like monoliths, membranes use convection rather than diffusion to facilitate the transport of solutes to and from the pore surface. Therefore, membranes use higher flow rates and have better dynamic binding capacities than conventional packed bed chromatography; however, membrane capacity is roughly 1/3 compared with monoliths [44]. Rotavirus-like particles have also been purified from a clarified lysate using an anion exchange membrane [186]. Although recovery was low in this case, it still provides a starting point for optimization and proof of concept. Work on ligand grafting and optimization of

grafted ligand densities has provided a 5-fold increase in the dynamic capacity for adenovirus purification. This optimized membrane with a ligand density of 2.4 μmol/cm2 gave a recovery of 60% [8].

Alternative membrane configurations are also being trailed, such as lateral flow (LFMC) instead of radial flow using different flow distributors. LMFC was used to purify adenovirus on a small scale with recoveries of 90% and HCP and DNA below 10% of load amounts [9]. Metal affinity Sartobind iminodiacetic acid (IDA) membranes have purified adenovirus with comparable recoveries to packed bed chromatography [187]. Additional to the benefits of higher flow rates and reduced production time, membranes can be single-use. This style of product is attractive to the pharmaceutical industry as an alternative to vigorous Clean In Place (CIP) methods to ensure equipment is sanitized and cleaned to FDA standards [92].

2.3.4 Miscellaneous purification strategies

ATPS formed by the mixing of two different liquid polymers has been used to purify adenovirus. Purification from crude lysate separated the adenovirus from contaminants capturing it in the top phase. The two-phase solution PEG 300- phosphate (20%, w/w PEG 300, 20% K2HPO4–KH2PO4 ratio 18:7, pH 7.5) gave a recovery of 82% from crude lysate [188]. AAV serotype 8 has also been purified by ATPS [189].

Chromatography methods currently run a positive capture mode where the virus is bound to the stationary phase and eluted after contaminants have passed through. Alternatively, purification is possible by negative mode chromatography where contaminates are bound to the column, and the virus is in the flow-through/non-bound phase. While being relatively new, resins and stationary phases specifically designed to run in this mode are being developed [190].

2.4 3D printing technology

2.4.1 General 3D printing

Additive manufacturing or more commonly termed 3D printing, has been around since the 1970s but has only recently become common technology [191]. Advancement in affordability and availability has increased its popularity and showcased its potential uses from bespoke plastic components for cars, airplanes, and computers, to patient-specific medical implants and dentistry [192-194]. Four forms of 3D printing are material extrusion, vat polymerization, material jetting, and powder bed fusion. Schematic style drawings of each printing technology as shown in Figure 2-9 [195]. Material extrusion or Fused Deposition Modelling (FDM) is the most common. A heated nozzle liquefies a feed filament of plastic that is pushed through an extrusion tip. This nozzle can then move along the X and Y axis, laying down the filament, which quickly cools and re-solidifies. The printing stage can then be moved down a set amount from the nozzle for another layer to be deposited building up the structure. Material extrusion has created microfluidic on-chip systems for automated colorimetric enzyme-linked immunosorbent assay (ELISA) to detect malaria [196].

Vat polymerization works because of the chemistry of resins that cure with UV light. A stage is dipped to be touching the top of a resin vat. A UV light of a particular pattern and wavelength is then shown onto the stage to cure the resin. The stage is drawn down so that the cured resin pattern is just touching the surface of the vat and a new pattern is shone through. This process is repeated building up the structure out of the resin vat. The structure is then washed in Isopropyl Alcohol (IPA) to remove the excess resin before a secondary UV curing process to complete the curing process and strengthen it.

Material jet printing uses existing inkjet printing technology applied to waxes and plastics to build up structures layer by layer [197]. A fine nozzle head sprays down small droplets of liquefied wax or plastic as it moves along the X and Y-axis. The printing stage is then lowered, similar to material extrusion, so that the printer can add another layer. The difference between material jet printing and material extrusion is layers are built out of combinations of small droplets instead of a continuously extruded filament. Jet printing offers a higher level of

precision because of the droplets' size compared with the extruded filament. Material Jet printing of wax has allowed for the fabrication of microfluidic channels not possible with other printing methods. The high precision offered by material jet printing can create channels with features as small as 100 μm [198, 199]. Wax printing has also helped fabricate tissue scaffolds with bio-compatible waxes and create a hydrogel scaffold using a negative templating method [200].

Powder bed fusion printing is specific to metal printing [201]. Small spherical beads of metal are spread evenly over a stage where a laser or electron beam can tracer over a pattern, sintering the beads together. The stage is then lowered, and more powder is spread across the stage. This process is then repeated, building up a structure. The 3D-printed part is porous because of the sintering process.

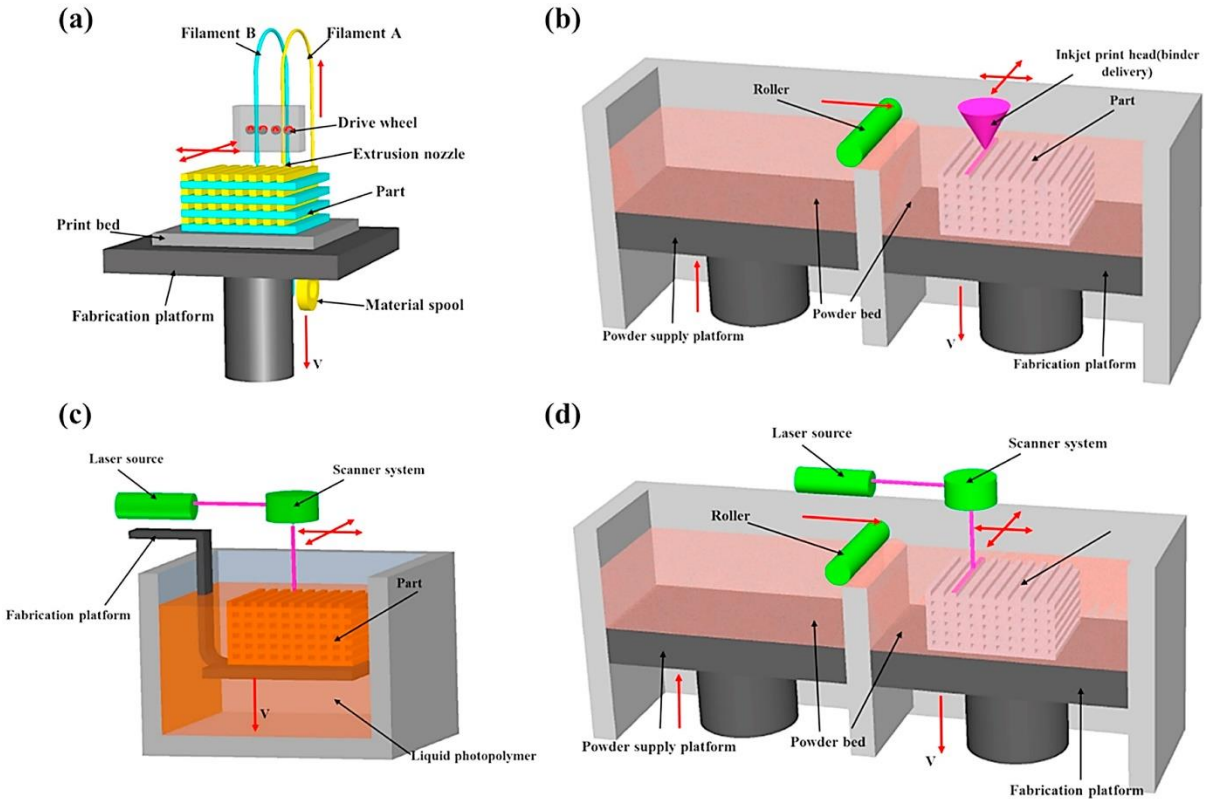

Figure 2-9: Schematic displaying each additive manufacturing technique. FDM (a); Material jet printing (b); Vat polymerization (c); powder bed fusion printing (d) [195].

2.4.2 3D printing for chromatography

3D printing in chromatography began in 2014 where the first structures were printed out of UV cured acrylonitrile-butadiene-styrene powder layers [202]. Comparisons between the 3D-printed structures and simulated models for ordered packed beds showed a close resemblance in performance. Further modeling showed improved performance over randomly packed beds of beads, with lower theoretical plate numbers for ordered structures [203, 204]. Advancement in printing technology allowed for 3D-printed wax templates via material jet printing [205]. Templates in the shape of triply periodic minima surfaces (TPMS) such as the Schoen gyroid were printed on a Solidscape 3Z Pro out of paraffin-based wax. A solution of either dissolved cellulose or agarose could be injected into the template's void spaces and solidified. The wax template was then melted away in boiling water, leaving behind the hydrogel-based 3D-printed column [15]. Functionalization of these columns with both anion and cation exchange ligands allowed the binding and elution of proteins. Direct printing of TPMS structures using thermal laser gelation of dissolved cellulose solution similar to vat polymerization printing provided mixed results [206]. Although possible, the resolution and troubleshooting issues of this technology prevented further development. Columns produced by 3D printing are single piece like monoliths; however, they differ by having defined ordered flow channels rather than randomly connected pores. They allow for any number of conceivable flow structures or packing geometries; additionally, flow distributors and collectors can be printed as a part of the column [202]. Control over packing can optimize reduced plate heights and other flow characteristics such as tortuosity that can affect performance [204].

Simon & Dimartino developed a 3D-printed stationary phase for chromatography [207]. They used UV-cured polymers functionalized with quaternary amine groups to produce a monolithic structure with ordered TPMS channels. They have also shown comparable Bovine Serum Albumin (BSA) protein binding capacities to commercially available packed bed resins and purification of protein directly from a simulated cell broth. The 3D-printed stationary phase was unaffected by the solids (cells) in solution [208]. Their process is currently limited by the printable structures' resolution and size because of the mechanical properties of the

solid phase and light scattering during printing. A different 3D-printed stationary phase for analytical planar chromatography was developed by Macdonald *et al.* [209]. The Thin Liquid Chromatography (TLC) plate separated small amounts of different dye molecules and proteins. There are no reported 3D-printed chromatography stationary phase columns used to purify viruses or virus-like particles reported in the literature at the time of this research.

Previous research suggests a 3D-printed monolithic columns of a triply periodic minimal surface (TPMS) such as a Schoen gyroid could purify virus or virus-like particles in a similar way to EBA chromatography [16]. Where the flow channels are large enough to passage solids allowing for purification directly from cell lysates and culture fluids. The governing equation for a Schoen Gyroid is shown in equation 2-3, where l is the length of a single unit cell of the repeating shape. The surface divides a given volume equally when t = 0 [210].

$$\sin\left(\frac{2\pi x}{l}\right)\cos\left(\frac{2\pi y}{l}\right)+\sin\left(\frac{2\pi y}{l}\right)\cos\left(\frac{2\pi z}{l}\right)+\sin\left(\frac{2\pi z}{l}\right)\cos\left(\frac{2\pi x}{l}\right)=t, \qquad (2\text{-}3)$$

Therefore, by printing a solid phase at all points where t is negative, a uniform periodic repeating network of channels is created. For reference, Figure 2-10 shows how the gyroid surface intersects a given volume. The Schoen Gyroid has been printed out of metal by additive manufacturing showing the complex shape can be constructed using this new manufacturing technique [211]. The Schoen gyroid is one of many different TPMS structures possible, defined by geometric equations [212].

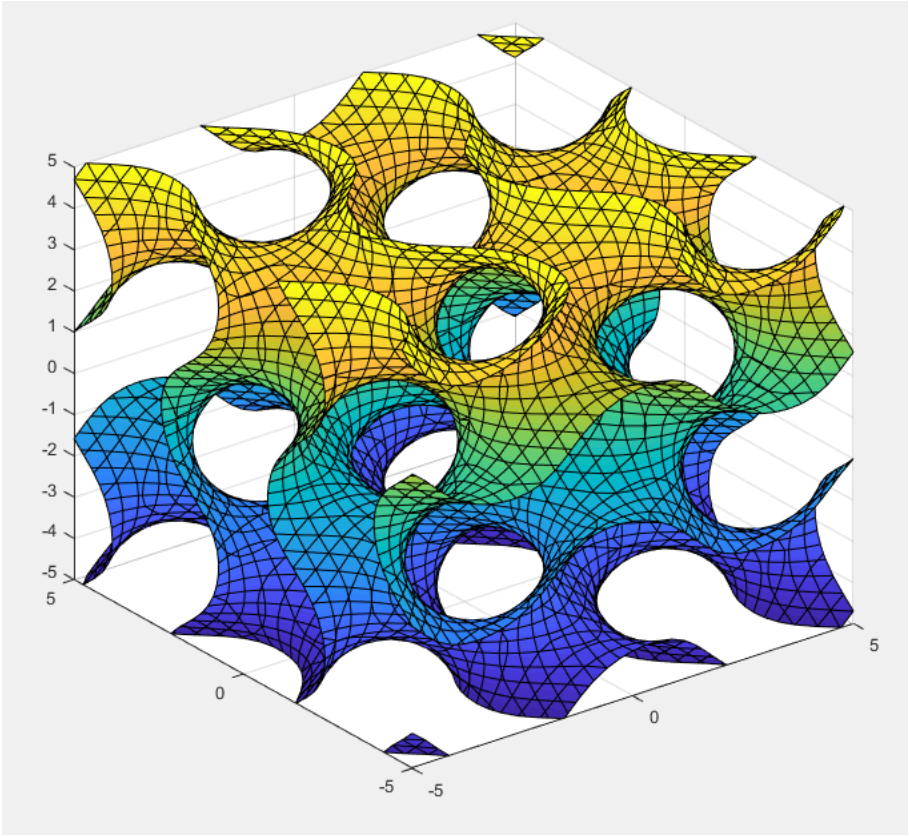

Figure 2-10: Matlab plot of the surface of a Schoen gyroid.

As previously mentioned, research by Conan Fee has suggested the possibility of using 3D-printed TPMS columns of cellulose hydrogel to facilitate the capture and purification of virus and virus-like particles from crude cell lysates [16]. The column's channels should allow cell debris and other larger contaminants to pass through easily while viral particles can penetrate the micro-pores. Anne Gordon confirmed this in her thesis "Development, Functionalization, and Characterization of Triply Periodic Minimum Surface Hydrogels for Solid-Tolerant Chromatography" [15]. Her work showed that 3D-printed columns were solid tolerant while binding and eluting proteins separating them from a broth of yeast cells. Both anion and cation ion exchange functionalities could be applied to agarose and cellulose columns to facilitate binding.

2.4.3 3D modelling

All printers require a 3D model of the desired structure in a specific file format, typically standard triangle language (STL). Each model has points in space that are connected to form triangles. The more triangles there are per a given area, the high the resolution of the structure. Figure 2-11 shows two Schoen gyroid columns that have been created with varying resolutions. Like other modeling software, Slicer software has limitations when working with large files. There is a compromise in terms of resolution and file size, especially for TPMS column structures. File sizes can quickly grow to multiple gigabytes because of the small size of the complex channels and the overall column's potentially large size. The model is translated into G code by the slicer software, which gives the printer direct instructions about printing the structure. Slicer software divides up the structure's Z-axis into traceable layers of a set thickness (layer height). This G code contains directional commands for each layer that the printer can follow.

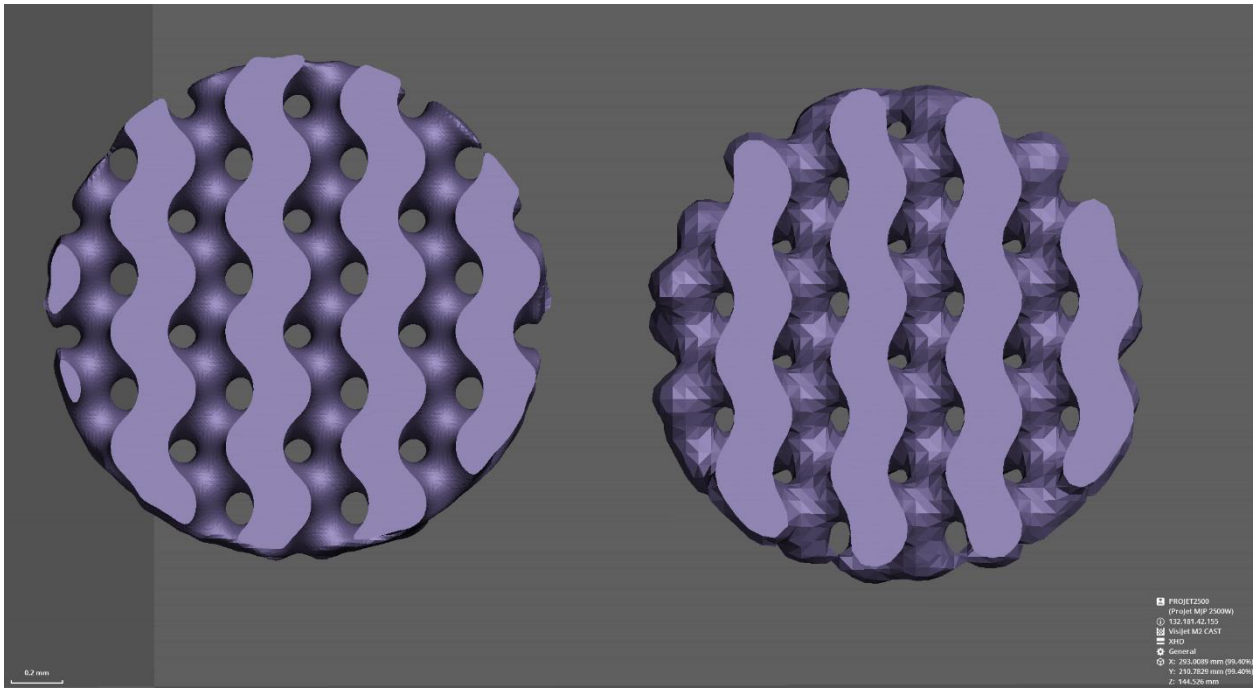

Figure 2-11: Comparison between two identical Schoen gyroid columns with different resolutions; Right side, 30 triangles per unit cell; Left side 10 triangles per unit cell.

2.4.4 Stationary phase material

As mentioned in section 2.4., 3D-printed columns are made by filling wax templates with a dissolved solution of agarose or cellulose. These two materials thermally set into gels with the agarose solidifying once cooled and the cellulose gelling with a temperature increase above 20 °C [213]. Agarose dissolves in hot water where cellulose requires a specific solvent. Cellulose polymer is made up of subunits, as shown in Figure 2-12.

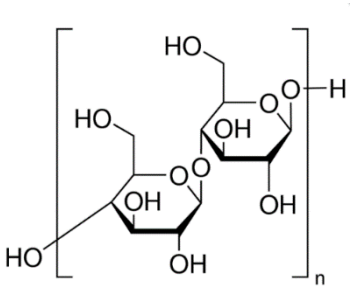

Figure 2-12: Chemical structure of a cellulose subunit [214].

Cellulose can be dissolved in a range of ionic liquids and is soluble in a urea/NaOH mixture at low temperatures (-12°C) [215-219]. The cellulose chains are broken apart by the NaOH and form complexes with the urea. These complexes break down upon heating, and hydrogen bonding is allowed between cellulose chains to form a gel structure [220]. Post gelation, the hydrogel is regenerated in water to remove the NaOH and urea trapped within the gel [221]. Anne Gordon's previous work with this technology investigated agarose columns predominantly; however, the main focus will be on cellulose for this work. This is because of the ability to increase the cellulose hydrogel's pore size above 1 μm into a range larger enough to theoretically allow viral diffusion [222]. Pore size alteration is possible by adding chemical cross-linking agents such as epichlorohydrin (ECH), which also increases the mechanical strength of the hydrogel [223].

2.4.5 Chemical functionalization

Both agarose and cellulose are common stationary phases for packed bed resins. Both polymers have free OH groups along their chains, which can be modified with various functional groups. Current functionalization tested on 3D-printed agarose and cellulose are DEAE and carboxymethyl [15]. As previously mentioned in Section 2.2.6, other potential functionalities include quaternary amine (Q), IMAC, and hydroxyapatite, which can be attached to a cellulose-based hydrogel [134, 135, 224-226]. A quaternary amine ligand attaches to cellulose via a reaction between the epoxide ring of the chemical glycidyl trimethylammonium chloride (GMAC) and the polymer chain's hydroxyl groups under alkaline conditions. While DEAE has two amine arms, a Q functionality has three. DEAE is a weak anion exchanger, and Q is a strong anion exchange ligand. A weak anion exchanger has a narrow range of pH where it maintains its positive charge, unlike a strong exchanger that maintains its charge across the entire pH range.

An IMAC ligand is attached to a cellulose stationary phase in a two-part reaction with ECH and iminodiacetic acid (IDA) under alkaline conditions. First, the epoxide ring of ECH reacts with the hydroxyl groups of the polymer chain. IDA then reacts with either the epoxide ring or the chloride group forming an amide bond [134]. The two acid arms of the IDA can then bind metal ions, specifically Ni^{2+}, for His-tag affinity. Nitrilotriacetic acid can also be used as a metal affinity ligand—first, tosylation of the celluloses hydroxyl groups followed by persilylation of nitrilotriacetic acid. The activated cellulose and nitrilotriacetic acid react together to form nitrilotriacetic -cellulose via an amination reaction [135]. The nitrilotriacetic-cellulose has three acidic arms that can co-ordinate metal ion immobilization. The difference in coordination can be seen in Figure 2-13. While both of these ligands immobilize metal ions, they provide different selectivities and binding capacities. Typically, IDA has a higher ion loading capacity and, therefore, protein binding capacity. Nitrilotriacetic-cellulose has a higher selectivity for His-Tagged proteins and stronger metal ion coordination, so it is less susceptible to metal ion leaching [227].

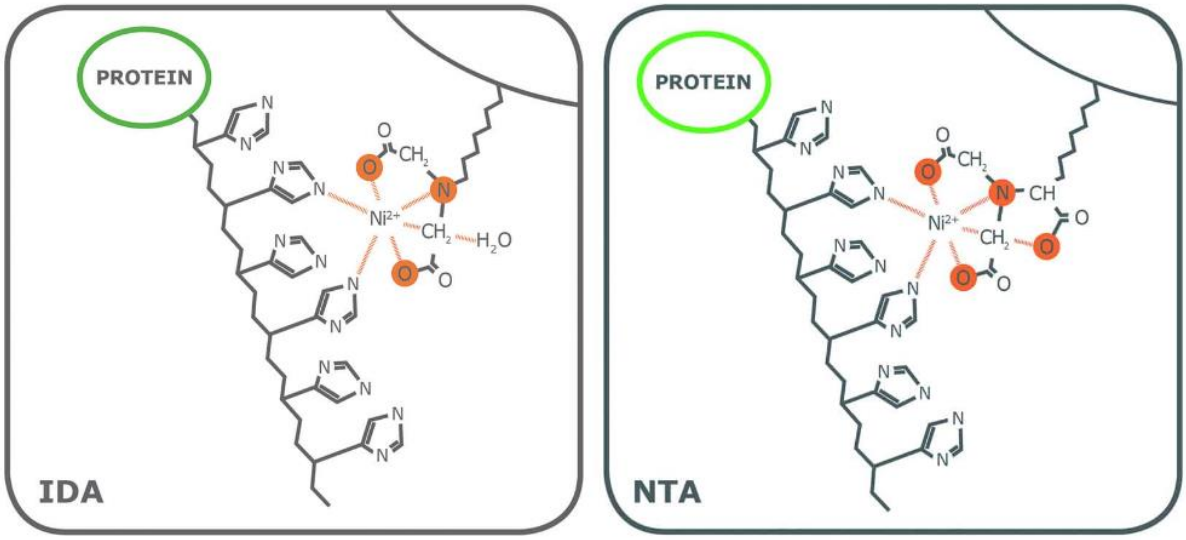

Figure 2-13: Depiction of IDA metal ion coordination compared with nitrilotriacetic acid [227].

HA has not previously been incorporated into a cellulose hydrogel; however, HA coatings of bacterial cellulose have been used in the medical field for bone implants [228-231]. In all cases, HA is mineralized onto the cellulose's surface using calcium and phosphate salt solutions, in some cases aided by citric acid. There are no reports that this mineral binds and elutes protein but does have favorable bio interactions. Mineralized Ha ($Ca_{10}(PO_4)(OH)_2$) is nearly always calcium deficient, meaning it contains fewer calcium atoms than should be stoichiometrically present (Ca to P ratio of less than 1.66). This ratio suggests the HA produced by mineralization is not pure and maybe a combination of other calcium phosphate minerals [232].

Other potential functionalities include specifically designed peptides or proteins attached to the stationary phase by click chemistry [233, 234]. Specifically, N-hydroxysuccinimide (NHS) ester reactions can be performed on cellulose to bind these designer molecules [235]. The hydroxyl groups of the cellulose can be oxidized into a carboxylic acid. Figure 2-14 then shows the potential reaction pathways for attaching a biological molecule with a stable amide bond. This reaction scheme is one of many click-type chemistries that can enable an affinity molecule to be bound to a stationary phase.

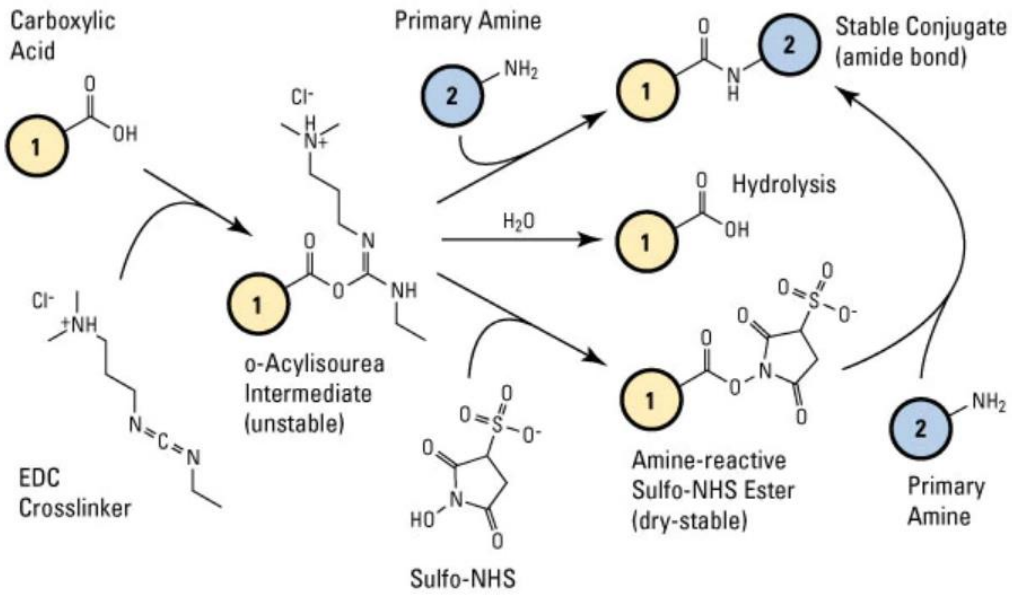

Figure 2-14: Reaction pathway for NHS-ester coupling of a potential peptide chain to a cellulose stationary phase via carboxylic acid [236].

2.5 Direction of current work

This chapter has described the promise of gene therapies in addition to the state-of-the-art downstream processing for them. Although there are new technologies such as membranes and monoliths, there isn't a specifically designed purification platform for viruses and viral particles. As such, difficulties in purification as self-evident, with low recoveries, a high number of processing steps, and variation in the process even between different serotypes of the same virus. 3D-printed chromatography columns have been identified as a potential platform technology for a capture step combining clarification, filtration, and initial chromatography purification. The combination of multiple steps should increase the overall recovery while minimizing processing time and therefore cost.

Previous work with 3D-printed columns has shown functionalization of cellulose and agarose stationary phases with cation and anion exchangers is possible. The columns could also passage solids efficiently while binding and eluting proteins. Additional ligands were also discussed concerning how they may be incorporated into a cellulose stationary phase. Specifically, a quaternary amine, hydroxyapatite, and IMAC are all possible functionalization's that have previously been used to purify viruses successfully. Cellulose hydrogel could be an alternative to agarose because of its larger pore size specifically advantages to viral purification. As the templating method is already established primary focus can be on optimizing ligands, stationary phase, and eventual scale-up.

Because of the number of different viruses being used for gene therapies and other applications (vaccines and phage therapy), testing will encompass as many of these as possible to show its versatility as a platform technology. Purification from clarified lysate and directly from cell culture will benefit traditional media by combining multiple processing steps. Column performance will be important and determined by multiple factors, including recovery, purity, processing time, dynamic and static binding capacity. Techniques for determining these indicators are common research practice but are outlined in Chapter 3 material and methods.

3 General materials and methods

The following list of chemicals shown in Table 3-1 and equipment shown in Table 3-2 summarize those used in the experimental work of this project. Many of these appear in multiple experimental steps. Appropriate figures and diagrams are listed for custom rigs and manufactured processing equipment within the method. Additional diagrams for these can be found and explained in more depth in Chapter 6. The experimental method is described in the same chronology as the subsequent chapters as accurately as possible. The methodology is referred to at the start of each experimental section with additional detail for experiments' variations. Chapter 6 is self-contained with its own methods section used for up-scaling of the 3D printing technology.

Table 3-1: Chemicals and materials used in experimentation.

Chemical	Grade	Source
2-chloro-N, N-diethylethylamine hydrochloride	Analytical	Sigma-Aldrich
A549 cells	Microbiology	ECACC
Acetone	Technical	Thermo Fisher Scientific
Adenovirus serotype 5	clarified lysate	iBET
Agar	Microbiology	Sigma-Aldrich
AgeI-HF	Analytical	Thermo Fisher Scientific
Anhydrous citric acid	ACS	Thermo Fisher Scientific
Anhydrous di-sodium orthophosphate	ACS	Thermo Fisher Scientific
Anhydrous sodium sulphate	ACS	Thermo Fisher Scientific
Anhydrous di-potassium orthophosphate	ACS	Thermo Fisher Scientific
Associate-adeno virus serotype 5 (CMV promoter, no insert)	Microbiology	Creative Biogene

Chemical	Grade	Source
Associate-adeno virus serotype 9	Crude lysate	US Southwestern medical
Bacto™ Tryptone	Microbiology	Fort Richards Laboratories
Benzonase	Microbiology	Merck
Bovine serum albumin	99%	Thermo Fisher Scientific
Cellulose powder, Type 20	Highly purified fibres	Sigma-Aldrich
CFM4HEK293 medium	Microbiology	GE Healthcare Life Sciences
Coomassie Brilliant Blue stain	Analytical	Thermo Fisher Scientific
Cytochrome C	99%	Thermo Fisher Scientific
Dithiothreitol (DTT), reducing agent	500 mM, 10x concentrated	Thermo Fisher Scientific
Dnase I, from bovine pancreas	Analytical	Thermo Fisher Scientific
Dulbecco's modified Eagle's medium	Microbiology	Thermo Fisher Scientific
EDTA	Analytical	Sigma-Aldrich
Epichlorohydrin	Analytical	Sigma-Aldrich
Escherichia coli (15669)	Microbiology	ATCC
Escherichia coli bacteriophage M13 (15669¬B1)	Microbiology	ATCC
Ethanol	Analytical	BDH Lab Supplies
Fetal bovine serum	Microbiology	GE Healthcare Life Sciences
Food colouring	Food	Local market
GlutaMAX	microbiology	Thermo Fisher Scientific
Glycidyltrimethylammonium chloride	Technical	Merck
Ham's F12 medium, Kaighn's modification	Microbiology	GE Healthcare Life Sciences
HEK 293 T cells	Microbiology	ATCC

Chemical	Grade	Source
High Pure Viral Nucleic Acid Kit	-	Roche
HIS-Tagged protein	crude	UC School of Biological Sciences
Hydrochloric acid	Analytical	Bio Lab
Hydroxyapatite 20 μm powder	Analytical	Acros Organics
Imidazole	Analytical	Thermo Fisher Scientific
Iminodiacetic acid	ACS	Sigma-Aldrich
INNOTEST HIV Antigen mAb	Microbiology	Fujirebio Diagnostics
Isopropanol	Analytical	BDH Lab Supplies
Lentivirus	clarified lysate	iBET
LightCycler® 480 Probes Master	Microbiology	Roche
Lithium dodecyl sulfate (LDS) buffer	4x concentrated	Thermo Fisher Scientific
Magnesium chloride hexahydrate	ACS	Scharlau
Methanol	Analytical	BDH Lab Supplies
Novex Sharp Pre-stained Protein Standard	Analytical	Thermo Fisher Scientific
Polysorbate 20	Analytical	Sigma-Aldrich
Proteinase K from Tritirachium album	Analytical	Thermo Fisher Scientific
Saccharomyces	Food	Local market
Sodium bicarbonate	ACS	Merck
Sodium chloride	ACS	Sigma-Aldrich
Sodium dihydrogen orthophosphate	ACS	Thermo Fisher Scientific
Sodium dodceyl sulfate buffer	20x concentrated	Thermo Fisher Scientific
Sodium hydroxide	97%	Thermo Fisher Scientific

Chemical	Grade	Source
Sodium Pyruvate	Analytical	Thermo Fisher Scientific
SYBR Master mix	Analytical	Thermo Fisher Scientific
Tyrosinase	99%	Sigma-Aldrich
UltraPure Tris buffer	Analytical	Invitrogen
UltraPure water	Analytical	Thermo Fisher Scientific
Urea	ACS	Sigma-Aldrich
VSO	Analytical	Regal Casting LTD

Table 3-2: List of equipment and machinery used for experimentation.

Equipment	Supplier
311DS environmental shaking incubator	Labnet
ÄKTA PURE Chromatography Hardware	GE Healthcare
ÄKTA Start Chromatography Hardware	GE Healthcare
ÄKTA10 Explorer Chromatography Hardware	GE Healthcare
Autoclave full automatic 60	Priorclave
Bruker Vertex 70 spectrometer with OPUS operating software	Bruker Optics
Custom cellulose infusion rig	University of Canterbury
Custom support wax removal rig version 1	University of Canterbury
Custom support wax removal rig version 2	University of Canterbury
Formlabs 2 resin printer	Formlabs
Frac-P90	GE Healthcare
Haier Freezer model HFZ-85A	Local Electronics Store

Equipment	Supplier
Hei-Tec hot plate and magnetic stirrer	Heidolph
Hitachi H-7650 120 kV electron microscope	Hitachi High-Technologies
iBlot dry blotting system	Invitrogen
Infinite 200 PRO NanoQuant microplate multimode reader	Tecan
Inverted TCS SP5 confocal microscope	Leica
JSN 7000F field emission high resolution scanning electron microscope	JEOL
LightCycler® 480 instrument	Roche
Mitsubishi refrigerator Mr-385E	Local Electronics Store
MJP ProJet 2500W	3D Systems
NanoDrop 2000	ThermoFisher
NanoSight NS300™	Malvern Instruments
pH-meter CP105	Elmetron
Purifier Biological safety cabinet	Labconco
Rotorgene qPCR machine	Qiagen
Samsung Timesaver 1000 W Microwave	Local Electronics Store
Silverson L4RT Stirrer	Advanced Packaging Systems Ltd
Smartlab 3kW powder XRD	Rigaku
Solidscape Pro 3Z	Solidscape
Spinning Wheel	University of Canterbury

Equipment	Supplier
TX3202L Top load balance	Shimadzu
Ultrospec 2100 Pro UV/Vis Spectrophotometer	Amersham Biosciences
Variable speed Console drive 100 rpm	MasterFlex

3.1 Column fabrication

3.1.1 Cellulose hydrogel synthesis

7 wt% sodium hydroxide and 12 wt% urea were mixed into deionized (DI) water and left to cool inside a fridge down to 4°C. Once cooled, 5 or 6 wt% cellulose powder was slowly added while the solution was mixed at 8000 rpm in a Silverson overhead mixer. After the cellulose was evenly dispersed, it was placed in a glycol bath (1:1 glycol to water) inside a freeze at -12°C. After one to two hours, the solution was removed and examined to ensure no cellulose particles could be seen in the solution then stored at 4 °C until use.

Formulation of the cellulose hydrogel was adjusted by the addition of a chemical (ECH) and physical (additional undissolved cellulose powder) cross-linker. Various amounts of each cross-linker were added depending on the experiment or formulation required for each chromatography column or test cube. After the addition of cross-linking agents, the solution was mixed at 8000 rpm in Silverson overhead mixer for one minute. Mixing occurred with the solution below 5 °C to reduce the chance of premature gelation. The solution was then heated to 50 °C in a water bath for two hours to gel the cellulose and activate the chemical cross-linker if present. The subsequent experimental methods will indicate the composition of the resulting cellulose hydrogel. Post gelation, all cellulose hydrogels were regenerated in tap water over five days [220].

3.1.2 3D models

Cylindrical column models of Schoen gyroids of varying channel diameters (150 to 500 μm) were modeled in a Matlab TPMS generation program and saved as STL files. This code was

developed by Dr. Daniel Clarke and can be found in the supplementary material. The equation (3-1) that describes the level surface of a Schoen Gyroid is:

$$sin\left(\frac{2\pi x}{l}\right)cos\left(\frac{2\pi y}{l}\right) + sin\left(\frac{2\pi y}{l}\right)cos\left(\frac{2\pi z}{l}\right) + sin\left(\frac{2\pi z}{l}\right)cos\left(\frac{2\pi x}{l}\right) = t, \quad (3\text{-}1)$$

At t = 0, the surface intersects a volume evenly, whereby filling in one side of the surface 50% of the volume is filled in. l is the length of the unit cell. The unit cell length is related to the channel diameter, d, by equation 3-2:

$$l = \left(\frac{sd}{4\varepsilon}\right)^{\frac{1}{3}}, \quad (3\text{-}2)$$

where ε is the porosity and s is the specific surface area of the unit cell. In the case of TPMS channels, a hydraulic diameter is used as the cross-sectional width of these channels is not circular. The hydraulic diameter was chosen and then the unit cell was scaled to match. The surface area was estimated by summing the area of triangular elements of a mesh that approximates the level surface. The Matlab program evaluates the level surface function for the Schoen gyroid over the spatial domain. Next, this scalar field was intersected with the level surface for the cylindrical exterior. The build material is assigned to where the scalar field is negative, the void space is where the scalar field is positive. The mesh describing the column was generated by applying the marching cube algorithm to the scalar field [237]. The marching cube algorithm is applied only to a cylinder either of a given length or one-unit cell in length. The face and vertex data are patterned along the vertical axis to produce a cylinder of the requisite length. The STL files are then sent to a wax 3D printer via the 3D Sprint software to be printed. An example STL file in 3D Sprint can be seen in Figure 3-1.

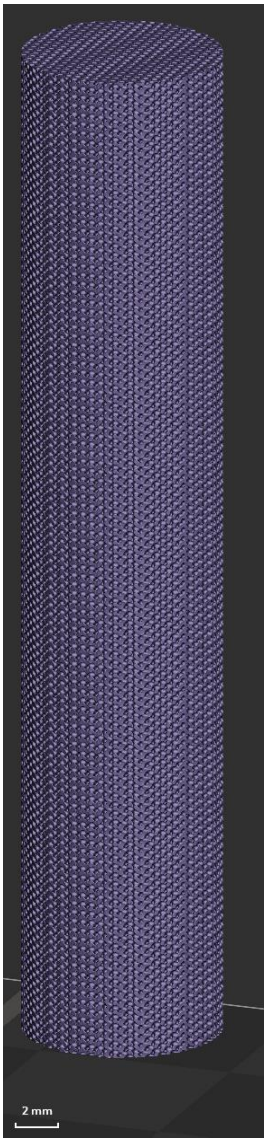

Figure 3-1: Computer generated model of 300-micron channel diameter Schoen gyroid

3.1.3 Wax templates

Two different 3D printers were used for the fabrication of TPMS wax templates, a SolidScape 3Z Pro printer (old) and a 3D systems MJP 2500W ProJet (new). The new printer produced the majority of the templates used however, some were printed on the old printer before the start of this project. Additionally, a set of columns were purchased from Regal Casting LTD (Auckland, New Zealand) which were printed on a 3D systems MJP 2500W ProJet. Both printers produced templates out of a build and support wax, however, each printer used a different set of waxes that required different post-processing methods.

3.1.3.1 SolidScape 3Z:

Column templates were placed into a beaker of 70% VSO on a hot plate with a temperature control probe. The VSO was heated to 50 °C to dissolve the support wax (bright red) from the column. VSO was replaced every two to three hours until all support wax was removed noted by no color change in the VSO. The template was dried at 50 °C in an oven for 48 hours.

3.1.3.2 3D systems MJP 2500W ProJet:

Column templates were placed into a beaker of IPA on a hot plate with a temperature control probe. The IPA was heated to 35 °C to dissolve the support wax from the column. IPA was replaced every four hours, a minimum of five times, before the template was placed in a 500 mL bottle of fresh IPA for one week to ensure complete removal of support wax. Unlike the SolidScape support wax, the 3D systems support wax is white and dissolves to be colorless. At the time of experimentation, there was no way to accurately determine complete support wax removal. Therefore, multiple columns were processed at the same time which could be used sacrificially to ensure complete support wax removal. This was done by breaking open one of the templates to examine the internal channels for remaining support wax. If support wax remained further IPA soaking was completed followed by checking of another template sacrificially. This ensured all of the support wax was removed from that batch of templates. After support wax removal templates were left to dry inside a fume hood for 48 hours.

3.1.4 Templates to hydrogel columns

Wax templates (post support wax removal) were placed inside a 3D resin printed hollow plastic cylinder with syringe attachable caps (Figure 3-2) at each end secured with Parafilm. This method was developed by Anne Gordon as described in her doctoral thesis [15]. A disposable syringe (10 to 20 mL depending on the template size) was filled with cellulose solution just after the addition and mixing of crosslinking agents. The syringe was attached to one end of the plastic mold via an end cap and slowly pressed to inject the solution into the cavities of the wax mold. 8 to 16 mL of the cellulose solution was injected in over two minutes. After injection the other end of the mold was capped with Parafilm™ and placed inside a water bath at 50 °C for two hours. The mold was then transferred to a fridge to cool to 4 °C for one hour before the caps and syringe were removed from the mold. The cellulose-infused template was gently pushed out of the plastic cylinder and place into a beaker of water. A drop of liquid hand soap was then added to the water before the beaker was placed onto a hot plate to boil. The water was replaced every three hours and allowed to boil again. This process is repeated two to eight times to ensure all wax was removed from the column. The column was visually inspected to determine if wax remained inside the translucent cellulose structure. The column was then placed in a container of tap water to regenerate. Water was replaced every 24 hours for three days.

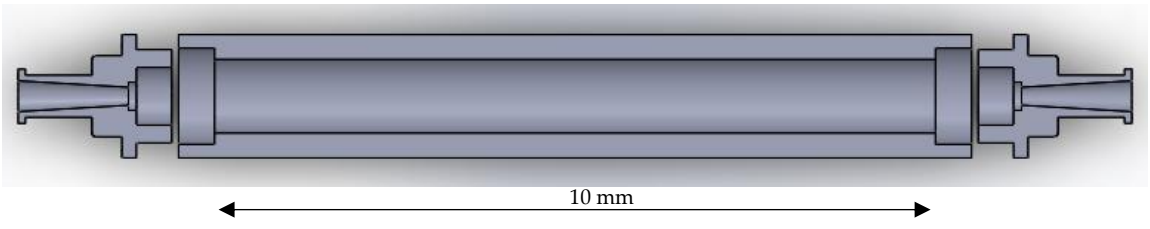

Figure 3-2: Cross-section of 3D-printed casing and end caps.

3.2 Cellulose functionalization

3.2.1 DEAE

The protocol for functionalizing cellulose with the DEAE ligand 2-chloro-N,N-diethylethylamine hydrochloride follows previous work by Gordon *et al.* [238]. Cellulose hydrogel (columns or pieces) was placed in glass beakers of 4 M NaOH and 3 M DEAE at a ratio of 1 g cellulose: 27 ml DEAE: 20 ml NaOH and stirred at 30 or 80 °C for six hours. Following the reaction, functionalized cellulose was washed with 1 M NaOH and three washes with DI water. DEAE cellulose was stored in DI water until use. Figure 3-3 shows the chemical structure of the 2-chloro-N, N-diethylethylamine hydrochloride used for the DEAE functionalization. The exposed hydroxyl groups of the cellulose are substituted with the diethylethylamine ligand under the caustic conditions [239].

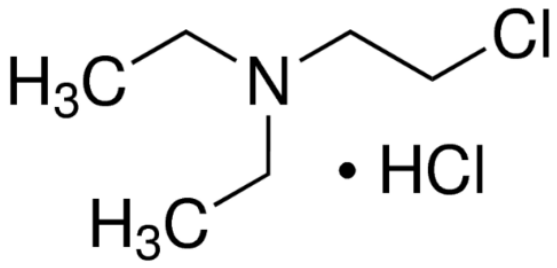

Figure 3-3: Chemical structure of 2-chloro-N,N-diethylethylamine hydrochloride [240].

3.2.2 Quaternary amine (Q)

The protocol for functionalizing cellulose with a Q ligand was based on works by He *et al.* who functionalized aerogels made from cellulose nanofibers [225]. Cellulose hydrogels (columns or pieces) were placed inside a conical flask with 1 M NaOH and 90% glycidyltrimethylammonium chloride (GMAC) at a ratio of 1 g cellulose: 50 g NaOH: 30 g GMAC and stirred at 80°C for six hours. Following the reaction, cellulose was washed with 1 M NaOH and three times with DI water. Q cellulose was stored in DI water until use. Figure

3-4 shows the chemical structure of GMAC, showing the epoxide ring, which reacts with the exposed hydroxyl groups of the cellulose forming an ester bond in caustic conditions.

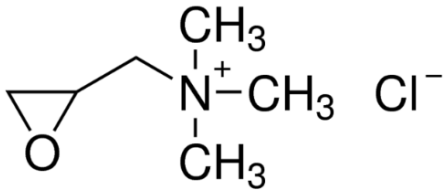

Figure 3-4: Chemical structure of GMAC [241].

3.2.3 Hydroxyapatite

Three different methods for HA functionalization were tested as follows:

3.2.3.1 Alternating solutions:

This functionalization was based on hydroxyapatite growth on bacterial cellulose for medical implants by Saska *et al.* [228]. Cellulose hydrogel (columns or pieces) was soaked in a solution of 11 g/L of $CaCl_2$ for 24 hours. The hydrogel was then briefly rinsed with DI water before being placed in a solution of 8.6 g/L Na_2HPO_4 for 24 hours. This cycle of alternating between calcium and phosphate solutions was repeated for 7 to 14 days. Post functionalization HA-cellulose was washed and stored in DI water until use.

3.2.3.2 Solid incorporation:

Before cellulose gelation fixed amounts of 20 μm hydroxyapatite powder (3 to 11 g) were added to 100 grams of 5% dissolved cellulose solution. The powder was mixed into the solution using the Silverson overhead mixer at 8000 rpm for three minutes. The solution was transferred into a square 30 x 30 x 20 mm fully sealed Tupperware™ container and placed in a drying oven at 50 °C for two hours. Post gelation hydrogels were removed from the container and regenerated in a 500 mL beaker of DI water. The water was replaced every 24 hours for five days.

3.2.3.3 Simulated Body Fluid (SBF) soaking:

The mineralization of hydroxyapatite onto bacterial cellulose by SBF soaking was based on works by Zimmermann *et al*. [229], and Rhee *et al.* [242]. An SBF solution containing citric acid was produced by adding the following reagents in order to 900 mL of DI water stirred on a hot plate at 37°C.

1. 6.5456 g NaCl
2. 2.2682 g $NaHCO_3$
3. 0.373 g KCl
4. 0.1419 g Na_2HPO_4
5. 0.3049 g $MgCl_2$ .6H2O
6. 0.3675 g $CaCl_2$ .2H2O
7. 0.071 g Na_2SO_4
8. 6.057 g Tris [$(CH_2OH)_3CNH_2$]
9. 30 mL of 1 M HCl
10. 0.192 g Citric acid

While maintain mixing, the pH was adjusted to 7.4 by additions of either 1 M NaOH or HCl and the volume made up to 1000 mL. Pieces of cellulose hydrogel (5 mm side length cubes) in a 500 mL plastic container of SBF fluid were placed in a shaker incubator at 37°C for 48 hours. The SBF fluid was then replaced and this cycle was repeated for 7 to 14 days until a white precipitate was seen to form inside the hydrogel.

3.2.4 Crystal growth control

In between soaking cellulose hydrogel in alternating solutions of $CaCl_2$ and Na_2HPO_4 (as described in 3.2.3.1) the hydrogel is washed with DI water. By lengthening the time of the wash step calcium and phosphate ions can be removed limiting the growth of the hydroxyapatite to the pores and not upon the surface. Wash times of 10 to 60 seconds were tested to determine the optimal length of time to restrict crystal growth to the pores of the hydrogels.

3.3 Microscopy and mineral analysis

3.3.1 Freeze drying

Various sized samples (columns and cubes) of cellulose hydrogel (functionalized and non-functionalized) were placed inside 50 mL centrifuge tubes with a needle-sized hole in the cap. These were then dipped into liquid nitrogen for a minimum of five minutes to snap freeze the hydrogel. Subsequently, the samples were freeze-dried using a Labconco freezone 2.5 freeze drier at -45 °C under vacuum. Samples were dried over 48 hours to ensure maximum removal of water.

3.3.2 Energy-Dispersive X-ray Spectroscopy (EDS) & Field Emission Scanning Electron Microscopy (FE-SEM) analysis

Various samples of cellulose hydrogel were freeze-dried as previously mentioned in Section 3.3.1. The samples were manually fractured or sliced open to reveal the inner structure of the column for SEM analysis. The samples were gold-coated for 60 s in three cycles at 25 mA at varying angles using an Emitech K975X coater. Samples were attached to a copper stage mount by carbon tape. FE-SEM was performed with a JEOL 7000F FE-SEM using a probe current of 7 mA under an acceleration voltage of 7.5kV.

EDS was performed with the same microscope with a probe current of 11 mA under an acceleration voltage of 15 kV. Complete surfaces of freeze-dried 5 mm cellulose gels cubes functionalized with HA were examined. Each EDS sample was examined in a minimum of five different locations with triplicate cubes of each HA variation tested. Overlapping maps were examined to see if the calcium and phosphate signals were coming from similar locations (crystal structures).

3.3.3 Fourier transform infrared spectroscopy (FTIR)

Samples were freeze-dried before analysis as described for SEM and EDS (Section 3.3.1). Small pieces of each sample were fractured and pressed under the pin arm. FTIR spectra were obtained using a Bruker Vertex 70 spectrometer and OPUS operating software. The

wavenumber range scanned was 4000 to 400 cm^{-1}; 10 scans of 4 cm^{-1} resolutions were signal averaged. Triplicates of each HA functionality were tested.

3.3.4 X-ray powder diffraction (XRD)

5 mm cubes of hydroxyapatite functionalized cellulose hydrogel and control without functionalization were freeze-dried as described in Section 3.3.1. Powder samples of each cube were made by lightly rubbing them with grit 60 sandpaper. Samples were processed in a Rigaku Smartlab 3kW using copper Kα radiation at 2θ 5-70° at a rate of 5°/minute. Results were checked for the presence of potential carborundum contamination from the sandpaper. Peaks were analyzed from a library of standards for various calcium phosphate minerals.

3.4 Viral diffusion

Confocal laser scanning microscopy (CLSM) was used to examine the depth fluorescently tagged AAV particles had diffused into cellulose hydrogels. Rhodamine Red™-X was used to fluorescently label the viral particles following their reactive ammine probe guide [243]. The virus was buffer exchanged into a sodium bicarbonate solution, pH 8.3 via centrifugation with a 30 Kda Vivaspin falcon tube. 50 ng of the fluorescent dye dissolved in dimethylformamide (DMF) at 2.5 mg/mL was then added per 1×10^{11} virus particles (VP) and incubated at room temperature in the dark for one hour. Post reaction, the tagged AAV particles were separated from unreacted dye molecules and buffer exchanged via centrifugation with another 30 Kda Vivaspin falcon tube into 10 nm pH 7 phosphate buffer. Viral adsorption and UV-Vis were measured by Nanodrop at 280 nm and 560 to 580 nm. 100 μL of fluorescently tagged virus ($1 \times 10^{11} VP/mL$) was pipetted into wells of a 96 well plate. The various cellulose hydrogels were cut into cubes with roughly 5 mm sides before being placed into the wells filled with virus. After one or 24 hours the solution was pipetted out of wells and collected. ~100-micron cross-sections of each hydrogel were cut with a razor blade to be examined under a Plan Apochromat 63x/1.4NA oil immersion objective at 560 nm. Images were examined using ImageJ software to determine the depth of penetration. 10 measurements per image were taken from the edge of the gel to the point of the band where the intensity starts to diminish. Three images for each cellulose composition or functionality were examined. Results were

averaged and the standard deviation was determined through Microsoft Excel's statistical function.

3.5 Adsorption studies

3.5.1 Binding mechanics:

5 mm cubes were cut out of cellulose hydrogel (various functionalities and hydrogel compositions) to be placed in 1.5 ml Eppendorf tubes with 1 ml of 10 mM phosphate buffer pH 7. Equilibration was left to take place overnight. Buffer was replaced with 1 M NaCl to add counter ions to the functional groups before being washed three times with 1 ml of 10 mM phosphate buffer pH 7. 1 mL of 2.5 mg/ml of BSA was pipetted into the Eppendorf tubes and allowed to adsorb for two hours. After adsorption gels were washed three times with equilibrium buffer before elution with 1 mL of 1 M NaCl or 1 M NaCl with 400 mM Na_2HPO_4. BSA concentration in elution was measured by Nanodrop. All tests were carried out in triplicate.

3.5.2 Static binding capacity (DEAE, Q and HA):

1 cm long pieces of a 3D-printed column (varying channel hydraulic diameters, 1 cm column diameter, 6 wt% cellulose + 3 wt% added cellulose powder, and 15 wt% ECH) were cut to be placed in individual 50 ml centrifuge tubes with 40 mL of 10 mM phosphate buffer pH 7. Tubes were placed on a spinning wheel to equilibrate for two hours. Model proteins of BSA and cytochrome C were dissolved in 10 mM phosphate buffer pH 7 at varying concentrations (1 mg/mL to 30 mg/mL). 20 mL of each protein solution was placed with the equilibrated piece of a column. Protein concentration was measured periodically by Nanodrop over 24 hours to determine adsorption. All tests were carried out in triplicate.

3.5.3 Protein binding selectivity and elution order:

Schoen gyroid columns, 300-micron hydraulic channel diameter, 1 cm column diameter by 5 cm in length (HA or DEAE functionalized) were loaded into individual SNAP column casings (S-10/125-PPSS-OV-FP20). The loaded casings were attached to an AKTA10 Explorer used for this set of chromatography experiments. For both columns, the following procedure was carried out with the appropriate buffers mention below:

Columns were equilibrated with 20 mL of running buffer (1 mL/min) before 200 μL of a model protein (varying protein at a concentration of 1 mg/mL) was loaded at 0.25 mL/min. The column was then washed with 20 mL of running buffer at 1 mL/min. Gradient elution was performed over 20 mL reaching a concentration of 100% elution buffer at 1 mL/min. UV signal was monitored at 280 and 260 nm for the elution peak. The retention time was measured to be from the start of the gradient to the maximum of the peak. All experiments were completed in triplicate.

HA buffers:

Running – 35 mM phosphate pH 7

Elution - 35 mM phosphate 1 M NaCl pH 7

DEAE buffers:

Running: 10 mM phosphate buffer pH 7

Elution: 10 mM phosphate 1 M NaCl pH 7

3.6 Viral culturing and analysis

3.6.1 M13 bacteriophage

3.6.1.1 Culturing:

Escherichia coli (E. Coli) strain ATCC 15669 was cultured according to the supplier's instructions. A culture medium of 1 % tryptone pH 7 was prepared and autoclaved at 121°C for 30 minutes. The contents of the suppliers' glass ampule were then re-suspended in 1 mL of culture medium and transferred to a 15 mL centrifuged tube containing 5 mL of culture medium. 1% tryptone agar plates were also streaked with the re-suspended E. coli culture and grown at 37°C for 24 hours. Liquid cultures of the E. coli were prepared using the same medium inoculated from single plate cultures inside a shaken incubator at 37°C for 24 hours.

M13 bacteriophage ATCC 15669-B1 was also cultured according to the supplier's instructions. A culture of host strain (E. coli strain ATCC 15669) was grown in 1% tryptone overnight to an OD 600 measurement between 0.8 to 1. 1 mL of cultured host strain was used to re-suspend

the contents of the glass ampule before being transferred to a 50 mL centrifuge tube with an additional 5 mL of the host culture. The inoculated culture was grown inside a shaker incubator at 37°C for 24 hours. 1 mL of this culture was then used to inoculate 150 mL of E. coli culture in 1% tryptone and kept in a shaking incubator at 37°C overnight. The crude cell culture samples were stored at 4°C for no longer than three days before use.

3.6.1.2 Plaque forming assays:

The titer of M13 phage samples was determined by plaque-forming assays with the units pfu/mL (plaque-forming units per milliliter). A culture of host strain E. coli was incubated overnight (1% tryptone) to an OD 600 measurement between 0.8 to 1. 1 mL of this culture was aspirated onto a 1% tryptone agar plate and tilted to completely cover the surface. The excess liquid was pipetted off the surface after one minute and the plate incubated for 15 minutes at 37°C. Phage samples were serially diluted in a fresh culture medium from 1×10^{-1} to 1×10^{-12} to be spotted on incubated plates. 5 μL × 5 of each dilution was spotted onto the pre-prepared plates and incubated overnight. Visible plaques were counted at the appropriate dilution to determine the titer. Each sample was tested on three individual plates to ensure consistent results.

3.6.1.3 Sodium Dodecyl Sulfate–Polyacrylamide Gel Electrophoresis (SDS-PAGE):

The purity of eluted M13 and AAV particles was analyzed by SDS-PAGE under denaturing conditions [31]. The virus samples were incubated with lithium dodecyl sulfate (LDS) sample buffer and reducing agent and heated at 70 °C for 10 min. Novex™ Sharp Pre-Stained Protein Standard was used as a protein molecular weight marker. Electrophoresis was performed with a 15% resolving polyacrylamide gel on a mini-protein 3 apparatus at constant voltage (100 V). The gel was stained with Coomassie® Brilliant Blue R-250 and destained with an aqueous destaining solution containing 40% (v/v) methanol and 10% (v/v) acetic acid.

3.6.2 Adenovirus and lentivirus

Culturing and quantification (purity and titer) of adenovirus and lentivirus was completed at iBET by Mafalda Moleirinho and Sofia Moreira. The following method for culturing, purity analysis, and quantification of adenovirus and lentivirus is taken from our paper '3D-printed

ordered bed structures for chromatographic purification of enveloped and non-enveloped viral particles' [244]. It has been included here for completeness of the upstream and downstream processing of these viral particles.

3.6.2.1 Adenovirus culturing:

A549 cells (86012804) were cultured in Ham's F12 medium, Kaighn's modification (SH30526.01) supplemented with 10% fetal bovine serum (SH30071.01). Oncolytic adenoviruses were produced as described elsewhere [245]. Briefly, cells were cultured in an HYPERflask® (10020), in a humidified atmosphere of 5% CO2 in air at 37 °C. After the cells achieved 90% of confluence, they were harvested by trypsinization and centrifugated at 200xg, to remove the serum-containing medium. The cell pellet was resuspended in CFM4HEK293 medium (SH30858.02) supplemented with 4 mM GlutaMAX (35050–038) and transferred to a ReadyToProcess WAVE™ 25 bioreactor. The bioreactor was inoculated at a cell concentration of 0.3 × 106 cells/mL to 0.6 × 106 cell/mL and after 72 h in culture, the cells were infected with a Multiplicity of Infection (MOI) of 10 infectious particles per cell. The harvest was performed 48 h post-infection (hpi) and the cell lysis was performed with Polysorbate 20 at a final concentration of 0.5% (v/v). For DNA digestion, 100 U/mL of Benzonase (1.01656.0001) was used. The digestion proceeded for 4 h at 37 °C in the bioreactor with agitation (16 rpm). Afterward, the virus culture was clarified using a ULTA Prime™ GF filter followed by a ULTA Prime™ CG filter (DGF-A-02-470, DMP-CG92-470). The clarification was performed at a constant flux of 600 LMH using a Tandem 1081 Pump and the pressure was monitored using a pressure transducer in-line (080-699PSX-5).

3.6.2.2 Lentivirus culturing:

HEK 293 T cells (ATCC® CRL-3216™) obtained from the American Type Culture Collection (ATCC) were cultured in Dulbecco's modified Eagle's medium (DMEM) (31053–028) supplemented with 10% (v/v) FBS (10270–106), 4 mM of GlutaMAX (35050–038) and 1 mM Sodium Pyruvate (11360–070), and maintained at 37 °C in an incubator with a humidified atmosphere of 5% CO_2 in the air. Cell concentration and viability were assessed by the trypan blue exclusion method. Transient lentivirus (LV) was produced by transfecting at seeding 293 T cells and using a four-plasmid system (pVSVg, pGag-Pol, pRev, and LV plasmid expressing

GFP, kindly provided by Dr. Didier Trono through Addgene plasmid repository) as described elsewhere [246]. Briefly, 1.5 × 105 cells/cm^2 were transfected in a 225 cm^2 tissue flask using linear 25 kDa polyethyleneimine, PEIpro®, (115–100, Polyplus transfection). The medium was exchanged 24 h after transfection and harvested 24 h upon the medium exchange. For DNA digestion, 50 U/mL of Benzonase (1.01656.0001) was used. The digestion proceeded for 30 min at room temperature. The supernatant collected was clarified with Sartopure® PP3 Sartoscale 0.45 μm filter (5055306PS--FF—M). The clarification was performed at a constant pressure of 0.5 bar using a Tandem 1081 Pump.

3.6.2.3 Adenovirus quantification

This method of quantitative polymerase chain reaction (qPCR) was also described in iBET's paper 'Clinical-Grade Oncolytic Adenovirus Purification Using Polysorbate 20 as an Alternative for Cell Lysis' [245]. To quantify the adenovirus particles qPCR was used to identify the number of copies of genomic DNA. To ensure only the quantification of viral particles and the removal of the free viral genome, 20 μL of viral samples were incubated with 10 U of DNAse for 30 minutes at 37°C. The reaction was then stopped by the addition of EDTA to bring the concentration up to 8 mM and then heated at 75°C for 10 minutes. The viruses' genomes were then extracted using High Pure Viral Nucleic Acid Kit according to the manufacturer's instructions (11858874001). The viral genome copies were quantified by qPCR using the LightCycler® 480 Probes Master in the LightCycler® 480 instrument.

Total particles were also quantified by Nanoparticle Tracking Analysis (NTA) using a NanoSight NS300™. Each sample was diluted before measurement in phosphate-buffer saline solution. Three videos of 30 seconds were taken for each sample and analyzed using the NTA 2.3 software. The camera level was set to 16 and kept constant during all measurements.

3.6.2.4 Lentivirus quantification

This method of qPCR quantification is also described in '3D-printed ordered bed structures for chromatographic purification of enveloped and non-enveloped viral particles' as performed by Mafalda G. Moleirinho and Anna S. Moreira [244]. The concentration of lentivirus physical particles (PP) was measured by the detection of p24 LV protein in

supernatants. The p24 protein detection was performed using the INNOTEST HIV Antigen mAb, following the manufacturer's instructions. It was assumed that 1 ng p24 corresponds to 1.25 × 107 PP (equation 3-3).

$$Titer\left(\frac{TU}{mL}\right) = [p24\ \text{Protein}] \times 1{,}250{,}000 \quad (3\text{-}3)$$

The functional LV titers were determined by transducing 293 T cells with the produced LV supernatants. Green fluorescent protein (GFP) expression was analyzed by flow cytometry as described elsewhere [246]. The concentration of LV Transducing Units (TU. mL^{-1}) was calculated using the following equation 3-4:

$$Titer = \frac{\%\ of\ GFP\ Postive\ cells \div 100}{Volume\ of\ transduction} \times dilution\ factor \times n°\ of\ cells\ at\ transduction\ time \quad (3\text{-}4)$$

3.6.2.5 Adenovirus purity

To confirm the presence and shape of oncolytic adenovirus, transmission electron microscopy (TEM) was performed. A drop of sample was adsorbed onto a formvar-coated 150 mesh copper grids from Veco for two min. The grid was washed five times with sterile filtered water then soaked in 2% (w/v) of uranyl acetate for two min and dried in air at room temperature. The grids were analyzed using a Hitachi H-7650 120 kV electron microscope.

To detect the presence of adenovirus proteins, SDS-PAGE followed by western blot analysis, was performed. Briefly, the virus samples were incubated with LDS sample buffer and reducing agent and heated at 70 °C for 10 min. NuPAGE Bis/Tris gels 4–12% were used for electrophoresis and SeeBlue Plus2 Pre-stained standard was used as a protein molecular weight marker. The SDS-PAGE gels were stained with InstantBlue™. Proteins were transferred onto a polyvinylidene difluoride membrane using iBlot dry blotting system and the membranes were blocked with 5% (w/v) of reconstituted milk powder in Tris-buffered saline with 0.1% (w/v) of Tween 20 (T-TBS buffer) for one hour. After blocking, membranes were incubated overnight with primary antibody anti-adenovirus type 5 (dilution 1:4000),

followed by secondary antibody incubation with goat anti-rabbit (dilution 1:5000) conjugated with peroxidase and developed using the ECL detection reagent protocol.

Total dsDNA was assessed using the Quant-iT™ Picogreen™ ds-DNA Assay Kit, according to the manufacturer's instructions. The assay was performed in a black 96 well microplate and the fluorescence was measured using the Infinite 200 PRO NanoQuant microplate multimode reader.

Total protein concentration was determined by BCA protein assay kit. The analysis was performed according to the manufacturer's instructions. The assay was performed in transparent 96 well plates and the absorbance was measured at 562 nm, using the Infinite 200 PRO NanoQuant microplate multimode reader.

3.6.3 AAV serotype 9

AAV serotype 9 clarified lysate samples were kindly donated by Associate Professor Steven Grey from US South-western Medical Centre. Samples were taken directly from their downstream processing post clarification.

3.6.3.1 qPCR tittering:

The protocol for quantification of AAV serotype 9 by qPCR was provided by Associate Professor Steven Gray from US South-western Medical Centre. The following procedure was used:

3.6.3.2 DNA extraction from samples:

10 µL of AAVs (upstream lysates, downstream purification) was added to 90uL of DNaseI mixture (Table 3-3) into a DNA/RNA free 1.5 mL Eppendorf and spun down at 1,000xg for two minutes. Eppendorf's were then incubated for one hour at 37° C. Post incubation 6 µL of 0.5 M EDTA was added and mixed by slow aspiration. 120 µL of Proteinase K solution (Table 3-4) was then added and again mixed by aspiration. The Eppendorf's were then spun down at 1000xg for two minutes and then incubated at 55°C for two hours followed by 10 minutes at 95°C to inactivated Proteinase K. Samples were then diluted 10x in Ultra-Pure water.

Table 3-3: DNase mix for qPCR.

DNase mix (1mL)	
DNase I (10mg/ml)	10 ul (added before use)
Tris HCl pH7.5 (1M)	10 ul
CaCl2 (1M)	2 ul
MgCl2 (1M)	10 ul
H2O	968ul

Table 3-4: Protease K mix for qPCR.

Protease K (1mL)	
5M NaCl	200 ul
10% sarcosyl	100 ul
Proteinase K (10mg/ml)	10 ul (added before use)
H2O	690 ul

3.6.3.3 Plasmid linearization and standards:

AAV plasmid was linearized by overnight digest with the enzyme AgeI-HF. 10 units of the enzyme were added for every 1 μg of plasmid DNA (checked by Nanodrop) with a total reaction volume of 50 μL. Post digest linearized plasmid was purified with a Qiagen kit (QIAquick PCR Purification Kit) into a Tris-EDTA buffer, pH 8. The plasmid was checked on a 1% agarose DNA gel stained with SYBR green, a band around 6,000 bp was indicative of the correctly linearized plasmid. The plasmid was then diluted with 10 mM Tris buffer, pH 8 into a working stock of 10 ng/μL. Serial dilutions of this working stock were used as standard points for a qPCR calibration graph. These points were as follows: 50 pg/μL, 5 pg/μL, 0.5 pg/μL, 50 fg/μL, 5 fg/μL, and 0.5 fg/μL.

3.6.3.4 qPCR reaction:

Into each well of a qPCR plate 8 μL master mix (Table 3-5) was pipetted along with 2 μL of DNA (sample or standard). 2 μL of Ultra-Pure water and 10 mM Tris were added to separate wells along with 8 μL of master mix to be used as controls. The plate was sealed with adhesive

PCR strips and spun down at 1000xg for two minutes. Following centrifugation, tubes were cycled into a qPCR light cycler.

Table 3-5: SYBR Green master mix for qPCR.

SYBR Green master mix	
2x SYBR mix	5 ul
Forward Primer (20uM)	0.25 ul
Reverse Primer (20uM)	0.25 ul
PCR certified H2O	2.5 ul

The number amount of DNA plasmid was determined by a comparison of Ct values between the samples and the known standard dilutions. Sample calculations can be found in

Appendix A. The number of plasmid copies per femtograms (fg) of DNA was determined by equation 3-5:

$$\text{Number of copies per fg} = \frac{fg \times 6.022 \times 10^{23}}{660 * size\ of\ plasmid(bp) \times 10^{15}} \quad 3\text{-}5$$

Where the size of the plasmid is 5.9 kbp. The titer of AAV of viral genomes per mL (VG/mL) could then be determined from the dilution factor shown in equation 3-6:

$$\text{Dilution factor} = \frac{starting\ volume}{starting\ \ volume + DNAse\ mix + EDTA + Prok\ mix + (water)} \times \frac{1}{5} \times \text{dilution before qPCR} \quad 3\text{-}6$$

The final titer in VG/mL can be found from equation 3-7:

$$\text{Final titer in mL} = \frac{Copies\ of\ virus\ genome}{dilution\ \ factor} \times 10^3 \quad 3\text{-}7$$

3.7 Chromatography and purification

The purification of varying viruses all used 1 cm diameter, 300-micron hydraulic channel diameter, Schoen gyroid cellulose hydrogel columns. All of the columns were made from the same cellulose composition (6 wt% dissolved cellulose, 3 wt% added cellulose powder acting as a physical cross-linker, and 15 wt% ECH as a chemical cross-linker). The variations in the functionality and bed height for each purification are shown in Table 3-6. These columns were all loaded into SNAP casings. For up to 10 cm bed height an S-10/125-PPSS-OV-FP20 was used and for up to 25 cm be heights an S-10/250-PPSS-OV-FP20 was used. Columns were shrunk in 100% ethanol before being slid into the glass casing. The columns were then re-swelled by flowing tap water through the glass casing. Air bubbles were removed from the column by flushing with degassed DI water over 15 minutes using the AKTA pump system.

Table 3-6: 3D-printed chromatography columns used for each virus purification (1 cm diameter, Schoen gyroid, 300 μm hydraulic diameter channels).

Virus	Functionality	Bed height cm
M13	Q	5, 10, 15
Adenovirus serotype 5	DEAE & HA	5
Lentivirus	DEAE	5
AAV serotype 9	Ha & Q	20, 10

3.7.1 Adenovirus and lentivirus purification

5 cm bed height DEAE and HA cellulose column of the same geometry and size were used to purify adenovirus and lentivirus from clarified cell lysate. The DEAE functionalization was completed at 30°C. This set of experiments was completed before ligand density optimization. The HA functionality used was alternating calcium and then phosphate solutions over three weeks. Details of functionalization can be found in Section 3.2. Both viruses were cultured on-site at iBET and details of this process can be found in our paper as well as in Section 3.6.2.1 [244]. Columns were placed in individual SNAP glass casings and attached to an AKTA 100 Explorer. For the column functionalized with DEAE, 20 mM Tris, pH 7 and, 20 mM Tris, 1 M

NaCl, pH 7 were used as equilibration and elution buffers, respectively for adenovirus. For the lentivirus, 50 mM Tris pH 7.5 and 50 mM Tris, 1 M NaCl, pH 7.5 were used as equilibration and elution buffers, respectively. For the hydroxyapatite column, 20 mM Tris pH 7 was used as equilibration buffer and 20 mM Tris, 1 M NaCl, 500 mM $NaHPO_4$, pH 7 as elution buffer. A 1 mL injection loop was used to load clarified lysate samples onto both columns, except for experiments to determine dynamic binding capacity in which the sample pump of the AKTA 100 was used. Elution was performed with a gradient over 5 column volumes (CV) for both columns. All eluted peaks and flow-through samples were collected and analyzed by qPCR and Nanosight particle tracking. The columns were cleaned with 20 mL of 2 M NaCl at 1 mL/min and then sanitized with 20 mL of 0.5 M NaOH at 1 mL/min. The linear velocity for loading was 8 cm/h and 76 cm/h for elution, for both columns, unless otherwise stated. Triplicate replicates were completed for each purification.

3.7.2 M13 purification

The SNAP casing containing the 3D-printed Q chromatography column (either 5, 10, or 15 cm bed height) was attached to an ÄKTA start protein purification system. All chromatography was completed at room temperature. Details of functionalization can be found in Section 3.2. From previous experimentation, the 3D-printed columns maximize their recovery with the lowest load flow rate possible [247]. Unless otherwise stated flow rate of the ÄKTA start system was 0.5 mL/min (linear velocity of 76 cm/h). Each column was equilibrated with 5 CV of equilibration buffer (10 mM phosphate, pH 7.5). The crude cell culture was injected onto the column through either a 2 mL sample loop or for larger samples the ÄKTA systems sample pump. Following loading, the column was washed with 40 mL of equilibration buffer to remove unbound or weakly bound phage particles or unwanted contaminants. The adsorbed phage particles were eluted stepwise over 30 mL of elution buffer (10 mM phosphate with 1 M NaCl pH 7.5). Eluted fractions were collected with a fraction collector included in the system (Frac-P90) at fixed volumes during elution (3 mL). Triplicates of each purification were completed.

Initially, CIP for the column was with 1 M NaOH over 8 CV at 1 mL/min, followed by 8 CV of 1 M NaCl and a 20 mL flush of DI water at 4 mL/min. This was then changed to mitigate fouling post each purification trial. The new procedure was as follows: The column was stripped with 1 M NaOH at 1 mL/min for 60 minutes until the UV signal had stabilized below 10 mAu. The column was then flushed with DI water (4 mL/min) until the conductivity was below 5 mS/cm. The column was then washed with an equilibration buffer over 10 CV (4 mL/min).

Purifications were also completed with similar operating conditions to an expanded bed purification completed by Ling *et al.* [20]. The same zero bed height of 15 cm was used with an adjusted load and elution flow rate of 0.8 mL/min (122 cm/h) to match the residence time of the expanded bed system. The same equilibration and elution buffer as the previous M13 purification tests were used. The same volumes for equilibration and wash steps were also used except at a flow rate of 4 mL/min (611 cm/h). The load volume used was 3 mL or 0.25 CV based on previous experimentation for the highest recovery. The elution was collected with the fraction collector included in the system (Frac-P90) at fixed volumes during elution (3 mL). Triplicates of each purification were completed.

3.7.3 AAV serotype 9 purification

3.7.3.1 Hydroxyapatite purification strategy:

The SNAP casing containing the 3D-printed HA chromatography column (4×5 cm plugs totaling a 20 cm bed height) was attached to an ÄKTA start protein purification system. The HA functionality used in this case was alternating solutions of calcium and then phosphate over two weeks. This was to maximize HA growth while still allowing for stationary phase penetration of the AAV particles. Details of functionalization can be found in Section 3.2. The column was equilibrated with 20 mL of equilibration buffer (16 mM imidazole, 25 mM NaCl and 5 mM phosphate, pH 6.5) at 611 cm/h. Clarified cell culture fluid was loaded directly onto the column as feed material at 76 cm/h using the sample pump. Alternatively, clarified cell lysate was diluted 10× in DI water before loading onto the column as feed material at 76 cm/h

using the sample pump. The column was then washed with 40 mL of equilibration buffer at 611 cm/h. The AAV particles were then eluted at 76 cm/h over 30 mL with an elution buffer (16 mM imidazole, 500 mM NaCl and 500 mM phosphate pH 6.5). The elution's were collected with a fraction collector included in the system (Frac-P90) at fixed volumes during elution (4 mL). CIP for this column follows the same procedure as for the Q columns used for M13 bacteriophage in Section 3.7.2. All purifications were repeated in triplicate.

3.7.3.2 Q purification strategy:

The SNAP casing containing the 3D-printed Q chromatography column (10 cm bed height) was attached to an ÄKTA Start protein purification system. The column was equilibrated with 20 mL of equilibration buffer (16 mM imidazole, 25 mM NaCl and 5 mM phosphate, pH 6.5) 611 cm/h. The clarified cell lysate was diluted 10× in DI water before loading onto the column as feed material at 76 cm/h using the sample pump of the ÄKTA Start. Instead of operating in a bind and elute, the column was used to bind the negatively charged contaminants in the lysate instead of the AAV particles. As such, the flow-through was collected instead of the elution. This was done manually as the ÄKTA Starts software would not facilitate flow-through collection. The flow-through was collected as soon as the UV signal spiked on the display screen, taken directly after the UV sensor on the ÄKTA. 50 mL of elution was collected to be analyzed by qPCR and SDS-PAGE. Contaminates were eluted at 152 cm/h over 30 mL with an elution buffer (1 M NaCl, 10 mM phosphate pH 6.5). The purity of flow-through samples was determined with SDS-PAGE as described in Section 3.6.1.3.

3.7.4 Chromatography calculations

3.7.4.1 Recovery:

The recovery of viral particles was determined by the ratio of total viral particles loaded onto the column compared with the total number of viral particles found in the elution (or flow-through in the case of AAV) (equation 3-8). The total number of viral particles was determined by the volume (V) multiplied by the titer (C). The number of viral particles was either determined in plaque-forming units (pfu), viral genomes (VG), or transducing units (TU). This is specified for each individual virus and the appropriate tittering technique used.

$$\frac{V_{eluted} \times C_{eluted}}{V_{feed} \times C_{feed}} \times 100 = Recovery\ \% \qquad (3\text{-}8)$$

3.7.4.2 Dynamic binding capacity:

To determine DBC samples of flow-through were collected and analyzed for viral content by qPCR. This determined a characteristic sigmoid-shaped curve from which the DBC could be calculated. The $DBC_{10\%}$ was calculated according to equation (3-9), where C_0 corresponds to the feed virus concentration, $V_{b,10\%}$ is the breakthrough volume at which the flow-through effluent reaches 10% of feed concentration, V_0 is the void volume, and CV is the column volume [248].

$$DBC_{10\%} = \frac{C_0 \times (V_{b,10\%} - V_0)}{CV} \qquad (3\text{-}9)$$

3.7.4.3 Ligand density

The charge density of both DEAE and Q functionalized columns was measured by the titration method adapted from Stone *et al.* [249]. 1 cm lengths of 1 cm diameter functionalized Schoen gyroid columns (varying channel diameter and ligand) as well as an un-functionalized control column were suspended in separate 50 mL centrifuge tubes with 1 M NaOH for 30 minutes. Column pieces were then washed in DI water until the effluent reached a pH of 7. Columns were then placed in separate 50 mL centrifuge tubes along with 20 mL of 0.5 M NaCl and 0.05 M HCl. 10 mL of the 20 mL was removed after 12 hours to be titrated against 0.1 M NaOH until a neutral pH was reached. The ligand charge density was then determined (3-10) by the difference in total moles required to neutralize the solution between the functionalized ($m_{functional}$) and the control ($m_{control}$) per mL of column (V_c) by a factor of 2. Sample calculations can be found in

Appendix A.

$$IEX(\mu mol/mL) = \frac{m_{control} - m_{functional}}{v_c} \times 2 \quad (3\text{-}10)$$

This was also converted into μmol/cm² to compare densities to membrane technology. TPMS shapes are defined by geometric equations which can be used to calculate their specific surface area.

4 Stationary phase analysis for viral purification chromatography

As described in the literature review, the previous production of 3D-printed hydrogel columns by Anne Gordon showed their fidelity to the templates used and their ability to bind and elute proteins while passaging solids [15]. As this technology is very novel, limited literature on ligand chemistry for the chosen stationary phase material (cellulose hydrogel) was available. Chemical functionalization's which have been previously used on agarose, bacterial cellulose, and aerogels will be adapted for this research [134, 225, 226, 242, 250, 251]. The first step of this research was to investigate the stationary phase material's potential to effectively bind and elute virus or virus-

like particles. As a different wax printer was used for most of this work, analyses of the printed columns' structural fidelity are briefly considered.

It was hypothesized that this cellulose hydrogel could be chemically modified to bind and elute protein and therefore be used as the stationary phase to purify virus or viral particles. Building on Anne Gordon's original work, the following chapter looks at extending the range of functionalities outside of ion exchange and optimizing ligand density and static protein binding capacity. Additionally, the stationary phase was investigated for its potential to allow diffusion of larger binding targets such as viruses inside of its pores. Literature showed that the pore size distribution should be theoretically large enough to allow diffusion but confirmation was need [222]. A unique hydroxyapatite ligand for the cellulose hydrogel was developed and characterized.

4.1 Hydroxyapatite functionalization

4.1.1 Hydroxyapatite Growth

Two methods for incorporation of HA into the cellulose hydrogel matrix were tested, before gelation and post gelation. Incorporation before gelation was achieved by the addition of premade HA powder into the dissolved cellulose solution, while post gelation was achieved by seeding crystal growth in regenerated hydrogels. Two methods of seeding hydroxyapatite were tested, one involving alternating calcium and phosphate salt solutions and the second using SBF fluid with citric acid. Details of each functionalization method can be found in Section 3.2.3. Both methods of seeding HA crystals into cellulose hydrogels were successful, producing different crystal structures. FE-SEM was used to examine functionalized cellulose samples as described in 3.3.2. Triplicates of each functionalization were examined along the entire length of the hydrogel sample. Figure 4-1 shows SEM images of a cellulose hydrogel with and without HA formed from alternating saturated solutions of $CaCl_2$ and Na_2HPO_4. The small spherical balls shown in Figure 4-1 panel B can be more clearly seen in Figure 4-2. After

one-week crystal structures were found in most of the pores in all cellulose hydrogels tested, and after two weeks pores were nearly filled with crystals.

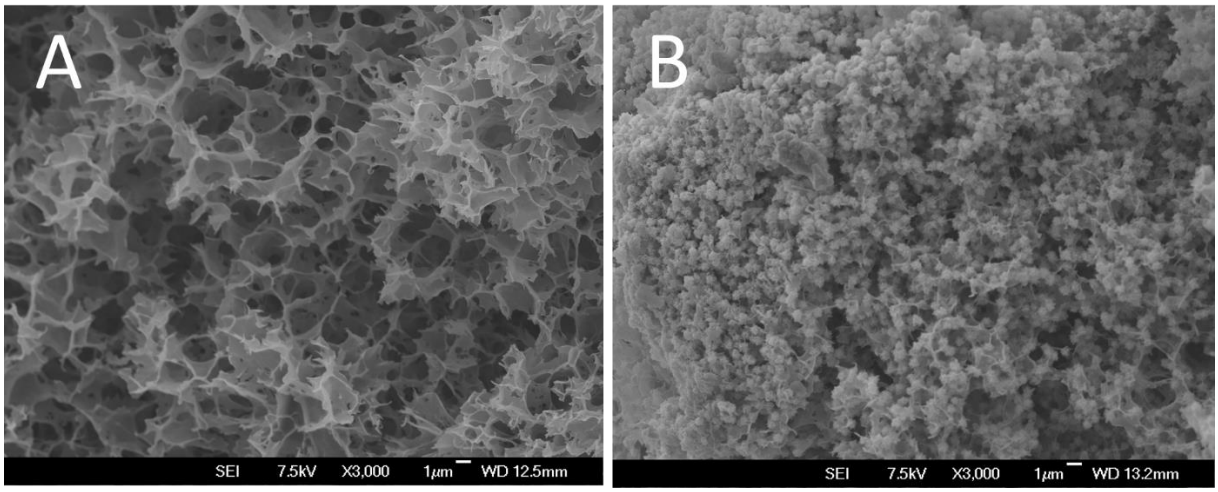

Figure 4-1: SEM image of the microstructure of a 5% cellulose hydrogel (A); 5 wt% cellulose hydrogel functionalized with HA grown with alternating solutions of calcium chloride and disodium phosphate over two weeks (B).

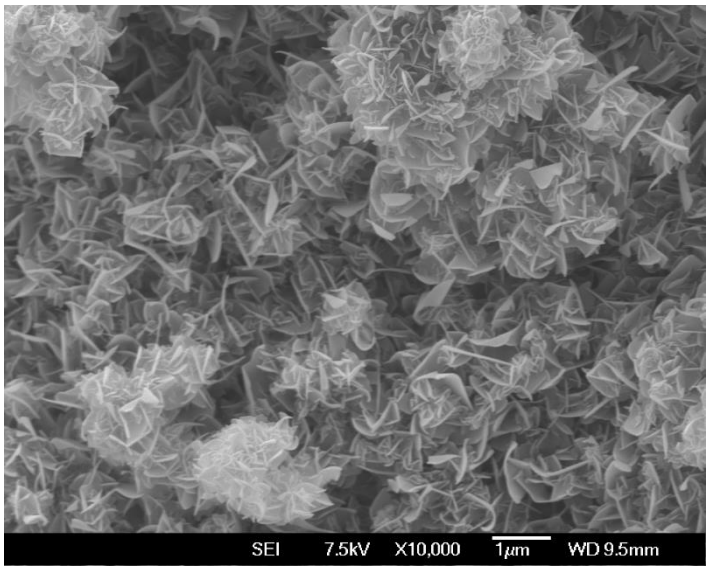

Figure 4-2: SEM of the HA crystal structure inside of a 5 wt% cellulose hydrogel. HA was grown with alternating solutions of calcium chloride and disodium phosphate over two weeks.

Figure 4-3 shows an SEM image of hydroxyapatite formed from exposure to 1.5 x SBF with 1 mM citric acid over one week. The structure of the crystal growth is significantly different from that shown in Figure 4-1 and Figure 4-2. The crystal structure from SBF is similar to a

coating of the gel instead of the sharp needle formations from alternating solutions. It has formed a layer over almost the entire external and internal walls of the gels pores with small patches of crystal squares starting to form.

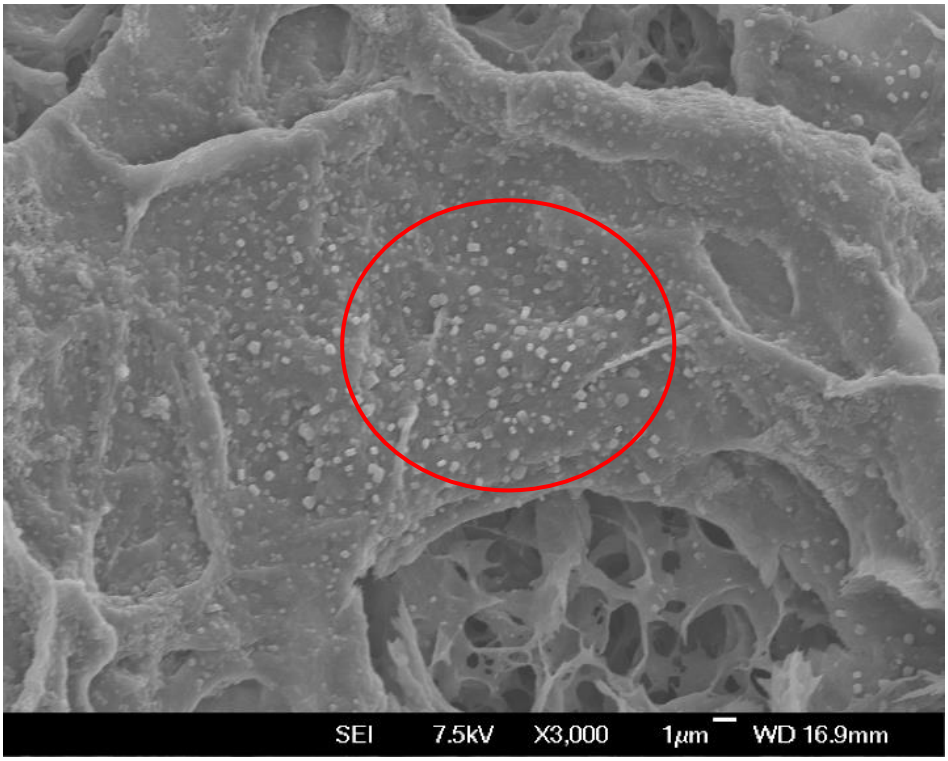

Figure 4-3. SEM image of HA crystal structure grown on 5 wt% cellulose hydrogels from exposure SBF with 1 mM citric acid for one week. The red circle shows the beginning of square crystal formations.

This difference in the crystal structure is due to how the initial hydroxyapatite crystals are seeded between the two methods. Alternating solutions of calcium chloride and di-sodium orthophosphate cause nucleation sites in small confined regions of the gel, specifically the pores. The positive Ca^{2+} ions loosely associate with the negatively charged free hydroxyl groups of the cellulose hydrogel. This has been shown previously with bacterial cellulose as well as other materials such as titanium, zirconium with hydroxyl groups, or natural polymers with free carboxylic acid groups [252, 253]. This was confirmed by Hutchens *et al*. who produced similar HA crystal structures as shown in his work [250]. Crystal growth is then stimulated from these nucleation sites outwards forming sharp needle structures. Over time smaller crystal structures meet, combining and forming the larger spherical needle ball shapes because of the curved shape of the cellulose pores. Crystal growth from the SBF solution occurs differently, facilitated by the citric acid initially binding to the exposed hydroxyl

groups of the cellulose [242]. The citrate then allows the binding of free Ca^{2+} ions creating a nucleation site for crystal growth. The citrate more favorably binds free Ca^{2+} ions than hydroxyl groups causing a larger covering of nucleation sites. This results in a complete saturation of HA crystals that grow like a coating versus a multitude of smaller structures. Interestingly, if the hydrogel is functionalized with alternating calcium chloride and di-sodium orthophosphate solutions for longer than three weeks, a complete surface will form over the hydrogel that still maintains the sharp needle-like shapes. Figure 4-4 shows this

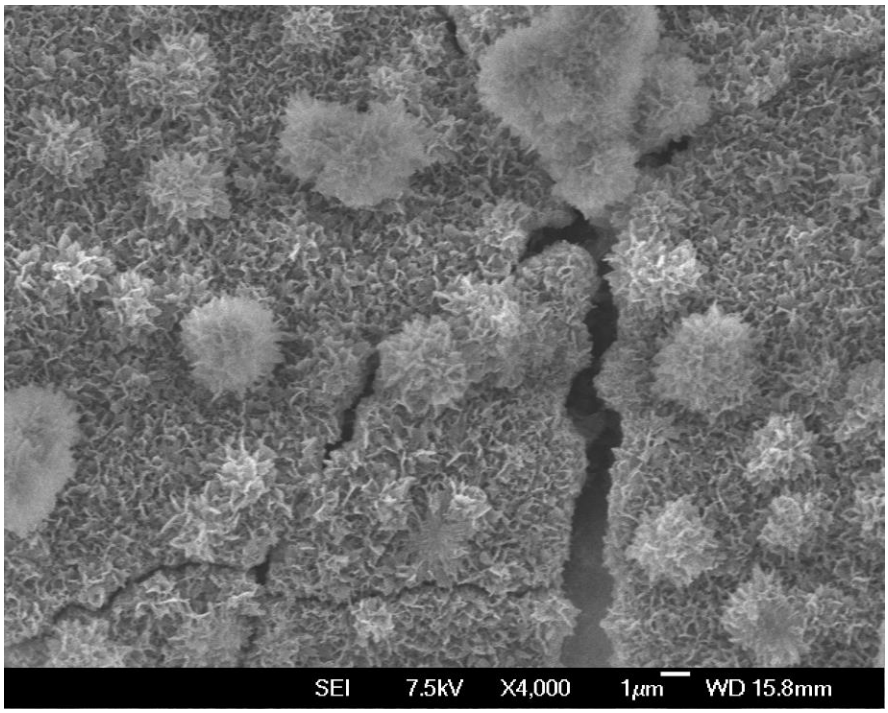

formation on a 6 wt% cellulose hydrogel cross-linked with 15 wt% ECH. The smaller crystal structures grow and meet, combining to cover the cellulose. The sharp structure of these crystals is still maintained but has covered the cellulose during their growth.

Figure 4-4: SEM image of HA crystal structure grown on a 6% cellulose hydrogel cross-linked with 15% ECH by alternating solutions over three weeks.

If hydrogels that alternating calcium and phosphate solutions have initially seeded crystals are exposed to SBF solution, the previously formed crystals become smoothed and rounded. Figure 4-5 shows a 5 wt% cellulose hydrogel initially seeded with alternating calcium and phosphate solutions followed by SBF treatment. The SBF and citric acid coating effect cover the initial crystals seed by the alternating solutions with a layer of this different crystal

structure. These new crystals fill in any gaps in the needle-like structures made by the alternating solutions joining them together.

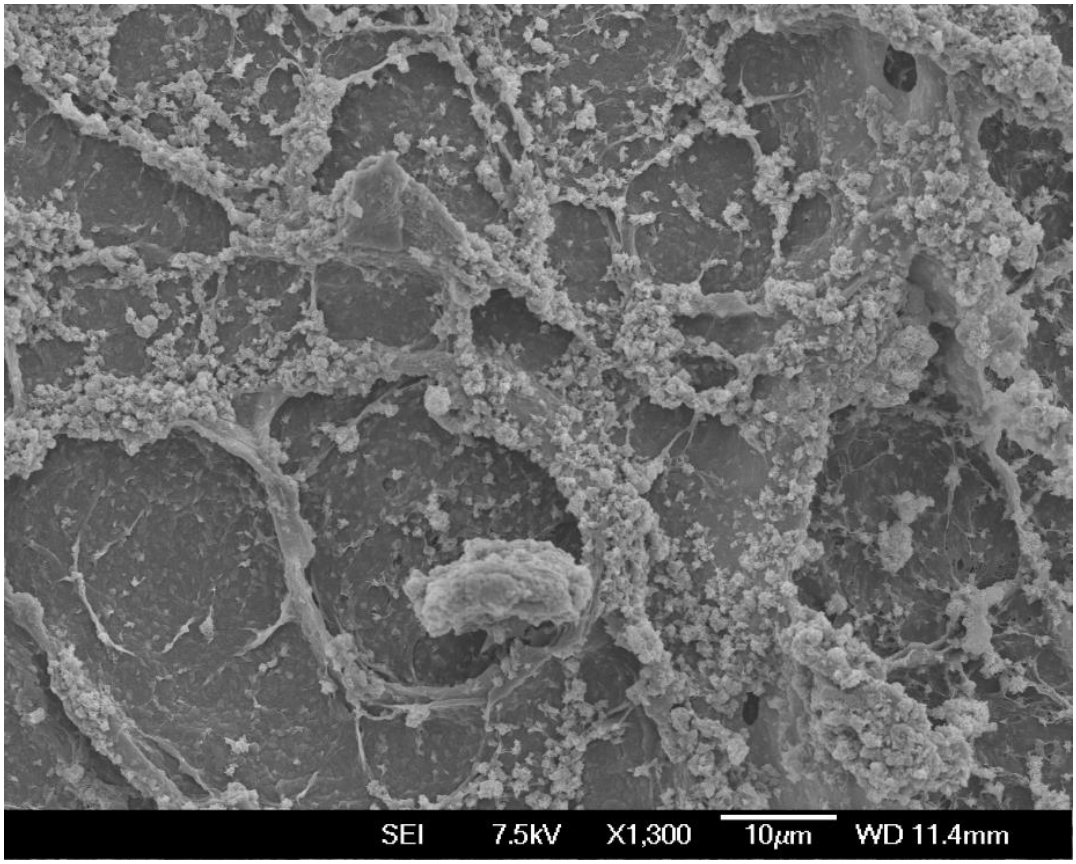

Figure 4-5: SEM image of HA crystal functionalized on a 5 wt% cellulose hydrogel after one week of alternating calcium then phosphate solutions followed by one week of SBF fluid.

The incorporation of HA powder before gelation resulted in a dense white hydrogel. Figure 4-6 shows an SEM image of cellulose hydrogels' internal structure made with HA powder added before gelation. The pores of the resulting cellulose hydrogels become clumped with large HA crystals covered by cellulose. This alteration of the pore structure is detrimental for any chromatography media as the pores maximize the binding capacity by increasing surface area [254]. If the pores are too small, proteins or viruses' binding will be limited to the surface.

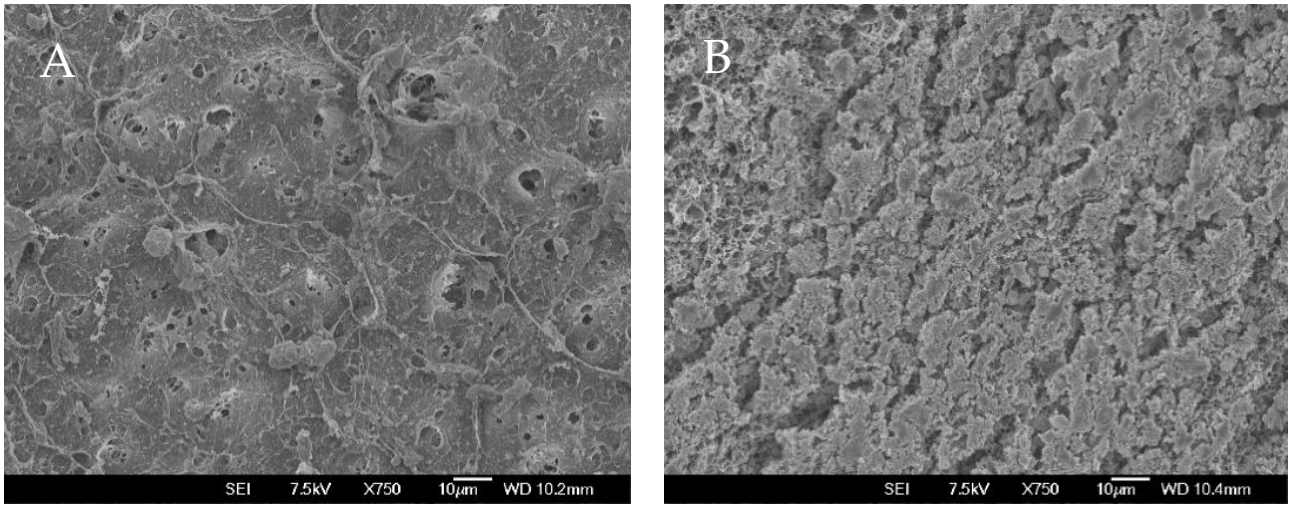

Figure 4-6: SEM image of a sliced cross-section of cellulose gels with HA powder added to the solution before gelation. A; 10 wt% HA and B; 20 wt% HA

HA also grew on native cellulose hydrogels and hydrogels that were physically cross-linked, chemically cross-linked or both. This benefits the functionality as control over chemical and physical cross-linking causes changes in the microstructure related to pore size and shape, as described previously in Section 2.4.4 [222]. Adjusting the pore size and limiting crystal growth inside the pores could allow the gel to act as a multimodal functional ligand combining size-exclusion and HA.

4.1.2 HA functionality

Protein adsorption studies were carried out on HA functionalized cellulose hydrogels as described in Section 3.5.1. Table 4-1 shows the amounts of BSA eluted from 5 mm cellulose hydrogels cubes functionalized with HA. Hydrogels were functionalized by alternating calcium chloride and disodium orthophosphate solutions for one week, followed by one week of exposure to SBF fluid with 1 mM of citric acid. Two different elution buffers were used to examine how the BSA was binding to the HA crystals in the gels' pores. Control gels used were of the same cellulose composition without HA functionality. In all cases, no adsorption was detected by the Nanodrop, indicating control gels had not bound any BSA. Similar results were found for hydrogels with HA formed from both alternating calcium and phosphate solutions and SBF with citric acid separately.

Table 4-1: Elution of BSA from HA cellulose hydrogels.

Gel Composition	Elution buffer	Protein eluted mg/mL	Standard Deviation mg/mL
5% cellulose	1 M NaCl	0.04	0.01
5% cellulose + cellulose 2.5%	1 M NaCl	0.06	0.01
5% cellulose + 2.5% cellulose + 5% ECH	1 M NaCl	0.05	0.01
5% cellulose	1 M NaCl + 400 mM Na_2HPO_4	0.29	0.02
5% cellulose + 2.5% cellulose	1 M NaCl + 400 mM Na_2HPO_4	0.48	0.01
5% cellulose + 2.5% cellulose + 5% ECH	1 M NaCl + 400 mM Na_2HPO_4	0.38	0.03

Over five times the amount of protein was eluted with a sodium chloride and phosphate salt buffer than with a sodium chloride salt buffer. This elution profile is a result of the binding characteristics of BSA to the HA functional groups. Predominantly, HA consists of three primary binding mechanics; (i) metal-chelating sites provided by the calcium ions for binding phosphates, (ii) cation exchange provide by the negatively charged phosphate ions, and (iii) small amounts of anion exchange can also be mediated by the positively charged calcium ions [255]. Only a small amount of BSA is bound to the ion exchange sites compared to the calcium-based metal affinity active sites. This is because of BSA's acidic nature, resulting in it having an overall negative charge at pH 7, therefore not having a great affinity for the cation exchange group [256]. For gels that were functionalized with HA before gelation, no BSA binding was achieved. The lack of protein binding was because of the cellulose covering the HA crystals restricting the proteins ability to access the binding sites. Even in gels with a high level of added HA (30 wt%), BSA was not bound.

4.1.3 HA protein binding selectivity

This work was completed in collaboration with Professor Steven Cramer at Rensselaer Polytechnic Institute (RPI) in Troy, New York. As the Solidscape printer was broken (before the Projet printer was purchased), only a limited number of templates were available to construct chromatography columns to take overseas. Therefore, only one HA column was taken functionalized with alternating calcium and phosphate solutions instead of SBF with

citric acid. This column was made from SolidScape wax templates as described in 3.1. Cellulose composition for these columns was 6 wt% dissolved cellulose, 3 wt% undissolved cellulose powder, and 15 wt% ECH. Conditions for binding and elution used were based on research into hydroxyapatite selectivity and binding mechanics analysis by Hou *et al*. to be used as a comparison [139]. The same running buffers and elution gradient was used. Details for this bind and elute chromatography can be found in Section 3.5.3. Table 4-2 shows the elution order for model proteins from a 5 cm bed height 300 micron Schoen gyroid column functionalized with HA (two weeks of alternating calcium and phosphate solutions).

Table 4-2: Retention time for model proteins from a 3D-printed 300 μm Schoen gyroid HA column.

Protein	Elution peak minutes	Standard deviation minutes	NaCl mM
Ribonuclease B	5.9	0.07	197
Beta lacto-globulin A	4.5	0.2	151
Cytochrome C	10.3	0.06	344

These experiments' results gave a different set of selectivities to those shown in the paper by Hou *et al*. using a commercial hydroxyapatite resin [139]. The resin they tested had an elution order from least to most retained of cytochrome C, beta-lactoglobulin A, ribonuclease B [139]. As shown in Table 4-2, the first eluted protein from the 3D-printed HA column was ribonuclease B followed by beta-lactoglobulin A and cytochrome C. An experiment was also completed with transferrin, a protein that should have been moderately retained at the equilibrated pH and salt concentration but did not bind at all. This unusual set of selectivities could be because of the mineralized HA's chemical composition (e.g., a large amount of chlorapatite or other calcium phosphate mineral instead of HA). Further analysis of the minerals composition and structure was required to determine if what had been synthesized is HA, as mentioned in previous papers [229, 231, 250, 257, 258]. Figure 4-7 shows the elution profile for bovine cytochrome C from the 300 μm CHT column.

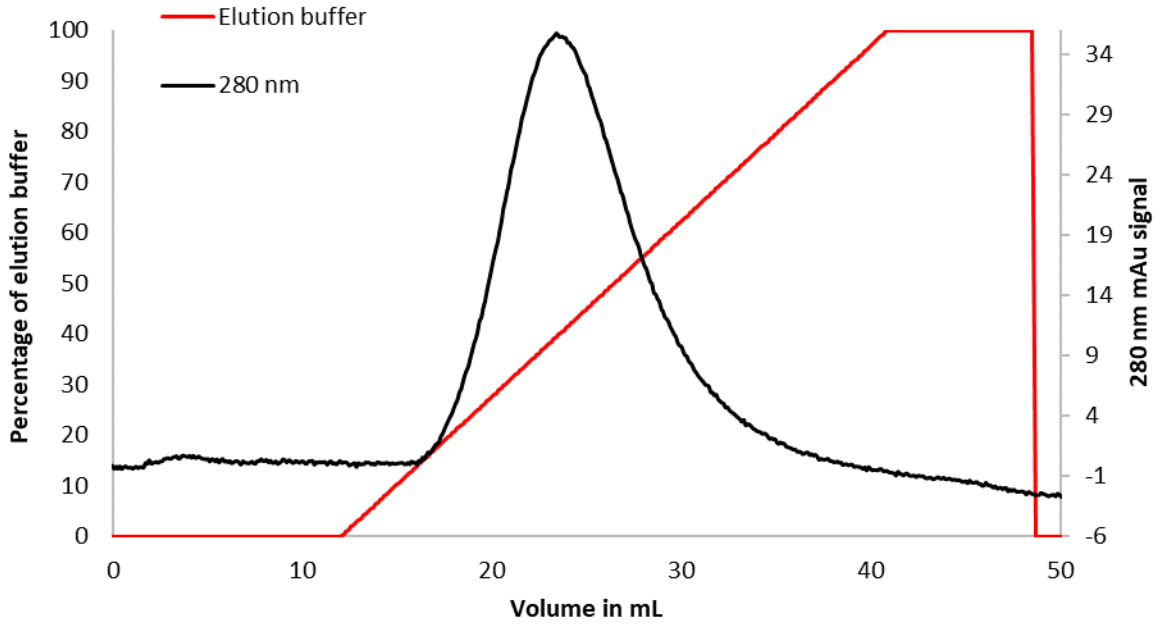

Figure 4-7. Elution profile of bovine cytochrome C from 5 cm bed height, 300 μm Schoen gyroid HA column. Linear gradient at 1 mL/min over 10 CV to 1 M NaCl 35 mM phosphate buffer pH 7.

This broad elution peak is consistent with the 3D-printed column used and not its functionality. 3D-printed columns elute in larger volumes than traditional packed beds because of the large channel size (300 um) and 50% voidage within the column. In previous work by Anne Gordon, elution peaks of BSA's from a similar DEAE column were equally as broad [15]. This peak broadness is similar to expanded bed chromatography, where because of the expansion required to passage cells, there is greater space between beads (higher voidage), and therefore, axial diffusion is higher [259]. Tailing was also observed for some of the proteins, most notably the larger globulin proteins (beta-lactoglobulin A and ribonuclease B). The protein's size affects its diffusivity, with larger proteins taking longer to diffuse out of the pores [248].

4.1.4 HA control

Initial HA growth work also uncovered an unexpected result shown below in Figure 4-8. The growth of HA could be limited to just inside the pores of the cellulose hydrogel. This is particularly interesting as it could provide another level of selectivity by excluding particles too large to diffuse into the pores.

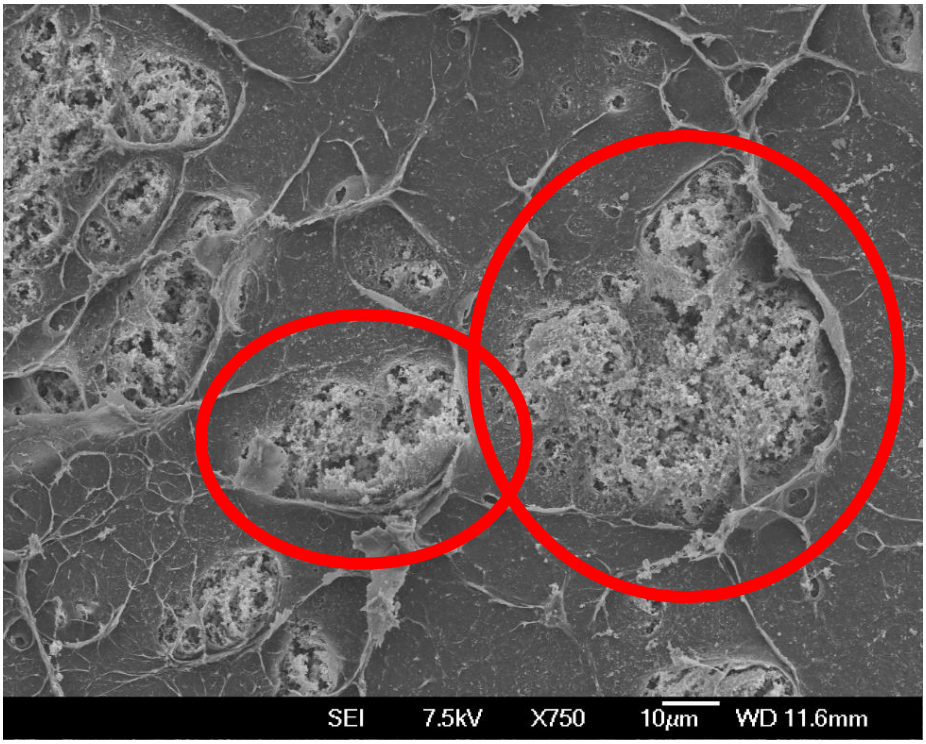

Figure 4-8. SEM of HA crystal structure (inside of the red rings) grown on a 5 wt% cellulose hydrogel.

The washing step with DI water between alternating solutions of calcium chloride and disodium orthophosphate caused this effect. By washing the cellulose hydrogel with DI water, the calcium ions bound to the free hydroxyl groups are removed and cannot create a crystal nucleation site when phosphate ions are introduced. Calcium ions bound inside the cellulose pores take longer to be removed as pore diffusion limits their migration out of the hydrogel. Therefore, controlling the length of time the washing occurs can control HA crystallization and where it occurs. This control can be seen in Figure 4-9, showing a relatively clean surface with a large amount of crystal growth below the surface. This 5 mm cube of cellulose hydrogel was washed for 20 seconds in DI water between each alternating salt solution.

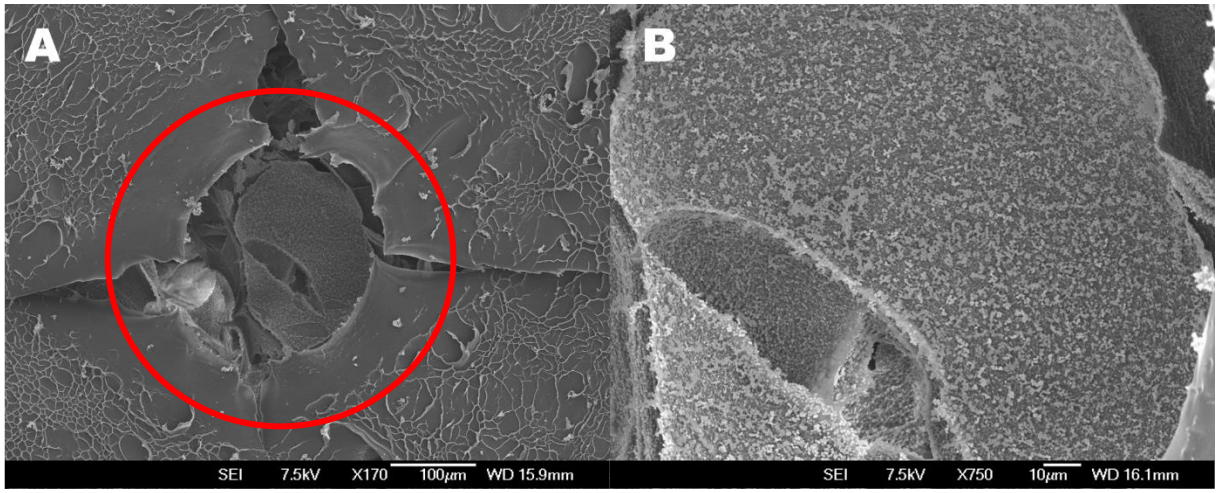

Figure 4-9: SEM image of HA crystal structure grown on a 6 wt% cellulose hydrogel cross-linked with 15 wt% ECH. Panel B shows a magnified in part of the crack in the red circle shown in A.

Dependent on the length of washing time, the crystal growth can be limited far below the hydrogel's surface. Excessive washing (>60 seconds) resulted in no HA formation in small cellulose cubes (5 mm sides) as all the calcium ions were removed. The surface can also be covered in HA without any washing step shown in Figure 4-10.

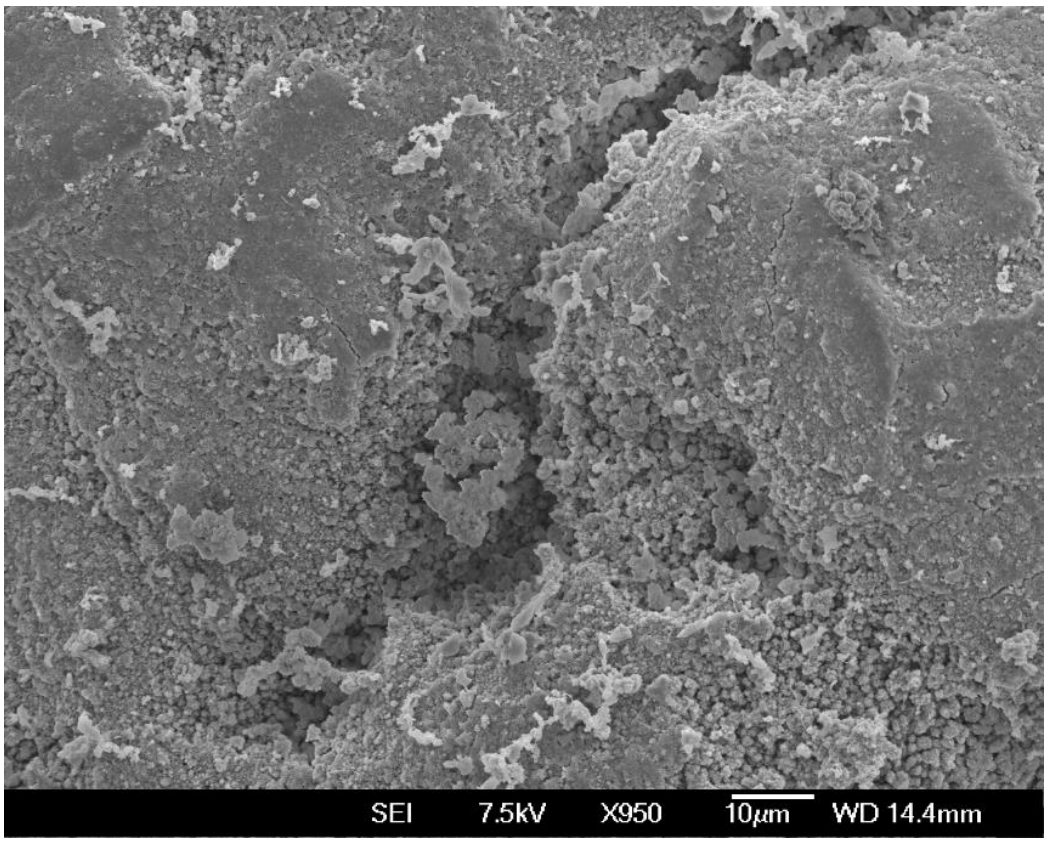

Figure 4-10: SEM image of HA crystal structure grown on a 6 wt% cellulose hydrogel cross-linked with 15 wt% ECH without an intermediate washing step.

Without a washing step, none of the Ca^{2+} ions are removed from the hydroxyl groups resulting in full surface coverage of nucleation sites. The entire surface is covered in a rough surface of crystals that fills the pores of the gel. This covering effect is similar to the HA growth facilitated by the SBF solution. This result reinforces that how the crystals are seeded defines the crystal structure's growth. Control over where HA grows could not be achieved with the SBF method as the crystal growth continued to cover the entire surface even with a long (>60 seconds) washing step. The citrate molecules favorably bind to the surface hydroxyl groups of the cellulose and become difficult to remove.

Further work was completed on HA control. However, its benefit could not be shown for chromatography. The HA mineral did not bind the larger contaminates that would be excluded by the pores, such as cells, cell debris, and DNA, all of which are predominantly negatively charged [154, 260]. The HA's cation exchange sites repel these negatively charged

contaminates anyway, so they do not bind during chromatography. Therefore, having the HA only inside the pores does not provide additional selectivity as excluded contaminates would not be bound anyway. Future works may use control of HA growth, but it has not been explored in this project.

4.1.5 HA compositional analysis

Based on the ability to control HA growth and the protein binding work completed at RPI, the mineral analysis was limited to the HA functionalization by alternating calcium and phosphate salt solutions. The mineral deposits of suspected HA were tested via EDS, FT-IR, SEM, and powder XRD, details of which can be found in Section 3.3. EDS compositional analysis showed the ratio of calcium and phosphate to be in the range of 1.5 to 1.8, depending on which salt solution was last in the cycle for seeding growth. Pure HA has a calcium to phosphate ratio of 1.67 based on its stoichiometric equation $Ca_5(PO_4)_3(OH)_2$. Upon repeats, with thoroughly washed gels, the ratio was found to be between 1.5 to 1.6. If the ratio is less than 1.67, the mineral may be known as calcium deficient HA. This data indicates a calcium phosphate mineral is present, but it may not all be HA, and some may be calcium deficient [232].

Interestingly, initial EDS results showed a large amount of chlorine present in the sample. Chlorine could indicate the presence of chlorapatite instead of HA. Further repeats of this experiment showed that if the samples were not washed properly before freeze-drying and analysis, excess calcium chloride or di-sodium orthophosphate could be detected. However, even with excessive washing, chlorine was still detected in varying amounts. EDS results indicated while most of the sample is potentially calcium deficient HA, up to 1 to 3 wt% is likely chlorapatite. The pH of both alternating salt solutions was adjusted above pH 9 to prevent chlorapatite formation, confirmed by EDS results showing no chlorine present. In basic conditions, more free OH^- ions are present and more favorably bind during mineral formation over Cl^- [261]. The EDS results proved inconclusive, only indicating a calcium phosphate mineral was present.

These EDS results for the calcium phosphate mineral presence were confirmed by FT-IR analysis shown in Figure 4-11. There are significant differences in the region of 450 to 700 and 900 to 1200 cm^{-1}. The peaks associated with PO_4^{-3} are at 600, 570, and 1050 to 1100 cm^{-1}, all of which can be seen in Figure 4-11 [228, 229, 231, 250].

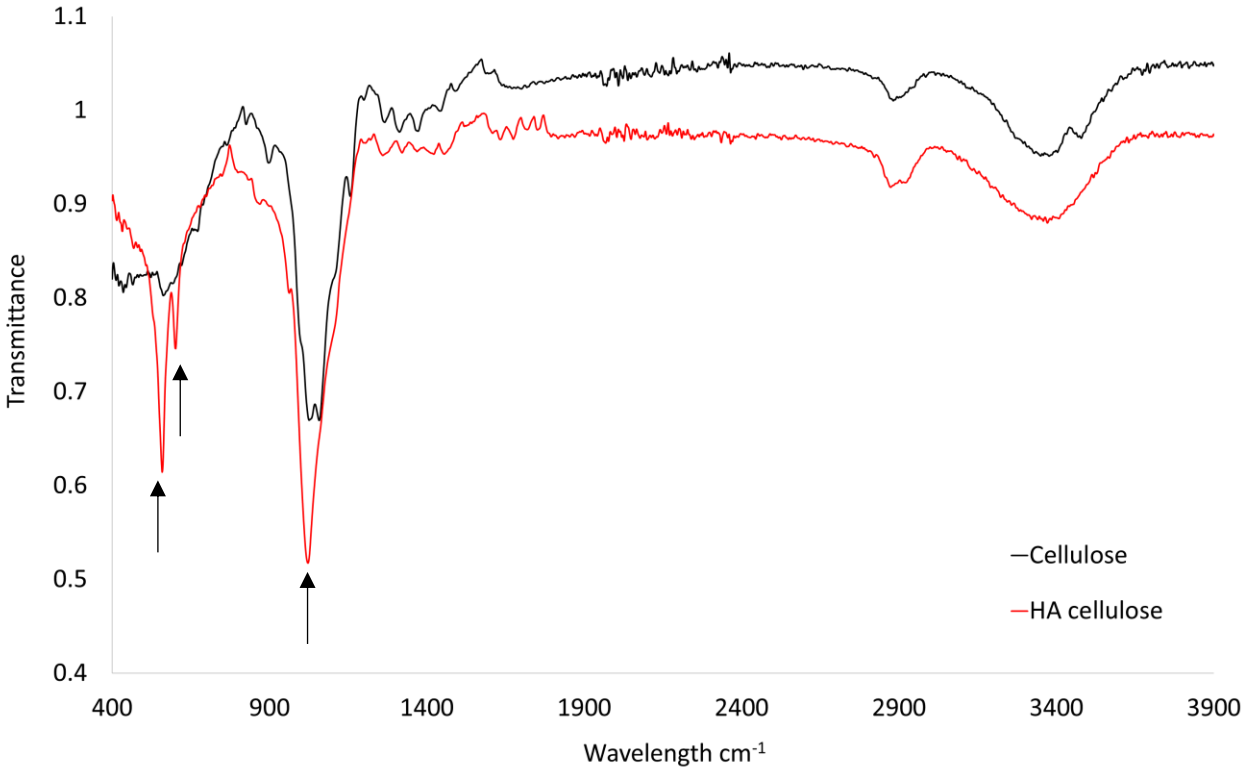

Figure 4-11: FT-IR transmittance results for HA cellulose and control cellulose hydrogels. Arrows indicate peaks associated with PO_4^{-3}

Peaks specific to hydroxyl groups can be seen in the 600 to 650 cm^{-1} region which could indicate HA. Figure 4-12 shows the 400 to 700 cm^{-1} region of Figure 4-11 specifically looking at the two peaks of the HA cellulose.

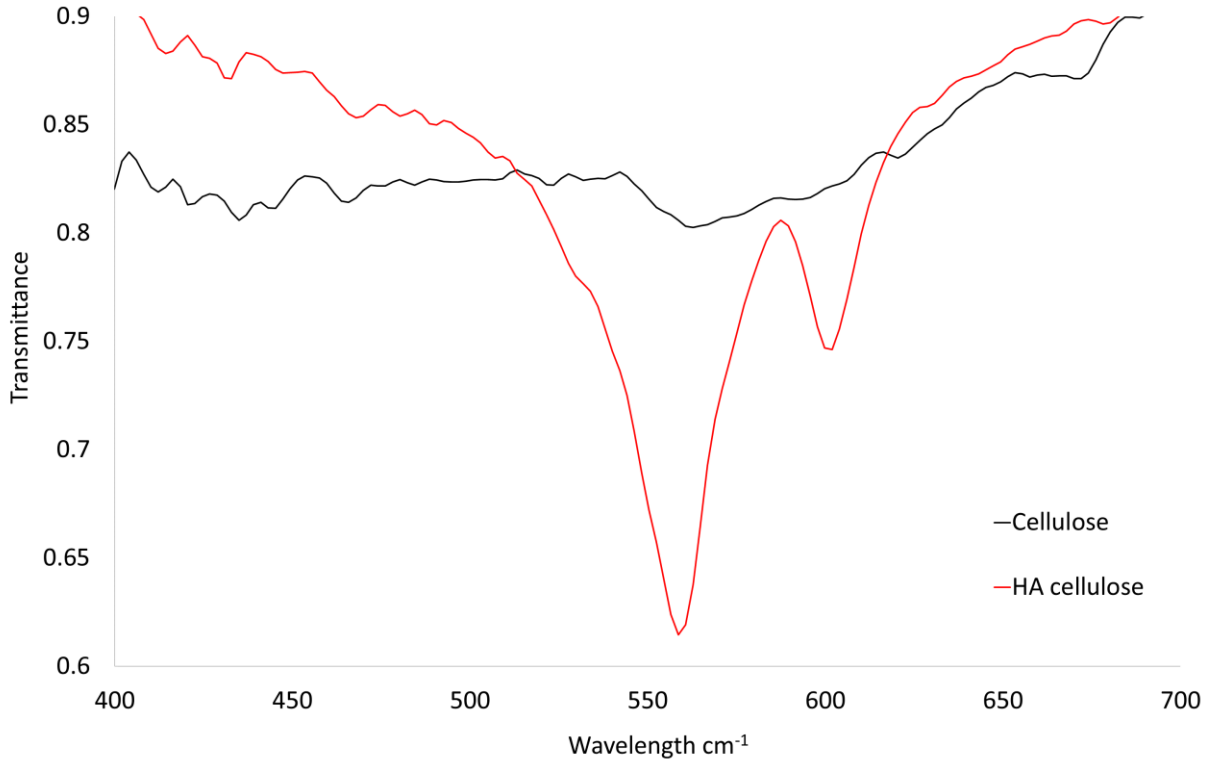

Figure 4-12: FT-IR transmittance results for HA cellulose and control cellulose hydrogels. Zoomed in on 400-700 cm^{-1} region.

For pure HA samples, a peak at 630 cm^{-1} should be present indicating the hydroxyl group associated with the mineral. This is not present in pure chlorapatite samples as the hydroxyl group is replaced by a Cl atom [262]. This peak is also missing from Figure 4-12 but is consistent with all other papers where they have claimed to have mineralized HA onto cellulose structures. Because of the poor crystallinity of un-sintered mineralized HA this peak may not be able to be seen, hidden by shouldering of the broad 600 cm^{-1} peak. Figure 4-13 shows the same region for HA grown at pH 9.

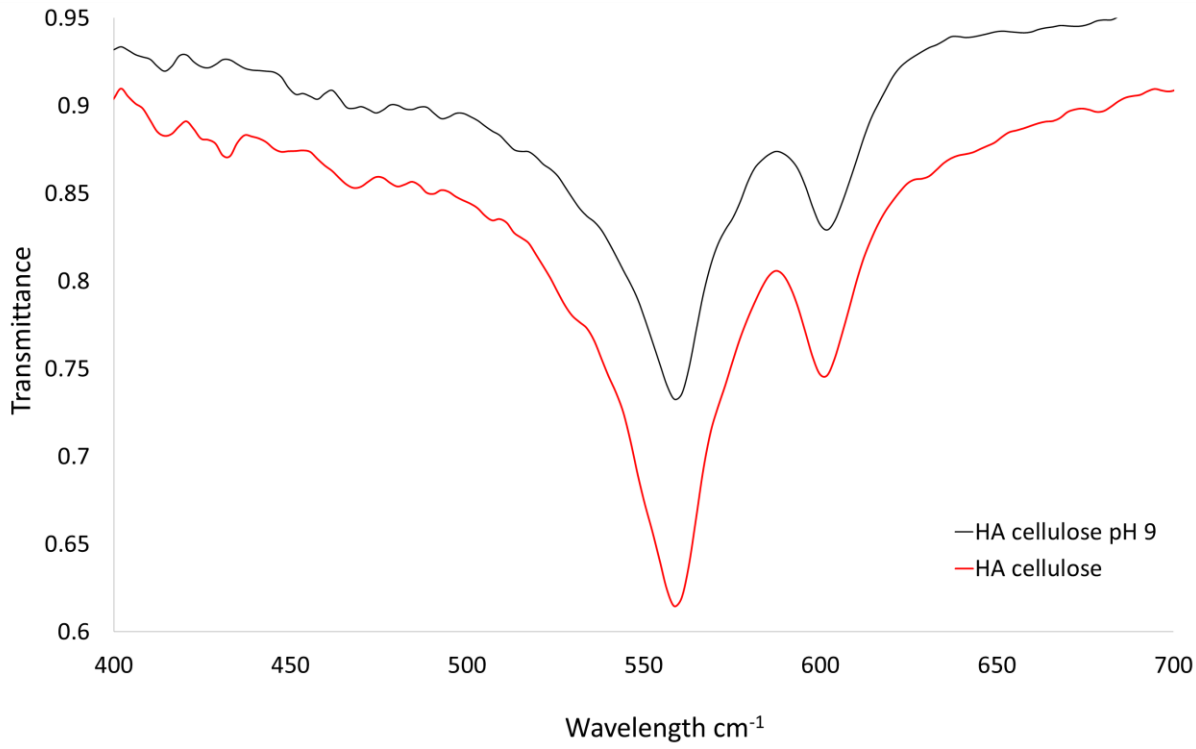

Figure 4-13: FT-IR transmittance comparison between standard HA cellulose and those grown at pH 9. Magnified in on the 400-700 cm^{-1} region.

Figure 4-13 shows that the peak around 600 cm^{-1} is broad, which could be caused by a stronger 630 cm^{-1} peak. With the previous EDS results, it can be assumed not all the calcium phosphate mineral formed is pure and at least some of it is chlorapatite, except those grown under alkaline conditions. Although the peaks associated with HA are present in the FT-IR analysis the contradictory binding selectivities suggest that it is not HA but a different calcium phosphate mineral. There are multiple different calcium phosphate minerals with different binding characteristics based on their calcium to phosphate ratio and crystal structure [263].

4.1.6 Powder XRD

Figure 4-14 shows the results of XRD analysis of two different HA cellulose hydrogels. The analysis shows both samples are a combination of HA and octacalcium phosphate (OCP, $Ca_8(PO_4)_6H_2 \bullet 5H_2O$) [264, 265]. Peaks at 9.5, 9.8, 26, and 54 indicate OCP, while the peak at 30 to 35 and 50 indicates HA [266, 267]. OCP is the precursor to HA in bone structures, being the initial mineral produced, converted into HA [268]. This analysis, alongside the FT-IR and EDS-SEM results, shows a mixture of calcium phosphate minerals (OCP, HA, and chlorapatite). Based on selectivity results, the predominant mineral is OCP, which has more calcium ions with a Ca/P ratio of 1.33. The reduction in calcium ions means more cation exchange sites than the metal chelating and anion exchange sites offered by the calcium ions. The additional phosphate sites would repel more negatively charged proteins such as BSA that predominantly bind to the calcium sites. Conversion of OCP into HA should benefit the binding of negatively charged proteins such as BSA.

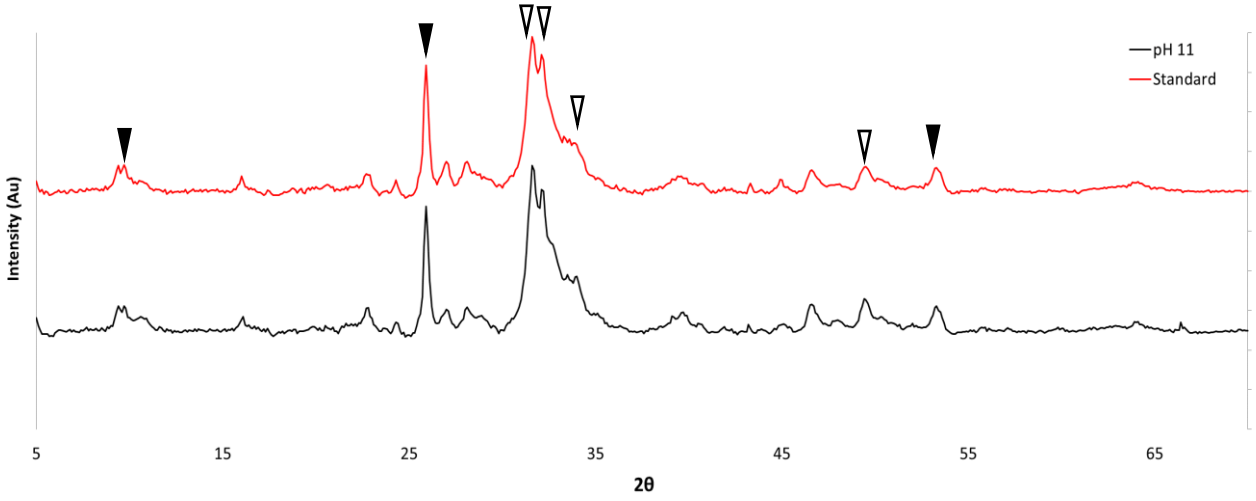

Figure 4-14: XRD intensity peaks for two cellulose HA composites (standard HA and HA grown at pH 11). ▼ indicates peaks associated with OCP while ▽ indicates peaks associated with HA.

To convert OCP to HA a hydrolysis reaction needs to take place as follows:

$$5Ca_8H_2(PO_4)_6.5H_2O \rightarrow 4Ca_{10}(PO_4)_6(OH)_2 + 6H_3PO_4 + 3H_2O$$

This reaction is catalyzed by tetracalcium phosphate (TetCP) in the correct ratio to form stoichiometric HA [264, 269]. This reaction occurs more rapidly at higher temperatures. Because of expenses associated with TetCP and time constraints, this conversion was not explored but future works should look at its effect on selectivity and binding capacity.

The calcium phosphate crystals that have been mineralized inside of cellulose hydrogels were shown to have two discrete binding mechanisms (cation exchange & phosphate binding) consistent with other HA media. While believed to be HA, characterization of the mineral using FT-IR, SEM-EDS and XRD showed it to be a mixture of OCP and HA with poor crystallinity. This mineral mixture caused a different set of protein selectivity during chromatography compared to traditional HA media. Although not pure HA, the mineral mixture can still effectively bind and elute proteins and can be used for the purification of viral particles.

4.2 Viral diffusion

The penetration depth of fluorescently tagged AAV particles into 5 mm cube blocks of cellulose hydrogels was examined under a confocal laser scanning microscope described in Section 3.4. Figure 4-15 shows the tagged viral particles' penetration into the cellulose hydrogels forming a thick fluorescent band. Note in Figure 4-15 there is a large amount of background noise or blurring. Because the hydrogel is translucent, the fluoresces from below the hydrogel's surface refracted through and were visible on the top layer. This blurring in images and variation between samples caused these experiments' standard deviation to be high (≤ 20%). Measurements were taken from the edge of the gel to the highest intensity point.

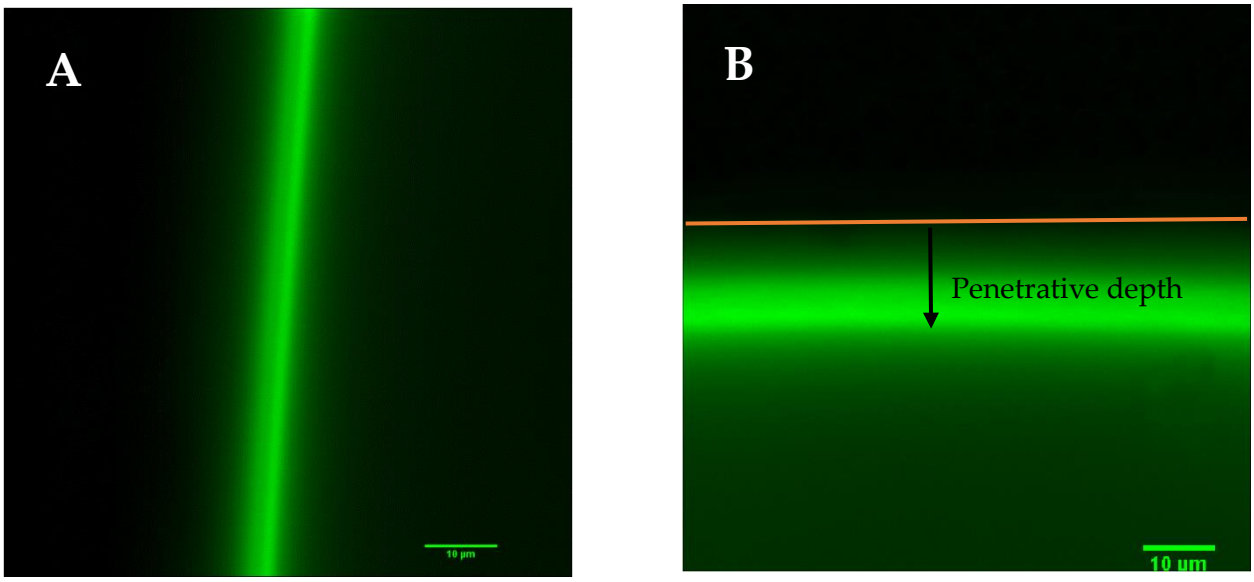

Figure 4-15: Confocal image of AAV particles tagged with Rhodamine red X diffused into 5 mm cellulose hydrogel blocks. **A;** 5 wt% cellulose + 15 wt% ECH functionalized with HA, two weeks' growth **B;** 5 wt% cellulose hydrogel. The orange line defines the gels surface and the arrow show where the depth of penetration has been measured to.

Table 4-3 shows the depth of penetration for various cellulose gel compositions and functionalities. The HA functionality used was alternating calcium chloride and disodium orthophosphate solutions over either one or two weeks. In a few cases, HA by alternating calcium and phosphate solutions was followed by exposure to SBF solution for another week. Comparatively, Wu *et al*. tested the diffusion distance of virus-like particles (VLP) tagged with Rhodamine red X into POROS® HS 50 chromatography beads whose pore size distribution is

50 to 1000 nm [158]. The VLP's used for their work had a hydraulic diameter of 100 nm. The average depth of penetration observed was nearly five times greater than the 1 to 2 μm normally observed in standard chromatography media [158]. The VLP used by Wu *et al*. were four times larger than the AAVs used for this work. However, these particles are of a similar order of magnitude and should be able to be compared.

Table 4-3: Diffusion depth over two hours of AVV 5 particles (1×10^{11} VP/mL) tagged with Rhodamine Red X into cellulose hydrogels of varying composition.

Gel Composition	Average penetration μm	Standard Deviation μm
Cellulose 5%	15.4	3
Cellulose 5% + 2.5%	11.4	1
Cellulose 5%+ 2.5% + 5% ECH	8.9	1
Cellulose 5% -DEAE	10.4	1
Cellulose 5% + 2.5% - DEAE	8.4	1
Cellulose 5% + 2.5% + 5% ECH -DEAE	10.8	1
Cellulose 5% + 15% ECH -HA -2 weeks	4.7	1
Cellulose 6% HA- 1 week + 1 week SBF	11.1	2
Cellulose 5% + 5% ECH – HA 1 week + 1 week SBF	6.7	1
Cellulose 5% + 15% ECH - HA 1 week	11.9	3
Cellulose 5% + 15% ECH - HA 1 week + 1 week SBF	7.2	1
Cellulose 5% - HA 1 weeks	11.2	1

The average penetration depth into a cellulose hydrogel was 15.4 ± 3 μm, over 700% deeper than traditional chromatography media [158]. The average penetration depth drops to ~10 μm for physically cross-linked cellulose hydrogels. Physically cross-linking cellulose hydrogels reduces the pore size distribution (0.1 to 2 μm), limiting accessible pores for AAV to penetrated [222]. A drop in penetration depth can also be seen for the gels functionalized with the anion exchange ligand DEAE. The viral particles have limited diffusion distances because of binding interactions between the negatively charged capsid of the AAV and the DEAE ligand [117]. The gels cross-linked with ECH (chemical cross-linker) have a lower penetration than expected even though they have the largest pore size distribution (5 to 15 μm) [222]. This low penetration suggests dead ends within the pore structure and that the pores are not fully interconnected. Poor interconnectivity can be caused by excessive cross-linking, as shown in other cellulose-based hydrogels [270, 271]. The 50% voidage of the 3D-printed

chromatography columns and the Schoen gyroid geometry results in the wall thickness being equal to the channels' hydraulic diameter. The stationary phase elements of the column are therefore thicker (200 to 300 μm) compared to packed bed beads (40 to 120 μm), which, if the virus fully penetrated, would take a long time to diffuse out of. This extended diffusion could potentially cause extended tailing during chromatography [272]. Functionalization of cellulose with HA results in crystal growths that fill the pores of the gels. The mineral blocks the pores of the hydrogel, restricting the virus's path. In all cases where crystal growth was longer than one week, the AAV penetration was reduced by nearly 50%. Therefore, it is important to limit crystal growth to provide enough functionality but still maximize viral penetration. Optimizing growth will maximize HA functionalized cellulose's binding capacity.

4.3 Anion exchange functionalization

4.3.1 Ligand density

The original methods of functionalization for DEAE cellulose were able to bind and elute protein successfully [15]. DEAE functionalization was designed for agarose hydrogel columns, which limited the temperature of the reaction below 50°C to not dissolve or weaken the agarose structure [273, 274]. Optimization of this method for cellulose hydrogels required increasing the temperature during the reaction to drive it further to completion. The typical functionalization temperature for chromatography material ranges from 20 to 80°C [275-278]. The reaction temperature was increased from 30 to 80°C, which resulted in a higher ligand density, as seen in Table 4-4. Additional to optimizing the DEAE functionality, a quaternary amine (Q) anion exchange was also developed. Section 3.2 outlines a complete description of chemical reactions and methods for functionalities. Table 4-4 below shows the ligand density for the anion exchange functionalities tested during this work. HA functionalities could not be measured this way because of the complex nature of their binding system.

Table 4-4: Ligand density of anion exchange functionalized 500 to 300 μm cellulose columns.

ligand	Charge density μeq/mL	Charge density μeq/cm²	Hydraulic diameter μm	Reaction temperature °C
DEAE	80	1.06	300 μm	30
DEAE	229	3.02	300 μm	80
Q	346	3.44	300 μm	80
Q	256	3.36	400 μm	80
Q	140	2.23	500 μm	80

By adjusting the reaction temperature, ligand density increased over 300% for the DEAE functionalization bringing it into the higher range of packed bed resins [279-281]. Maximizing ligand density is also an important factor for increasing the potential binding capacity of proteins [282]. Although the ligand density is similar on micro equivalences per milliliter basis, it should also be considered based on the surface area, seen in Table 4-4 to compare against membrane technologies. The charge per cm² is similar to that of anion exchange membranes used for viral purifications [283]. Although the charge per mL of resin changes between hydraulic diameters, it remains consistent as a function of surface area for 300 to 400 microns. Therefore, it can be assumed that the functionalization does not fully penetrate all the cellulose hydrogel but just a partial distance into it. If the functionalization reached completion throughout the gel, the resin's charge density would be the same and not surface area dependent. If the surface area was increased further with decreasing hydraulic diameter, charge density per mL could exceed values for packed bed resins.

4.3.2 Binding capacity

The static binding capacity of both the Q ligand and the optimized DEAE ligand was determined using BSA as a model protein, details of procedures for this can be found in Section 3.5.2. Figure 4-16 shows the Q ligand results, while Figure 4-17 shows the results from the DEAE.

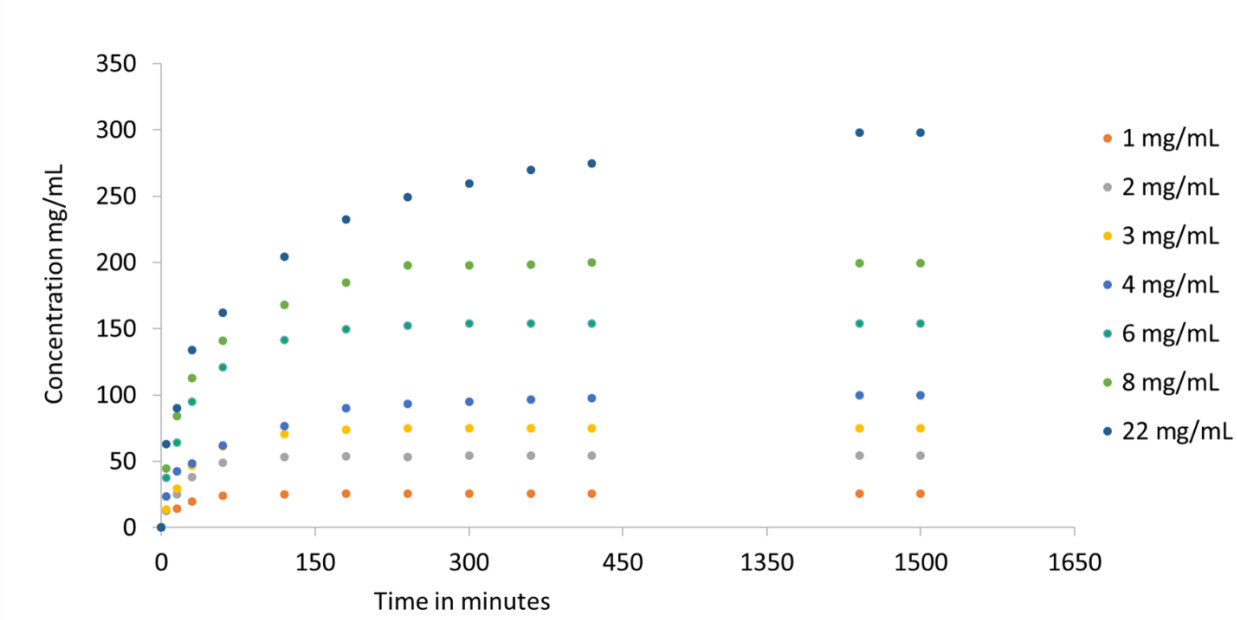

Figure 4-16: Static binding of BSA at various concentrations onto a Q ligand functionalized, 400 µm Schoen gyroid, cellulose column (5% dissolved +50% added cellulose and 15% ECH) over time.

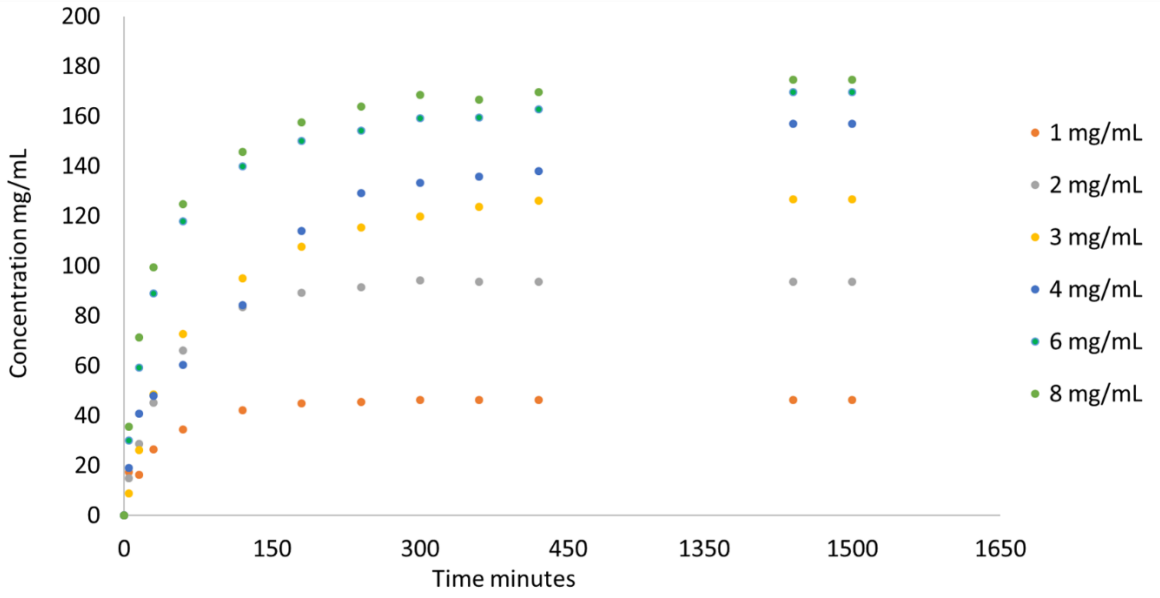

Figure 4-17: Static binding of BSA at various concentrations onto a DEAE ligand functionalized, 400 µm Schoen gyroid, cellulose column (5% dissolved +50% added cellulose and 15% ECH) over time.

The majority of BSA uptake occurs in the first two to four hours, on average 80%; however, reaching maximum binding for high protein concentrations takes up to 24 hours. Chromatography beads can reach equilibrium in two to three hours [284, 285]. Traditional chromatography beads have a diameter between 20 to 80 microns, an order of magnitude smaller than the printed columns (300 to 500 microns). Therefore, the protein has further to

travel via pore diffusion into the hydrogel to reach all potential binding sites. Because of the pore diffusion-limited nature of the system, equilibrium can take a longer time to reach higher protein concentrations that approach the static binding capacity (Q_{max}).

Table 4-5 shows Q_{max} for each anion exchange ligand and varying column hydraulic diameter. One mL of each column variation was allowed to bind protein for 24 hours in a saturated BSA solution (20 mL of 25 mg/mL) with protein uptake measured by Nanodrop. The Q ligand binds almost twice the BSA amount compared to a DEAE column of the same channel size. This capacity seems to be independent of the ligand density as both DEAE and Q ligands have similar densities. This difference shows the importance of having multiple anion exchange functionalities even for the same overarching binding style. Differences in ligand between DEAE and Q can be because of hydrophobicity, ionic strength, or effective pH range, which can play a large part in protein and nucleic acid binding [286-289]. The effects of pore size in these experiments should be minimal because of their size (5 to 15 μm) compared with the hydrodynamic diameter of BSA (3.49 nm) [222, 282].

Table 4-5: Static binding capacity of 3D-printed columns of varying channel size and ligand functionality.

Ligand	Static binding capacity (BSA) Q_{max} mg/mL	Uncertainty ± mg/mL	Hydraulic diameter μm	Reaction temperature °C
DEAE	41	2	400	30
DEAE	85	3	400	80
Q	135	10	300	80
Q	138	8	400	80
Q	105	8	500	80

A maximum binding capacity seems to be reached independently on the columns' surface area for 400 and 300 μm Q columns. This limit suggests the BSA has completely penetrated the stationary phase at 400 μm with no additional static binding improvement in reducing the hydraulic channel diameter. Therefore, the increase of ligand density from 400 to 300 μm does not provide any additional BSA binding capacity. The values for 400 and 300 μm Q columns are at the high end of packed bed resins for BSA binding capacity [106, 281, 290, 291]. Traditional chromatography columns are packed tightly and aim for a void volume between 0.3 to 0.4 for optimal separation [292, 293]. This voidage maximizes the surface area and media

by fitting many spherical beads within a given volume. A further reduction of hydraulic diameter would increase specific surface however current 3D printers are limited by their resolution to produce such columns. However, based on the capacity results for Q ligands an increase in specific surface area may not increase static BSA capacity.

4.3.3 Functionality selectivity of DEAE

Table 4-6 shows the retention times for each model protein's peaks and how this corresponded to elution buffer salt concentration. Also shown is the model proteins isoelectric point (pI). The retention time was measured from the beginning of the run, including injection.

Table 4-6: Selectivity of DEAE with model protein

Protein	Elution peak minutes	Standard deviation minutes	Salt M	pI
Amyloglucosidase	34.4	0.04	0.217	3.6
HSA	31.0	0.2	0.165	5.2
Transferrin	29.1	0.4	0.137	6.2

Cytochrome C was also tested which is a basic protein that should not bind to the column because of its negative charge at pH 7. No binding occurred and was seen coming out during the flow-through of the wash step post-injection. The elution order was similar to other anion exchange resins [294]. Eluted peaks had a similar shape and broadness compared with those eluted from a HA column of the same size and geometry.

4.4 Conclusion

In this chapter, varying chromatography ligands were evaluated for their ligand density and static binding capacity. By increasing the reaction temperature for DEAE immobilization, the ligand density was increased by 300% and static binding capacity by 200%. Comparatively, the BSA Q_{max} values for 300 and 400 micron Q columns are in the top range for the static binding capacity of traditional packed bed media. However, these columns are pore diffusion-limited, as shown by the extended time (24 hours) to reach Q_{max} values. The calcium phosphate mineral functionalization described was shown to be a mixture of HA and OCP. It binds various model proteins more so dominated by its cation exchange mode than its metal chelation sites. This combination of calcium phosphate minerals resulted in different selectivities than those shown by traditional HA media. Conversion of OCP into HA is possible, as shown in literature, but because time and cost constraints have not been explored in this work. Selectivity depositing of this mineral solely into the hydrogel's pores may also add another level of selectivity by excluding molecules too big to fit inside the pores.

The cellulose hydrogel has a microstructure capable of penetration by AAV particles. This penetration allows the particles access to the internal surface area of the media. A larger surface area to access will improve the binding capacity of viral targets. For HA functionalities, consideration needs to be made on the length of time allowed for crystal growth. Larger crystals add additional potential binding sites but limit penetration depth. One to two week's growth should allow for maximum penetration while still maintaining adequate growth for binding.

5 Purification of virus from crude and clarified lysate

5.1 Introduction

In chapter 4, chromatography ligands (Q and HA) were adapted for cellulose hydrogels, and static protein binding capacity was determined. Improvement to both ligand density and the resulting protein binding capacity should translate to an improved virus binding capacity. Determination of the mineral composition of HA explained the difference in protein binding selectivities compared to those found in the literature. HA has been previously shown to be effective for viral purification, especially for AAV serotype 9 [50, 295]. The stationary phased microstructure used for these 3D-printed columns (cellulose hydrogel) could be accessed by viral particles, as shown by CSLM diffusion experiments. A penetrable stationary phase should improve the columns' viral binding capacity by increasing the surface area, and therefore, the number of binding sites.

In this chapter, various viruses were purified from clarified lysates and unclarified cell cultures by 3D-printed columns using FPLC. Dynamic binding capacities, recovery, and purity of each viral purification are assed and compared with current literature. Purifications use both anion exchange, and HA functionalized columns. M13 bacteriophage is purified directly from cell culture similar to expanded bed adsorption. Individual steps in the FPLC method are optimized to minimize processing time while maximizing recovery. The benefits and current limitations of this technology are discussed concerning viral purification.

5.2 Test scale column fabrication

The prior work completed by Anne Gordon produced wax templates using a 3Z Pro Solidscape lost wax printer [15]. A new 3D system's ProJet MJP 2500W was purchased after the Solidscape printer could not be repaired. Comparatively, the new printer has a higher resolution and speed than the previous printer with improved capabilities. Test prints were completed to ensure fidelity between STL file, wax templates, and resulting cellulose hydrogels. The determination that these templates could be created at the same or a better standard allowed for the work's scientific contingency. A full comparison between printers and printing technology can be found in Chapter 6. Columns were made using the negative templating process as described in Section 3.1.

5.3 Purification from clarified lysate

5.3.1 Purification of Adenovirus

In collaboration with iBET (Lisbon, Portugal), a DEAE and HA functionalized 3D-printed cellulose column (300 μm, Schoen gyroid, 5 cm bed height, 1 cm diameter) was used to purify adenovirus and lentivirus from the clarified feedstock. Details of the method for purification, quantification, and purity can be found in Section 3.6.2, 3.7.1, and in our paper '3D-printed ordered bed structures for chromatographic purification of enveloped and non-enveloped viral particles' [244]. This work was completed before DEAE ligand improvement, Q ligand development, and the Projet printer's acquisition, limiting both the length of the tested columns (5 cm) and the number available to use. As a result, because of the limited number of columns available, only one variation of a HA functionalized column was tested. The HA functionalization used was alternating calcium and then phosphate solutions for three weeks. This extended crystal growth was to maximize the amount of HA present in the column. Chromatographs from the purification of 1 mL of clarified adenovirus lysate using each of the functionalized 3D-printed columns are shown in Figure 5-1. The elution peaks are broad and asymmetrical because of the slow diffusion of the virus out of the column's pores. Tailing was previously suggested in Chapter 4 due to the accessible pore structure and the slow pore diffusion of large viral particles (40 to 200 nm). In both cases, the elution occurs over 10 to 15 mL (2 to 3 CV).

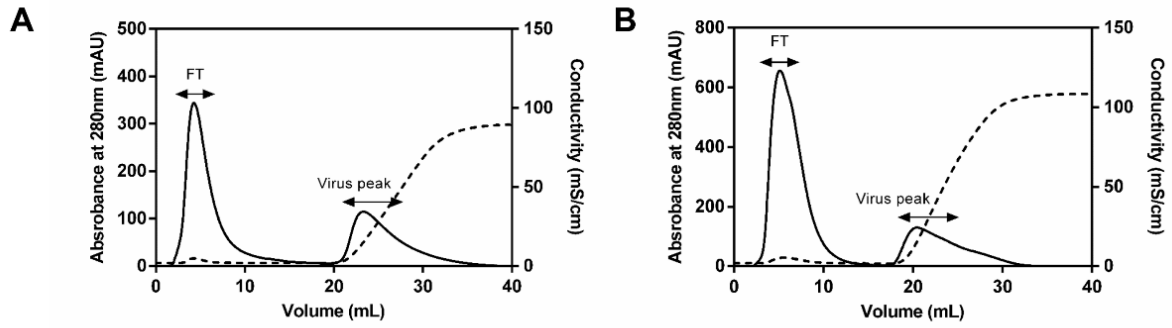

Figure 5-1: Chromatographs of adenovirus purification on DEAE (A) and HA (B) 3D-printed 300-micron Schoen gyroid column [244].

The DEAE column was used to purify adenovirus from 1 mL of clarified lysate under varying load flow rates. The recovery of adenovirus from the elution peak was dependent on the load flow rate (linear velocity) of the clarified lysate, as shown in Figure 5-2. The maximum recovery of 69 ± 6% for the DEAE column and 64 ± 6% for the HA column occurred at the lowest load velocity (8 cm/h). These recovery values are similar to those reported in the literature for purification by traditional packed bed columns and anion exchange membranes [93, 296, 297]. The adenovirus recovery from the DEAE column halves when the load flow rate was increased from 8 to 23 cm/h suggesting a high residence time is needed to ensure the viral particles diffuse through the solution and contact the column walls and internal pores to bind. These flow rates are also considered low compared to those used by packed beds for adenovirus purification (100 cm/h) [120]. By comparison, a packed bed process would have a considerably faster processing time for clarified lysate than this 3D-printed column. Residence time increases will be possible as bed height is increased above 5 cm. longer bed lengths will allow an increase in linear velocity or potentially increase the recovery if linear velocity is not changed.

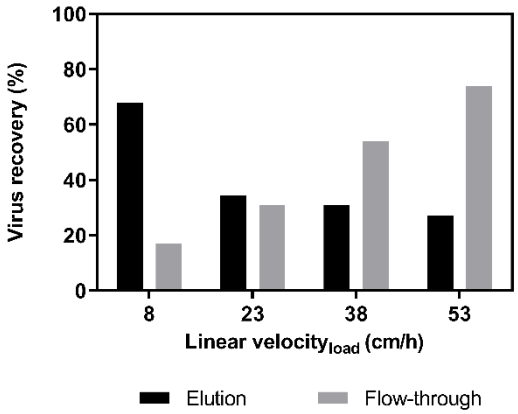

Figure 5-2: Recovery of adenovirus based on the linear velocity during the load of the feedstock onto the column from qPCR results. Black bars show viral genomes found in elution while the grey bar represents viral genomes found in flow-through fractions [244].

Two linear load velocities 8 and 38 cm/h were used to calculate a dynamic binding capacity at 10% ($DBC_{10\%}$) from the breakthrough curves Figure 5-3. Calculations for these values can be found in Section 3.7.4.2. The linear velocity of 8 cm/h gave a $DBC_{10\%}$ of 1.9×10^{10} VG/mL for the DEAE column. A 4.75-fold increase in the linear flow rate resulted in a 60% drop in the $DBC_{10\%}$ at a linear load velocity of 38 cm/h.

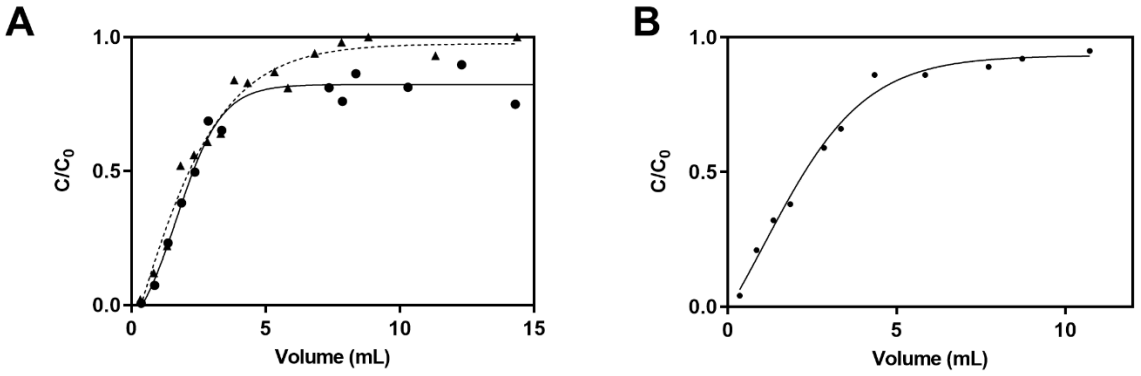

Figure 5-3: Break through curves of adenovirus on both DEAE (A) and HA (B) 300-micron Schoen gyroid columns. load flow velocity of 8 cm/h (•, solid line) and 38 cm/h (▲, dashed line) where C is the virus concentration of flow-through samples and C_0 is the virus concentration of injected feed material [244].

Further analysis of the clarified lysate before and after purification can be seen in Figure 5-4. The Nanoparticle Tracking Analysis (NTA) results show a reduction in the size distribution of around 100 nm indicating some of the smaller and larger contaminants have been removed

during purification. The TEM images also show the purified adenovirus particles surrounded by less debris and foreign particulate. There are still contaminants present in the adenovirus solution indicating a further polishing step is required. However, this technology is designed as a capture step in the downstream process, aimed at high recovery and separation from large contaminates such as cells, cell debris, organelles, and DNA. A high purity, free of smaller contaminants such as proteins and endotoxins, would be desirable but downstream processes typically require at least one or two additional purification and "polishing" steps [64, 84, 298]. The TEM images also show that the adenovirus's morphology is intact, and the process has not damaged the virus which could cause loss of infectivity [122, 299, 300]. Western blot analysis was also used to confirm the presence of proteins that make up the adenovirus structure (hexon and penton) and showed good protein clearance in the eluate.

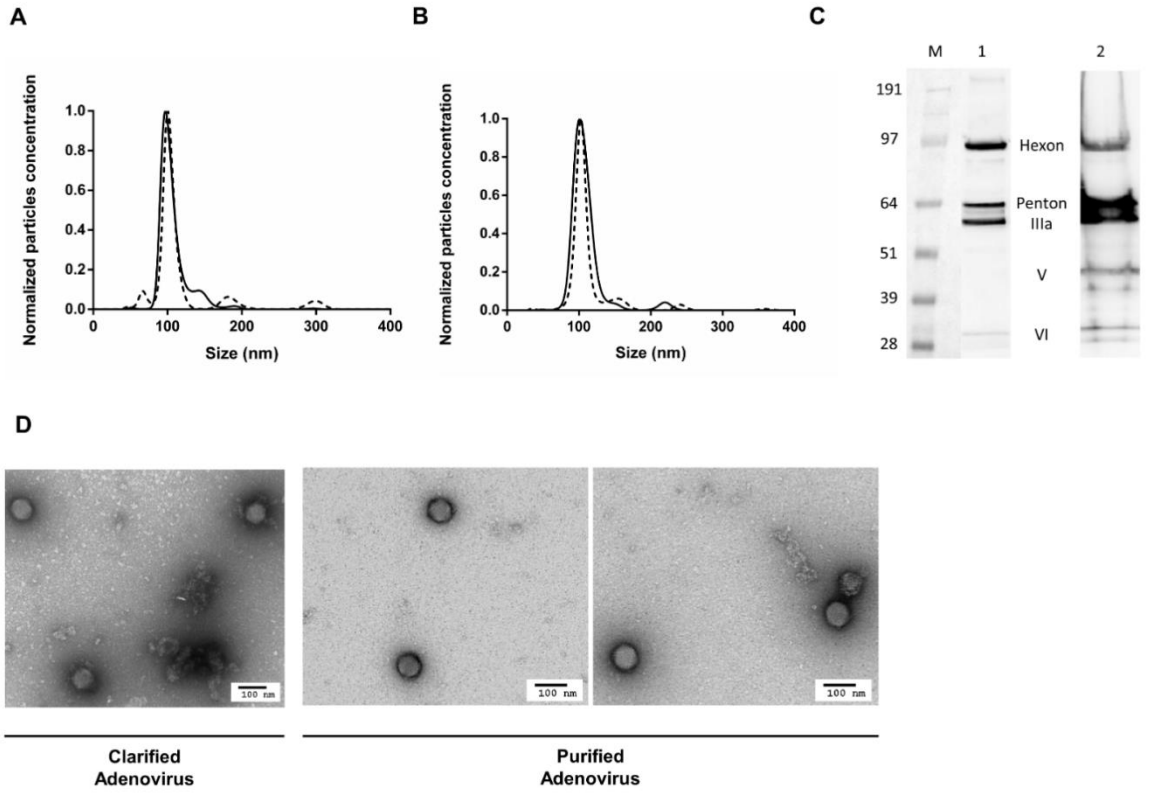

Figure 5-4: Characterization of purified oncolytic adenovirus. NTA profiles from (A) DEAE column purification and (B) HA column purification. The solid line represents the initial virus loaded on the columns and the dashed line the purified virus. (C) Western blot of purified oncolytic adenovirus from both 3D-printed columns. M: Molecular weight markers; Lane 1: Virus eluted from the DEAE column; Lane 2: Virus eluted from the HA column. Hexon, Penton IIIa, V, VI are Adenovirus capsid proteins. (D) Transmission electron microscopy images of initial clarified virus loaded on the 3D-printed column and the purified virus. Scale bars indicate 100 nm [244].

5.3.2 Purification of Lentivirus

The initial work with adenovirus was used to set the flow rate conditions for lentivirus purification to maximize the potential recovery. A recovery of 57% for infectious particles was obtained from the elution peak (approximately 9 mL) from a 1 mL load of clarified lysate at 8 cm/h. This is at the higher end of the range of lentivirus recoveries from a packed bed or membrane chromatography techniques [65, 124]. Figure 5-5 shows the elution profile and break-through curve for lentivirus purified on the DEAE column. A linear velocity of 8 cm/h gave a $DBC_{10\%}$ of 2.0×10^9 PP/mL. As with adenovirus, the elution profile of lentivirus exhibits significant tailing, which can be attributed to the large viral particles' diffusion out of the stationary phase pores.

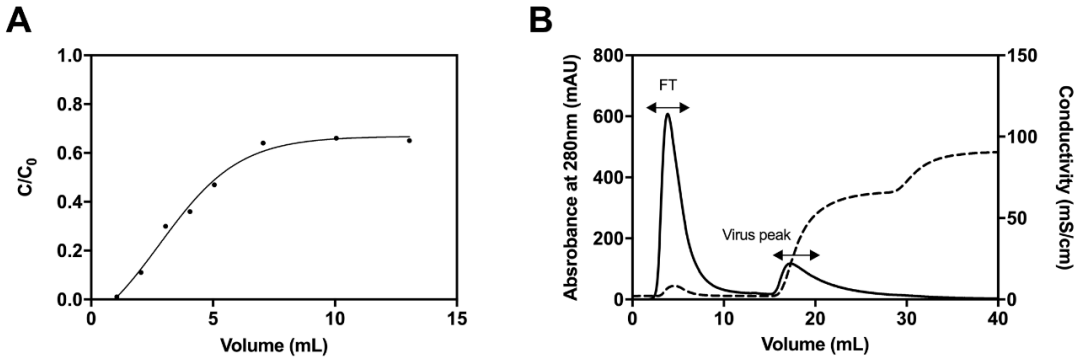

Figure 5-5: Performance evaluation for Lentivirus. (A) Breakthrough curve for the DEAE 3D-printed column. The load flow velocity was 8 cm/h, where C is the virus concentration of flow-through samples and C_0 is the virus concentration of injected feed material. Physical particles concentration was determined by p24 LV protein detection. (B) Chromatographic profile of Lentivirus purification in bind-and-elution mode [244].

The initial results purifying both adenovirus and lentivirus showed comparable recovery to the current state-of-the-art purification methods. However, although recovery is comparable, the linear load velocities required for purification from clarified lysate are significantly slower (>10×). After this work, the Projet printer was purchased to produce longer column templates and therefore longer hydrogel columns. Additionally, anion exchange ligand densities were improved and a Q functionality was developed. Longer columns with the higher ligand density Q functionality have been used for both the AAV and M13 purifications. This was to increase residence time in the system and allow for more binding sites for the viral particles.

For details regarding the differences in ligand density and static protein binding capacity for these functionalities see Chapter 4.

5.3.3 Purification of AAV serotype 9

Samples of AAV serotype 9, provided by South Western Medical Centre (Texas, USA), were taken from a downstream process post clarification. Although cells and other large debris had been removed from the solution, the viral particles remain in the culture fluid. This culture fluid contained 500 mM NaCl giving a conductivity greater than 60 mS/cm. This conductivity level prevents the use of ion exchange to bind the viral particles because of the excessive counter ions in the solution. Three options were considered; (i) to use HA to bind the virus using only calcium coordination sites, (ii) to dilute the fluid 10× to reduce conductivity below 7 mS/cm, and bind the virus with HA using both the calcium coordination sites and the phosphate cation exchange sites. (iii) to dilute the fluid 10× to reduce conductivity below 7 mS/cm and bind the contaminates using anion exchange, leaving the purified virus in the flow-through. Full details for purification, quantification, and purity analysis can be found in Sections 3.6.3 and 3.7.3.

Table 5-1 shows the recovery from varying load volumes for direct purification from clarified lysate on a HA column (20 cm bed height by 1 cm diameter, 300 micron Schoen gyroid). The load flow rate was set to the minimum possible by the AKTA Start at 76 cm/h to maximize the eluate recovery. For a 1 mL load, recovery of 12% was achieved with a binding capacity of 3.28×10^{8} VG per mL of the column. Additionally, recovery drops off rapidly for load volumes above 1 mL, showing that the maximum binding capacity is reached quickly because of the high salt concentration (500 mM NaCl) within the clarified lysate, limiting the binding of viral particles to the calcium metal-chelation sites.

The load's conductivity was reduced by diluting the sample 10 fold to allow the virus to bind to the cation exchange sites. For a 1 mL load, recovery of 50 ± 5% was achieved for a binding capacity of 1.34×10^{9} VG/mL of the column. While this is a significant increase in both recovery and capacity, it is still too low for a capture step in the downstream process. Although comparable to older purification methods (CsCl density gradients), recoveries for AAV9 are now up above 70% for ion exchange with capacities in 10^{12} VG per mL of resin [50, 295]. qPCR results have a high variation because of the small DNA concentration present in the recovered samples, with some samples being at the limits of acceptable detection levels.

Table 5-1: Recovery of AAV 9 from undiluted culture fluid using 3D-printed HA chromatography under various load volumes.

Load volume mL	Recovery %	Standard deviation %	Total titer VG
1	12	4.9	5.13E+09
2	7.2	2.7	6.17E+09
3	6.8	3.8	8.81E+09
5	0.31	1.9	3.67E+09
10	0.34	7.9	7.94E+09
15	0.31	13	1.10E+10
20	0.19	4.7	9.12E+09

Figure 5-6 shows the chromatographs of AAV9 purification with varying load volumes of clarified cell culture using a 3D-printed HA column. Peaks were eluted in volumes between 10 to 16 mL with large flow-through peaks compared to elution. As seen in both adenovirus and lentivirus the elution's exhibit tailing because of the virus's slow diffusion out of the pores of the column.

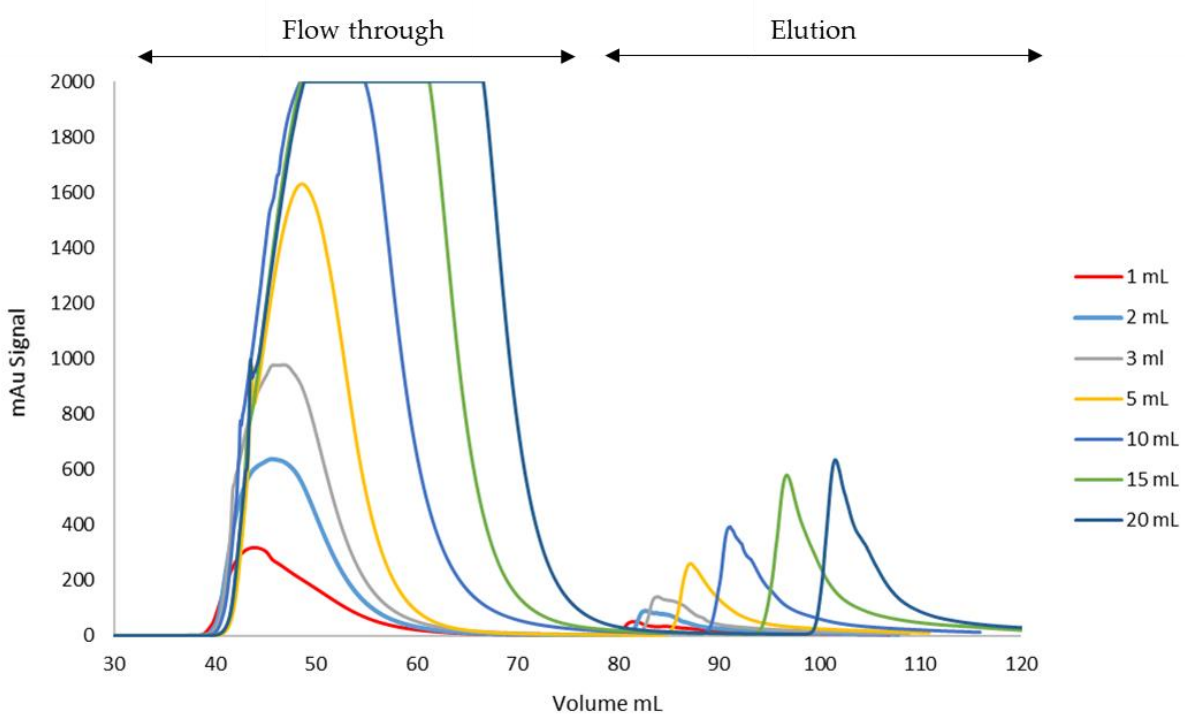

Figure 5-6: Combined chromatograph of AAV purification from 20 cm HA column under varying load volumes at 76 cm/h of undiluted culture medium (1×10^{10} VG/mL).

HA resins used in packed bed chromatography have a high crystallinity or are in a ceramic form achieved by sintering at temperatures greater than 400°C [301]. This heat-treating process not only affects selectivity but increases the binding capacity of the resins [301]. As the HA used in this work is deposited onto a hydrogel matrix heat treatment is not possible without the destruction of the stationary phase. Further improvement of this functionality may be possible as previously mentioned in Chapter 4, by thermal conversion into pure HA. Changing the HA functionalization by reducing or increasing the time the mineral is grown for was considered. As shown in the viral penetration study, a decrease in HA functionalization time to one week would double the potential penetration depth achievable by AAV particles. However, the capacity of the column was considered so low (two orders of magnitude below the state-of-the-art) even by doubling capacity this purification method would not be comparable.

Instead of using bind and elute chromatography, the stationary phase can bind contaminants and allow the flow-through of the viral particles. 50 mL of 10× diluted clarified AAV9 cell culture was passed through a Q functionalized column (10 cm bed height by 1 cm diameter,

300 micron Schoen gyroid). As the lysate flows through the column, the number of viral genomes detected by qPCR stabilized between 6×10^9 and 4.5×10^9 per mL after an initial amount flown through (10 to 15 mL). The overall recovery from 50 mL of 10× diluted load was 80 ± 5%. This suggests some of the viral particles are either being bound or trapped within the column. Post flow through a 1 M NaCl, 10 mM phosphate buffer pH 6.5 was used to elute off any bound virus. qPCR of this elution was inconclusive, indicating some DNA material present but not enough to accurately quantify. It can therefore be assumed some AAV was bound to the column.

Figure 5-7 shows an SDS-PAGE stained with Coomassie Brilliant Blue of AAV9 samples from the 3D-printed Q column at different points in the flow-through. A reduction in protein contaminates is observed, but it is hard to distinguish because of the 10-fold dilution required for the anion exchange column to bind contaminates. The remaining bands seen in 5 and 4 are potentially capsid proteins (VP2) from the AAV [302]. The lack of bands before lanes 5 and 4 suggests that some AAV is bound to the column. Comparatively, to the state-of-the-art purification from the clarified lysate, AAVX and AAV capture series resins offer 99% recovery for up to 10^{13} VG/mL over the range of AAV serotypes [6]. These resins have much higher recovery and load capacity than what is currently possible with 3D-printed columns. This is because of the strong affinity AAV particles have for the camelid antibody used as the ligand on these resins.

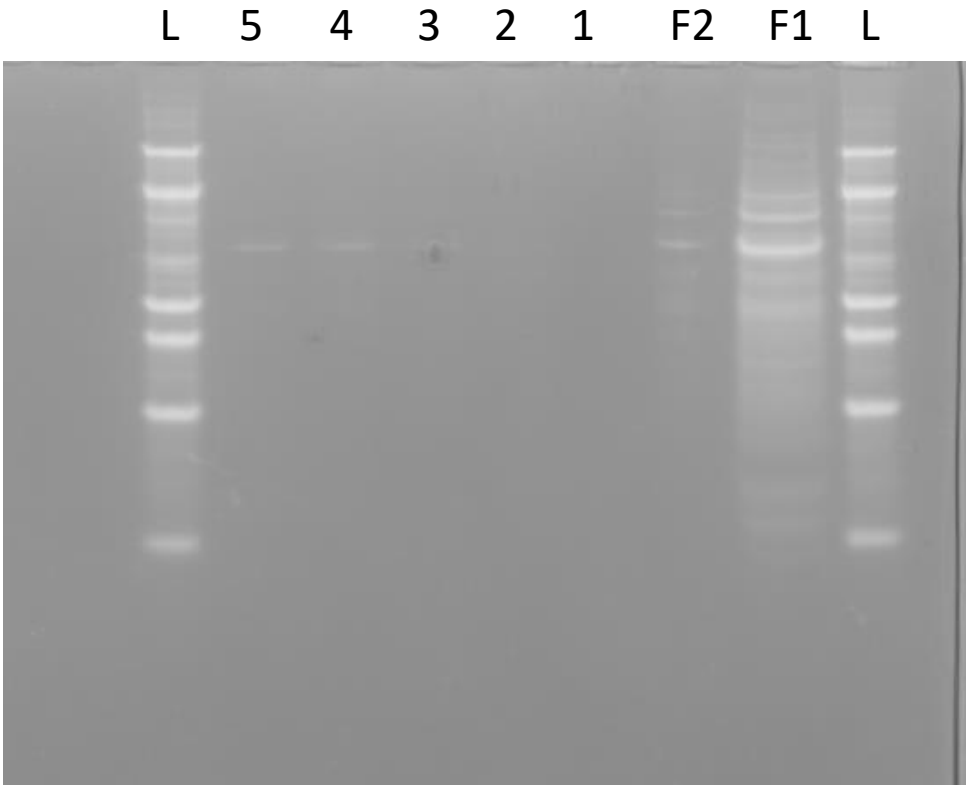

Figure 5-7: SDS-PAGE gel of AAV9 load and flow through of AAV9 on 10 cm 300-micron Schoen gyroid Q column. L-Ladder; F1 – clarified lysate; F2 – 10× diluted clarified lysate; 1- 10 mL; 2- 20 mL; 3 – 30 mL; 4 – 40 mL; 5 – 50 mL.

5.4 Purification from crude cell culture

Purification of M13 bacteriophage directly from cell culture was completed with three different bed height (5, 10, 15 cm) Q anion exchange columns (1 cm diameter, 300 μm Schoen gyroid). Details of culturing, chromatography, SDS-PAGE, and quantification can be found in Sections 3.6.1 and 3.7.2.

3.1.1 Purification of M13 bacteriophage

The recovery of M13 bacteriophage particles from 2 mL (0.5 CV) of crude cell culture over varying load flow rates is shown in Figure 5-8. The effect of flow rate on the recovery of M13 bacteriophage is significant, losing over 20% for an increase from 76 to 153 cm/h. If the load flow rate is too high, the M13 particles do not have enough time to diffuse through the liquid to contact the column's solid phase. Therefore, the residence time of this style of chromatography media is an important variable to consider. Minimizing the flow rate to lengthen residence time through the column during loading should maximize recovery. The highest recovery was 69 ± 4% for 3.1 x 10^{11} pfu/mL of resin for a 2 mL load at the lowest flow rate (76 cm/h).

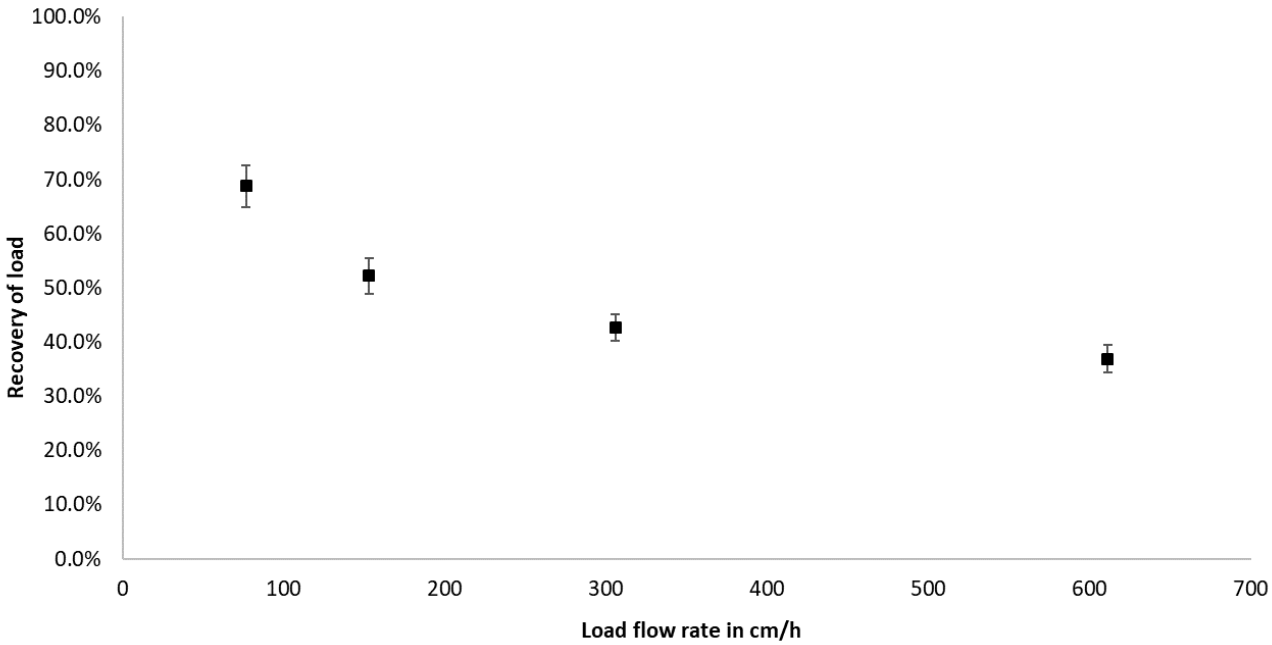

Figure 5-8: The recovery of M13 bacteriophage (2 mL load of 1×10^{12} pfu/mL) from cell culture under varying load flow rates on a 5 cm bed height, 300 micron Schoen gyroid column.

While maintaining the lowest possible flow rate on the ÄKTA start (76 cm/h), the load volume was adjusted to measure its effect on the recovery. Figure 5-9 shows the recovery drops to a plateau (between 1 to 2 CV) as load volume increases before starting to decrease again. These two distinct areas in Figure 5-9 suggest two different binding mechanisms are occurring within the system. The initial binding of phage particles is thought to occur on the channel walls (surface binding), followed by phage diffusion and binding inside the stationary phase pores (pore binding). The pore binding occurs slower than the initial surface binding resulting in the plateau seen in Figure 5-9.

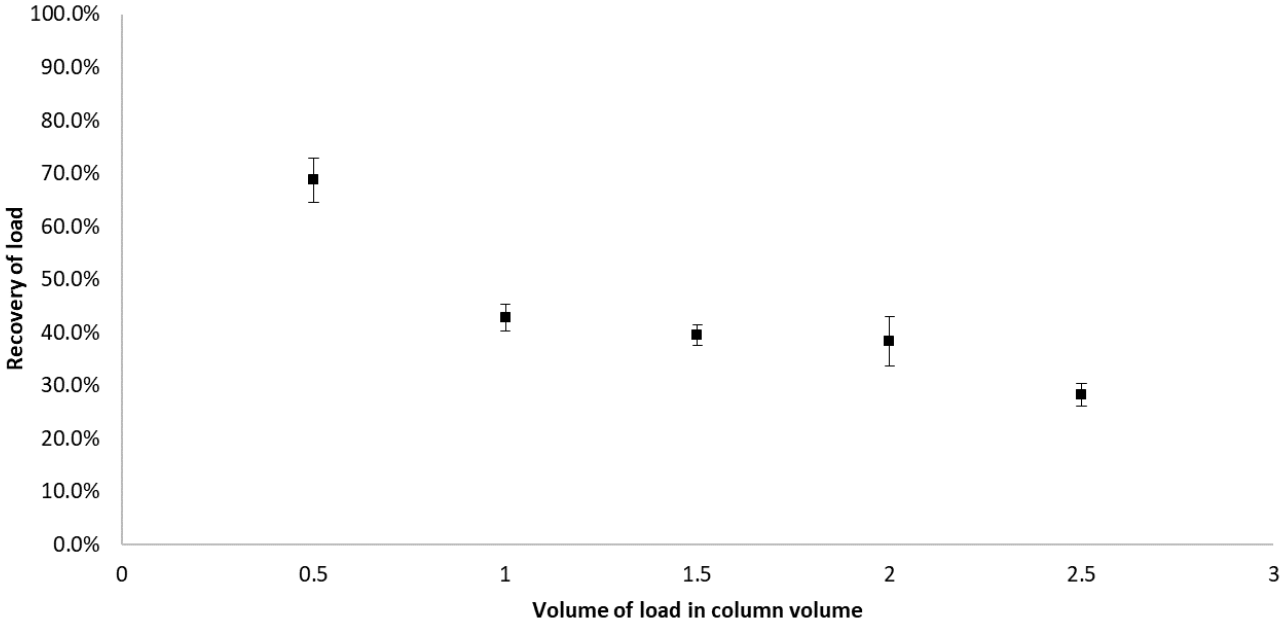

Figure 5-9: The recovery of M13 bacteriophage from crude cell culture at 76 cm/h under varying load volumes (1×10^{12} pfu/mL) from a 5 cm bed height, 300 micron Schoen gyroid column.

A repeat of this experiment with a bed height of 10 cm was completed, shown in Figure 5-10. The same trend is seen with a plateau region between 0.75 to 2 CV. Interestingly, the recovery and capacity for 0.5 CV of load on the 10 cm (71 ± 6% for 3.2 x 10^{11} pfu/mL of resin) was similar to that of the 5 cm column (69 ± 4% for 3.1 x 10^{11} pfu/mL). Although a slight recovery improvement is shown, surface binding still dominates and is less affected by increased residence time. However, an increase is seen in the plateau region (the area dominated by pore diffusion); for the 5 cm column, it occurs at a recovery of ~40%, while the 10 cm column occurs higher at ~50%. The increase in column length effectively doubles the residence time

for the phage particles passing through. This increase in time allows for more of the slower pore-based binding to occur, resulting in a higher recovery rate during this period. If these columns were solely limited by diffusion, particles of M13's size would take many hours to reach the walls from the center of the bulk needing to travel up to 150 μm. An investigation into the flow-through gyroid structures by magnetic resonance imaging showed fluid streams spitting and recombining from one unit cell to the next [303]. Therefore, this splitting and recombining are thought to aid in transporting viral particles from the bulk to the adsorptive walls through radial mixing.

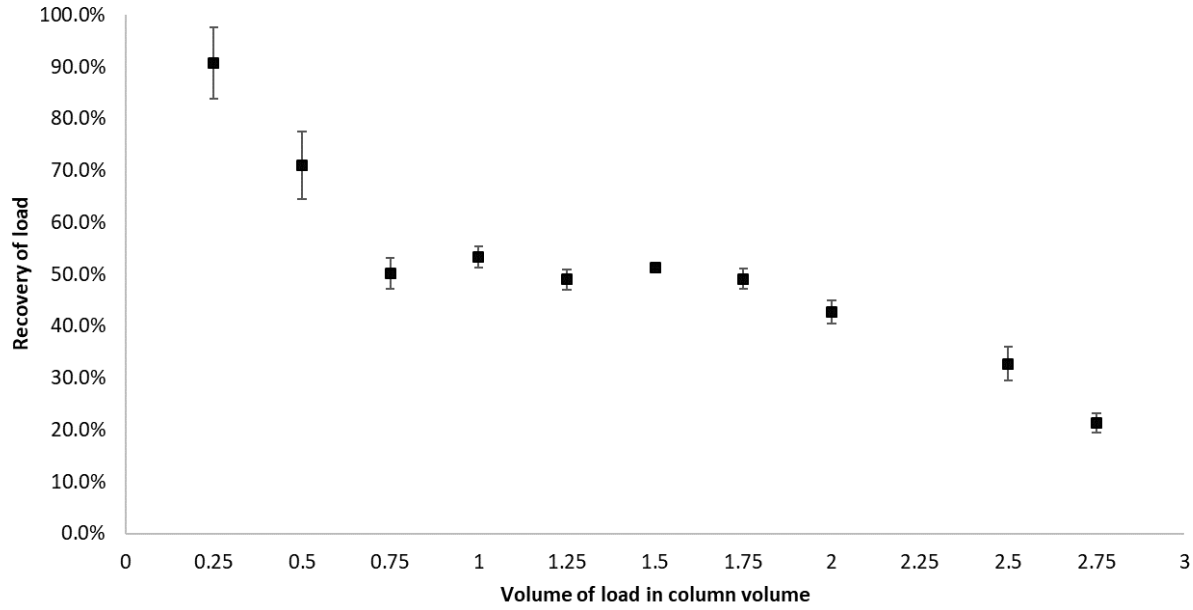

Figure 5-10: Recovery of M13 bacteriophage from cell culture under load volumes at 76 cm/h from a 10 cm bed height, 300 micron Schoen gyroid column

By minimizing the load volume to 0.25 CV to maximizing surface binding, the recovery increased to 89.7% ± 6% for 1.4 x 10^{11} pfu/mL of resin. Because of the large size of the ordered channels within the 3D-printed columns, the pressure drop (between 0.01 and 0.02 MPa at 611 cm/h) is minimal compared to a packed bed [16, 304]. Therefore, by maintaining the residence time in longer columns (>50 cm) by using higher flow rates, it will be possible to process larger volumes while maintaining a high recovery and similar processing time. The chromatograph for this purification is shown in Figure 5-11. The elution peak is tailing, as seen previously in chromatographs of AAV, lentivirus, and adenovirus. The tailing seen in Figure 5-11 is caused by the slow diffusion of M13 particles out of the stationary phase's pores.

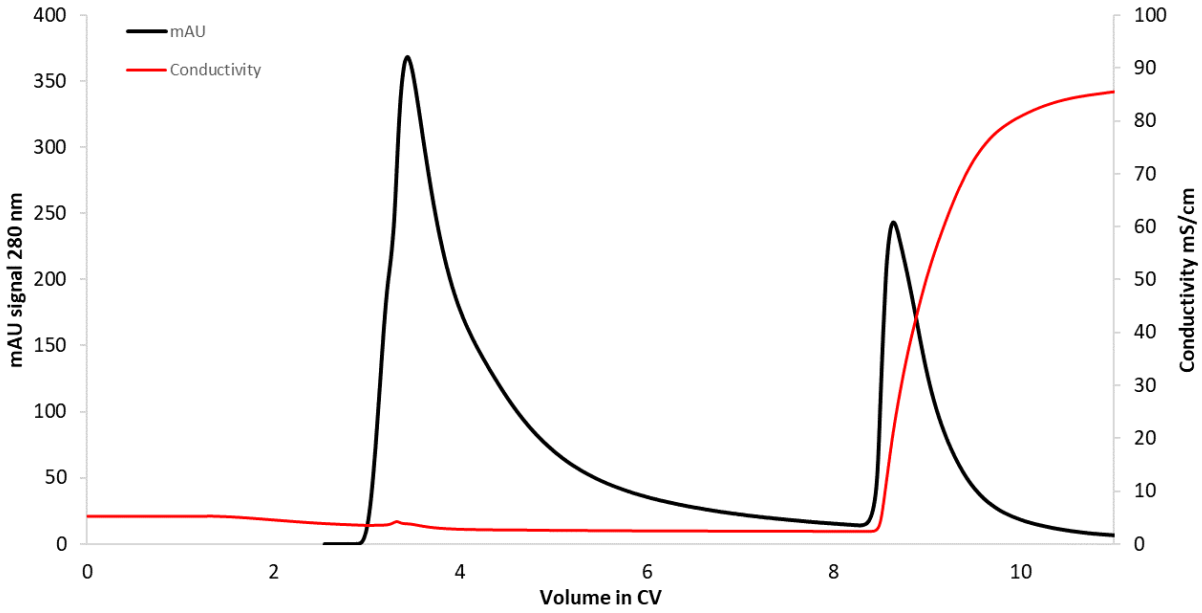

Figure 5-11: Chromatograph of 0.25 CV load on a 10 cm bed height, 300 μm Schoen gyroid column at 76 cm/h.

5.4.1 Purity

The SDS-PAGE results (stained with Coomassie Brilliant Blue) in Figure 5-12 show a clear reduction in HCP visible on the gel between the load (lane 1) and the elution's (lanes 2 to 7). OD600 measurements of elution samples were also compared to the initial cell culture load (OD600 values between 0.8 and 1). Values for OD600 of between 0.01 to 0.02 absorbance suggest low turbidity for the eluted samples. Both of these results indicate that further purification or polishing by packed bed chromatography should be possible without significant fouling caused by large contaminates such as cells or cell debris common in crude load material. Crude load material containing solids or large particulates can cause fouling, tailing, and a reduction in dynamic binding capacity for packed bed columns [305, 306]. The combined capture and clarification step demonstrated by this 3D-printed column purification would eliminate the need for centrifugation or filtration to remove solids. Secondary purification will primarily be used for further HCP, DNA, and endotoxin removal.

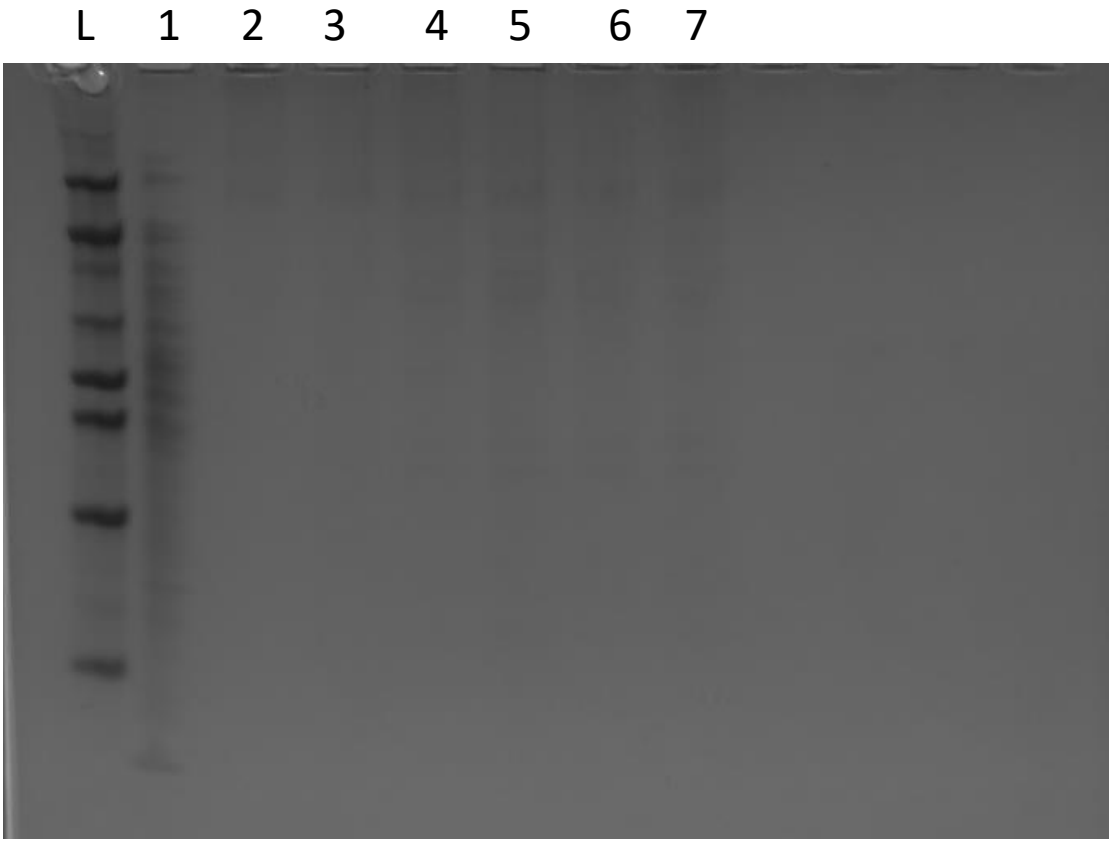

Figure 5-12: SDS-PAGE gel of M13 elution's from a 10 cm bed height column based on varying load volumes; L – Ladder; 1- load; 2- 0.25 CV; 3 – 0.5 CV; 4 – 1.25 CV; 5 – 1.75 CV; 6 – 2.5 CV; 7 – 2.75 CV.

5.4.2 Expanded bed adsorption process comparison

Ling *et al*. performed an EBA purification of M13 bacteriophage to show its advantage over the traditional PEG/NaCl precipitation method [307]. Their purification gave a recovery of 82.86% for 3.1 x 10^{11} pfu/mL of resin compared with a 36% recovery using PEG/NaCl. This EBA process was used as a model to compare with 3D-printed column purification. Table 5-2 outlines the key results and processing conditions for each method. For similar operating conditions, purification using a 3D-printed column achieved a recovery rate of 87.7% ± 5% for 1.49×10^{11} pfu/mL of resin. Although a higher recovery was achieved, a potential reduction in the EBA process's load volume may have yielded a similar result. Load volume was minimized to ensure a high recovery as capacity can be adjusted in scale-up. As previously mentioned, lengthening the column and increasing load velocity to maintain residence time

should be possible because of the minimal pressure drop over the 3D-printed column. Maximizing recovery is critical for high-value targets such as gene therapies, as costs to culture recombinant viruses are a large majority of production costs [308]. High recoveries are also critical for early downstream processing steps like capture because of the follow-on effect in subsequent steps. Improving recovery rates for clarification and filtration steps has also been acknowledged as a potential area of process improvement [309]. There is also a considerable difference in elution volume between the EBA and 3D-printed column processes. The EBA process elutes in 300% more buffer than what was required for the 3D-printed column. However, this is because their elution occurred while the bed was expanded [307]. This choice in mode caused their elution volume to be higher than a packed mode elution because of the flow rate required to maintain expansion [164].

Table 5-2: Comparison of key features between EBA and 3D-printed column (6% cellulose +50% added and 15% ECH) purification of M13 bacteriophage [307].

	3D-printed	EBA
Recovery (Yield)	87.75 ± 5%	82.86%
Resin material	Cross-linked cellulose, 300 μm diameter Schoen gyroid	Streamline DEAE
pfu/mL of resin	1.49E+11	3.17E+11
linear velocity (cm/hr)	122	250
residence time (min)	7.4	7.4
Elution volume (CV)	1.53	4.63
Processing time (min)	70	228

The chromatograph of this purification is shown in Figure 5-13, which has a similarly shaped elution peak to Figure 5-12. The 3D-printed column purification was completed in 70 minutes, three times faster than the EBA process.

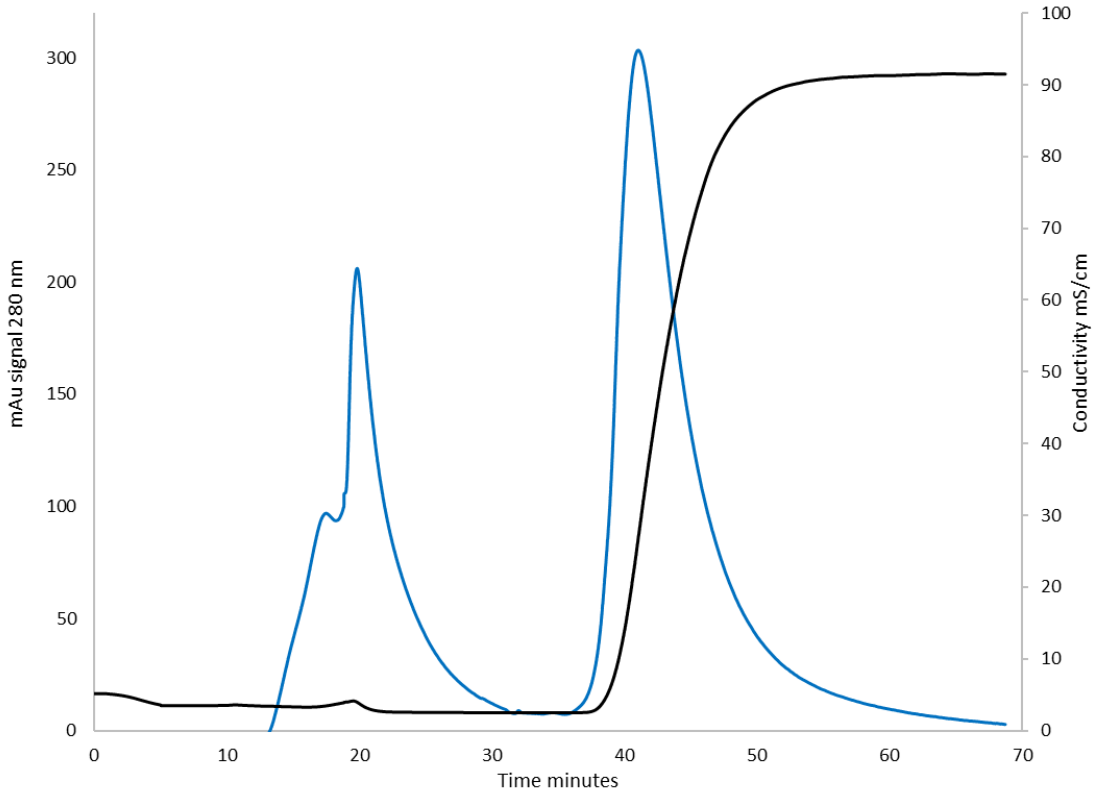

Figure 5-13: Chromatograph of 3 mL load on a 15 cm, 300 μm Schoen gyroid column at a load flow rate of 122 cm/h.

Figure 5-14 shows the time for each step in the compared processes. Conventional purification requires repeated cycles of PEG salt precipitations and centrifugations, which are time and labor-consuming. EBA adsorption can be completed in a fraction of the time. However, this does not account for the setup, maintenance, or cleaning of the column. Purification by 3D-printed chromatography can be completed faster than EBA because of the ability to vary the flow rate at each step of the process. The equilibration and wash steps can be completed at high flow rates to minimize processing time (611 cm/h). Flow rates could have been increased further but were limited to the ÄKTA Start's hardware's maximum flow rate. For the same

column tested on an ÄKTA Pure capable of flow rates up to 20 mL/min, a back pressure of 0.1 MPa was observed for a linear velocity of 3055 cm/h. Because of the physical containment level required to work with M13, the only available chromatography system was an ÄKTA Start.

The flow rates for EBA directly relate to the degree of bed expansion and operational performance. Flow rate is optimized depending on the load material, degree of expansion required, adsorbent used, and target biological. Expansion is typically between two to three times the original packed bed height for optimal performance. During the EBA setup, the fluidized bed needs time to become stable before sample loading. The bed also requires re-stabilization if the flow rate is changed during operation. The degree of expansion limits EBA's maximum flow rates and discourages flow rate changes during operation. Time is also required for EBA setup (bed fluidization) before the purification can commence. The initial expansion can take 30 to 40 minutes to stabilize before the flow rate is adjusted to reach the correct degree of expansion, followed by another 30 to 40 minutes to re-stabilize [310]. Fluidization is an iterative process until the desired expansion is achieved. The overall setup and running of an expanded bed system is a complex process and requires expertise. In comparison, this 3D-printed column can be operated with traditional packed bed hardware without any additional setup time or specialized equipment. The monolithic style stationary phase also does not require any specialized packing technique, being able to be slide inside a conventional casing designed for a packed bed column. 3D-printed columns do not suffer from the same issues, such as channeling and bed collapse, because of their self-supporting channels [164].

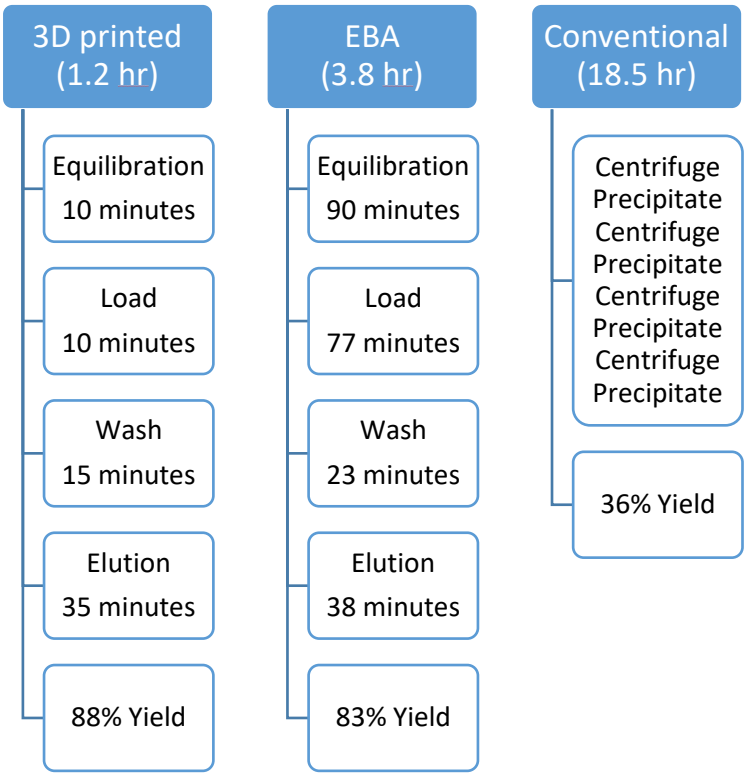

Figure 5-14: Comparison between the individual steps of M13 purification and the time required for each for an EBA process, the conventional technique and a 3D-printed column [307].

5.4.3 Column cleaning and fouling mitigation

Notably, no build-up of cells or other debris was observed at the column's inlet or outlet under visual inspection post purification even after multiple cycles (>10). Effective CIP and sanitation are crucial for meeting goods and manufacturing regulations and FDA guidelines. The build-up of cells or lipids at the inlet or outlet was a common EBA issue, which affected its adoption in the industry[14, 167].

The column's initial cleaning method was based on the CIP used for traditional anion exchange packed bed resins [281, 290, 311]. The column was stripped with 1 M NaOH over 8 CV at 1 mL/min, followed by 8 CV of 1 M NaCl and a flush of DI water. Figure 5-15 shows how the recovery of a 2 mL load at 76 cm/h on a 10 cm column (300 µm Schoen gyroid, 1 cm diameter) decreases after multiple purifications using a CIP system like packed bed resins. The recovery rapidly decreases over 10 to 30 purifications using this CIP method. This recovery decrease indicates that fouling has occurred, and the cleaning cycle is not adequate for the column.

Instead of basing cleaning on volume, a timed method was implemented. 1 M NaOH was passed through the column at 76 cm/h for one hour, followed by a flush of 1 M NaCl (611 cm/h for 5 minutes) and then DI water (611 cm/h for five minutes). This slower process lets the NaOH penetrate the 300 μm walls of the column to break up any biological material causing the fouling (DNA, protein, cell debris) and then diffuse out of the pores to be flushed from the column. This CIP method was implemented after 34 cycles, which quickly reversed low recoveries from the column because of fouling. Removal of fouling is shown in Figure 5-15, where at 35 cycles and onwards, the recovery goes back to ~90%. The ability to reverse this fouling shows these columns' potential longevity even under heavily contaminated feed streams and rigorous CIP methods.

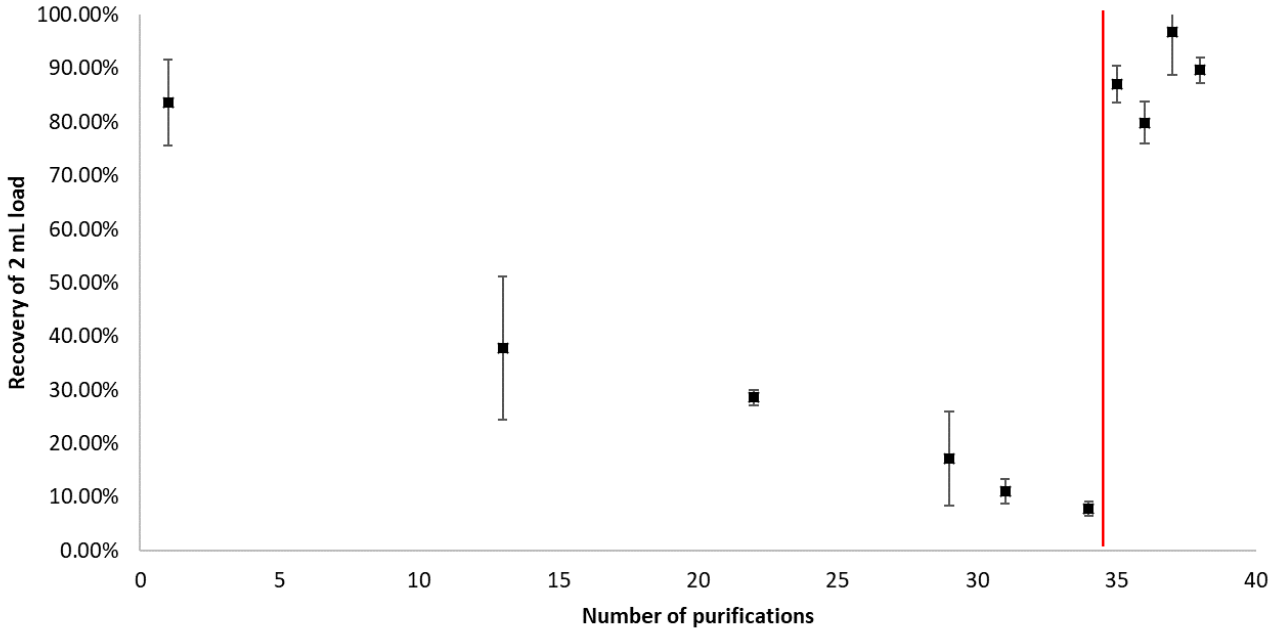

Figure 5-15: Recovery of M13 from a 2 mL load at 76 cm/h using a 10 cm bed height, 300 μm Schoen gyroid column. Recovery of repeat purifications using the same column are shown after numerous trials. Red line indicates where CIP method was changed from a traditional protocol to one hour of continuous 1 M NaOH washing.

5.5 Conclusion

In this chapter, a range of viruses was purified from clarified cell lysates and crude cell culture. Most notably, purification of lentivirus and M13 bacteriophage showed high recoveries compared to the art's current state. Because of the column's mass transfer limitations, to maximize recovery, loading of the column needs to be completed at a minimal flow rate (< 76 cm/h). The slower flow rate gives viral particles the maximum amount of time to diffuse through a solution and contact the column's walls and internal pores to bind. Alternatively, to minimizing the load flow rate, bed height can be lengthened to increase the residence time. Higher residence time improves pore binding as shown for M13 bacteriophage where the plateau region (pore binding) of recovery increased (+10%) for a bed height increase from 5 to 10 cm.

Purification of AAV serotype 9 was possible by both HA and anion exchange but was not comparable to the current state of the art in recovery or capacity. Although the HA functionality can bind and elute viral particles, its capacity is low compared with the optimized Q and DEAE anion exchange ligands. An investigation into an affinity style ligand is thought to improve both capacity and recovery for AAV.

3D-printed columns are a simple alternative to an expanded bed chromatography for the purification of M13 directly from cell culture. The 3D-printed column purification has comparable recoveries, but was able to be completed three times faster than EBA. The ability to freely adjust flow rate allows for each step within the process to be optimized, saving time. This advantage over expanded bed chromatography alongside ease of use and setup shows this technology's potential benefits for downstream virus processing. The low-pressure drop over 3D-printed columns could also be exploited further with higher flow rates and longer bed heights. An effective CIP process to minimize column fouling was required to prevent build-up over multiple purification cycles. An extended caustic wash was used to break up any biological material bound to the column. No reduction in recovery or capacity could be seen after CIP changes were made, even after numerous purifications (40+).

6 Advancement of 3D printing and upscaling

6.1 Introduction

Chapter 5 showed that purification of viruses and viral particles using 3D-printed chromatography columns was possible, achieving high recoveries comparable to current packed bed standards. Furthermore, this technology's benefit over expanded bed adsorption was shown in faster processing time, ease of use, and high recovery. For this technology to be adopted by the industry, it must be scalable and process commercial volumes of feedstock. Emerging technologies such as monoliths experience issues reaching preparative or pilot-scale because of inconsistent processing and limitations in current fabrication methods [10, 312, 313]. Current pilot-scale packed bed chromatography columns have bed volumes between 400 mL up to 25 L, capable of processing liters of feedstock per batch process [314]. For this technology, a pilot-scale column's goal would be 5 cm in diameter by 50 cm bed height, equivalent to a volume of 980 mL. This chapter looks at the 3D-printing technology used for templating and if scale-up is currently possible with this method.

This chapter investigates the size of wax templates producible on the 3D-systems ProJet MJP 2500w printer and unique ways of making larger columns. The entire templating process is examined, focusing on the most time-consuming steps and those that limit column size. Currently, the longest step of the templating process is in support wax removal which is expected to lengthen exponentially as the column's size increases. Determining the current process limits will help guide future work on upscaling while informing what is possible now. Design of specialized equipment to aid a larger templating process was also required for support wax removal and cellulose infusion into templates. A unique column stacking method is examined as an alternative to needing a single-piece monolithic column. Residence time distribution (RTD) was used to compare performance between a single piece column and multiple smaller columns (plugs) stacked on top of each other.

6.1 Methods & materials

Materials used for Chapter 6 of work have previously been mentioned in Chapter 3 and are the same used for the printing and creation of 3D-printed columns as outlined in Section 3.1.1 and 3.1.4.

6.1.1 Printer comparison

Product information for both the SolidScape Pro 3z and the 3D Systems ProJet MJP 2500w wax 3D printers were obtained from the manufacturers to compare specifications. Printing time and file size data from the SolidScape printer were then compared with the experimental data from the ProJet printer. A base case was used to compare printers, a 1 cm diameter by 5 cm long, 300 μm Schoen gyroid column. The time required to print, the number of individual templates made in one print, and the printer's slicer software's maximum file size were all recorded.

Trial prints of smaller hydraulic diameters were tested with the ProJet printer. 150, 200, and 250 μm Schoen gyroid templates (1 cm diameter by 5 cm long) were produced. Post printing templates were placed in a beaker of IPA stirred at room temperature to remove the support wax (Figure 6-1). IPA was replaced every 48 hours for between 7-20 days until support wax had been removed. Templates were then dried in a fume hood for 24 hours before being gelled using the standard method described in 3.1.4. After gelation, columns were boiled in a beaker with a drop of liquid hand soap for up to 100 hours to remove build wax from the cellulose structure. After removal of build wax, three of each channel diameter were snap-frozen, freeze-dried, fractured, and had their cross-sections imaged using SEM as described in Section 3.3.2.

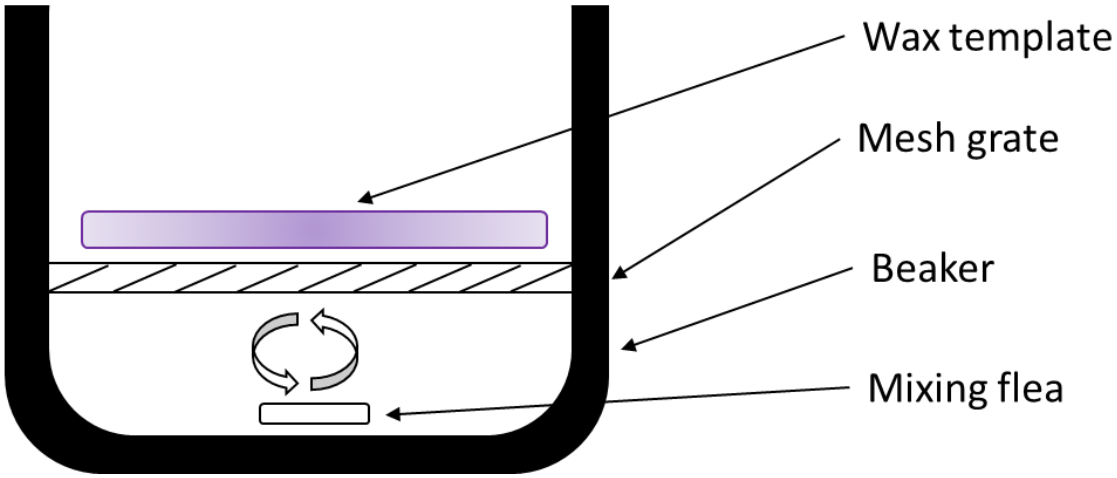

Figure 6-1: First support wax removal method. A beaker is filled with IPA and placed on top of a temperature controlled hot plate (30-40 °C).

6.1.2 Slicer file size

Various sized 300 μm hydraulic diameter Schoen gyroid template STL files were made using the Matlab TPMS generation program described in 3.1.2 and attempted to be loaded in 3D sprint slicer software used by the ProJet MJP 2500W printer. Determination of file size and compatibility of the printer was recorded.

A patterning technique was used to avoid the file size limitation of the 3D sprint slicer software used by the ProJet MJP 2500W printer. The TPMS geometries (Schoen gyroid) used for these 3D-printed columns are periodic along the x, y, and z-axis. Therefore, each unit cell is identical to the next and can be patterned along each axis. Patterning can be done within the 3D systems software "3D sprint" where a circular slice, one unit-cell thick, can be patterned along the y axis to increase the column's length. This pattern by-passes the computer and software's file size limits, allowing for larger columns to be printed. Using this method, a 5 cm diameter by 20 cm long, 300 μm Schoen gyroid template was printed on the Projet printer. Because of this template's size, support wax removal was attempted by leaving it inside a glass jar with 2 L of IPA. The jar was left stagnant to slowly dissolve away the

support wax, with the IPA being replaced every five days for one month. The template was then visually assessed for damage and dissected to determine if the support wax had been completely removed.

6.1.3 Segmentation method

Dividing up a column template into multiple smaller pieces (column segmentation) was used as an approach to upscale this technology. Two methods of column segmentation were tested to achieve larger structures and reduce overall column production time. The first was to produce smaller pieces (1 cm in length by 1.5 cm in diameter) of column template (plugs) with locater keys along the edge of each (Figure 6-2). A modified column casing was then used to line these smaller plugs together in the correct orientation using the template's locator key. These plugs were then gently forced together and gelled as a single-piece column described in Section 3.1.4. Post-processing occurred similar to a standard column, with the build wax being boiled away with a drop of liquid hand soap until no wax could be seen inside the hydrogel.

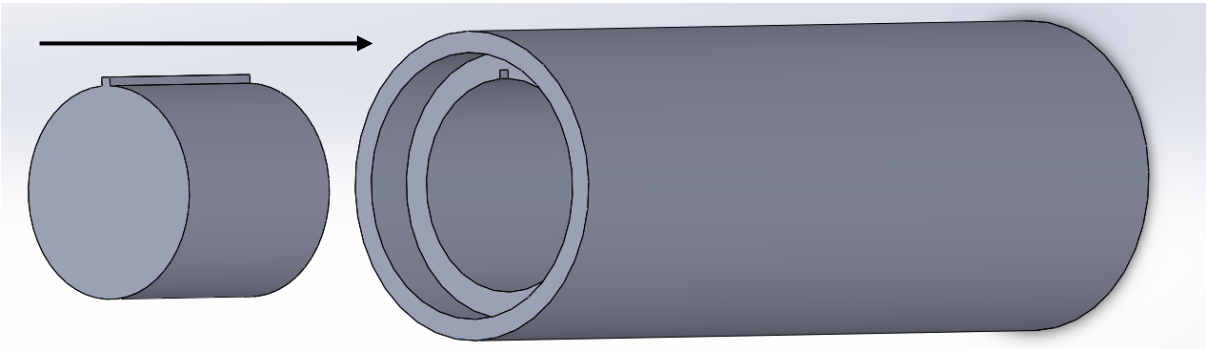

Figure 6-2: 3D model locator on plug (left) and locator slot on column casing (right)

The second method was to again make smaller plugs (1 cm diameter by 2 cm long) without a locator key. The smaller plugs would be gelled individually in short casings to make smaller pieces of cellulose column. These plugs were then stacked together inside the appropriate size SNAP casings to the desired bed height. The plugs were stacked randomly inside the casing.

6.1.4 Column tracer study

One cellulose column 10 cm long (1 cm in diameter, 300 μm Schoen gyroid) or 4 × 2.5 cm long were placed in SNAP glass casings fitted with plastic pistons containing 20 μm glass frits (S-10/125-PPSS-OV-FP20). The column was attached by plastic tubing and fittings to an ÄKTA Pure chromatography system. Tracers of 1% acetone were injected, 0.5 mL per trial (6% of the column volume), into the column at different flow rates between 0.1 and 4 mL/min. Unicorn 5.4 software was then used to measure the 280 nm absorbency response from the ÄKTA's detectors. Peaks were then normalized and analyzed to compare asymmetry and HETP values. Asymmetry was determined by the half-peak method (equation 6-1). Where a and b are found at 10% of the peak height on each side of the peak maximum as shown in Figure 6-3.

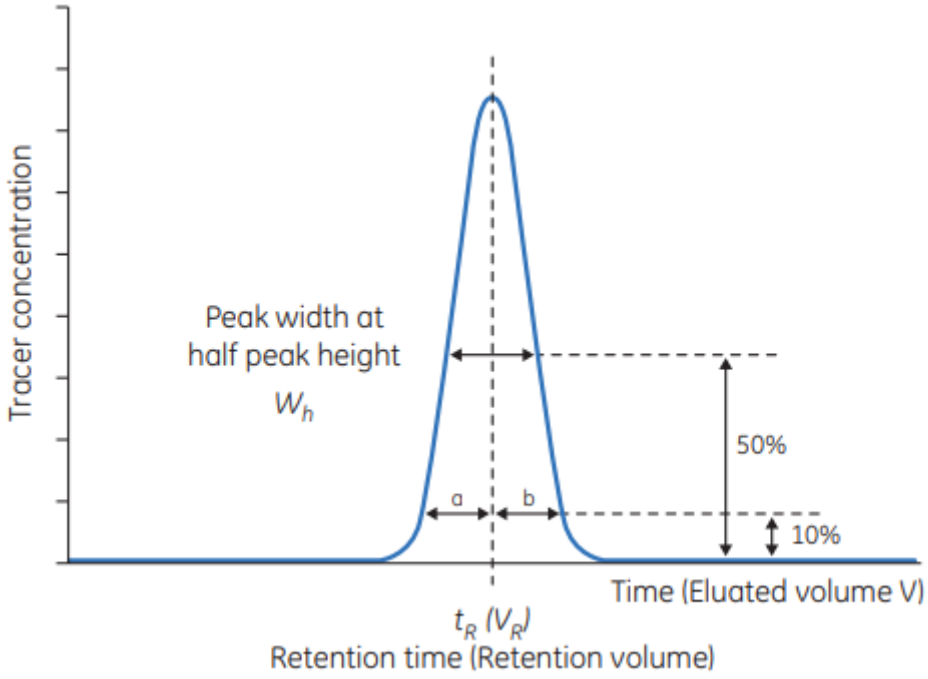

Figure 6-3: Example of a tracer elution peak from a packed bed chromatography column [160].

$$A_s = b/a \tag{6-1}$$

The HETP values were also calculated from the normalized peaks using equation 6-2. Where L is the length of the column, V_R is the retention volume and W_h is the peak width at half peak height.

$$HETP \approx \frac{L}{5.54\left(\frac{V_R}{W_h}\right)^2} \quad (6\text{-}2)$$

Sample calculations can be found in Appendix A

6.1.5 Support wax removal advancement

The first iteration of a support wax removal rig (Custom support wax removal rig version 1) is shown in Figure 6-4. This rig was designed to have a consistent and repeatable method for support wax removal from longer column templates too large for beakers. A cylindrical tube with a mesh grate at the bottom and top held the template in place while a peristaltic pump (Master flex Console drive) pumped IPA from a tank up through the cylinder. The flow rate was set to 40 mL/min, which was the highest possible by the pump. No heating was applied to this rig because of the wearing down of the peristatic tubing over long runs (>24 hours) and IPA's flammability. The glass tube could only fit single columns up to 3 cm in diameter and 20 cm long. Templates of various channel diameters and column diameters were printed at a length of 15 cm. Individual trials of each of these templates used a fresh 1.5 L of IPA recirculated through the rig at 40 mL/min. Templates were removed each day and had 0.5 cm cut off from one end to visually determine if support wax remained inside. Templates were then returned to the rig for a further 24 hours if support wax remained. Upon determination of complete support wax removal, a repeat trial was completed, with the template being left undisturbed in the rig for the predetermined length of time to confirm prior results. Figure 6-5 shows the rig's experimental setup where the tank of IPA used is a 2 L glass bottle.

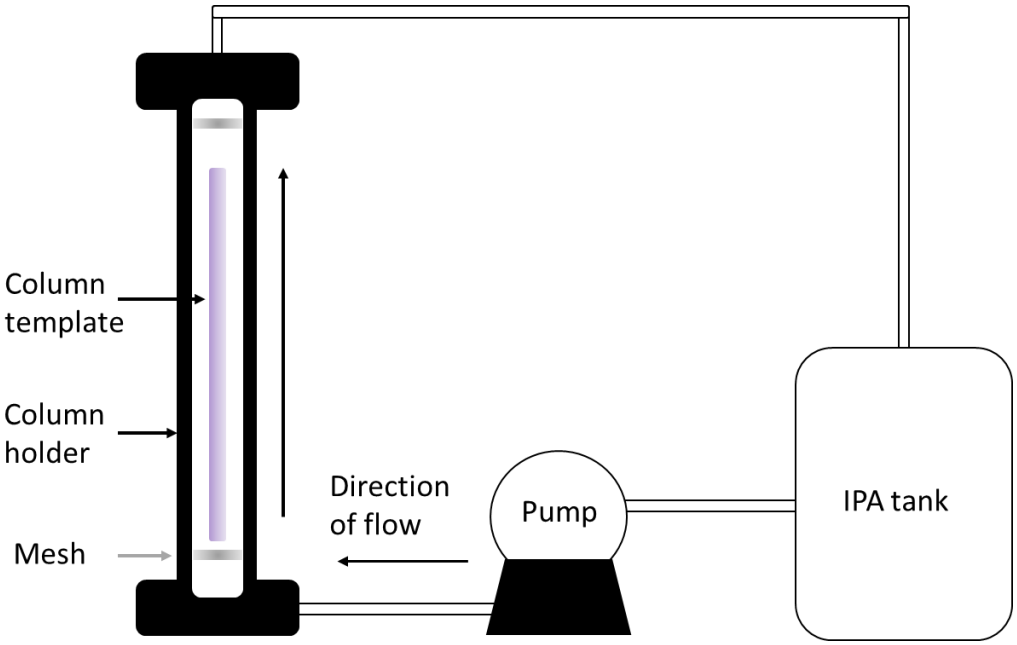

Figure 6-4: Custom support wax removal rig version one. IPA recirculation by pump up through holder over column template and back to tank.

Figure 6-5: Support wax removal rig version one. Brown bottle is filled with IPA and the Master flex console drive recirculates it though the column.

The second iteration of a support wax removal rig (Custom support wax removal rig version 2) was designed for template 'plugs' as described as a part of the column segmentation method. These plug templates were 5 cm in diameter by 2 cm thick, 300 μm Schoen gyroid. The second version (Figure 6-6) of the support wax removal rig was developed alongside Craig Stocker (undergraduate student contributing as part of his final year project). The tank was 30 cm in diameter, and 20 cm deep with six 3D FDM printed mesh cages (Figure 6-7) arranged evenly in a circular pattern around the tank's sides. The mesh cages are held in place by the lid on top of the tank. IPA is stirred inside the tank by an overhead mixer, and the temperature is controlled through a temperature probe connected to the hot plate. The mesh cages can hold columns up to 5 cm in diameter by 15 cm long templates. Templates of varying sizes and hydraulic diameters had their support wax removed using this rig as described in their relevant experiments.

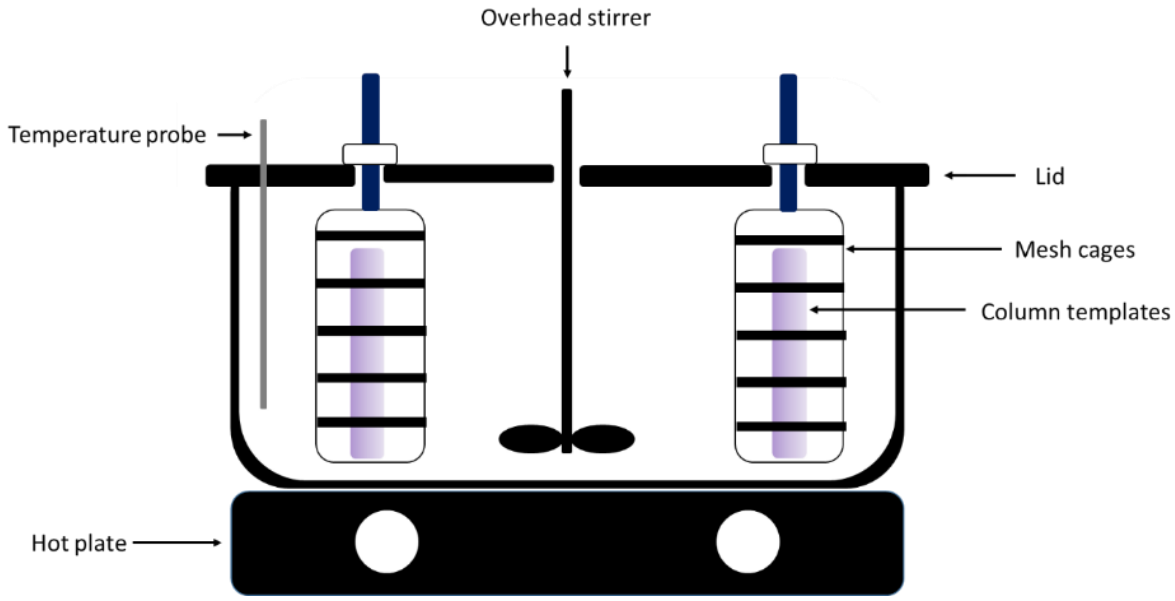

Figure 6-6 Custom support wax removal rig version 2. A stirred tank containing IPA sitting on top of a hot plate with temperature control provided by a temperature probe.

Figure 6-7: Custom 3D-printed mesh cages for holding wax templates inside support wax removal rig version 2. Pins fit through the smaller holes to hold templates.

The following series of experiments using the second iteration of the support wax removal rig was designed to optimize the wax removal from 2 cm by 5 cm, 300 μm hydraulic diameter Schoen gyroid template.

1. Timed support wax removal

The second support wax removal rig with filled with 8 L of fresh IPA before each trial. Five wax templates were placed in the mesh cages for each experiment and submerged into the IPA within the tank. The temperature was controlled using a probe connected to a hot plate beneath the tank. A fixed stirring rate of 400 rpm was used for these experiments. Three temperatures were tested 40°C, 35°C, and room temperature (~22 °C). One template was removed from the rig at regular one-hour intervals after starting the experiment and left to dry overnight inside a fume hood. Each disc's mass was recorded at the experiment's start and then after each had dried the next morning. These measurements allowed the mass change of the disc because of support wax removal to be quantified. Each morning, the templates would

be reloaded into the rig to repeat the cycle until the templates' mass change had stabilized over three or more hours. The template removed first on the previous day would be the last to be removed on the following day. Visual inspection of the templates was also performed to detect any damage. After support, wax removal templates were cut in half to examine their cross-sections to ensure complete support wax removal.

2. Adjusted template thickness

5 cm diameter, 300 μm Schoen gyroid templates of varying thickness (0.8, 1, 1.2, 1.4, 1.6, and 1.8 cm) were placed inside the mesh cages in the tank. The tank was filled with 8 L of fresh IPA and stirred at a constant rate of 400 rpm. No heating was used for this trial. The trial was left to run for 72 hours before the templates were removed, visually inspected, and left to dry for 24 hours inside a fume hood. Upon drying, the templates were weighed before the process was repeated until either the templates cracked or no mass change was observed between cycles.

Following the results of the adjusted template thickness experiment, the mixing conditions were changed. First, a new holder was designed that held the template vertically, as shown in Figure 6-8. For each trial, two of these holders containing 1 cm thick (5 cm diameter, 300 μm) templates were placed into the tank with 8 L of fresh IPA. The first trial used a fixed mixing rate of 400 rpm, while the second was fixed at 900 rpm. The templates were removed from the tank after 72 hours and left to dry for 24 hours inside a fume hood. Upon drying, the templates were weighed before the process was repeated until either the templates cracked or no mass change was observed between cycles.

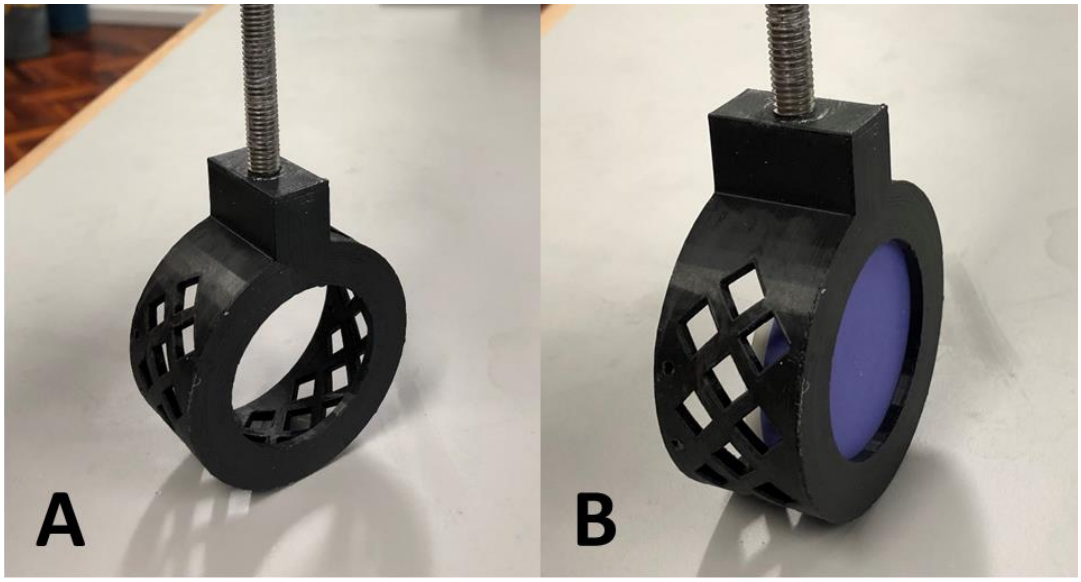

Figure 6-8: Second design of wax removal template holder for 5 cm diameter templates.

3. Decreasing template diameter

After determining results from adjusting the thickness of the template, a similar trial was completed with varying column diameters of a set thickness (1 cm). Two of each template of varying diameter (2, 3, and 4 cm) were placed inside the originally designed mesh cages inside the tank. The tank was filled with 8 L of fresh IPA and stirred at a constant rate of 400 rpm. The trial was left to run for 72 hours at room temperature before the templates were removed, visually inspected, and left to dry for 24 hours inside a fume hood. Upon drying, the templates were weighed before the process was repeated until either the templates cracked or no mass change was observed between cycles.

4. Increase of hydraulic channel diameter

The last test of the second support wax removal rig was a repeat of the timed support wax removal experiment with templates (5 cm diameter by 1 cm thick) of varying hydraulic channel diameters (500, 400, and 350 μm). Four wax templates were placed in the mesh cages for each hydraulic diameter and submerged into the IPA within the tank. The temperature was controlled using a probe connected to a hot plate beneath the tank. A fixed stirring rate of 400 rpm was used for all of these experiments. Two temperatures were used in individual repeats of this test at 40°C and room temperature (~22 °C). For the trial at 40°C, templates were removed from the rig at regular two-hour intervals after starting the experiment and left to

dry overnight inside a fume hood for 24 hours. Each disc's mass was recorded at the experiment's start and then after each had dried the next morning. Measurements were repeated until the mass of the templates had stabilized or the template had cracked. This method was repeated for the room temperature trial, except templates were removed at 24-hour intervals instead of two hours.

6.1.6 Column plug template filling rig

The cellulose infusion rig designed alongside Craig Stocker (undergraduate student contributing as part of his final year project) is shown in Figure 6-9 below. This rig is attempting to replicate filling wax templates with dissolved cellulose solution at a larger scale. The rig was also designed to fill either multiple larger (>2 cm diameter) column templates at a time or a single template.

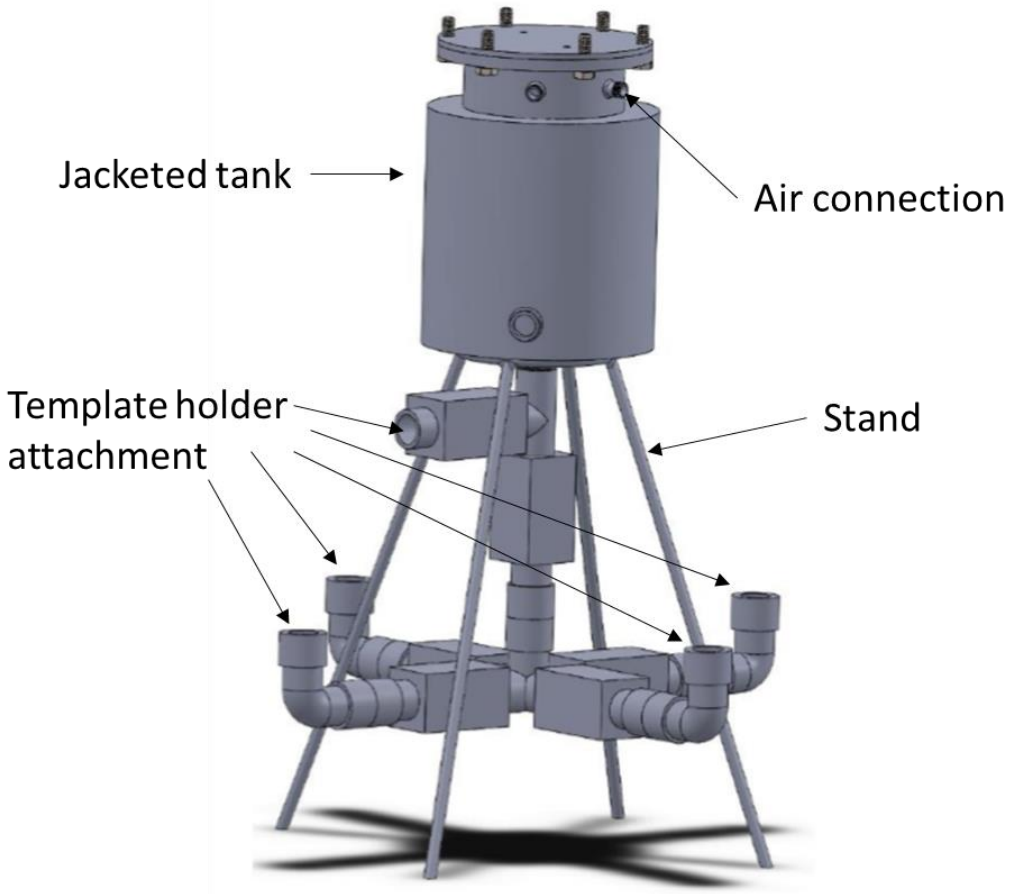

Figure 6-9: 3D Solidworks model of the custom wax template cellulose infusion rig.

The tank holds up to 3 L of dissolved cellulose solution kept cold by an ice bath recirculated through the tank's jacket. The rig was also designed for eventual use with other polymer solutions such as dissolved agarose that would need to be kept warm using a heated water bath to prevent premature gelling. The flow of solution through the pipework is driven by air pressure (100 PSI) in the head. This pressure is supplied by an airline and controlled by a regulator valve. Manual ball valves were used to stop and start the solution's flow, with one before each of the template holder attachments.

Template holders were designed and 3D-printed out of resin to be attached to the cellulose infusion rig's arms. The design could be altered to hold varying sizes of wax templates. They are attached by female Cam Lock fittings that screw into the 3D-printed holder and connected to the rig's pipework's male Cam Lock fittings. Figure 6-10 shows the design of one of these template holders below. The holders' tapered slides are to minimize air pockets forming and allow for an even distribution of solution through the template.

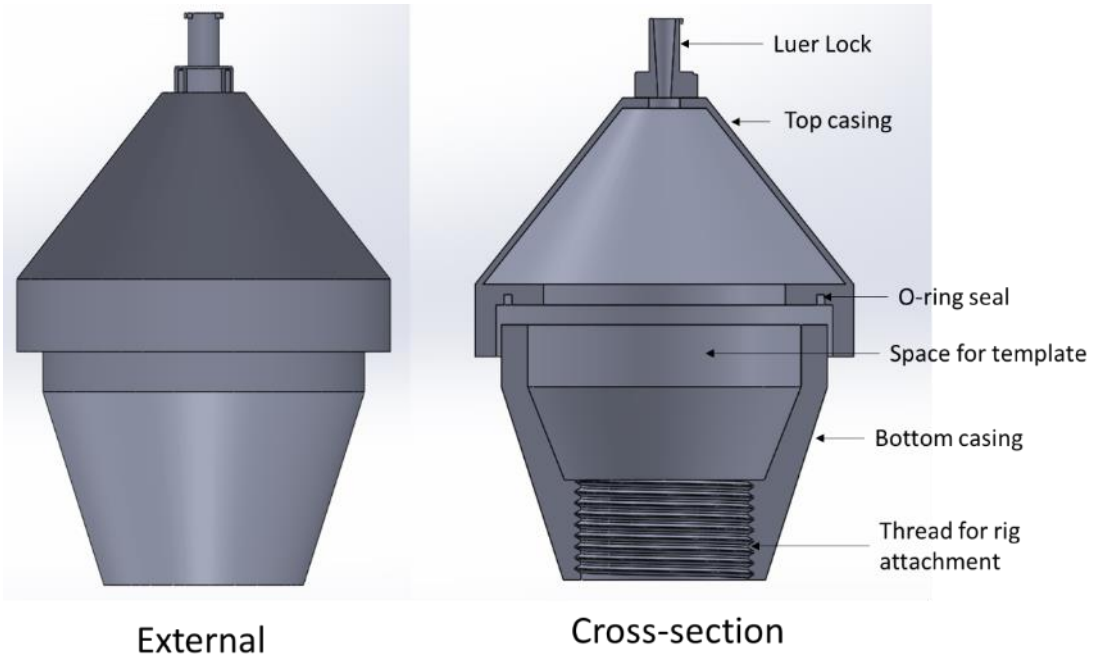

Figure 6-10: 3D Solidworks model of the custom template holders for cellulose infusion rig. The external image shows the outside of the template while the cross-section shows it internal structure.

A top and bottom casing are held together by an external clamp (Figure 6-11), which seals the O-ring. The Luer Lock attachment on the top casing can be sealed with a cap to prevent cellulose solution from leaking out after infusion has been completed. A screw cap that fits the thread for the Cam Lock is used once the template holder is removed from the rig to plug the holder.

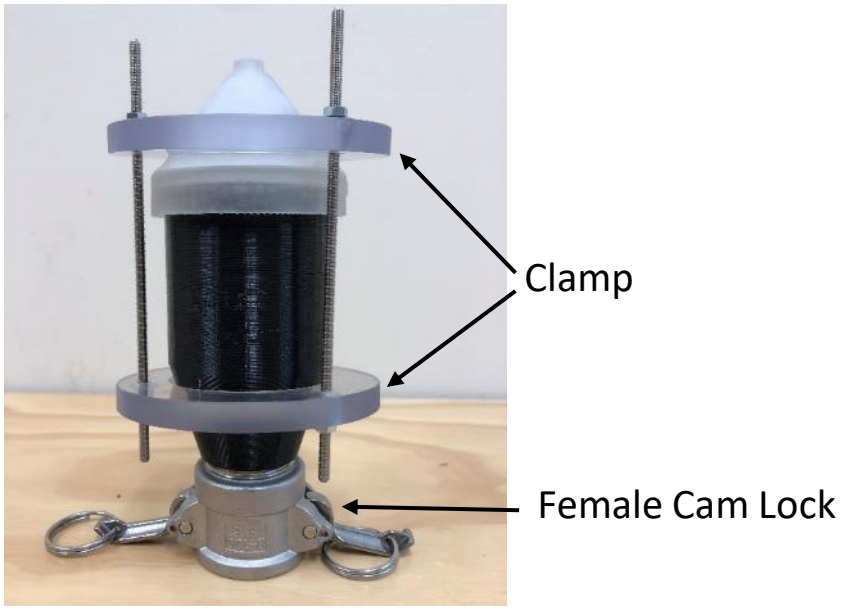

Figure 6-11: Printed template holder for the cellulose infusion rig showing female Cam attachment and clamp holding the top and bottom casing together.

A four-way splitter value (Figure 6-12) attached to the bottom of the tank, with identical length pipework, can be used to fill multiple templates simultaneously. The rig can also be rearranged using Cam Lock fittings to fill one or any number of templates up to five at a time.

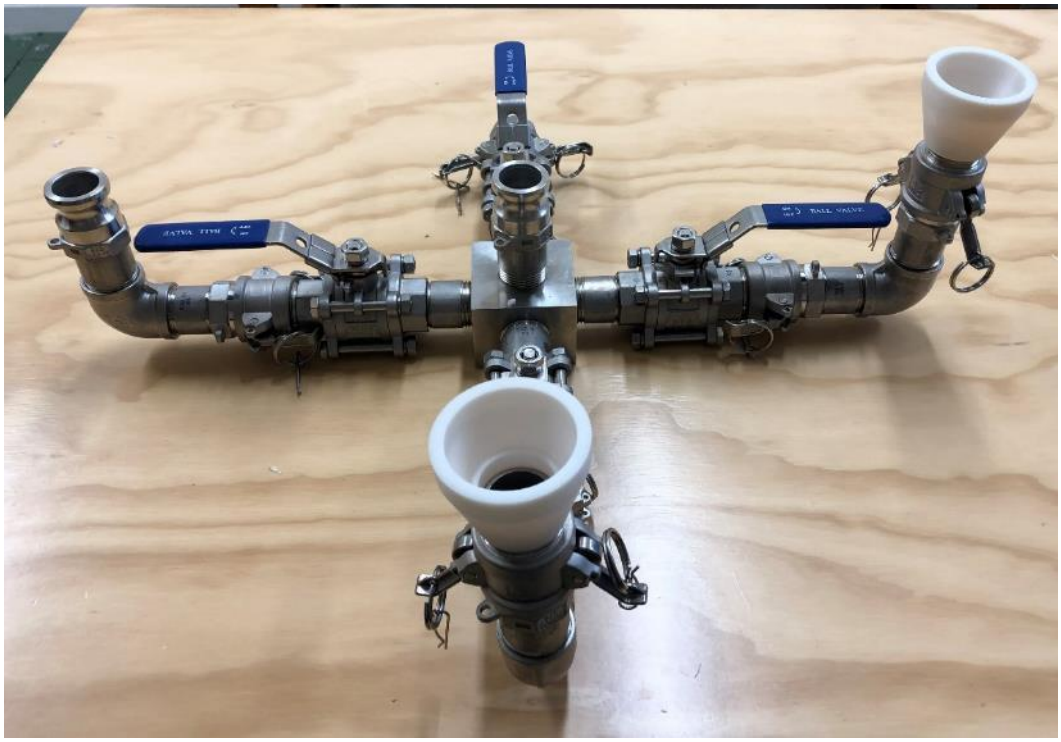

Figure 6-12: 4-way splitter attachment for cellulose infusion rig. Each arm has its own Cam fitting for holder attachment.

Figure 6-13 shows the rig set up to fill one template at a time. The bottom pipe was used as a purge valve to empty the tank after the infusion has been completed. The rig was operated inside a fume hood because of the volatility and toxicity of the chemical cross-linker ECH. This requirement for the rig's operation prevented the 4-way splitter valve from being tested because of the lack of space inside the fume hood. Upon confirmation, the rig works a more permeant setup with an extractor fan is planned for construction.

Figure 6-13: Cellulose template infusion rig setup without 4-way splitter pipework. Blue line: air connection; Green line: recirculated water for jacket.

6.1.7 Cellulose infusion operational testing

Two different sized templates were used to determine if the rig performed as designed. In the first test, 1 kg of 6% dissolved cellulose solution (as described in Section 3.1.1) was combined with 30 g of cellulose powder in an overhead mixer at 8000 RPM for five minutes. No chemical cross-linker was used in case the rig leaked or did not have enough pressure to force the flow of the cellulose solution. The solution was then sieved to remove any large clumps of the remaining powder. Only a very small number of clumps were removed compared with a large amount of cellulose added. Cellulose lost in clumps was considered minor and would not affect the desired cellulose composition. The rig was set up as previously shown in Figure 6-13 to gel a single 5 cm diameter by 1 cm thick, 500 μm Schoen gyroid template. The rig's tank was cooled with the recirculating ice bath 10 minutes before infusion. The cellulose solution was poured into the tank, lid closed and wing nuts tightened. The ball valve from the tank to the template holder was opened and the air regulator slowly adjusted to pressurize the tank

and force the solution up through the template. The ball valve was then closed once the solution started to flow out of the holder's top. The top of the holder was then capped and removed from the arm. The holder's bottom was plugged and placed in a water bath at 50°C for four hours. Post gelation, the infused template was removed from the holder and lightly scrapped to remove excess hydrogel. The infused template was then boiled in water with a drop of liquid hand soap for 8 hours. After build wax removal, the resulting hydrogel piece was visually examined and dissected to identify defects.

The second experiment used a 5 cm diameter by 6 cm thick, 500 μm Schoen gyroid template. The previous experiment was replicated with the addition of 100 grams of chemical cross-linker (ECH) mixed in with the cellulose powder by the overhead mixer for five minutes. Post gelation and build wax removal, the hydrogel piece was visually examined and dissected for defects.

The final experiment was a repeat of the second experiment with two templates infused one after the other. Upon the filling and removing the first holder, a second holder was attached to the rig, and the ball valve reopened to fill the second template. Post gelation, the templates were visually examined and dissected for defects. All three resulting hydrogel structures with chemical cross-linker were sliced into 0.5 cm thick discs, freeze-dried, and examined under SEM as described in Section 3.3.2.

6.2 Results and discussion

6.2.1 Printer advancement

SEM was used to ensure the template structure from the Projet printer was transferred to the cellulose hydrogel through the templating process. Multiple columns of varying channel sizes (500 to 200 μm) were freeze-dried according to Section 3.3.1 then fractured to examined the internal cross-section under SEM according to Section 3.3.2 Figure 6-14 shows the resulting cellulose hydrogel structure from a wax template produced by the 3D Systems printer.

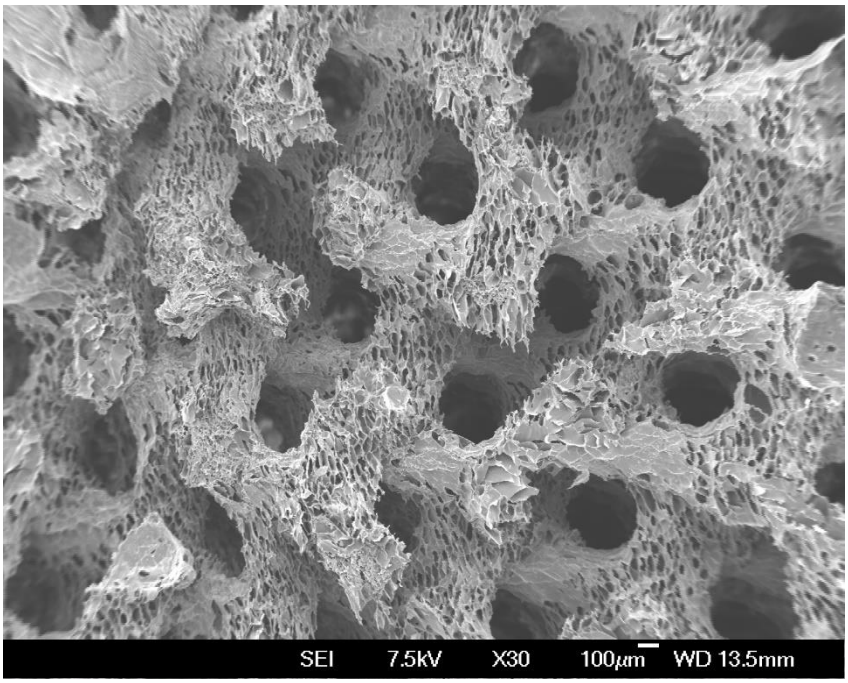

Figure 6-14: SEM image of a cross-section of a freeze-dried 300-micron hydraulic diameter, Schoen gyroid cellulose column made from a wax template printed on the 2500w ProJet wax printer.

Cleary defined channels can be seen in Figure 6-14 alongside the microstructure of the cellulose hydrogel that makes up the solid phase. On inspection, the shape of the resulting structure matched the requested Schoen gyroid defined by the STL file sent to the printer. This determined that a similar quality TPMS column could be produced with templates from the newly purchased printer.

6.2.2 Resolution and speed

The Solidscape 3Z pro was purchased in 2015, while the Projet 2500w was purchased recently in 2020. Table 6-1 shows the manufactures specifications for each model. Interestingly, the Solidscape printer's resolution in dots per square inch (DPI) is higher than the Projet printer. The DPI difference means the Solidscape printer places a much finer set of wax droplets than the Projet. Additionally, the layer thickness is lower for the Solidscape printer, allowing it to fit over twice the amount of layers into a single structure. However, the actual accuracy of the SolidScape printer is significantly worse. The Projet printer's accuracy is 500% greater, allowing it to produce much finer features than the SolidScape, even with a lower DPI and higher layer thickness. The larger layer thickness of the Projet also allows for a quicker print time as it lays down more wax in each pass, reducing the total overall passes required to produce a structure. The Projet build volume is 450% larger, allowing for the production of not only bigger parts but multiple parts simultaneously.

Table 6-1: Comparison of 3D wax printer manufacturers specifications.

	Solidscape 3Z pro	Projet 2500w
Resolution DPI	5000	1600
Accuracy (mm)	0.0254	0.005
Layer thickness (μm)	6.4	16
Build volume (mm)	152.4 X 152.4 X 101.6	298 x 183 x 203

A base case print of a 1 cm diameter by 5 cm long, 300 μm Schoen gyroid column was used to compare each printer's resolution, speed, and capacity. Table 6-2 shows the data from these tests and the original data from the SolidScape printer. The Project is not only faster (22.5×) but can produce multiple parts at the same time. The increased speed results in a capacity increase of 4500%. This capacity increase overcomes a considerable hurdle for this technology in the ability to produce columns rapidly. For commercialization of these columns, they need to be produced on a large scale and quantity. This capacity improvement shows the potential for a commercial-sized process of lab-scale columns. However, as with all 3D printing techniques, upscaling is eventually limited by the number of 3D printers [315, 316].

Table 6-2: Comparison of printing a 1 cm diameter by 5 cm long Schoen gyroid column.

	Solidscape 3Z pro	Projet 2500w
Time (hours)	36 - 48	1.6
Volume (number of parts)	1	20
Resolution (minimum hydraulic diameter μm)	300	150

The improvement in resolution and reduction in hydraulic channel diameter is important as it reduces the potential diffusion distance for target biologicals during chromatography. Additionally, a reduction of hydraulic diameter inversely relates to an increase in specific surface area. However, although templates with smaller hydraulic diameters are possible, they need to be translated into hydrogel columns.

6.2.3 File size limitations

Advancements in printing technology have improved the speed and number of simultaneous prints; however, limitations that affect large-size templates still exist. The preparative software (slicer software) and computing power limit the file size the wax printers can handle. The slicer software ModelWorks used by the SolidScape Pro 3Z could process files up to 500 MB, while '3D Sprint' used by the Projet 2500w has a higher capacity of 7 to 8 GB. Even with this improvement, printing larger columns' is an issue as the file sizes rapidly become too large for the printer's slicer software to handle. Table 6-3 shows the file size for 300 μm Schoen gyroid columns of the same resolution but varying column size. A commercial-sized packed bed column can be between 45 cm in diameter by up to a bed height of 80 cm [317]. The file size for a 3D-printed column that size would be multiple terabytes, far greater than standardly used 3D-printing software could handle (Cura, Slic3r, etc.).

Table 6-3: Comparison of STL file size a 300 micron Schoen gyroid in gigabytes.

	Diameter cm			
Length cm	1	1.5	2	2.5
5	0.8	1.9	3.4	5.2
10	1.7	3.8	6.8	10.5
15	2.5	5.7	10.1	15.7
20	3.4	7.6	13.5	21.0

A patterning method was used to avoid file size limits to print larger templates described in Section 6.2.3. Figure 6-15 below shows the largest column printed to date (50 mm diameter by 200 mm long, Schoen gyroid 300 microns' hydraulic diameter channels). This template was the largest possible by this technique using the 3D Sprint software. Even by patterning, the software would crash when a file was copied too often, preventing larger structures from being created by this method.

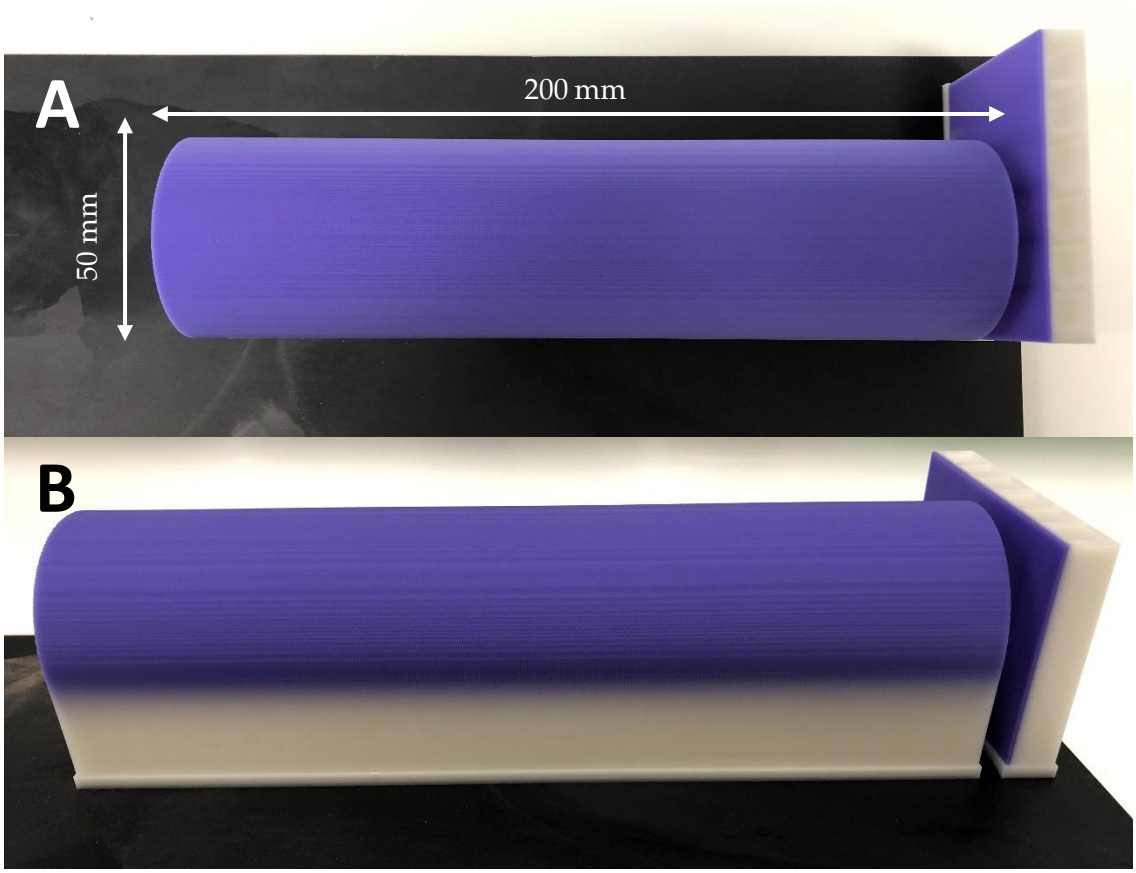

Figure 6-15: Wax print of a Schoen gyroid template (50 mm diameter by 200 mm long, 300-micron hydraulic diameter channels).

6.2.4 Support wax removal

Printing of the wax templates is the first of four steps in the cellulose column production process. As both the templates' size increases and the hydraulic channel diameter decreases, removal of support wax becomes more difficult. Two factors were considered to reduce the time required to clear all of the template channels of support wax; IPA temperature and mixing velocity. The supplier of the printer recommended the increasing temperature to reduce processing time [318]. An increase in mixing velocity should help move the saturated IPA away from the dissolving wax's surface, aiding dissolution [319]. The temperature of the IPA could be increased to a maximum of 40 °C. At temperatures higher than this, the wax templates became soft and quickly distorted in shape. A similar issue was found with the initial setup's mixing velocity (beaker and mixing flea, Figure 6-1).

The force generated on the ends of the template during high-velocity mixing caused the structure to warp and bend predominantly for longer templates (> 5 cm length, 1 cm diameter). Warping happened faster at higher IPA temperatures. If the IPA was not heated, warping could be minimized; however, the length of time for support wax removal would increase (~4× slower room temperature than at 35°C). Based on these initial observations, a rig was designed to better support the templates during this process. A description of this rig and the experimental method of testing is described in Section 6.2.4. In this first version, a narrow tube is used to hold the template vertically while IPA is slowly (40 mL/min) pumped from the bottom up. This slow directional flow along the axis prevented warping and could remove support wax from long (20 cm) 300-micron structures in under 48 hours. For comparison, a column of the same diameter and hydraulic diameter 10 cm long took 20 hours to process at 35°C. Although slower because of the lack of heating, these structures previously could not have their support wax removed because of their length and warping. The size of the column diameter limits the design. It had to be narrow enough to support the template but large enough to accommodate varying column diameters. Therefore, multiple cylinder sizes would be needed to be used depending on the dimensions of the template.

The time required rose when removing support wax from larger diameter structures and those with hydraulic diameters smaller than 300 μm. In both cases, the time required to remove the support wax increased, as seen in Table 6-4. The time for support wax removal comparing a 1 cm column (300 μm Schoen gyroid) to a 2 cm column of the same internal geometry requires 700% longer. Extrapolating this result suggests a pilot-scale size column (5 cm diameter, 15 cm long) would take two or more months to process. This length of time is too long for this to be a viable method for upscaling this technology.

Table 6-4: Time taken for support wax to be removed from varying wax templates of a nominal length (15 cm, second iteration support wax removal rig).

Channel diameter μm	Column diameter mm	Time hours
300	10	48
300	15	168
300	20	336
250	10	120
200	10	288

As well as the length of time taken to remove support wax from some structures, damage to the template was noticed on 150 μm hydraulic diameter channel templates. Figure 6-16 shows an example of this cracking on a piece of 150 μm Schoen gyroid template. Additionally, the purple support wax had noticeably whitened. The IPA was also bright purple after support wax removal suggesting the dye had leached out during the process. This cracking ruins the template as during infusion, it will fill with the cellulose solution creating an axial wall through the column, disrupting the channels. Similar cracking was also observed after the attempted support wax removal from 5 cm diameter by 20 cm long, 300 μm Schoen gyroid template. Figure 6-17 shows the extent of this cracking. Further investigation of this cracking phenomenon is presented later in this chapter.

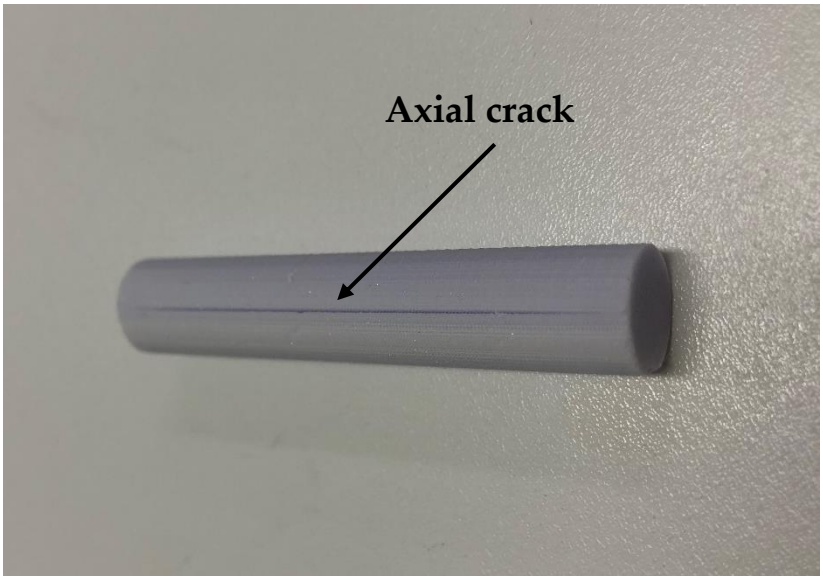

Figure 6-16: 5 cm long piece of 1 cm diameter, 200 μm Schoen gyroid template post support wax removal showing cracking.

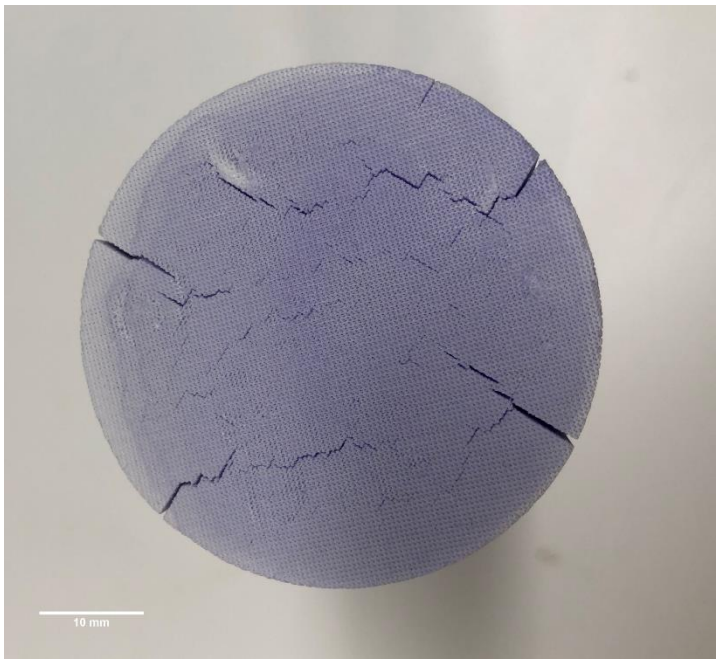

Figure 6-17: Top view of 5 cm diameter by 200 mm long, 300 micron Schoen gyroid template post support wax removal.

6.2.5 Build wax removal

Post support wax removal and cellulose hydrogel injection, the remaining build wax needs to be removed from the structure. Similar to support wax removal, this process takes longer the smaller the hydraulic diameter of the channels. These column templates were gelled are described in Section 3.1.4 and analyzed under SEM (Section 3.3.2). The narrower channels seem to slow the migration of molten wax out of the structure during boiling. The time required to fully remove wax from a 300 micron Schoen gyroid compared to a 200 micron Schoen gyroid (1 cm diameter by 5 cm long) is nearly four times greater (80 hours). Figure 6-18 shows a cross-section of a 200 micron Schoen gyroid column with trap build wax inside the channels.

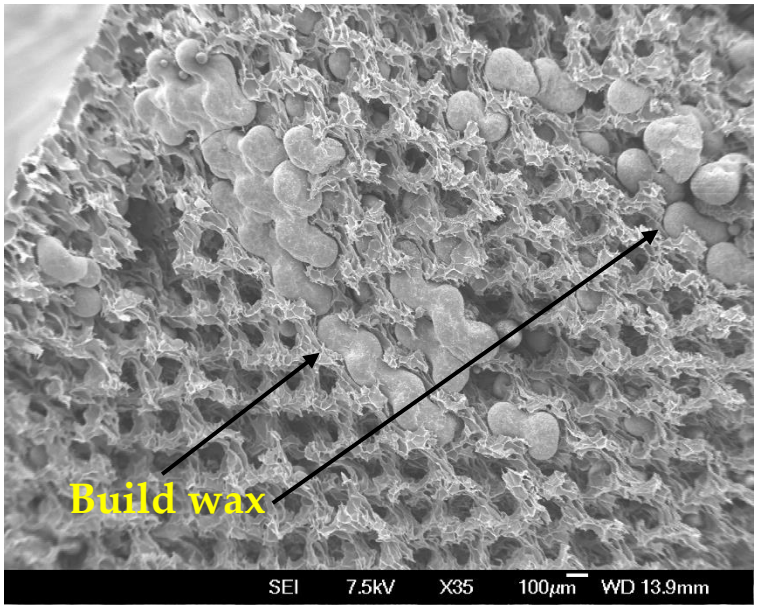

Figure 6-18: SEM cross-section image of a 200 micron Schoen gyroid with build wax trapped inside of the channel network.

Pockets of wax that are trapped within the structure require excessive boiling to remove. Build wax removal is another potential bottleneck in the process, as larger columns with small hydraulic channel diameters will increase the amount of time to clear wax. Build wax removal from these small channel diameters (200 microns) is possible as shown in Figure 6-19.

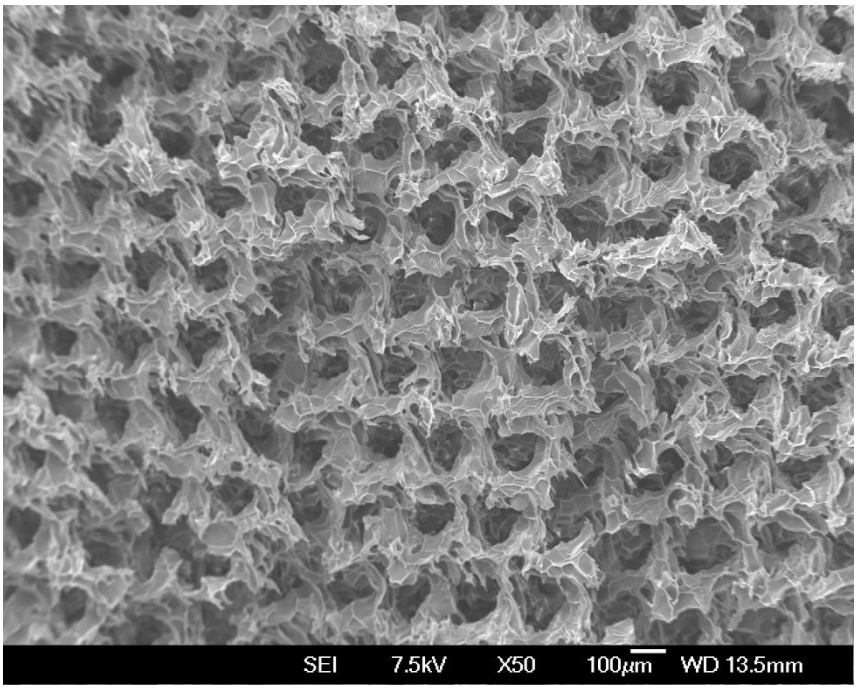

Figure 6-19: SEM image of a 200 micron Schoen gyroid cellulose column cross-section.

6.2.6 Segmentation of columns

As the ProJet wax printer could not print templates larger than 5 cm by 20 cm, as shown in Section 6.2.3 because of the slicer software, a segmentation method was proposed as an alternative to single-piece columns. Larger columns could be created by dividing up the desired column length into smaller printable pieces. Two different methods were tested, template segmentation with combined gelling and template segmentation with individual gelling. Details of these two methods can be found in Section 6.1.3. The time required to remove support wax should be reduced by limiting each template's length to 2 cm while minimizing potential warping.

6.2.7 Combined gelling

Multiple segments of the template were stacked together to be gelled as one piece as described in Section 6.1.3. Figure 6-20 shows the plug templates inside of the casing used to gel them together. They have been tightly pressed together, but gaps between them can still be seen. In a previous attempt, excessive force was used during loading into the casing to minimize these gaps; however, the templates deformed, blocking the channels.

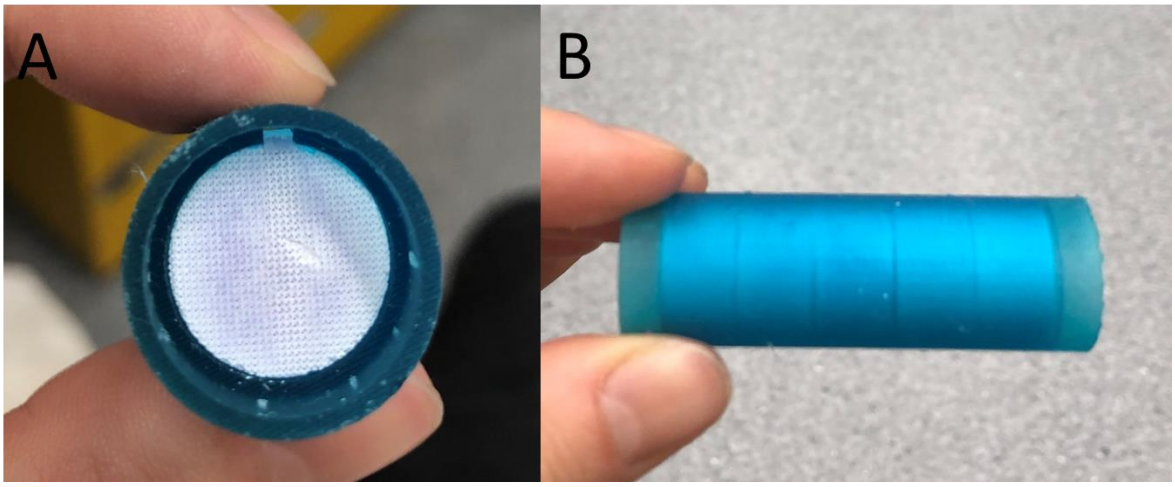

Figure 6-20: Image of wax templates inside casing used to hold them during cellulose infusion and gelling. A front view; B Side view.

During the infusion process, the pressure applied by the syringe forced the segments tightly together. However, the cellulose solution still seeped its way between them. This seeping resulted in a combined structure with slices of solid hydrogel between segments. The unwanted hydrogel blocked the axial flow through the column. Increased pressure on the templates to minimize seeping was tested in a repeat experiment. However, the paraffin-based build wax deforms under the additional pressure shown in Figure 6-21. The templates' rough face surface has contributed to the gaps the solution filled between the templates. Shaving the surfaces of the templates was suggested post support wax removal. However, this would misalign the TPMS structure channels unless a perfect unit cell was removed from each face. There would be no way to tell if this was correctly achieved during the shaving process.

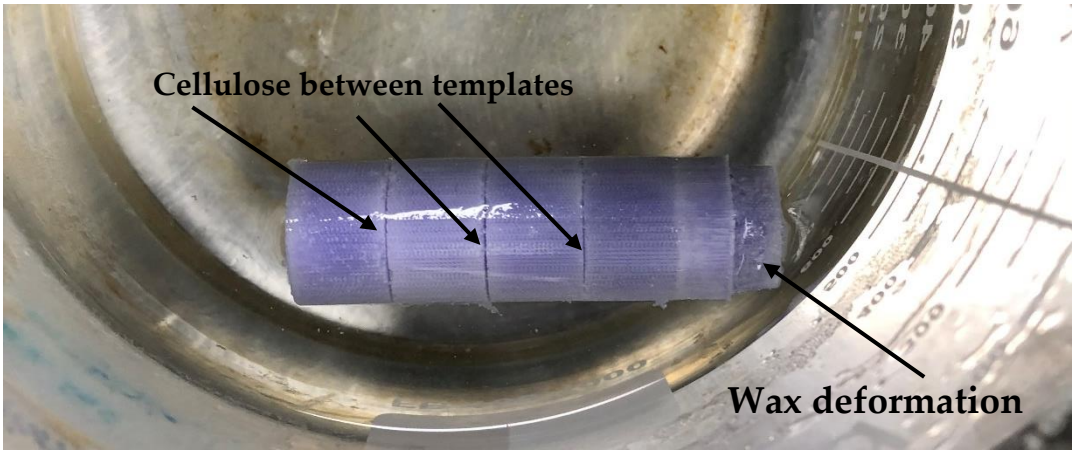

Figure 6-21: Image of wax templates gelled together showing the gaps of cellulose between each template blocking channels.

An alternative segmentation method was used to avoid channel blocking resulting from combined gelling. The smaller 2 cm thick templates were gelled separately to be stacked onto each other inside the column casing after building wax removal. Figure 6-22 shows a combination of these 'plugs' inside of a casing. The plugs were shrunk in IPA and slide inside the casing one at a time. Each plug was re-swelled with water before the next plug was inserted. Each plug was placed as close to the previous as possible to minimize the gaps between them. Initial flow testing of this stack of plugs showed no difference in pressure drop between this and an equivalent single-piece column (0.02 MPa). Therefore, it was concluded potential misalignment of the plugs was not significantly affecting flow or blocking channels.

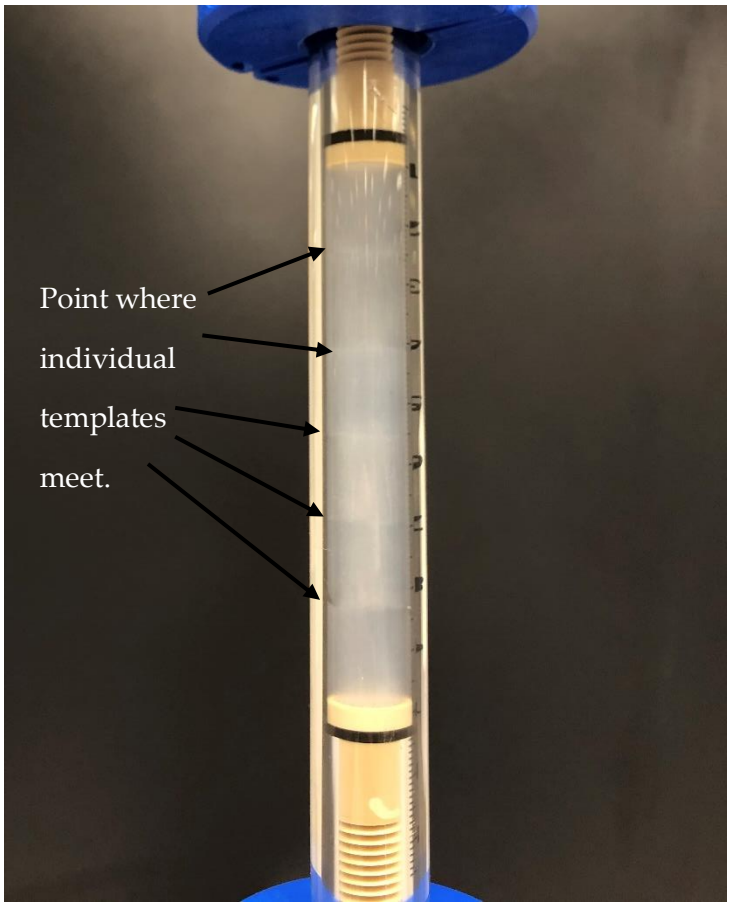

Figure 6-22: SNAP column casing filled with 6 × 2 cm 3D-printed cellulose plugs (300 micron Schoen gyroid).

6.2.8 Column stacking

6.2.8.1 Tracers analysis

A tracer analysis was completed to determine if there was a significant performance drop between a single piece or a combination of four separate plugs. Details for this method can be found in Section 6.1.4 RTD profiles were determined from 1% acetone tracers at varying flow rates through a 10 cm bed height, 1 cm diameter, 300 micron Schoen gyroid column. The same column was then cut into four individual 2.5 cm plugs and stacked back inside the same SNAP casing. The same tracer experiment was then repeated. Figure 6-23 below shows the normalized peaks from these tracers overlapped.

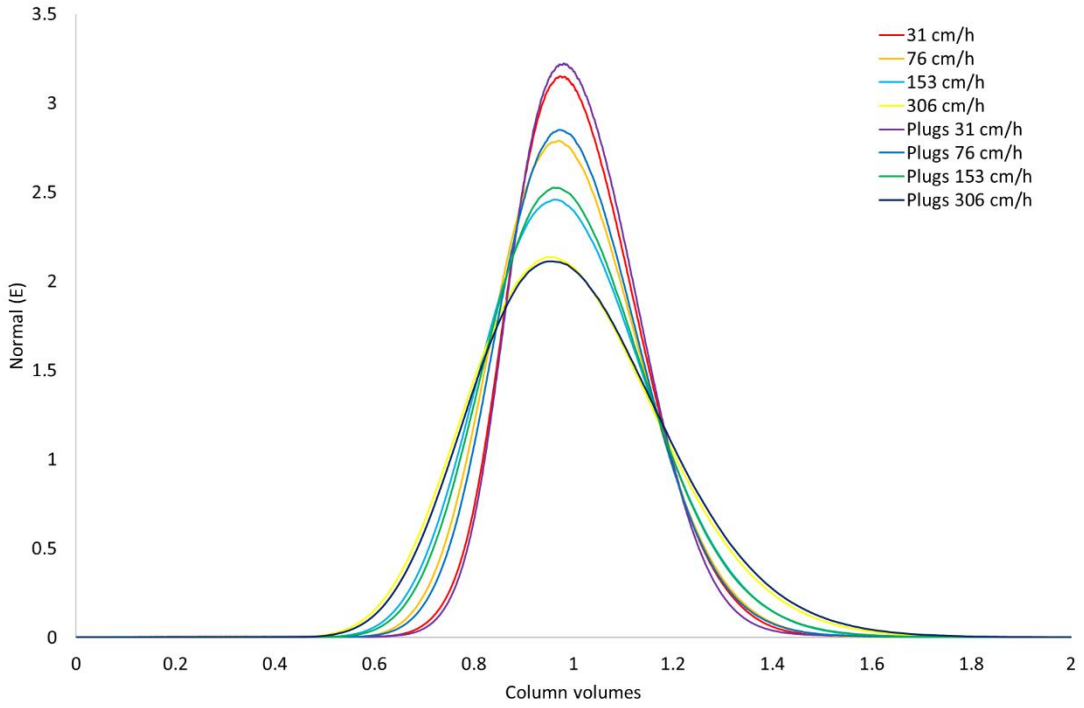

Figure 6-23: 1% Acetone tracers at varying flow rates through a 10 cm 300 μm hydraulic diameter Schoen gyroid in a single piece and in four separate plugs.

The overlap of all four flow rates matches between the two variations of the same column. The overlapping peaks show minimal disruption by segmenting the column into multiple pieces. To further analyses these peaks, Asymmetry and the HETP values were found and compared; details of these calculations can be found in 6.1.4, and sample calculations can be found in Appendix A. Figure 6-24 shows how asymmetry values compare between the single piece and multiple plugs for the acetone tracers. For all peaks shown, the asymmetry values

are within the recommended values for packed bed columns (0.8 to 1.8) [160]. The best symmetry is achieved not at the lowest flow (15 cm/h) rate but a higher 76 cm/h.

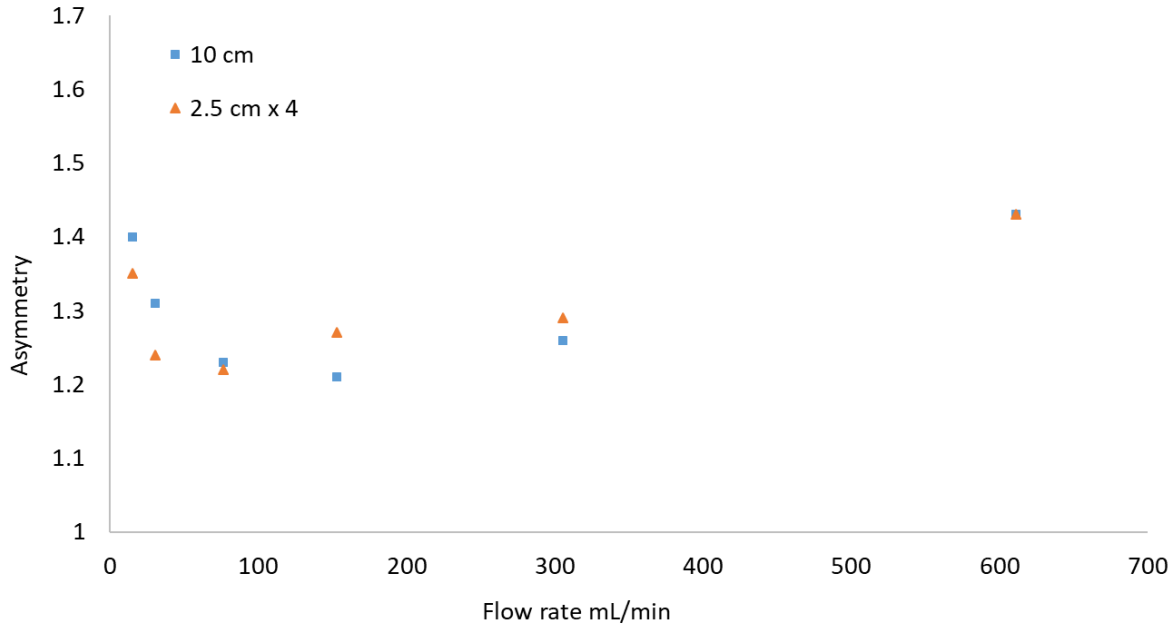

Figure 6-24: 10% Asymmetry values calculated from 1% acetone tracer peaks (10 cm, 300-micron Schoen gyroid, single column and 2.5 cm stacked plugs) from Figure 6-7.

The HETP values for each peak can be seen in Figure 6-25 below, as with packed bed columns, as the flow rate is increased, the performance decreases. However, this does not follow the tick shape of a traditional Van Deemter plot. The Van Deemter equation consists of three factors, A, B, and C, as shown in Equation 6-7, where u is fluid phase velocity [320]. A is related to eddy dispersion, B is related to molecular diffusion, and C is related to mass transfer.

$$HETP = A + \frac{B}{u} + Cu, \tag{6-7}$$

Based on the shape of Figure 6-25, it would suggest that the dominating factor is the mass transfer term C. The mass transfer can therefore be assumed to be the limiting factor for plate height. The large hydraulic diameter (300 μm) of the channels causes poor mass transfer within the column. A similar trend is seen in EBA because of the expansion required to passage solids, where again the C term is dominant for the Van Deemter plots [321]. A reduction in the hydraulic diameter of the channels should reduce HETP values. However,

channels still need to be large enough to passage solids for capture recovery from crude cell lysates. Hydraulic diameter is limited by the current 3D printing technology, which dictates the smallest possible channel diameter possible, being ~200 µm. As advancements are made with 3D printers, the minimum printable hydraulic diameter is expected to reduce.

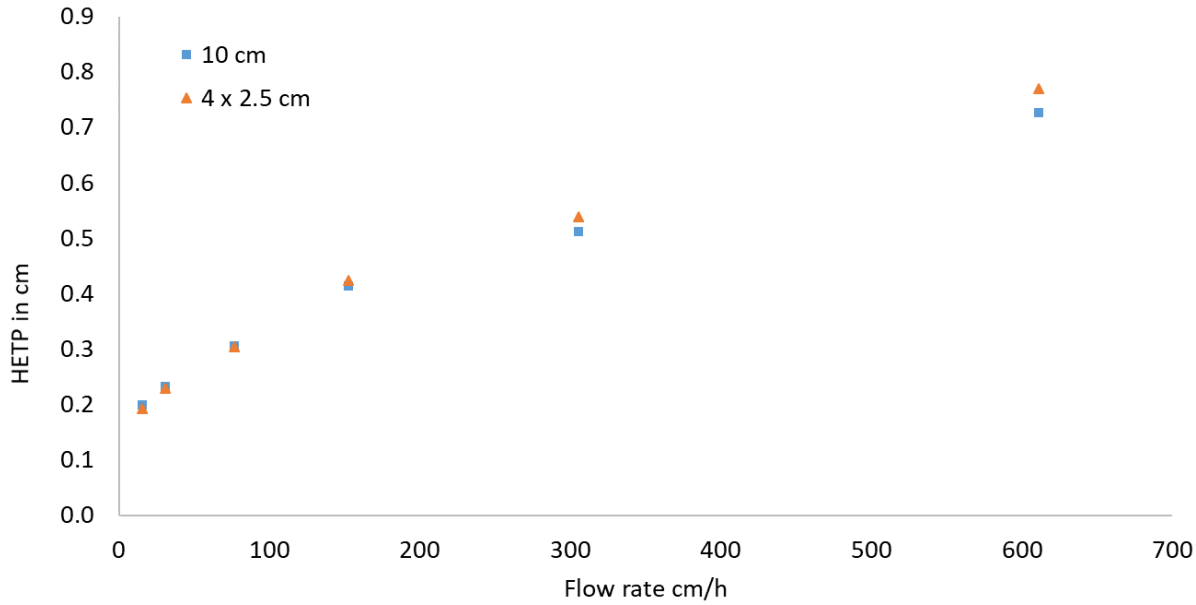

Figure 6-25: HETP values calculated from 1% acetone tracer peaks (10 cm, 300-micron Schoen gyroid, single column and 2.5 cm stacked plugs) from Figure 6-7.

6.2.9 Pilot scale column creation

The segmentation method was shown not to affect the performance of 3D-printed columns on a small scale. It also provides a potential method for upscaling this technology, circumventing printable templates' size limits because of the slicer software and long templates' warping. Therefore, a new support wax removal rig was designed for 'plug' templates up to 5 cm in diameter by a given thickness up to 10 cm. A 2 cm diameter column could successfully have its support wax removed without heating based on previous experimentation. A 2 cm thickness was used as a starting point for this work, hypothesizing that heating would shorten the time required. If the templates need to be thinner than 2 cm, more will be required to be stacked together to reach the desired column length. Therefore, there is a potential trade-off between the time taken to create one plug versus how many total plugs are needed for a column. Table 6-5 shows which templates were used in each test of this rig. Experiments are described in Section 6.1.5. Each test followed the previous to determine if upscaling by segmentation was possible with current technology.

Table 6-5: list of the various templates used for testing of the second support wax removal rig.

	Thickness	Channel hydraulic diameter	Diameter
	cm	μm	cm
Test 1	2	300	5
Test 2	0.8, 1, 1.2, 1.4, 1.6 and 1.8	300	5
Test 3	1	300	4, 3 and 2
Test 4	1	350, 400 and 500	5

6.2.10 Test 1 - Effect of temperature

Three different temperatures (40°C, 35°C, and room temperature) were tested to remove the support wax from the plug templates. All three of the temperatures tested resulted in cracking of the wax template after different periods. This cracking occurred in all three cases at a mass removal between 30 to 35% of the starting mass. For higher temperatures, this happened earlier as support wax removal occurred at a faster rate. At 40 °C, cracking occurred within two hours compared to room temperature, which took up to 24 hours. Templates were broken open to see how far the support wax removal had progressed. Figure 6-26 shows the cracks

found on these templates' external surfaces, while Figure 6-27 shows the template's internal structure after being cut in half. The lighter purple front around the outside of the template shows the distance support wax removal had reached. A similar depth of support wax removal (3 to 4 mm) occurred before cracking was noticed in all cases.

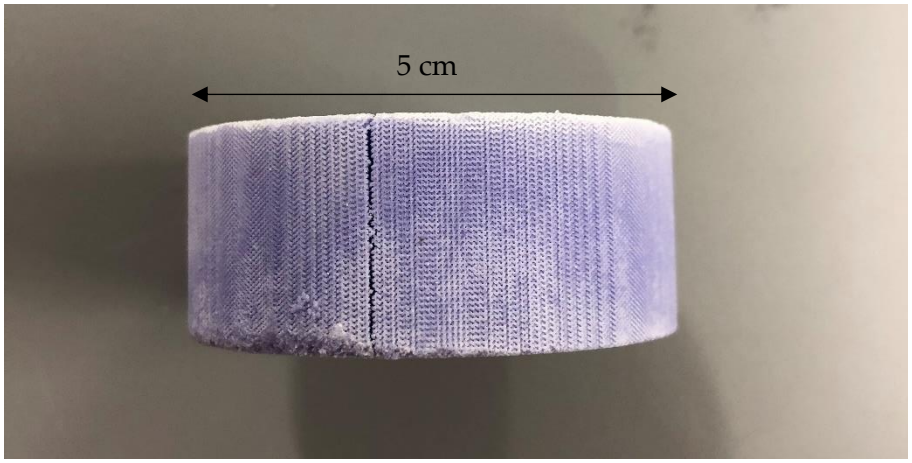

Figure 6-26: Plug wax template (2 cm thick by 5 cm diameter, 300 µm Schoen gyroid) side view showing cracking seen post dissolution. Wax removal occurred at room temperature over 5 days.

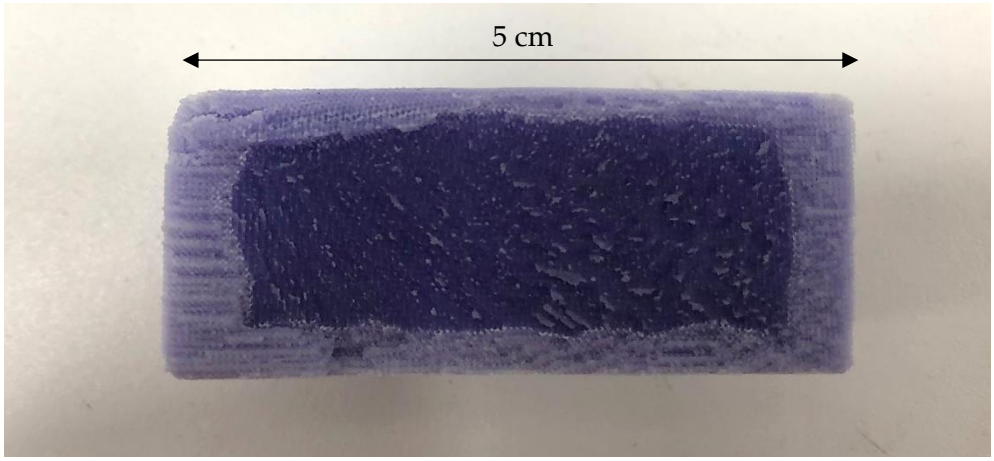

Figure 6-27: Plug wax template (2 cm thick by 5 cm diameter, 300 µm Schoen gyroid) cross-section view showing IPA front of support wax removal. Wax removal occurred at room temperature over 5 days.

The purple support wax was whitened during the support wax removal process. The whitening indicates again that the dye of the build wax has leached out into the solution. This leaching possibly causes the weakening of the wax's mechanical properties and eventually

cracking. Based on these initial results, the template size was reduced to find a point where cracking would not occur.

6.2.11 Test 2 - Template thickness

The support wax from various thickness (0.8 cm to 2 cm) templates (5 cm diameter, 300 μm Schoen gyroid) could not successfully be removed from any of these structures without cracking, even those thinner than the 1 cm diameter columns. The template's position within the tank was modified to increase the surface area exposed to IPA flow. A new template mesh cage was designed to allow the template's cross-section to be normal to the tank's flow. The rig was tested with two normal-facing templates shown in Figure 6-7 with optimal conditions (room temperature, fresh IPA). Both templates cracked before the support wax had dissolved.

Interestingly, the template had a similar support wax removal pattern to those dissolved in the original template holder when dissected. Figure 6-28 shows a cross-section of one of the templates that cracked during support wax removal using the new holder. Even though the flow was directed at a different part of the structure, the support wax removal pattern was the same. This pattern suggests that the IPA flow does not affect the support wax removal process. The mixer's speed was increased from 400 rpm to 900 for a repeat of this trial. Again the template cracked, and upon dissection, had a similar removal pattern inside the template. The small size of the channels within the structure slows the IPA's velocity and eventually stagnates because of the dead ends due to support wax. Therefore, most support wax dissolving is limited by diffusion, not convection of saturated IPA away from the solid support wax. As the system is diffusion-limited, increases in the IPA temperature will speed up the support wax removal process [318].

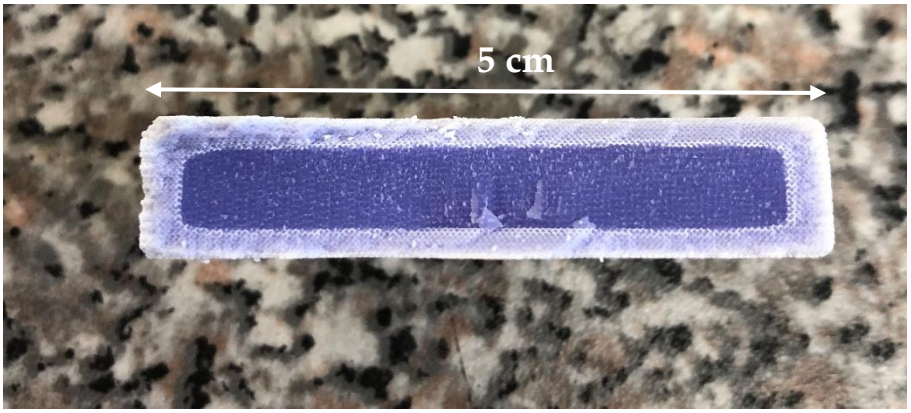

Figure 6-28: Cross-section of wax template after cracking during support wax dissolution at 900 rpm.

6.2.12 Test 3 - Column diameter

Previous experimentation with the first support wax removal rig could remove support wax from 2 cm diameter columns (15 cm long, 300 μm Schoen gyroid) with cracking occurring. Therefore, instead of varying template thickness, the diameter was altered. Templates (1 cm thick, 300 μm Schoen gyroid) with diameters between 5 and 2 cm had their support wax removed using the second iteration rig. Table 6-6 shows the templates larger than 3 cm in diameter cracked before the support wax could be removed. The template diameter variation seems to have a greater effect on preventing cracking than changing the thickness of the template. Altering of the diameter suggests the cracking may depend on the template's circumference surface area rather than its length.

Table 6-6: Results of support wax removal trial on various template diameters.

Template diameter	Cracking
1	no
2	no
3	no
4	yes
5	yes

6.2.13 Test 4 - Hydraulic diameter

Based on previous results indicating support wax removal was diffusion limited, the channels' hydraulic diameter within the templates was increased. The increase in channel hydraulic diameter increases the template channels' wall thickness, potentially increasing its resistance to stress during support wax removal. Table 6-7 shows repeat trial results removing support wax from varying hydraulic diameters (5 cm diameter, 1 cm thick, 300 μm Schoen gyroid). The Schoen gyroid templates with a hydraulic diameter of above 350 μm did not crack during the support wax removal process. For both temperatures tested (room temperature and 40°C), the same result occurs, indicating if the template cracked during support wax removal at 40°C, it would crack at room temperature. The effect of temperature only decreases the time taken to reach the cracking point or complete support wax removal for templates.

Table 6-7: Results of support wax removal trial on various template channel hydraulic diameters.

Hydraulic diameter	Cracking
500	no
400	no
350	yes
300	yes

Figure 6-29 shows the mass change for a 5 cm diameter by 1 cm thick, 500 μm Schoen gyroid template over 4 hours in the second support wax removal rig at 40°C. The mass loss stabilized after two hours, indicating that no support wax was left. The template was fractured post drying to visually confirm that all the channels were clear of support wax. Comparing the weight of build wax used (specified by the printer) to that of the template (post support wax removal) shows a 50% reduction in mass. This weight reduction in the build wax suggests that the components of the wax dissolve during the support wax removal process.

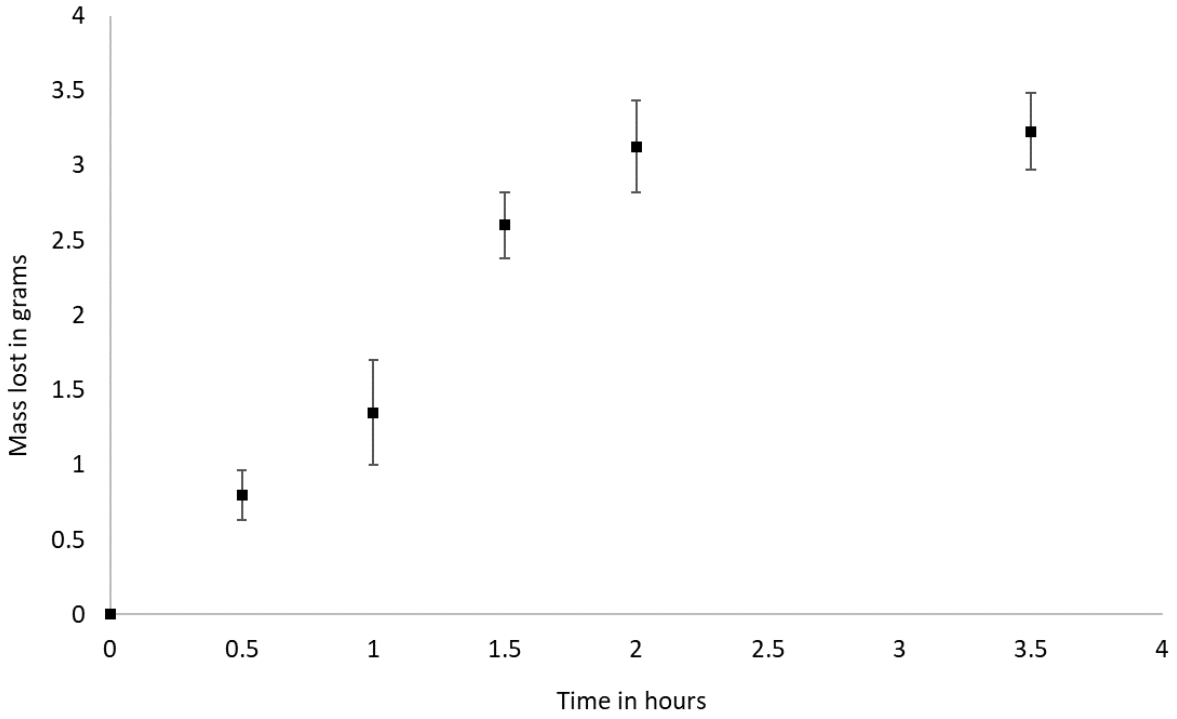

Figure 6-29: Change in mass over time of templates (5 cm diameter by 1 cm thick, 500 μm Schoen gyroid) at 40°C inside support wax removal rig.

To continue upscaling work creating larger cellulose column pieces, 500 μm hydraulic diameter templates were used as most smaller hydraulic diameter templates cracked during testing. The build wax formulation is mostly unknown and not disclosed by the producer. The MSDS sheet provided with the wax says it is 60 to 90% paraffin [322]. A more detailed study into the wax materials, dissolution process, and other potential solvents would be required to understand if cracking could be prevented in larger (>3 cm diameter) 300 μm hydraulic channel diameter templates. The dissolution process analysis was outside of this work scope, where the goal was to show what is currently possible with current 3D printing technology. A larger 500 μm Schoen gyroid template (5 cm diameter by 6 cm thick) was produced and had its support wax successfully removed without cracking (5 hours at 40°C) inside the second support wax removal rig. Figure 6-30 shows a comparison of a 500 micron Schoen gyroid template, 5 cm diameter by 6 cm thick, pre and post-support wax removal.

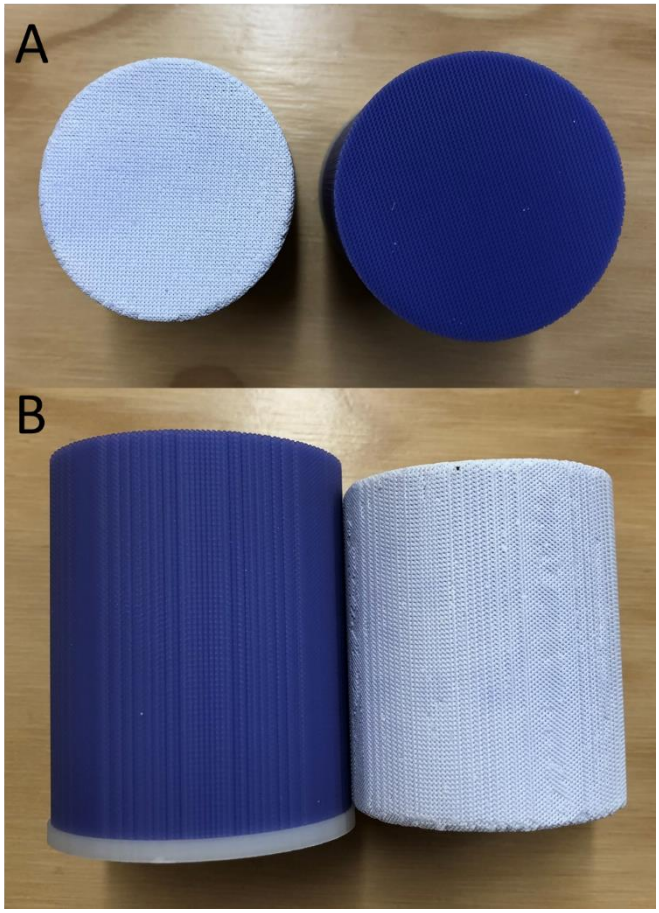

Figure 6-30: Side by side comparison of 500 μm Schoen gyroid template (5 cm diameter by 6 cm thick) pre (purple) and post support wax removal (white/violet). A: top view; B: side view.

A reduction in size and change in build wax color between template pre and post support wax removal is shown in Figure 6-30—the wax template shrunk by 28.4% by volume and 50% by mass. The supplier of the wax states shrinkage at 40°C in IPA is 2% by volume, but they do not specify over what period. However, they suggest support wax removal should only take one hour [323]. The extended time (5 hours at 40°C) in IPA to completely remove support wax could result in the greater shrinkage seen in these templates than what was reported by the manufacturer. This shrinking effect may also cause the cracking found in templates with smaller hydraulic diameters and larger template diameters. The surface may be under tension if shrinking occurs on the template's surface before the internal support wax is removed. Surface stress is a common occurrence in concrete curing where the surface cracks as the concrete dries because of water loss shrinking at the exposed surface [324]. Cracking happens

more frequently with objects that have a high surface area to volume ratio [325]. As the template's channel size decreases, the surface area to volume ratio increases. This increased surface area to volume ratio could explain why templates with smaller channel diameters crack while templates with larger channels do not. Based on the results of support wax dissolving, the limits of the current process have been shown. Testing of the cellulose infusion rig took place with 500 μm hydraulic diameter Schoen gyroid templates.

6.2.14 Cellulose injection rig operation

The cellulose infusion rig used for these experiments is described and operated according to Section 6.2.14. Figure 6-31 shows the resulting cellulose structure produced from the first trial with a 5 cm diameter by 1 cm thick template. An air bubble was trapped on top of the template caused by the template's loose-fitting within the holder. The cellulose traveled up and around the sides of the template, trapping air. This air bubble prevented the entire template from being infused with the solution, which left the large cavity seen in Figure 6-31. For the second trial, the tolerance between the holder's sides and the template was reduced (2 mm to 0.5 mm) to be a tighter fit to the template's sides. The first trial showed the rig was operational and the air pressure supplied to the tank was more than enough to force the solution through the template.

Figure 6-31: Result of first trial of cellulose infusion rig post wax removal, showing the resulting level of cellulose penetration because of air bubble formation.

Another 5 cm diameter by 6 cm thick template was infused using the previous trials' method. Additional to the physical cross-linker, 10 wt.% chemical cross-linker (ECH) was included in the hydrogel formulation. The cooling jacket was used with an ice bath to keep the solution as close to 0°C as possible during infusion to prevent premature gelling [222]. Figure 6-32 shows the chemically cross-linked column piece post-build wax removal. The build wax removal for this template took only 8 hours because of the channel size (500 μm). The larger hydraulic diameter of the channels within the column piece provided less resistance for wax migration out of the structure. Although not explored because of the cracking of 300 μm templates, build wax removal should be investigated in future work once larger templates with smaller channels can be produced. The cellulose column piece resulting from the infusion process has rough edges resulting from minor damage to the template during support wax removal and the boiling for build wax removal. Apart from these minor surface defects, the template's overall structure and size are reflected in the resulting hydrogel.

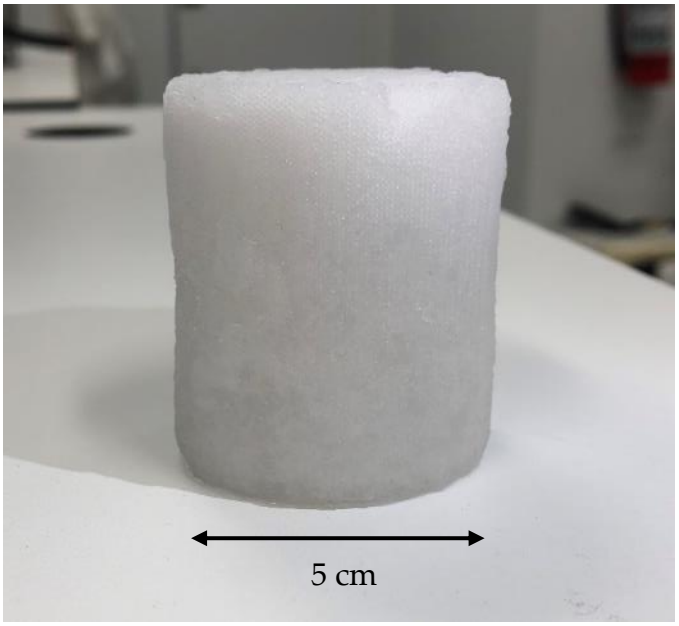

Figure 6-32: Result of the third trial of cellulose infusion rig post wax removal.

Figure 6-33 shows a cross-section of this gelled column piece showing the internal structure. There were no internal cavities within the structure confirming complete cellulose infusion. Figure 6-34 shows an SEM image of a slice from the chemically cross-linked cellulose columns. The periodic shape of the channels shows the structure from the template has been transferred to the hydrogel. This stackable column piece represents a 15× volumetric increase in a producible single-piece 3D-printed column size.

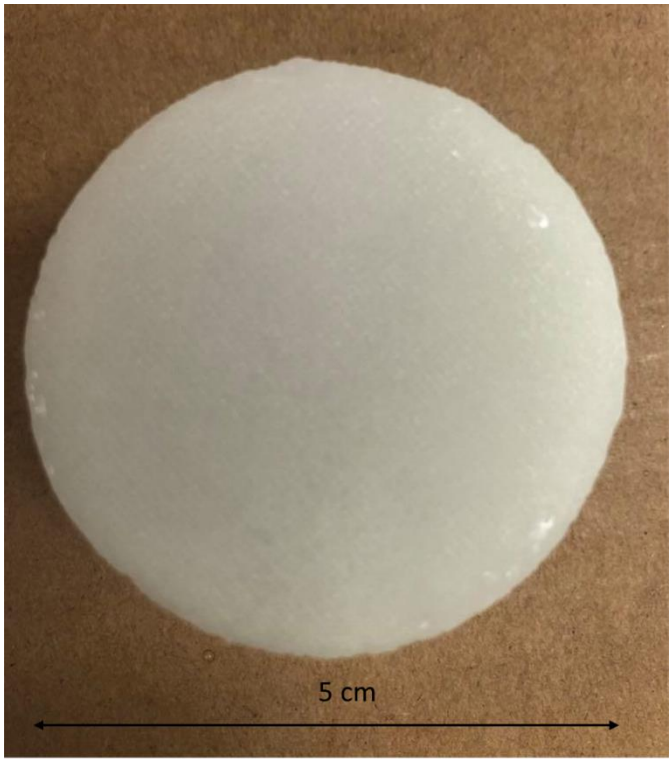

Figure 6-33: Image of a cross-section of the result of the third trial showing no internal cavities.

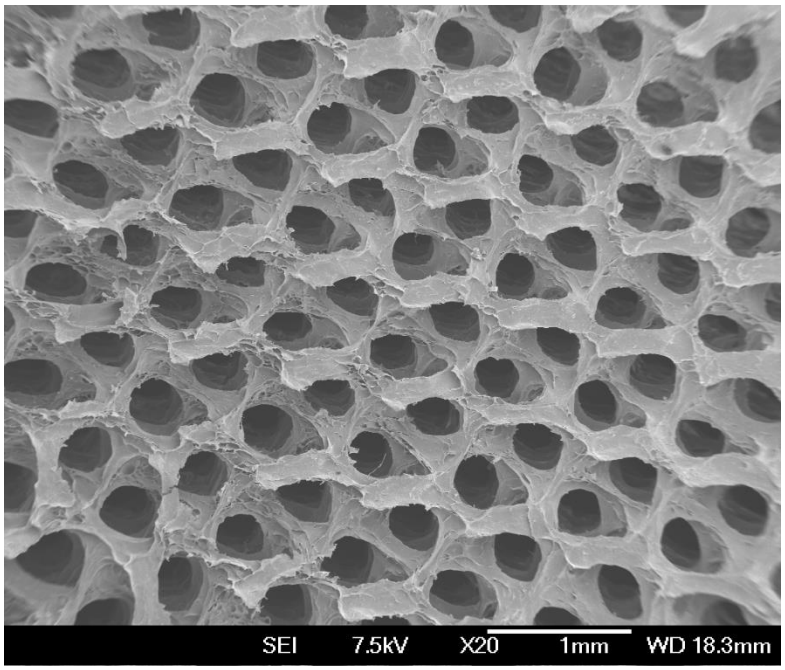

Figure 6-34: SEM image of a freeze dried slice from one of the 5 cm diameter by 6 cm thick, 500 μm Schoen gyroid cellulose hydrogel columns.

Multiple column templates could be filled at once by changing template holders during operation. Two holders were successfully filled, capped, and gelled within five minutes from starting the infusion process. Additional templates could have been filled if available. Based on the volume of solution used to fill two templates (~600 mL), up to 8 or more could be potentially filled in one run. Therefore, in two full runs of this rig, assuming all templates are filled correctly and are undamaged, enough 'plugs' would be created to stack a column 5 cm in diameter by 72 cm bed height. Table 6-8 summarizes the process steps for creating these column pieces and their times. Build wax removal currently is performed in a 1 L beaker on top of a hot plate, which multiple of these could be set up to run in parallel. Therefore, the total time to make a batch of 5 × 5 cm diameter, 6 cm long, 500 μm Schoen gyroid pieces would be around 20 hours.

Table 6-8: Summary of processing steps for creation of a 5 cm diameter by 6 cm long, 500μm Schoen gyroid column piece.

Step	Number per batch	Time per batch hours
Template printing	5	6
Support wax removal	6	5
Cellulose infusion	8	1
Build wax removal	1	8
Total		20

This simple, straightforward process does not require complicated machinery to produce 3D chromatography columns at a pilot scale in under 24 hours from start to finish. With further process optimization, larger columns with smaller hydraulic diameters may be possible. This upscaling method is potentially a pathway for industrial scaling of this technology, testing these columns at pilot scale now possible.

6.3 Conclusion

In this final chapter, 3D-printed chromatography columns' scalability via a templating method using current technology was investigated. Advancement in printing technology has shown a significant improvement in capacity, speed, and resolution over the past five years. The largest single-piece template (5 cm by 20 cm, 300 μm Schoen gyroid) was printed on the ProJet 2500W printer using a patterning technique to avoid the slicer software's file size limitations. A stackable segmentation method was developed to circumvent the need for single piece chromatography columns, allowing columns of the desired length to be created from multiple smaller 'plugs.' Comparing a single piece column's performance to a column made from multiple smaller plugs showed no drop in the performance. Additionally, the best performance of these 3D-printed columns was found at the lowest possible flow rate. This result showed these columns are mass transfer limited because of the large size of the structure's channels.

Although larger plug templates can be printed on commercially available wax printers, post-processing of these templates (support wax removal) limits the size of viable templates and the hydraulic diameters of internal channels. Shrinking based cracking during support wax removal was found to damage templates rendering them unusable for the templating process. The process seems to be diffusion-limited with increases in IPA temperature during elution speeding wax removal. However, templates too large or with small hydraulic diameter channels will crack at low and high temperatures. Support wax removal is the major bottleneck for this technology as printing without support wax is currently not possible.

A cellulose infusion rig was tested using 500 μm hydraulic diameter plug templates. Air pressure was used instead of a pump to force the dissolved cellulose solution through the templates. Multiple 5 cm diameter by 6 cm long, 500 μm Schoen gyroid templates could be filled at once. Upon build wax removal, cellulose hydrogel columns were found to have the template's desired internal channels. These larger hydrogel pieces mark a 1500% increase in the size of a single piece of 3D-printed hydrogel column. The stacking of these column pieces will allow for creating a 5 cm diameter pilot-scale column of any desired length. The total processing time for up to 5 of these parts is 20 hours.

7 Conclusion and recommendations for future work

7.1 Conclusions

The work present in this thesis displays how 3D-printed chromatography columns can be used for the capture step in the downstream processing of viruses. Cellulose hydrogels were formed into monolithic structures with custom-designed internal channels by a negative templating method. Three different functional ligands (DEAE, Q, and HA) were attached to the cellulose hydrogel by covalent or hydrogen bonds. These ligands were then used to bind and elute target viruses to separate them from contaminates found in their feed streams. Upscaling of the columns was achieved with currently available wax printing technology.

In chapter 4, the cellulose hydrogel was investigated for use as the 3D-printed chromatography columns' stationary phase. The hydrogel pores were large enough to allow diffusion of virus-like particles to an average depth of 10 μm, 500% deeper than traditional media. A calcium phosphate mineral was mineralized into the pores of the cellulose hydrogel. This ligand was shown to have multimodal functionality with both cation exchange and metal affinity binding sites. Although not pure or highly crystalline HA, the mineral could still bind and elute various proteins. The anion exchange functionalities, Q and DEAE, were optimized for high protein static binding capacities and ligand densities comparable to current packed bed media.

Chromatography-based purification of viruses from both clarified and unclarified feed streams was examined in chapter 5. Purification of adenovirus and lentivirus from clarified lysate was shown to have comparable recoveries to packed bed chromatography. However, load and elution flow rates needed to be minimal to maximize recovery. Both the HA and DEAE ligands had similar capacities before DEAE ligand optimization. AAV serotype 9 was purified using HA (bind and elute) and Q (flow-through) style chromatography. Although possible, recoveries and capacities were low compared to the state-of-the-art affinity ligands now used for AAV. M13 bacteriophage was used as a model virus for comparison to an expanded bed purification process. Q functionalized 3D-printed chromatography columns were shown to be as effective as expanded bed chromatography with significant advantages

in processing time and simplicity in use. Varying flow rates at different steps during chromatography allowed for an optimized purification that was 300% faster than a similar expanded bed operation.

The final experimental chapter investigated the potential for upscaling this technology from lab to preparative/pilot scale. Using current wax 3D printing templates as large as 5 cm in diameter by 20 cm long, 300 μm Schoen gyroid could be made. However, support wax removal from larger templates and smaller hydraulic diameters proved to be a limiting step for upscaling—issues including time required for complete removal and template cracking limited useable templates. A segmentation and stacking method were used to circumvent the need for single-piece columns with no performance drawback shown in small-scale testing. 500 μm Schoen gyroid, 5 cm diameter by 6 cm long templates were printed, had their support wax removed, and were turned into cellulose structures using newly designed equipment. This method produced a single-piece of 3D-printed hydrogel column, which is a 1500% size increase.

Overall, this work has shown 3D-printed chromatography columns to be a potential alternative to expanded bed chromatography to directly purify viruses from cell culture. High capacity anion exchange functionalities combined with solid tolerant 3D-printed chromatography columns can operate similarly to expanded bed chromatography without complications arising from fluidized beds. For this technology to be adopted by the industry, it will require upscaling, which has been shown in a limited capacity is currently possible. Advancements in printing and post-processing technology will allow 3D-printed columns to move from lab scale to pilot scale to test industrial-scale feed streams.

7.2 Recommendations for future work

From the work completed in this thesis, the following recommendations are made for the future development of 3D-printed chromatography columns.

1. HA optimization

Although HA could be used for the purification of viruses, poor capacity limited its usefulness. Chapter 4 showed the mineral was not pure HA and suggested a possible reaction scheme for the conversion of OCP into HA which should be explored. Additionally, improvements to the mineral's crystallinity by may also improve capacity and selectivity.

2. Testing of purification from cell lysates

Purification of M13 bacteriophage from cell culture was possible, however, cell cultures have significantly less contaminates in them than cell lysates. The majority of viruses used in gene therapies require cell lysis to release the viral particle into solution from inside the cell. Therefore, purification from these more contaminated feed streams (such as crude adenovirus lysate) needs to be shown if this technology is to replace expanded bed chromatography. Moreover, a variety of different cell lysates should be tested to show this is indeed a platform-style technology.

3. Affinity ligands

Purification of viruses and other proteins by affinity ligands is extremely effective as selectivity binding them away from contaminates. Incorporation of these affinity ligands into 3D-printed columns should allow for direct purification from cell culture or lysates with high capacity, recovery and purity. A starting point for this would be an investigation into camelid anti-body fragments used for AAV purification. Development of chemistry to bind these ligands onto the cellulose or agarose stationary phase would be required.

4. Upscale testing

Chapter 6 produced a method to create a pilot-scale sized column with 500 μm hydraulic diameter channels. A full pilot-scale column using these column segments should be tested

with tracers to determine performance. A method will also need to be developed to functionalize larger columns before they can be used to purify viruses from a model feedstream. A cylindrical flow reactor similar to the setup used by the first support wax removal rig could help evenly mix reaction chemicals through long pieces of column.

5. 3D printing process

The post-processing of templates constrains the current templating process for the creation of these columns. A full study into the wax materials used for build and support wax and how the dissolution of support wax occurs may resolve this issue. Development of new post-processing techniques or an alternative solvent may also be required. Identification of wax material composition followed by dissolution studies would help better understand the support wax removal process.

6. Column structure

Lastly, in this work, only one channel shape based on the TPMS structure, the Schoen gyroid, was used. An investigation into varying channel shape and column voidage may influence performance and increase available surface area for binding. Tracer peak analysis studies alongside protein DBC testing using a range of these structures could be used to determine differences in performance.

References

1. Ginn, Samantha L., Ian E. Alexander, Michael L. Edelstein, Mohammad R. Abedi, and Jo Wixon, *Gene therapy clinical trials worldwide to 2012 - an update.* The Journal of Gene Medicine, 2013. **15**(2): p. 65-77.
2. FDA, *BLA Approval*, Inc. Spark Therapeutics, Editor. 2017, U.S. Food and Drug Administration.
3. Ylä-Herttuala, Seppo, *Endgame: glybera finally recommended for approval as the first gene therapy drug in the European union.* Molecular Therapy, 2012. **20**(10): p. 1831-1832.
4. Ginn, Samantha L, Anais K Amaya, Ian E Alexander, Michael Edelstein, and Mohammad R Abedi, *Gene therapy clinical trials worldwide to 2017: An update.* The journal of gene medicine, 2018. **20**(5).
5. Cornell, B. *Overveiw of Gene therapy*. 2016 14/12/2020]; Available from: https://ib.bioninja.com.au/standard-level/topic-3-genetics/35-genetic-modification-and/gene-therapy.html.
6. Terova, Orjana, Stephen Soltys, Pim Hermans, Jessica De Rooij, and Frank Detmers, *Overcoming Downstream Purification Challenges for Viral Vector Manufacturing: Enabling Advancement of Gene Therapies in the Clinic.* Cell and Gene Therapy Insights, 2018. **4**(2): p. 101-111.
7. Fernandes, Cláudia S. M., Bianca Gonçalves, Margarida Sousa, Duarte L. Martins, Telma Barroso, Ana Sofia Pina, Cristina Peixoto, Ana Aguiar-Ricardo, and A. Cecília A. Roque, *Biobased Monoliths for Adenovirus Purification.* ACS Applied Materials & Interfaces, 2015. **7**(12): p. 6605-6612.
8. Nestola, Piergiuseppe, Louis Villain, Cristina Peixoto, Duarte L. Martins, Paula M. Alves, Manuel J. T. Carrondo, and José P. B. Mota, *Impact of grafting on the design of new membrane adsorbers for adenovirus purification.* Journal of Biotechnology, 2014. **181**: p. 1-11.
9. Kawka, Karina, Pedram Madadkar, Umatheny Umatheva, Shabnam Shoaebargh, Maria Fe C. Medina, Brian D. Lichty, Raja Ghosh, and David R. Latulippe, *Purification of therapeutic adenoviruses using laterally-fed membrane chromatography.* Journal of Membrane Science, 2019. **579**: p. 351-358.
10. Ongkudon, Clarence M, Tamar Kansil, and Charlotte Wong, *Challenges and strategies in the preparation of large-volume polymer-based monolithic chromatography adsorbents.* Journal of separation science, 2014. **37**(5): p. 455-464.
11. Adams, Benjamin, Hanne Bak, and Andrew D. Tustian, *Moving from the bench towards a large scale, industrial platform process for adeno-associated viral vector purification.* Biotechnology and Bioengineering, 2020. **117**(10): p. 3199-3211.
12. Chase, Howard A., *Purification of proteins by adsorption chromatography in expanded beds.* Trends in Biotechnology, 1994. **12**(8): p. 296-303.
13. Fernandez-Lahore, HM, R Kleef, M-R Kula, and J Thömmes, *The influence of complex biological feedstock on the fluidization and bed stability in expanded bed adsorption.* Biotechnology and bioengineering, 1999. **64**(4): p. 484-496.
14. Jin, Zuwei, *Expanded bed Absorption-Challenges and advances in column and process design.* Pharmaceutical engineering, 2015.
15. Gordon, Anne, *Development, Functionalisation, and Characterisation of Triply Periodic Minimum Surface Hydrogels for Solid-Tolerant Chromatography*, in *PhD thesis*. 2019, University of Canterbury
16. Fee, Conan, *3D-printed porous bed structures.* Current Opinion in Chemical Engineering, 2017. **18**: p. 10-15.
17. van Deutekom, Judith C. T. and Gert-Jan B. van Ommen, *Advances in Duchenne muscular dystrophy gene therapy.* Nature Reviews Genetics, 2003. **4**(10): p. 774-783.
18. Bowles, Dawn E., Scott W. J. McPhee, Chengwen Li, Steven J. Gray, Jade J. Samulski, Angelique S. Camp, Juan Li, Bing Wang, Paul E. Monahan, Joseph E. Rabinowitz, Joshua C. Grieger, Lakshmanan Govindasamy, Mavis Agbandje-McKenna, Xiao Xiao, and R. Jude Samulski, *Phase 1 Gene Therapy for Duchenne Muscular Dystrophy Using a Translational Optimized AAV Vector.* Molecular Therapy, 2012. **20**(2): p. 443-455.
19. Crudele, Julie M and Jeffrey S Chamberlain, *AAV-based gene therapies for the muscular dystrophies.* Human Molecular Genetics, 2019. **28**(R1): p. R102-R107.
20. Kaiser, Jocelyn, *Seeking the Cause of Induced Leukemias in X-SCID Trial.* Science, 2003. **299**(5606): p. 495-495.
21. Bender, Eric, *Regulating a revolution - Health authorities wade into the flood of gene therapies.* Nature Outlook: Gene therapy, 2018. **564**: p. 20-22.

22. Hu, Yu-Chen, *Gene Therapy for Cartilage and Bone Tissue Engineering*. 2014. p. 17-31.
23. Douglas, Joanne T., *Adenoviral vectors for gene therapy.* Molecular Biotechnology, 2007. **36**(1): p. 71-80.
24. Ghosh, Siddhartha S., P. Gopinath, and A. Ramesh, *Adenoviral Vectors: A Promising Tool for Gene Therapy.* Applied Biochemistry and Biotechnology, 2006. **133**(1): p. 9-30.
25. Turnbull, J., B. Wright, N. K. Green, R. Tarrant, I. Roberts, O. Hardick, and D. G. Bracewell, *Adenovirus 5 recovery using nanofiber ion-exchange adsorbents.* Biotechnol Bioeng, 2019. **116**(7): p. 1698-1709.
26. Huaben, Bo, Chen Jun, Liang Ting, Li Senhai, Shao Hongwei, and Huang Shulin, *Chromatographic purification of adenoviral vectors on anion-exchange resins.* European Journal of Pharmaceutical Sciences, 2015. **67**: p. 119-125.
27. Konz, John O., Rebecca C. Livingood, Andrew J. Bett, Aaron R. Goerke, Michael E. Laska, and Sangeetha L. Sagar, *Serotype specificity of adenovirus purification using anion-exchange chromatography.* Human Gene Therapy, 2005. **16**(11): p. 1346-1353.
28. Hassou, Najwa, Rihab Bouseettine, Nabil Abouchoaib, and Moulay Mustapha Ennaji, *Chapter 39 - Enteric Adenoviruses: Emerging of a Public Health Threat*, in *Emerging and Reemerging Viral Pathogens*, Moulay Mustapha Ennaji, Editor. 2020, Academic Press. p. 879-905.
29. Harui, Airi, Shinobu Suzuki, Stefan Kochanek, and Kohnosuke Mitani, *Frequency and stability of chromosomal integration of adenovirus vectors.* Journal of virology, 1999. **73**(7): p. 6141-6146.
30. Tollefson, A E, A Scaria, T W Hermiston, J S Ryerse, L J Wold, and W S Wold, *The adenovirus death protein (E3-11.6K) is required at very late stages of infection for efficient cell lysis and release of adenovirus from infected cells.* Journal of Virology, 1996. **70**(4): p. 2296-2306.
31. Palomino, Maria Angelica, Carmen Larranaga, Eliecer Villagra, Jorge Camacho, and Luis F Avendano, *Adenovirus and respiratory syncytial virus-adenovirus mixed acute lower respiratory infections in Chilean infants.* The Pediatric infectious disease journal, 2004. **23**(4): p. 337-341.
32. Muruve, Daniel A., *The Innate Immune Response to Adenovirus Vectors.* Human Gene Therapy, 2004. **15**(12): p. 1157-1166.
33. James N. Warnock, Claire Daigre, and Mohamed Al-Rubeai *Viral Vectors for Gene Therapy methods and protocols*. Methods in molecular biology. 2011.
34. Thomas, Philip and Trevor G. Smart, *HEK293 cell line: A vehicle for the expression of recombinant proteins.* Journal of Pharmacological and Toxicological Methods, 2005. **51**(3): p. 187-200.
35. Griesenbach, Uta, Duncan M Geddes, and EWFW Alton, *Gene therapy progress and prospects: cystic fibrosis.* Gene therapy, 2006. **13**(14): p. 1061.
36. Chamberlain, Joel R. and Jeffrey S. Chamberlain, *Progress toward Gene Therapy for Duchenne Muscular Dystrophy.* Molecular Therapy, 2017. **25**(5): p. 1125-1131.
37. Vecil, Giacomo G. and Frederick F. Lang, *Clinical Trials of Adenoviruses in Brain Tumors: A Review of Ad-p53 and Oncolytic Adenoviruses.* Journal of Neuro-Oncology, 2003. **65**(3): p. 237-246.
38. Khalighinejad, Nima, Hesammodin Hariri, Omid Behnamfar, Arash Yousefi, and Amir Momeni, *Adenoviral gene therapy in gastric cancer: a review.* World journal of gastroenterology, 2008. **14**(2): p. 180-184.
39. Borrás, Teresa, *The Pathway From Genes to Gene Therapy in Glaucoma: A Review of Possibilities for Using Genes as Glaucoma Drugs.* Asia-Pacific journal of ophthalmology (Philadelphia, Pa.), 2017. **6**(1): p. 80-93.
40. Freytag, Svend O., Benjamin Movsas, and Hans Stricker, *514. Clinical Trials of Oncolytic Adenovirus-Mediated Gene Therapy.* Molecular Therapy, 2016. **24**: p. S205.
41. Rosewell Shaw, Amanda and Masataka Suzuki, *Recent advances in oncolytic adenovirus therapies for cancer.* Current opinion in virology, 2016. **21**: p. 9-15.
42. Roth, Jack A., *Adenovirus p53 gene therapy.* Expert Opinion on Biological Therapy, 2006. **6**(1): p. 55-61.
43. Wu, Shipo, Gongxun Zhong, Jun Zhang, Lei Shuai, Zhe Zhang, Zhiyuan Wen, Busen Wang, Zhenghao Zhao, Xiaohong Song, Yi Chen, Renqiang Liu, Ling Fu, Jinlong Zhang, Qiang Guo, Chong Wang, Yilong Yang, Ting Fang, Peng Lv, Jinliang Wang, Junjie Xu, Jianmin Li, Changming Yu, Lihua Hou, Zhigao Bu, and Wei Chen, *A single dose of an adenovirus-vectored vaccine provides protection against SARS-CoV-2 challenge.* Nature Communications, 2020. **11**(1): p. 4081.
44. Gagnon, Pete, *The Emerging Generation of chromatography tools for virus purification.* BioProcess International, 2008(October): p. 24-30.
45. Becerra, S Patricia, James A Rose, Medora Hardy, Bahige M Baroudy, and Carl W Anderson, *Direct mapping of adeno-associated virus capsid proteins B and C: a possible ACG initiation codon.* Proceedings of the National Academy of Sciences, 1985. **82**(23): p. 7919-7923.

46. Wu, Z., A. Asokan, and R. J. Samulski, *Adeno-associated virus serotypes: vector toolkit for human gene therapy.* Mol Ther, 2006. **14**(3): p. 316-27.
47. Brument, N., R. Morenweiser, V. Blouin, E. Toublanc, I. Raimbaud, Y. Cherel, S. Folliot, F. Gaden, P. Boulanger, G. Kroner-Lux, P. Moullier, F. Rolling, and A. Salvetti, *A versatile and scalable two-step ion-exchange chromatography process for the purification of recombinant adeno-associated virus serotypes-2 and -5.* Mol Ther, 2002. **6**(5): p. 678-86.
48. Urabe, Masashi, Ke-Qin Xin, Yoko Obara, Takayo Nakakura, Hiroaki Mizukami, Akihiro Kume, Kenji Okuda, and Keiya Ozawa, *Removal of Empty Capsids from Type 1 Adeno-Associated Virus Vector Stocks by Anion-Exchange Chromatography Potentiates Transgene Expression.* Molecular Therapy, 2006. **13**(4): p. 823-828.
49. Qu, G., J. Bahr-Davidson, J. Prado, A. Tai, F. Cataniag, J. McDonnell, J. Zhou, B. Hauck, J. Luna, J. M. Sommer, P. Smith, S. Zhou, P. Colosi, K. A. High, G. F. Pierce, and J. F. Wright, *Separation of adeno-associated virus type 2 empty particles from genome containing vectors by anion-exchange column chromatography.* J Virol Methods, 2007. **140**(1-2): p. 183-92.
50. Tomono, T., Y. Hirai, H. Okada, Y. Miyagawa, K. Adachi, S. Sakamoto, Y. Kawano, H. Chono, J. Mineno, A. Ishii, T. Shimada, M. Onodera, A. Tamaoka, and T. Okada, *Highly Efficient Ultracentrifugation-free Chromatographic Purification of Recombinant AAV Serotype 9.* Mol Ther Methods Clin Dev, 2018. **11**: p. 180-190.
51. Snyder, Richard O. and Philippe Moullier, *Adeno-associated virus: methods and protocols*. Vol. 807.;807;. 2011, New York: Humana Press.
52. Zaiss, Anne K., Matthew J. Cotter, Lindsay R. White, Sharon A. Clark, Norman C. W. Wong, V. Michael Holers, Jeffrey S. Bartlett, and Daniel A. Muruve, *Complement Is an Essential Component of the Immune Response to Adeno-Associated Virus Vectors.* Journal of Virology, 2008. **82**(6): p. 2727-2740.
53. Berns, Kenneth I. and R. Michael Linden, *The cryptic life style of adenoassociated virus.* BioEssays, 1995. **17**(3): p. 237-245.
54. Berns, K. I. and C. Giraud, *Biology of Adeno-associated Virus*, in *Adeno-Associated Virus (AAV) Vectors in Gene Therapy*, Kenneth I. Berns and Catherine Giraud, Editors. 1996, Springer Berlin Heidelberg: Berlin, Heidelberg. p. 1-23.
55. Leonard, C. J. and Kenneth I. Berns, *Adeno-associated Virus Type 2: A Latent Life Cycle*, in *Progress in Nucleic Acid Research and Molecular Biology*, Waldo E. Cohn and Kivie Moldave, Editors. 1994, Academic Press. p. 29-52.
56. Morrison, C., *$1-million price tag set for Glybera gene therapy.* Nat Biotechnol, 2015. **33**(3): p. 217-8.
57. Darrow, Jonathan J., *Luxturna: FDA documents reveal the value of a costly gene therapy.* Drug Discovery Today, 2019. **24**(4): p. 949-954.
58. Wolfgang, Walther and Stein Ulrike, *Viral Vectors for Gene Transfer.* Drugs, 2000. **60**(2): p. 249-271.
59. Yi, Youngsuk, Moon Jong Noh, and Kwan Hee Lee, *Current Advances in Retroviral Gene Therapy.* Current Gene Therapy, 2011. **11**: p. 218-228.
60. Balaggan, K. S. and R. R. Ali, *Ocular gene delivery using lentiviral vectors.* Gene Therapy, 2012. **19**(2): p. 145-153.
61. Goldman, Mitchell J, Po-Shun Lee, Joo-Sung Yang, and James M Wilson, *Lentiviral vectors for gene therapy of cystic fibrosis.* Human gene therapy, 1997. **8**(18): p. 2261-2268.
62. Dullaers, Melissa, Sonja Van Meirvenne, Carlo Heirman, L Straetman, Aude Bonehill, JL Aerts, Kris Thielemans, and Karine Breckpot, *Induction of effective therapeutic antitumor immunity by direct in vivo administration of lentiviral vectors.* Gene therapy, 2006. **13**(7): p. 630-640.
63. Holic, Nathalie, Ababacar K. Seye, Saliha Majdoul, Samia Martin, Otto W. Merten, Anne Galy, and David Fenard, *Influence of Mildly Acidic pH Conditions on the Production of Lentiviral and Retroviral Vectors.* Human Gene Therapy Clinical Development, 2014. **25**(3): p. 178-185.
64. de las Mercedes Segura, María, Amine Kamen, and Alain Garnier, *Downstream processing of oncoretroviral and lentiviral gene therapy vectors.* Biotechnology Advances, 2006. **24**(3): p. 321-337.
65. Tiscornia, G., O. Singer, and I. M. Verma, *Production and purification of lentiviral vectors.* Nat Protoc, 2006. **1**(1): p. 241-5.
66. McCarron, Alexandra, Martin Donnelley, Chantelle McIntyre, and David Parsons, *Challenges of up-scaling lentivirus production and processing.* Journal of biotechnology, 2016. **240**: p. 23-30.
67. Seitz, Harald and Christoph Weigel, *Bacteriophage replication modules.* FEMS Microbiology Reviews, 2006. **30**(3): p. 321-381.
68. Campbell, Allen, *The future of bacteriophage biology.* Nature Reviews.Genetics, 2003. **4**(6): p. 471-477.

69. Ackermann, H. W., *Bacteriophage observations and evolution.* Research in Microbiology, 2003. **154**(4): p. 245-251.
70. Yang, Sung Ho, Woo-Jae Chung, Sean McFarland, and Seung-Wuk Lee, *Assembly of Bacteriophage into Functional Materials.* The Chemical Record, 2013. **13**(1): p. 43-59.
71. Olson, Norman H., Mari Gingery, Frederick A. Eiserling, and Timothy S. Baker, *The Structure of Isometric Capsids of Bacteriophage T4.* Virology, 2001. **279**(2): p. 385-391.
72. Hu, Guo-Bin, Hui Wei, William J. Rice, David L. Stokes, and Paul Gottlieb, *Electron cryo-tomographic structure of cystovirus ϕ12.* Virology, 2008. **372**(1): p. 1-9.
73. Golkar, Zhabiz, Omar Bagasra, and Donald Gene Pace, *Bacteriophage therapy: a potential solution for the antibiotic resistance crisis.* The Journal of Infection in Developing Countries, 2014. **8**(02).
74. Yamamoto, Keith R., Bruce M. Alberts, Rolf Benzinger, Larry Lawhorne, and Gerda Treiber, *Rapid bacteriophage sedimentation in the presence of polyethylene glycol and its application to large-scale virus purification.* Virology, 1970. **40**(3): p. 734-744.
75. González-Mora, Alejandro, Federico Ruiz-Ruiz, Jorge Benavides, Richard C. Willson, and Marco Rito-Palomares, *Recovery and primary purification of bacteriophage M13 using aqueous two-phase systems.* Journal of Chemical Technology & Biotechnology, 2017. **92**(11): p. 2808-2816.
76. Monjezi, R., B. T. Tey, C. C. Sieo, and W. S. Tan, *Purification of bacteriophage M13 by anion exchange chromatography.* J Chromatogr B Analyt Technol Biomed Life Sci, 2010. **878**(21): p. 1855-9.
77. Warner, C. M., N. Barker, S. W. Lee, and E. J. Perkins, *M13 bacteriophage production for large-scale applications.* Bioprocess Biosyst Eng, 2014. **37**(10): p. 2067-72.
78. Yumi Kanegae, Miho Makimura, and Izumu Saito, *A simple and efficent method for purification of infectious recombinant adenovirus.* Japanese Journal of Medical Science and BiologyJapanese Journal of Medical Science and Biology, 1994. **47**: p. 157-166.
79. Gagnon, Pete, *Downstream Industrial Biotechnology : Recovery and Purification.* 2013: p. 415-435.
80. Kovesdi, Imre and Susan J. Hedley, *Adenoviral Producer Cells.* Viruses, 2010. **2**(8): p. 1681-1703.
81. Clément, Nathalie and Joshua C. Grieger, *Manufacturing of recombinant adeno-associated viral vectors for clinical trials.* Molecular Therapy - Methods & Clinical Development, 2016. **3**: p. 16002.
82. Miller, A. Dusty and Carol Buttimore, *Redesign of Retrovirus Packaging Cell Lines To Avoid Recombination leading to helper virus production.* Molecular and Cellular Biology, 1986. **6**(8): p. 2895-2902.
83. Kamen, A. and O. Henry, *Development and optimization of an adenovirus production process.* J Gene Med, 2004. **6 Suppl 1**: p. S184-92.
84. Morenweiser, R., *Downstream processing of viral vectors and vaccines.* Gene Therapy, 2005. **12**(1): p. S103-S110.
85. Tseng, Y. F., T. C. Weng, C. C. Lai, P. L. Chen, M. S. Lee, and A. Y. Hu, *A fast and efficient purification platform for cell-based influenza viruses by flow-through chromatography.* Vaccine, 2018. **36**(22): p. 3146-3152.
86. Revel, J. P., Pamela Hoch, and D. Ho, *Adhesion of culture cells to their substratum.* Experimental Cell Research, 1974. **84**(1): p. 207-218.
87. Laposova, Katarina, Ingrid Oveckova, and Jana Tomaskova, *A simple method for isolation of cell-associated viral particles from cell culture.* Journal of Virological Methods, 2017. **249**: p. 194-196.
88. Geraerts, Martine, Martine Michiels, Veerle Baekelandt, Zeger Debyser, and Rik Gijsbers, *Upscaling of lentiviral vector production by tangential flow filtration.* The Journal of Gene Medicine, 2005. **7**(10): p. 1299-1310.
89. D'hondt, E, Judit Martin-Juarez, S Bolado, J Kasperoviciene, J Koreiviene, S Sulcius, K Elst, and L Bastiaens, *Cell disruption technologies*, in *Microalgae-based biofuels and bioproducts*. 2017, Elsevier. p. 133-154.
90. Lin, Dong-Qiang, Jian-Nan Dong, and Shan-Jing Yao, *Target Control of Cell Disruption To Minimize the Biomass Electrostatic Adhesion during Anion-Exchange Expanded Bed Adsorption.* Biotechnol, 2007. **23**: p. 162-167.
91. Nestola, Piergiuseppe, Cristina Peixoto, Ricardo R. J. S Silva, Paula M. Alves, Jose P. B. Mota, and Manuel J. T. Carrondo, *Improved Virus Purification Processes for Vaccines and Gene Therapy.* Biotechnology and Bioengineering, 2015. **112**(5).
92. Moleirinho, Mafalda G., Ricardo J. S. Silva, Paula M. Alves, Manuel J. T. Carrondo, and Cristina Peixoto, *Current challenges in biotherapeutic particles manufacturing.* Expert Opinion on Biological Therapy, 2020. **20**(5): p. 451-465.

93. Mafalda, G. Moleirinho, Rosa Sara, J. T. Carrondo Manuel, J. S. Silva Ricardo, Hagner-McWhirter Åsa, Ahlén Gustaf, Lundgren Mats, M. Alves Paula, and Peixoto Cristina, *Clinical-Grade Oncolytic Adenovirus Purification Using Polysorbate 20 as an Alternative for Cell Lysis.* Current Gene Therapy, 2018. **18**(6): p. 366-374.
94. Bracewell, D.G., M. Boychyn, H. Baldascini, S.A. Storey, M. Bulmer, J. More, and M. Hoare, *Impact of clarification strategy on chromatographic separations: Pre-processing of cell homogenates.* Biotechnology and Bioengineering, 2008. **100**(5): p. 941-949.
95. Shabram, Paul, Gary Vellekamp, Qian Ruan, and Carl Scandella, *Adenoviral vectors for gene therapy*. second ed. 2002.
96. Reis, Robert van and Andrew Zydney, *Membrane separations in biotechnology.* Biotechnology, 2001. **12**: p. 208-211.
97. Cherradi, Youness, Sarah Le Merdy, Li-Jun Sim, Takao Ito, Priyabrata Pattnaik, and Josselyn Haas, *Filter-based clarification of viral vaccines and vectors.* Bioprocess Int, 2018. **16**(4): p. 48-53.
98. Yigzaw, Yinges, Robert Piper, Minh Tran, and Abhinav A Shukla, *Exploitation of the adsorptive properties of depth filters for host cell protein removal during monoclonal antibody purification.* Biotechnology progress, 2006. **22**(1): p. 288-296.
99. Iammarino, M, J Nti-Gyabaah, M Chandler, D Roush, and K Goklen, *Impact of cell density and viability on primary clarification of mammalian cell broth: An analysis using disc-stack centrifugation and charged depth filtration.* BioProcess International, 2007. **5**(10): p. 38.
100. Reeves, L and Kenneth Cornetta, *Clinical retroviral vector production: step filtration using clinically approved filters improves titers.* Gene therapy, 2000. **7**(23): p. 1993-1998.
101. Gousseniov, Elina, Willem Kools, and Priyabratta Pattnaik. *Nucleic Acid impurity reduction in viral vaccine manufacturing*. 2014 02/20/2018].
102. *FDA Briefing Document: vaccines and related biological products*, in *FDA Advisory Committee*. 2012.
103. Oxford Biomedica plc, *SecNunc™ for AAVs, lentiviral vectors and adenovirus (Application Note)*. 2019. p. 1-2.
104. Wickramasinghe, S. R., B. Kalbfuß, A. Zimmermann, V. Thom, and U. Reichl, *Tangential flow microfiltration and ultrafiltration for human influenza A virus concentration and purification.* Biotechnology and Bioengineering, 2005. **92**(2): p. 199-208.
105. Ismail, Baraem and S Suzanne Nielsen, *Basic principles of chromatography*, in *Food analysis*. 2010, Springer. p. 473-498.
106. Thermoscientific, *POROS™ Anion Exchange Resins: XQ*, in *Thermofisher*. 2018.
107. Brument, Nicole, Robert Morenweiser, Véronique Blouin, Estelle Toublanc, Isabelle Raimbaud, Yan Chérel, Sébastien Folliot, Florence Gaden, Pierre Boulanger, Gabrielle Kroner-Lux, Philippe Moullier, Fabienne Rolling, and Anna Salvetti, *A Versatile and Scalable Two-Step Ion-Exchange Chromatography Process for the Purification of Recombinant Adeno-associated Virus Serotypes-2 and -5.* Molecular Therapy, 2002. **6**(5): p. 678-686.
108. Yamada, Kaoru, Douglas M. McCarty, Victoria J. Madden, and Christopher E. Walsh, *Lentivirus Vector Purification Using Anion exchange HPLC leads to improved gene transfer.* BioTechniques, 2003. **34**: p. 1074-1080.
109. Burova, E. and E. Ioffe, *Chromatographic purification of recombinant adenoviral and adeno-associated viral vectors: methods and implications.* Gene Therapy, 2005. **12**(S1): p. 55-517.
110. Gao, Guangping, Guang Qu, Michael S. Burnham, James Huang, Narendra Chirmule, Bindu Joshi, Qian-Chun Yu, Jonathan A. Marsh, Christina M. Conceicao, and and James M. Wilson, *Purification of Recombinant Adeno-Associated Virus Vectors by Column Chromatography and Its Performance in Vivo.* Human Gene Therapy, 2004. **11**(15): p. 2079-2091.
111. Qu, Guang, Jennifer Bahr-Davidson, Joseph Prado, Alex Tai, Floro Cataniag, Jennifer McDonnell, Jingmin Zhou, Bernd Hauck, Jac Luna, Jurg M. Sommer, Peter Smith, Shangzhen Zhou, Peter Colosi, Katherine A. High, Glenn F. Pierce, and J. Fraser Wright, *Separation of adeno-associated virus type 2 empty particles from genome containing vectors by anion-exchange column chromatography.* Journal of Virological Methods, 2007. **140**(1-2): p. 183-192.
112. Wang, Chunlei, Sri Hari Raju Mulagapati, Zhongying Chen, Jing Du, Xiaohui Zhao, Guoling Xi, Liyan Chen, Thomas Linke, Cuihua Gao, and Albert E Schmelzer, *Developing an Anion Exchange Chromatography Assay for Determining Empty and Full Capsid Contents in AAV6. 2.* Molecular Therapy-Methods & Clinical Development, 2019. **15**: p. 257-263.

113. Gagnon, Pete, Richard Richieri, Simin Zaidi, and Francis Aolin. *A Comparison of Microparticulate, Membrane, and Monolithic Anion Exchangers for Polishing Applications in the Purification of Monoclonal Antibodies.* in *BioProcess International Conference and Exposition*. 2007. Boston.
114. Scherr, M., K. Battmer, M. Eder, S. Schüle, H. Hohenberg, A. Ganser, M. Grez, and U. Blömer, *Efficient gene transfer into the CNS by lentiviral vectors purified by anion exchange chromatography.* Gene Therapy, 2002. **9**(24): p. 1708-1714.
115. Kutner, Robert H., Xian-yang Zhang, and Jakob Reiser, *Production, concentration and titration of pseudotyped HIV-1-based lentiviral vectors.* Nature Protocols, 2009. **4**(4): p. 495-505.
116. Davidoff, Andrew M., Catherine Y. C. Ng, Susan Sleep, John Gray, Selina Azam, Yuan Zhao, Jenny H. McIntosh, Morteza Karimipoor, and Amit C. Nathwani, *Purification of recombinant adeno-associated virus type 8 vectors by ion exchange chromatography generates clinical grade vector stock.* Journal of Virological Methods, 2004. **121**(2): p. 209-215.
117. Zolotukhin, Sergei, Mark Potter, Irene Zolotukhin, Yoshihisa Sakai, Scott Loiler, Thomas J. Fraites, Vince A. Chiodo, Tina Phillipsberg, Nicholas Muzyczka, William W. Hauswirth, Terance R. Flotte, Barry J. Byrne, and Richard O. Snyder, *Production and purification of serotype 1, 2, and 5 recombinant adeno-associated viral vectors.* Methods, 2002. **28**(2): p. 158-167.
118. Grieger, J. C., S. M. Soltys, and R. J. Samulski, *Production of Recombinant Adeno-associated Virus Vectors Using Suspension HEK293 Cells and Continuous Harvest of Vector From the Culture Media for GMP FIX and FLT1 Clinical Vector.* Mol Ther, 2016. **24**(2): p. 287-297.
119. Debelak, D., J. Fisher, S. Iuliano, D. Sesholtz, D. L. Sloane, and E. M. Atkinson, *Cation-exchange high-performance liquid chromatography of recombinant adeno-associated virus type 2.* Journal of Chromatography B: Biomedical Sciences and Applications, 2000. **740**(2): p. 195-202.
120. Eglon, Marc N., Aoife M. Duffy, Timothy O'Brien, and Padraig M. Strappe, *Purification of adenoviral vectors by combined anion exchange and gel filtration chromatography.* The Journal of Gene Medicine, 2009. **11**(11): p. 978-989.
121. Hagner-McWhirter, Åsa, Gustaf Ahlén, Magnus Bergman, Mats Lundgren, Åsa Lagerlöf, Anna Åkerblom, Elisabeth Wallby, Sravani Musunuri, Maria Soultsioti, and Pelle Sjöholm, *A scalable adenovirus production process, from cell culture to purified bulk.* 2018.
122. Nestola, Piergiuseppe, Ricardo J. S. Silva, Cristina Peixoto, Paula M. Alves, Manuel J. T. Carrondo, and José P. B. Mota, *Adenovirus purification by two-column, size-exclusion, simulated countercurrent chromatography.* J Chromatogr A, 2014. **1347**: p. 111-21.
123. Nestola, Piergiuseppe, Ricardo J. S. Silva, Cristina Peixoto, Paula M. Alves, Manuel J. T. Carrondo, and José P. B. Mota, *Robust design of adenovirus purification by two-column, simulated moving-bed, size-exclusion chromatography.* Journal of Biotechnology, 2015. **213**: p. 109-119.
124. Segura, M. M., M. Mangion, B. Gaillet, and A. Garnier, *New developments in lentiviral vector design, production and purification.* Expert Opin Biol Ther, 2013. **13**(7): p. 987-1011.
125. Burova, E. and E. Ioffe, *Chromatographic purification of recombinant adenoviral and adeno-associated viral vectors: methods and implications.* Gene Ther, 2005. **12 Suppl 1**: p. S5-17.
126. Potter, M., B. Lins, M. Mietzsch, R. Heilbronn, K. Van Vliet, P. Chipman, M. Agbandje-McKenna, B. D. Cleaver, N. Clement, B. J. Byrne, and S. Zolotukhin, *A simplified purification protocol for recombinant adeno-associated virus vectors.* Mol Ther Methods Clin Dev, 2014. **1**: p. 14034.
127. Segura, María Mercedes, Alain Garnier, Yves Durocher, Helene Coelho, and Amine Kamen, *Production of lentiviral vectors by large-scale transient transfection of suspension cultures and affinity chromatography purification.* Biotechnology and Bioengineering, 2007. **98**(4): p. 789-799.
128. Zhang, Xiao and Jin-Ping Li, *Heparan sulfate proteoglycan in amyloidosis*. Progress in Molecular biology and translational science. Vol. 93. 2010.
129. Nass, Shelley A., Maryellen A. Mattingly, Denise A. Woodcock, Brenda L. Burnham, Jeffrey A. Ardinger, Shayla E. Osmond, Amy M. Frederick, Abraham Scaria, Seng H. Cheng, and Catherine R. O'Riordan, *Universal Method for the Purification of Recombinant AAV Vectors of Differing Serotypes.* Molecular Therapy - Methods & Clinical Development, 2018. **9**: p. 33-46.
130. Terova, Orjana, Shelly Parra, Remko Clasen, Pim Hermans, and S Soltys, *Innovative Downstream Purification Solutions for Viral Vectors: Enabling Platform Approaches to Advance Gene Therapies.* Bioprocess Int, 2016.
131. Smith, James K. S., Vibhu Banala, Mario Mietzsch, Paul Chipman, and Mavis Agbandje-McKenna, *294. Characterizing AAV CaptureSelect Affinity Ligand Interactions.* Molecular Therapy, 2016. **24**: p. S118.
132. Łącki, Karol M. and Frank J. Riske, *Affinity Chromatography: An Enabling Technology for Large-Scale Bioprocessing.* Biotechnology Journal, 2020. **15**(1): p. 1800397.

133. Thermoscientific, *CaptureSelect™ AVB Sepharose HP Leakage ELISA product infomation sheet.* 2019: p. 1-3.
134. Hu, Hui-Ling, Min-Ying Wang, Chiung-Hsuah Chung, and Shing-Yi Suen, *Purification of VP3 protein of infectious bursal disease virus using nickel ion-immobilized regenerated cellulose-based membranes.* J Chromatogr B Analyt Technol Biomed Life Sci, 2006. **840**(2): p. 76-84.
135. Diekmann, Stephan, Grit Siegmund, Anja Roecker, and Dieter O. Klemm, *Regioselective nitrilotriacetic acid cellulose nickel complexes for immobilisation of His6-tag proteins.* Cellulose, 2003: p. 53-63.
136. Koerber, James T., Jae-Hyung Jang, Julie H. Yu, Ravi S. Kane, and David V. Schaffer, *Engineering Adeno-Associated Virus for One-Step Purification via Immobilized Metal Affinity Chromatography.* Human Gene Therapy, 2007. **18**(4): p. 367-378.
137. Jiang, Canping, Joseph C. Glorioso, and Mohammad Ataai, *Presence of imidazole in loading buffer prevents formation of free radical in immobilized metal affinity chromatography and dramatically improves the recovery of herpes simplex virus type 1 gene therapy vectors.* Journal of Chromatography A, 2006. **1121**(1): p. 40-45.
138. Synder, Mark A *Working with a Powerful and Robust Mixed-Mode Resin for Protein Purification*. 2011.
139. Hou, Ying, Christopher J. Morrison, and Steven M. Cramer, *Classification of Protein Binding in Hydroxyapatite Chromatography: Synergistic Interactions on the Molecular Scale.* Analytical Chemistry, 2011. **83**(10): p. 3709-3716.
140. Kuiper, Marcel, Raquel M. Sanches, James A. Walford, and Nigel K. H. Slater, *Purification of a functional gene therapy vector derived from Moloney murine leukaemia virus using membrane filtration and ceramic hydroxyapatite chromatography.* Biotechnology and Bioengineering, 2002. **80**(4): p. 445-453.
141. O'riordan, Catherine E, Amy L Erickson, and Alan E Smith, *Purification of adenovirus and aav*. 2010: United States. p. US20100279385A1.
142. Sheldon, Pauline McLean Quigley, Peter S Gagnon, Gina Nichols, and Barbara A Thorne, *Methods for purification of recombinant AAV vectors*. 2018, Google Patents.
143. Cannon-Carlson, Susan, Collette Cutler, Gary Vellekamp, and Marcio Voloch, *Method for purifying adenoviruses*. 2002, Google Patents.
144. Van Herk, Herman and Alfred Luitjens, *Method for the production of ad26 adenoviral vectors*. 2018, Google Patents.
145. Luitjens, Alfred and John A Lewis, *Method for the production of adenoviral vectors*. 2018, Google Patents.
146. O'Riordan, Catherine R., Amy L. Lachapelle, Karen A. Vincent, and Samuel C. Wadsworth, *Scaleable chromatographic purification process for recombinant adeno-associated virus (rAAV).* The Journal of Gene Medicine, 2000. **2**(6): p. 444-454.
147. Kurosawa, Yae, Shigehiro Sato, Tsuneo Okuyama, and Masato Taoka, *Sequential two-step chromatographic purification of infectious poliovirus using ceramic fluoroapatite and ceramic hydroxyapatite columns.* PloS one, 2019. **14**(9).
148. Pato, Tânia P., Marta C. O. Souza, Diogo A. Mattos, Elena Caride, Davis F. Ferreira, Luciane P. Gaspar, Marcos S. Freire, and Leda R. Castilho, *Purification of yellow fever virus produced in Vero cells for inactivated vaccine manufacture.* Vaccine, 2019. **37**(24): p. 3214-3220.
149. Reiter, Katrin, Patricia Pereira Aguilar, Viktoria Wetter, Petra Steppert, Andres Tover, and Alois Jungbauer, *Separation of virus-like particles and extracellular vesicles by flow-through and heparin affinity chromatography.* Journal of Chromatography A, 2019. **1588**: p. 77-84.
150. GE Healthcare, *Multimodal Chromatography Handbook*, in *Sigma-Aldrich*. 2013. p. 115.
151. Segura, María Mercedes, Amine A Kamen, and Alain Garnier, *Viral Vectors for Gene Therapy methods and protocols*. 2011.
152. Nestola, Piergiuseppe, Ricardo J. S. Silva, Cristina Peixoto, Paula M. Alves, Manuel J. T. Carrondo, and José P. B. Mota, *Adenovirus purification by two-column, size-exclusion, simulated countercurrent chromatography.* Journal of Chromatography A, 2014. **1347**: p. 111-121.
153. Leung, Wallace Woon-Fong, *Centrifugal Separations in Biotechnology*. 2007. 312.
154. van Hee, Pim, Anton P. J. Middelberg, Rob G. J. M. van der Lans, and Luuk A. M. van der Wielen, *Relation between cell disruption conditions, cell debris particle size, and inclusion body release.* Biotechnology and Bioengineering, 2004. **88**(1): p. 100-110.
155. Erickson, Harold P., *Size and Shape of Protein Molecules at the Nanometer Level Determined by Sedimentation, Gel Filtration, and Electron Microscopy.* Biological Procedures Online, 2009. **11**(1): p. 32-51.

156. Flickinger, Michael C., *Downstream Industrial Biotechnology : Recovery and Purification*. 2013, New York, USA: John Wiley & Sons, Incorporated.
157. Kramberger, Petra, Lidija Urbas, and Aleš Štrancar, *Downstream processing and chromatography based analytical methods for production of vaccines, gene therapy vectors, and bacteriophages.* Human Vaccines & Immunotherapeutics, 2015. **11**(4): p. 1010-1021.
158. Wu, Yige, Jared Simons, Sarah Hooson, Dicky Abraham, and Giorgio Carta, *Protein and virus-like particle adsorption on perfusion chromatography media.* Journal of Chromatography A, 2013. **1297**: p. 96-105.
159. Peixoto, C., T. B. Ferreira, M. J. T. Carrondo, P. E. Cruz, and P. M. Alves, *Purification of adenoviral vectors using expanded bed chromatography.* Journal of Virological Methods, 2006. **132**(1-2): p. 121-126.
160. GE Healthcare, *Column efficiency testing* 2010. p. 6.
161. Crawford Scientific. *The Lockdown guide to the Van Deemter equation*. Chromatography Blog 2020 [cited 2020; Available from: https://www.crawfordscientific.com/technical/chromatography-blog/hplc-chromatography-tips/hplc-practice/van-deemter-equation-the-lockdown-guide.
162. Carr, Peter W., Xiaoli Wang, and Dwight R. Stoll, *Effect of Pressure, Particle Size, and Time on Optimizing Performance in Liquid Chromatography.* Analytical Chemistry, 2009. **81**(13): p. 5342-5353.
163. Johansson, H. J., C. Jägersten, and J. Shiloach, *Large scale recovery and purification of periplasmic recombinant protein from E. coli using expanded bed adsorption chromatography followed by new ion exchange media.* Journal of Biotechnology, 1996. **48**(1): p. 9-14.
164. Anspach, F. Birger, David Curbelo, Ralf Hartmann, Gunnar Garke, and Wolf-Dieter Deckwer, *Expanded-bed chromatography in primary protein purification.* Journal of Chromatography A, 1999. **865**(1): p. 129-144.
165. Jan Feuser, Joachim Walter, Maria-Regina Kula & Jörg Thömmes, *Cell adsorbent interactions in expanded bed adsorption of proteins.* Bioseparation, 1999. **8**: p. 99-109.
166. Gericke, Martin, Jani Trygg, and Pedro Fardim, *Functional cellulose beads: preparation, characterization, and applications.* Chemical reviews, 2013. **113**(7): p. 4812-4836.
167. Lahore, Marcelo Fernandez, Oscar Aguliar, Rami Reddy Vennapusa, and Muhammad Aasim, *Expanded bed chromatography, surface energetics of biomass deposition.* Downstream industrial biotechnology: recovery and purification, 2013: p. 95-115.
168. Feuser, Jan, Joachim Walter, Maria-Regina Kula, and Jörg Thömmes, *Cell adsorbent interactions in expanded bed adsorption of proteins.* Bioseparation, 1999. **8**: p. 99-109.
169. Lin, Dong-Qiang, Hector Marcelo Fern, andez-Lahore, Maria-Regina Kula, and Jörg Thömmes, *Minimising biomass adsorbent interactions in expanded bed adsorption processes - a methodological design approach.* Bioseparation, 2001. **10**: p. 7-19.
170. Dainiak, Maria B., Igor Yu Galaev, and Bo Mattiasson, *Polyelectrolyte-Coated Ion Exchangers for Cell-Resistant Expanded Bed Adsorption.* Biotechnol, 2002. **18**: p. 815-820.
171. Viloria-Cols, Maria E., Rajni Hatti-Kaul, and Bo Mattiasson, *Agarose-coated anion exchanger prevents cell-adsorbent interactions.* Journal of Chromatography A, 2004. **1043**(2): p. 195-200.
172. Bauer, Steven R, Anne M Pilaro, and Karen D Weiss, *Testing of Adenoviral vector gene transfer products: FDA expectations.* Adenoviral vectors for gene therapy, 2002: p. 615-654.
173. Schagen, FHE, HJ Rademaker, MJWE Rabelink, H van Ormondt, FJ Fallaux, AJ van der Eb, and RC Hoeben, *Ammonium sulphate precipitation of recombinant adenovirus from culture medium - an easy methof to increase the total virus yield.* Gene Therapy 2000. **7**: p. 1570-1574.
174. Ling, Tau Chuan, Chee Kin Loong, Wen Siang Tan, Beng Ti Tey, Wan Mohammad Wan Abdullah, and Arbakariya Ariff, *Purification of filamentous bacteriophage M13 by expanded bed anion exchange chromatography.* Journal of microbiology (Seoul, Korea), 2004. **42**(3): p. 228.
175. *Monolithic Materials Preparation, Properties and Applications*. Journal of Chromatography, ed. František Švec, Tatiana B. Tennikova, and Zdeněk Dey. Vol. 67. 2003. 1-773.
176. Benčina, Katja, Mojca Benčina, Aleš Podgornik, and Aleš Štrancar, *Influence of the methacrylate monolith structure on genomic DNA mechanical degradation, enzymes activity and clogging.* Journal of Chromatography A, 2007. **1160**(1-2): p. 176-183.
177. Williams, Sharon L., Mark E. Eccleston, and Nigel K. H. Slater, *Affinity capture of a biotinylated retrovirus on macroporous monolithic adsorbents: Towards a rapid single-step purification process.* Biotechnology and Bioengineering, 2005. **89**(7): p. 783-787.
178. Arvidsson, Pär, Fatima M. Plieva, Vladimir I. Lozinsky, Igor Yu Galaev, and Bo Mattiasson, *Direct chromatographic capture of enzyme from crude homogenate using immobilized metal affinity chromatography on a continuous supermacroporous adsorbent.* Journal of Chromatography A, 2003. **986**(2): p. 275-290.

179. Burden, Claire S., Jing Jin, Aleš Podgornik, and Daniel G. Bracewell, *A monolith purification process for virus-like particles from yeast homogenate.* Journal of Chromatography B, 2012. **880**: p. 82-89.
180. Gerster, Petra, Eva-Maria Kopecky, Nikolaus Hammerschmidt, Miriam Klausberger, Florian Krammer, Reingard Grabherr, Christa Mersich, Lidija Urbas, Petra Kramberger, Tina Paril, Matthias Schreiner, Katharina Nöbauer, Ebrahim Razzazi-Fazeli, and Alois Jungbauer, *Purification of infective baculoviruses by monoliths.* Journal of Chromatography A, 2013. **1290**: p. 36-45.
181. Fischer, Laura M., Michael W. Wolff, and Udo Reichl, *Purification of cell culture-derived influenza A virus via continuous anion exchange chromatography on monoliths.* Vaccine, 2018. **36**(22): p. 3153-3160.
182. Oksanen, Hanna M., Ausra Domanska, and Dennis H. Bamford, *Monolithic ion exchange chromatographic methods for virus purification.* Virology, 2012. **434**(2): p. 271-277.
183. Fernandes, Cláudia S. M., Bianca Gonçalves, Margarida Sousa, Duarte L. Martins, Telma Barroso, Ana Sofia Pina, Cristina Peixoto, Ana Aguiar-Ricardo, and A. Cecília A. Roque, *Biobased monoliths for adenovirus purification.* ACS Appl Mater Interfaces, 2015. **7**(12): p. 6605-12.
184. Kalbfuss, Bernd, Michael Wolff, Liane Geisler, Alexander Tappe, Ranil Wickramasinghe, Volkmar Thom, and Udo Reichl, *Direct capture of influenza A virus from cell culture supernatant with Sartobind anion-exchange membrane adsorbers.* Journal of Membrane Science, 2007. **299**(1-2): p. 251-260.
185. Duffy, A. M., A. M. O'Doherty, T. O'Brien, and P. M. Strappe, *Purification of adenovirus and adeno-associated virus: comparison of novel membrane-based technology to conventional techniques.* Gene Therapy, 2005. **12**(S1): p. S62-S72.
186. Vicente, Tiago, Marcos F. Q. Sousa, Cristina Peixoto, José P. B. Mota, Paula M. Alves, and Manuel J. T. Carrondo, *Anion-exchange membrane chromatography for purification of rotavirus-like particles.* Journal of Membrane Science, 2008. **311**(1-2): p. 270-283.
187. Lee, Dong-Sop, Byong-Moon Kim, and Dai-Wu Seol, *Improved purification of recombinant adenoviral vector by metal affinity membrane chromatography.* Biochemical and Biophysical Research Communications, 2009. **378**(3): p. 640-644.
188. Negrete, Alejandro, Tau Chuan Ling, and Andrew Lyddiatt, *Production of adenoviral vectors and its recovery.* Process Biochemistry, 2007. **42**(7): p. 1107-1113.
189. Guo, Ping, Yousef El-Gohary, Krishna Prasadan, Chiyo Shiota, Xiangwei Xiao, John Wiersch, Jose Paredes, Sidhartha Tulachan, and George K. Gittes, *Rapid and simplified purification of recombinant adeno-associated virus.* Journal of Virological Methods, 2012. **183**(2): p. 139-146.
190. Lee, Micky Fu Xiang, Eng Seng Chan, and Beng Ti Tey, *Negative chromatography: Progress, applications and future perspectives.* Process Biochemistry, 2014. **49**(6): p. 1005-1011.
191. Gottwald, Johannes F, *Liquid metal recorder*. 1971, Google Patents.
192. Rengier, Fabian, Amit Mehndiratta, Hendrik Von Tengg-Kobligk, Christian M Zechmann, Roland Unterhinninghofen, H-U Kauczor, and Frederik L Giesel, *3D printing based on imaging data: review of medical applications.* International Journal of Computer Assisted Radiology and Surgery, 2010. **5**(4): p. 335-341.
193. Shafiee, Ashkan and Anthony Atala, *Printing Technologies for Medical Applications.* Trends in Molecular Medicine, 2016. **22**(3): p. 254-265.
194. Ligon, Samuel Clark, Robert Liska, Jürgen Stampfl, Matthias Gurr, and Rolf Mülhaupt, *Polymers for 3D Printing and Customized Additive Manufacturing.* Chemical Reviews, 2017. **117**(15): p. 10212-10290.
195. Ngo, Tuan D, Alireza Kashani, Gabriele Imbalzano, Kate TQ Nguyen, and David Hui, *Additive manufacturing (3D printing): A review of materials, methods, applications and challenges.* Composites Part B: Engineering, 2018. **143**: p. 172-196.
196. Bauer, Maria and Lawrence Kulinsky, *Fabrication of a lab-on-chip device using material extrusion (3D printing) and demonstration via Malaria-Ab ELISA.* Micromachines, 2018. **9**(1): p. 27.
197. Paulsen, Jason A, Michael Renn, Kurt Christenson, and Richard Plourde. *Printing conformal electronics on 3D structures with Aerosol Jet technology*. in *2012 Future of Instrumentation International Workshop (FIIW) Proceedings*. 2012. IEEE.
198. Yang, Jiquan, Kelou Li, Li Zhu, and Wencheng Tang, *Fabrication of PDMS microfluidic devices with 3D wax jetting.* Rsc Advances, 2017. **7**(6): p. 3313-3320.
199. Raoufi, Mohammad Amin, Sajad Razavi Bazaz, Hamid Niazmand, Omid Rouhi, Mohsen Asadnia, Amir Razmjou, and Majid Ebrahimi Warkiani, *Fabrication of unconventional inertial microfluidic channels using wax 3D printing.* Soft Matter, 2020. **16**(10): p. 2448-2459.
200. Do, Anh-Vu, Behnoush Khorsand, Sean M. Geary, and Aliasger K. Salem, *3D Printing of Scaffolds for Tissue Regeneration Applications.* Advanced Healthcare Materials, 2015. **4**(12): p. 1742-1762.

201. Matthews, Manyalibo J, Gabe Guss, Saad A Khairallah, Alexander M Rubenchik, Philip J Depond, and Wayne E King, *Denudation of metal powder layers in laser powder bed fusion processes.* Acta Materialia, 2016. **114**: p. 33-42.
202. Fee, Conan, Suhas Nawada, and Simone Dimartino, *3D printed porous media columns with fine control of column packing morphology.* Journal of Chromatography A, 2014. **1333**: p. 18-24.
203. Nawada, Suhas, Simone Dimartino, and Conan Fee, *Dispersion behavior of 3D-printed columns with homogeneous microstructures comprising differing element shapes.* Chemical Engineering Science, 2017. **164**: p. 90-98.
204. Dolamore, Fabian, Conan Fee, and Simone Dimartino, *Modelling ordered packed beds of spheres: The importance of bed orientation and the influence of tortuosity on dispersion.* Journal of Chromatography A, 2018. **1532**: p. 150-160.
205. Fee, Conan, Simone Dimartino, and Tim Huber, *Seperation medium*, WO2017103863Al, Editor. 2016.
206. Huber, Tim, Don Clucas, Mathieu Vilmay, Birte Pupkes, James Stuart, Simone Dimartino, and Conan Fee, *3D Printing Cellulose Hydrogels Using LASER Induced Thermal Gelation.* Journal of Manufacturing and Materials Processing, 2018. **2**(3): p. 42.
207. Simon, Ursula and Simone Dimartino, *Direct 3D printing of monolithic ion exchange adsorbers.* Journal of Chromatography A, 2019. **1587**: p. 119-128.
208. Simon, Ursula, Livia C T Scorza, Sarah Teworte, Alistair J McCormick, and Simone Dimartino, *Demonstration of protein capture and separation using three-dimensional printed anion exchange monoliths fabricated in one-step.* Journal of Separation Science. **n/a**(n/a).
209. Macdonald, Niall P, Sinead A Currivan, Laura Tedone, and Brett Paull, *Direct production of microstructured surfaces for planar chromatography using 3D printing.* Analytical chemistry, 2017. **89**(4): p. 2457-2463.
210. Schoen, A. H., *Reflections concerning triply-periodic minimal surfaces.* Interface Focus, 2012. **2**(5): p. 658-668.
211. Hao, Liang, David Raymont, Chunze Yan, Ahmed Hussein, and Philippe Young, *Design and additive manufacturing of cellular lattice structures.* 2011: p. 249-254.
212. Meeks III, William H, *The theory of triply periodic minimal surfaces.* Indiana University Mathematics Journal, 1990: p. 877-936.
213. Ruan, Dong, Ang Lue, and Lina Zhang, *Gelation behaviors of cellulose solution dissolved in aqueous NaOH/thiourea at low temperature.* Polymer, 2008. **49**(4): p. 1027-1036.
214. Merck-Sigma-Aldrich. *α-Cellulose*. 2020 30/09/2020]; Available from: https://www.sigmaaldrich.com/catalog/product/sigma/c8002?lang=en&region=NZ&gclid=Cj0KCQjwtsv7BRCmARIsANu-CQe5mjvVdg-frBgQcArzio9GMtiPplO9roTDf-fedKwjcu1h7sglOfIaAhKjEALw_wcB.
215. Zhang, Lina, Dong Ruan, and Shanjun Gao, *Dissolution and regeneration of cellulose in NaOH/thiourea aqueous solution.* Journal of Polymer Science Part B: Polymer Physics, 2002. **40**(14): p. 1521-1529.
216. Xiong, Bi, Pingping Zhao, Kai Hu, Lina Zhang, and Gongzhen Cheng, *Dissolution of cellulose in aqueous NaOH/urea solution: role of urea.* Cellulose, 2014. **21**(3): p. 1183-1192.
217. Zhu, Shengdong, Yuanxin Wu, Qiming Chen, Ziniu Yu, Cunwen Wang, Shiwei Jin, Yigang Ding, and Gang Wu, *Dissolution of cellulose with ionic liquids and its application: a mini-review.* Green Chemistry, 2006. **8**(4): p. 325.
218. Qi, Haisong, Chunyu Chang, and Lina Zhang, *Effects of temperature and molecular weight on dissolution of cellulose in NaOH/urea aqueous solution.* Cellulose, 2008. **15**(6): p. 779-787.
219. Cai, Jie and Lina Zhang, *Rapid Dissolution of Cellulose in LiOH/Urea and NaOH/Urea Aqueous Solutions.* Macromolecular Bioscience, 2005. **5**(6): p. 539-548.
220. Yamane, Chihiro, Ryuji Hirase, Hitomi Miyamoto, Shigeo Kuwamoto, and Yoshiaki Yuguchi, *Mechanism of structure formation and dissolution of regenerated cellulose from cellulose/aqueous sodium hydroxide solution and formation of molecular sheets deduced from the mechanism.* Cellulose, 2015. **22**(5): p. 2971-2982.
221. Medronho, Bruno and Björn Lindman, *Brief overview on cellulose dissolution/regeneration interactions and mechanisms.* Advances in Colloid and Interface Science, 2015. **222**: p. 502-508.
222. Huber, Tim, Sean Feast, Simone Dimartino, Wanwen Cen, and Conan Fee, *Analysis of the Effect of Processing Conditions on Physical Properties of Thermally Set Cellulose Hydrogels.* Materials, 2019. **12**(7): p. 1066.
223. Qin, Xingzhen, Ang Lu, and Lina Zhang, *Gelation behavior of cellulose in NaOH/urea aqueous system via cross-linking.* Cellulose, 2013. **20**(4): p. 1669-1677.

224. Wu, Chun-Yi, Shing-Yi Suen, Shiow-Ching Chen, and Jau-Hwan Tzeng, *Analysis of protein adsorption on regenerated cellulose-based immobilized copper ion affinity membranes.* Journal of Chromatography A, 2003. **996**(1-2): p. 53-70.
225. He, Xu, Long Cheng, Yaru Wang, Jiangqi Zhao, Wei Zhang, and Canhui Lu, *Aerogels from quaternary ammonium-functionalized cellulose nanofibers for rapid removal of Cr(VI) from water.* Carbohydrate Polymers, 2014. **111**: p. 683-687.
226. Zaman, M., H. Xiao, F. Chibante, and Y. Ni, *Synthesis and characterization of cationically modified nanocrystalline cellulose.* Carbohydr Polym, 2012. **89**(1): p. 163-70.
227. Cube Biotech. *NTA versus IDA: what's the difference?* 2020 26/10/2020]; Available from: https://cube-biotech.com/us/nta-versus-ida-what-s-the-difference.
228. Saska, S, HS Barud, AMM Gaspar, Reinaldo Marchetto, Sidney José Lima Ribeiro, and Younes Messaddeq, *Bacterial Cellulose-Hydroxyapatite Nanocomposites for Bone Regeneration.* International Journal of Biomaterials, 2011. **2011**: p. 1-8.
229. Zimmermann, Kristen A., Jill M. LeBlanc, Kevin T. Sheets, Robert W. Fox, and Paul Gatenholm, *Biomimetic design of a bacterial cellulose/hydroxyapatite nanocomposite for bone healing applications.* Materials Science and Engineering: C, 2011. **31**(1): p. 43-49.
230. Grande, Cristian J., Fernando G. Torres, Clara M. Gomez, and M. Carmen Bañó, *Nanocomposites of bacterial cellulose/hydroxyapatite for biomedical applications.* Acta Biomaterialia, 2009. **5**(5): p. 1605-1615.
231. Wan, YZ, L Hong, SR Jia, Y Huang, Y Zhu, YL Wang, and HJ Jiang, *Synthesis and characterization of hydroxyapatite–bacterial cellulose nanocomposites.* Composites Science and Technology, 2006. **66**(11-12): p. 1825-1832.
232. Ishikawa, K., P. Ducheyne, and S. Radin, *Determination of the Ca/P ratio in calcium-deficient hydroxyapatite using X-ray diffraction analysis.* Journal of Materials Science: Materials in Medicine, 1993. **4**(2): p. 165-168.
233. Urh, Marjeta, Dan Simpson, and Kate Zhao, *Affinity chromatography: general methods*, in *Methods in enzymology*. 2009, Elsevier. p. 417-438.
234. Castro, Vida, Hortensia Rodríguez, and Fernando Albericio, *CuAAC: an efficient click chemistry reaction on solid phase.* ACS combinatorial science, 2016. **18**(1): p. 1-14.
235. Aïssa, Kevin, Muzaffer A Karaaslan, Scott Renneckar, and Jack N Saddler, *Functionalizing Cellulose Nanocrystals with Click Modifiable Carbohydrate-Binding Modules.* Biomacromolecules, 2019. **20**(8): p. 3087-3093.
236. ThermoFisher scientific. *Carbodiimide Crosslinker Chemistry*. 2020 24/09/2020]; Available from: https://www.thermofisher.com/nz/en/home/life-science/protein-biology/protein-biology-learning-center/protein-biology-resource-library/pierce-protein-methods/carbodiimide-crosslinker-chemistry.html.
237. Lorensen, William E and Harvey E Cline, *Marching cubes: A high resolution 3D surface construction algorithm.* ACM siggraph computer graphics, 1987. **21**(4): p. 163-169.
238. Gordon, Anne and Samuel O'Neil, *Production of 3D printed Agarose column*. 2016, University of Canterbury.
239. Liesiene, Jolanta and Jurgita Kazlauske, *Functionalization of cellulose: Synthesis of water-soluble cationic cellulose derivatives.* Cellul. Chem. Technol, 2013. **47**: p. 515-525.
240. Merck-Sigma-Aldrich. *2-Chloro-N,N-diethylethylamine hydrochloride*. 2020 26/09/2020]; Available from: https://www.sigmaaldrich.com/catalog/product/sigma/d4003?lang=en&region=NZ.
241. Merck-Sigma-Aldrich. *Glycidyltrimethylammonium chloride*. 2020 26/09/2020]; Available from: https://www.sigmaaldrich.com/catalog/substance/glycidyltrimethylammoniumchloride15163303377011?lang=en&region=NZ.
242. Rhee, Sang-Hoo and Junzo Tanaka, *Hydroxyapatite formation on cellulose cloth induced by citric acid.* Material science: Materials in medicine, 2000. **11**: p. 449-452.
243. Life technologies, *Amine-Reactive Probes*. 2013, Thermo Fisher Scientific.
244. Moleirinho, Mafalda G., Sean Feast, Ana S. Moreira, Ricardo J. S. Silva, Paula M. Alves, Manuel J. T. Carrondo, Tim Huber, Conan Fee, and Cristina Peixoto, *3D-printed ordered bed structures for chromatographic purification of enveloped and non-enveloped viral particles.* Separation and Purification Technology, 2021: p. 117681.
245. Moleirinho, Mafalda G., Sara Rosa, Manuel J. T. Carrondo, Ricardo J. S. Silva, Åsa Hagner-McWhirter, Gustaf Ahlén, Mats Lundgren, Paula M. Alves, and Cristina Peixoto, *Clinical-Grade Oncolytic Adenovirus*

Purification Using Polysorbate 20 as an Alternative for Cell Lysis. Current gene therapy, 2018. **18**(6): p. 366-374.
246. Tomás, HA, AF Rodrigues, MJT Carrondo, and AS Coroadinha, *LentiPro26: novel stable cell lines for constitutive lentiviral vector production.* Scientific reports, 2018. **8**(1): p. 1-11.
247. Watanabe, J. and M. Akashi, *Anisotropic hydroxyapatite formation inside agarose gels by integration of electrophoretic and alternate soaking approaches.* J Biomater Sci Polym Ed, 2008. **19**(12): p. 1625-35.
248. Carta, Giorgio and Alois Jungbauer, *Protein chromatography: process development and scale-up*. 2020: John Wiley & Sons.
249. Stone, Melani C. and Giorgio Carta, *Protein adsorption and transport in agarose and dextran-grafted agarose media for ion exchange chromatography.* Journal of chromatography. A, 2007. **1146**(2): p. 202-215.
250. Hutchens, S., R. Benson, B. Evans, H. Oneill, and C. Rawn, *Biomimetic synthesis of calcium-deficient hydroxyapatite in a natural hydrogel.* Biomaterials, 2006. **27**(26): p. 4661-4670.
251. Czernuszka, DA Wahl and JT, *Collagen-Hydroxyapatite composites for hard tissue repair.* European Cells and Materials, 2006. **11**: p. 43-56.
252. Dupraz, A., T. P. Nguyen, M. Richard, G. Daculsi, and N. Passuti, *Influence of a cellulosic ether carrier on the structure of biphasic calcium phosphate ceramic particles in an injectable composite material.* Biomaterials, 1999. **20**(7): p. 663-673.
253. Kokubo, Tadashi, Hyun-Min Kim, and Masakazu Kawashita, *Novel bioactive materials with different mechanical properties.* Biomaterials, 2003. **24**(13): p. 2161-2175.
254. Yao, Yan and Abraham M. Lenhoff, *Pore size distributions of ion exchangers and relation to protein binding capacity.* Journal of Chromatography A, 2006. **1126**(1): p. 107-119.
255. Itoh, Daisuke, Noriko Yoshimoto, and Shuichi Yamamoto, *Retention Mechanism of Proteins in Hydroxyapatite Chromatography - Multimodal Interaction Based Protein Separations: A Model Study.* Current protein & peptide science, 2019. **20**(1): p. 75-81.
256. He, Jie and Andrew Cohen, *CHT Ceramic Hydroxyapatite - Instruction manual*, Bio-Rad, Editor. 2008.
257. Duarte, Eden B., Bruna S. das Chagas, Fábia K. Andrade, Ana I. S. Brígida, Maria F. Borges, Celli R. Muniz, Men de Sá M. Souza Filho, João P. S. Morais, Judith P. A. Feitosa, and Morsyleide F. Rosa, *Production of hydroxyapatite–bacterial cellulose nanocomposites from agroindustrial wastes.* Cellulose, 2015. **22**(5): p. 3177-3187.
258. He, Meng, Chunyu Chang, Na Peng, and Lina Zhang, *Structure and properties of hydroxyapatite/cellulose nanocomposite films.* Carbohydrate Polymers, 2012. **87**(4): p. 2512-2518.
259. Yamamoto, Shuichi, Nagomu Akazaki, Oliver Kaltenbrunner, and Peter Watler, *Factors affecting dispersion in expanded bed chromatography*, in *Expanded Bed Chromatography*. 1999, Springer. p. 33-41.
260. Siddiqi, Somayia F., Nigel J. Titchener-Hooker, and Parviz Ayazi Shamlou, *High Pressure Disruption of Yeast Cells-The Use of Scale Down Operations forthe Prediction of Protein Release and Cell Debris Size Distribution.* Biotechnology and Bioengineering, 1997. **55**: p. 642-649.
261. Yanagisawa, K., J. C. Rendon-Angeles, N. Ishizawa, and S. Oishi, *Topotaxial replacement of chlorapatite by hydroxyapatite during hydrothermal ion exchange.* American Mineralogist, 1999. **84**(11-12): p. 1861-1869.
262. Demnati, I., D. Grossin, O. Marsan, G. Bertrand, G. Collonges, C. Combes, M. Parco, I. Braceras, J. Alexis, Y. Balcaen, and C. Rey, *Comparison of Physical-chemical and Mechanical Properties of Chlorapatite and Hydroxyapatite Plasma Sprayed Coatings.* Open Biomed Eng J, 2015. **9**: p. 42-55.
263. Ohta, Kazushi, Hideki Monma, and Satoshi Takahashi, *Adsorption characteristics of proteins on calcium phosphates using liquid chromatography.* Journal of Biomedical Materials Research, 2001. **55**(3): p. 409-414.
264. Bigi, A., A. Ripamonti, G. Cojazzi, M. Gazzano, and N. Roveri, *Thermal conversion of octacalcium phosphate into hydroxyapatite.* Journal of Inorganic Biochemistry, 1990. **40**(4): p. 293-299.
265. Arellano-Jiménez, M. J., R. García-García, and J. Reyes-Gasga, *Synthesis and hydrolysis of octacalcium phosphate and its characterization by electron microscopy and X-ray diffraction.* Journal of Physics and Chemistry of Solids, 2009. **70**(2): p. 390-395.
266. Horváthová, Renáta, Lenka Müller, Aleš Helebrant, Peter Greil, and Frank A. Müller, *In vitro transformation of OCP into carbonated HA under physiological conditions.* Materials Science and Engineering: C, 2008. **28**(8): p. 1414-1419.

267. Cheng, Pei-Tak, *Formation of octacalcium phosphate and subsequent transformation to hydroxyapatite at low supersaturation: A model for cartilage calcification.* Calcified Tissue International, 1987. **40**(6): p. 339-343.
268. LeGeros, R. Z., R. Kijkowska, and J. P. LeGeros, *Formation and transformation of octacalcium phosphate, OCP: a preliminary report.* Scanning electron microscopy, 1984(Pt 4): p. 1771-1777.
269. Graham, Stephan and Paul W. Brown, *Reactions of octacalcium phosphate to form hydroxyapatite.* Journal of Crystal Growth, 1996. **165**: p. 106-115.
270. Kabra, Bhagwati G, Stevin H Gehrke, and Richard J Spontak, *Microporous, responsive hydroxypropyl cellulose gels. 1. Synthesis and microstructure.* Macromolecules, 1998. **31**(7): p. 2166-2173.
271. Kumar, Anuj, Yujin Lee, Doyeon Kim, Kummara Madhusudana Rao, Jisoo Kim, Soyoung Park, Adnan Haider, Do Hyun Lee, and Sung Soo Han, *Effect of crosslinking functionality on microstructure, mechanical properties, and in vitro cytocompatibility of cellulose nanocrystals reinforced poly (vinyl alcohol)/sodium alginate hybrid scaffolds.* International Journal of Biological Macromolecules, 2017. **95**: p. 962-973.
272. Ma, Z., R. D. Whitley, and N. H. L. Wang, *Pore and surface diffusion in multicomponent adsorption and liquid chromatography systems.* AIChE Journal, 1996. **42**(5): p. 1244-1262.
273. Shi, Qing-Hong, Xin Zhou, and Yan Sun, *A novel superporous agarose medium for high-speed protein chromatography.* Biotechnology and Bioengineering, 2005. **92**(5): p. 643-651.
274. Zhou, Qing-Zhu, Lian-Yan Wang, Guang-Hui Ma, and Zhi-Guo Su, *Preparation of uniform-sized agarose beads by microporous membrane emulsification technique.* Journal of Colloid and Interface Science, 2007. **311**(1): p. 118-127.
275. Toufik, Jamila and Denis Labarre, *Relationship between reduction of complement activation by polysaccharide surfaces bearing diethylaminoethyl groups and their degree of substitution.* Biomaterials, 1995. **16**(14): p. 1081-1088.
276. Ishimura, Daisuke, Yasuo Morimoto, and Hidenao Saito, *Influences of chemical modifications on the mechanical strength of cellulose beads.* Cellulose, 1998. **5**(2): p. 135-151.
277. Du, Kai-Feng, Min Yan, Quan-Yi Wang, and Hang Song, *Preparation and characterization of novel macroporous cellulose beads regenerated from ionic liquid for fast chromatography.* Journal of Chromatography A, 2010. **1217**(8): p. 1298-1304.
278. Boeden, H. F., K. Pommerening, M. Becker, C. Rupprich, M. Holtzhauer, F. Loth, R. Müller, and D. Bertram, *Bead cellulose derivatives as supports for immobilization and chromatographic purification of proteins.* Journal of chromatography A, 1991. **552**(1-2): p. 389.
279. Hui-Li, Lu, Lin Dong-Qiang, Zhu Mi-Mi, and Yao Shan-Jing, *Protein adsorption on DEAE ion-exchange resins with different ligand densities and pore sizes.* Journal of Separation Science, 2012. **35**(22): p. 3084-3090.
280. Wu, Danlin and Rodney R. Walters, *Effects of stationary phase ligand density on high-performance ion-exchange chromatography of proteins.* Journal of Chromatography A, 1992. **598**(1): p. 7-13.
281. GE Healthcare, *Capto™ Q XP*. 2020.
282. Lu, Hui-Li, Dong-Qiang Lin, Mi-Mi Zhu, and Shan-Jing Yao, *Effects of ligand density and pore size on the adsorption of bovine IgG with DEAE ion-exchange resins.* Journal of Separation Science, 2012. **35**(16): p. 2131-2137.
283. Vicente, Tiago, René Fáber, Paula M. Alves, Manuel J. T. Carrondo, and José P. B. Mota, *Impact of ligand density on the optimization of ion-exchange membrane chromatography for viral vector purification.* Biotechnology and Bioengineering, 2011. **108**(6): p. 1347-1359.
284. Carta, Giorgio and Antonio Ubiera, *Particle-size distribution effects in batch adsorption.* AIChE Journal, 2003. **49**(12): p. 3066-3073.
285. Zhang, Songping and Yan Sun, *Study on protein adsorption kinetics to a dye–ligand adsorbent by the pore diffusion model.* Journal of Chromatography A, 2002. **964**(1): p. 35-46.
286. Gooding, Karen M. and Mary Nell Schmuck, *Comparison of weak strong high-performance anion-exchange chromatography.* Journal of Chromatography A, 1985. **327**: p. 139-146.
287. Staby, Arne, Inge Holm Jensen, and Inger Mollerup, *Comparison of chromatographic ion-exchange resins: I. Strong anion-exchange resins.* Journal of Chromatography A, 2000. **897**(1): p. 99-111.
288. Staby, Arne, Randi Holm Jensen, Matthias Bensch, Jürgen Hubbuch, Dorte L. Dünweber, Janus Krarup, Jacob Nielsen, Mette Lund, Steffen Kidal, Thomas Budde Hansen, and Inge Holm Jensen, *Comparison of chromatographic ion-exchange resins: VI. Weak anion-exchange resins.* Journal of Chromatography A, 2007. **1164**(1): p. 82-94.

289. Chen, Wen-hsiang, Joseph Y. Fu, Katerina Kourentzi, and Richard C. Willson, *Nucleic acid affinity of clustered-charge anion exchange adsorbents: Effects of ionic strength and ligand density.* Journal of Chromatography A, 2011. **1218**(2): p. 258-262.
290. Thermoscientific, *POROS™ Anion Exchange Resins: XQ, 50 HQ, 50 PI, and 50 D*. 2020.
291. Bio-Rad, *Bio-Rad Introduces Nuvia™ Q, An Ultra–High Binding Capacity Anion Exchanger for Biopharmaceutical Downstream Processing*. 2011: Bio-Rad. p. 1.
292. Johnson, TF, PR Levison, PR Shearing, and DG Bracewell, *X-ray computed tomography of packed bed chromatography columns for three dimensional imaging and analysis.* Journal of Chromatography A, 2017. **1487**: p. 108-115.
293. De Smet, J., P. Gzil, N. Vervoort, H. Verelst, G. V. Baron, and G. Desmet, *On the optimisation of the bed porosity and the particle shape of ordered chromatographic separation media.* Journal of Chromatography A, 2005. **1073**(1): p. 43-51.
294. Hou, Ying and Steven M Cramer, *Evaluation of selectivity in multimodal anion exchange systems: A priori prediction of protein retention and examination of mobile phase modifier effects.* Journal of Chromatography A, 2011. **1218**(43): p. 7813-7820.
295. Zhou, Jingmin, Xiao Yang, J. Fraser Wright, Katherine A. High, Linda Couto, and Guang Qu, *PEG-modulated column chromatography for purification of recombinant adeno-associated virus serotype 9.* Journal of Virological Methods, 2011. **173**(1): p. 99-107.
296. Peixoto, Cristina, Tiago B. Ferreira, Marcos F. Q. Sousa, Manuel J. T. Carrondo, and Paula M. Alves, *Towards purification of adenoviral vectors based on membrane technology.* Biotechnology Progress, 2008. **24**(6): p. 1290-1296.
297. Green, Anthony P., James J. Huang, Miller O. Scott, Timothy D. Kierstead, Irene Beaupré, Guang-Ping Gao, and James M. Wilson, *A New Scalable Method for the Purification of Recombinant Adenovirus Vectors.* Human Gene Therapy, 2002. **13**(16): p. 1921-1934.
298. Wolf, Michael W. and Udo Reichl, *Downstream processing of cell culture-derived virus particles.* Expert Review of Vaccines, 2011. **10**(10): p. 1451-1475.
299. Walther, W. and U. Stein, *Viral vectors for gene transfer: a review of their use in the treatment of human diseases.* Drugs, 2000. **60**(2): p. 249-71.
300. Douglas, J. T., *Adenoviral vectors for gene therapy.* Mol Biotechnol, 2007. **36**(1): p. 71-80.
301. Bio-Rad. *CHT Ceramic Hydroxyapatite Type I Media*. 2020 18/11/2020]; Available from: https://www.bio-rad.com/en-nz/product/cht-ceramic-hydroxyapatite-type-i-media?ID=7b9e4566-4a07-482a-8082-62dfcb1dd0b1.
302. Catherine R. O'Riordan, Amy L. Lachapelle, Karen A. Vincent, and Samuel C. Wadsworth, *Scaleable chromatographic purification process for recombinant adeno-associated virus (rAAV).* The Journal of Gene Medicine, 2000. **2**: p. 444-454.
303. Clarke, Daniel A., Fabian Dolamore, Conan J. Fee, Petrik Galvosas, and Daniel J. Holland, *Investigation of flow through triply periodic minimal surface-structured porous media using MRI and CFD.* Chemical Engineering Science, 2021. **231**: p. 116264.
304. Salmean, Christopher and Simone Dimartino, *3D-Printed Stationary Phases with Ordered Morphology: State of the Art and Future Development in Liquid Chromatography.* Chromatographia, 2018. **82**(1): p. 443-463.
305. Siu, Sun Chau, Helen Baldascini, David C Hearle, Mike Hoare, and Nigel J. Tichener-Hooker, *Effect of fouling on the capacity and breakthrough characteristics of a packed bed ion exchnage chromatography column.* Bioprocess Biosyst Eng, 2006: p. 405-414.
306. Baldascini, Rihab Boushaba Helen, Spyridon Gerontas, Nigel J. Titchener-Hooker, and Daniel G. Bracewell, *Demonstration of the use of windows of operation to visualize the effects of fouling on the performance of a chromatographic step.* Bioseperations and Downstream Processing, 2011.
307. Ling, Tau Chuan, Wen Siang Tan, Beng Ti Tey, and Arbakariya Ariff, *Purification of filamentous bacteriophage M13 by expanded bed anion exchange chromatography.* The Journal of Microbiology, 2004. **42**(3): p. 228-232.
308. Cesari, Mathieu, Pascal Lefebvre, and Andreia Pedregal. *Cost Modeling of Upstream Production Process of Lentiviral Vectors in HEK-293 Cells Comparing Multi-Tray 10 Stacks and Fixed-Bed Bioreactor*. in *ESACT*. 2017. Pall Life Sciences.
309. Merten, Otto-Wilhelm, Matthias Schweizer, Parminder Chahal, and Amine A Kamen, *Manufacturing of viral vectors for gene therapy: part I. Upstream processing.* Pharm Bioprocess, 2014. **2**(2): p. 183-203.
310. biotech, Amersham pharmacia, *5. Experimental technique*, in *Expanded bed adsorption*. 2015.

311. Ng, Paul K and Valerie McLaughlin, *Regeneration studies of anion-exchange chromatography resins.* BioProcess International, 2007. **5**(5): p. 52.
312. Chan, Yi Wei, Siti Nurul N. Adam, Eugene M. Obeng, and Clarence M. Ongkudon, *Fabrication of a homogeneous large-volume polymethacrylate monolith: A thermal mixing approach.* SEPARATION SCIENCE PLUS, 2018. **1**(10): p. 702-709.
313. Ladisch, Michael and Leyu Zhang, *Fiber-based monolithic columns for liquid chromatography.* Analytical and bioanalytical chemistry, 2016. **408**(25): p. 6871-6883.
314. YMC. *Pilot scale glass columns*. 2020 8/12/2020]; Available from: http://www.ymc.co.jp/en/chromato/glass/pilot_glass_columns.html.
315. Chan, Hing Kai, James Griffin, Jia Jia Lim, Fangli Zeng, and Anthony SF Chiu, *The impact of 3D Printing Technology on the supply chain: Manufacturing and legal perspectives.* International Journal of Production Economics, 2018. **205**: p. 156-162.
316. Ben-Ner, Avner and Enno Siemsen, *Decentralization and localization of production: The organizational and economic consequences of additive manufacturing (3D printing).* California Management Review, 2017. **59**(2): p. 5-23.
317. Solutions, Essential Life, *Upscale® Laboratory Glass Columns*. 2020. p. 13.
318. Okubo, Akira and Simon A Levin, *The basics of diffusion*, in *Diffusion and ecological problems: Modern perspectives*. 2001, Springer. p. 10-30.
319. Yuan, Qingwang, Shanshan Yao, Xiang Zhou, Fanhua Zeng, Kelvin D. Knorr, and Muhammad Imran, *Miscible displacements with concentration-dependent diffusion and velocity-induced dispersion in porous media.* Journal of Petroleum Science and Engineering, 2017. **159**: p. 344-359.
320. Knox, John H. and Hugh P. Scott, *B and C terms in the Van Deemter equation for liquid chromatography.* Journal of Chromatography A, 1983. **282**: p. 297-313.
321. Pai, Anita, Shyamal Gondkar, and Arvind Lali, *Enhanced performance of expanded bed chromatography on rigid superporous adsorbent matrix.* Journal of Chromatography A, 2000. **867**(1): p. 113-130.
322. 3D Systems, *VisiJet® M2 ICast*. 2015.
323. 3d Systems, *ProJet® MJP 2500W, 3600W & 3600W MAX*. 2019.
324. Nagy, George, Tong Zhang, W Randolph Franklin, Eric Landis, Edwin Nagy, and Denis T Keane. *Volume and surface area distributions of cracks in concrete*. in *International Workshop on Visual Form*. 2001. Springer.
325. Rahmani, Tara, Behnam Kiani, Mehdi Bakhshi, and Mohammad Shekarchizadeh. *Application of different fibers to reduce plastic shrinkage cracking of concrete*. in *7th RILEM International Conference on Cracking in Pavements*. 2012. Springer.

Appendix A

Ligand density – Calculations

The below calculations show how the ligand density was calculated for each of the various anion exchangers tested:

1 mL of Q functionalized 500 μm, Schoen gyroid column.

Initial pH = 1.30

Final pH = 7.00

Initial level =20.30 mL

Final level = 24.25 mL

Blank column 500 μm

Initial pH = 1.26

Final pH = 7.00

Initial level =27.90 mL

Final level = 31.50 mL

Q 500

$$24.25 - 20.30 = 3.95\ mL$$

No column

$$31.50 - 27.90 = 4.5\ mL$$

Difference

$$4.5 - 3.95 = 0.55\ mL$$

Conversion to Moles

$$0.55\ mL \times 0.1 \frac{mole}{L} \times 0.001 \frac{L}{mL} \times 2 = 0.00011\ moles$$

Micro moles per mL of resin

$$0.00011\ moles\ \div 0.785\ mL \times 1{,}000{,}000 \frac{\mu m}{moles} = 140\ \mu m/mL$$

qPCR Calculations

The below calculations show how the titer of AAV serotype 9 samples were calculated from qPCR:

Ct = 20.11

Equation for known standards to determine femto genomes (fg) is given by the Thermocycler as shown in Figure A-1.

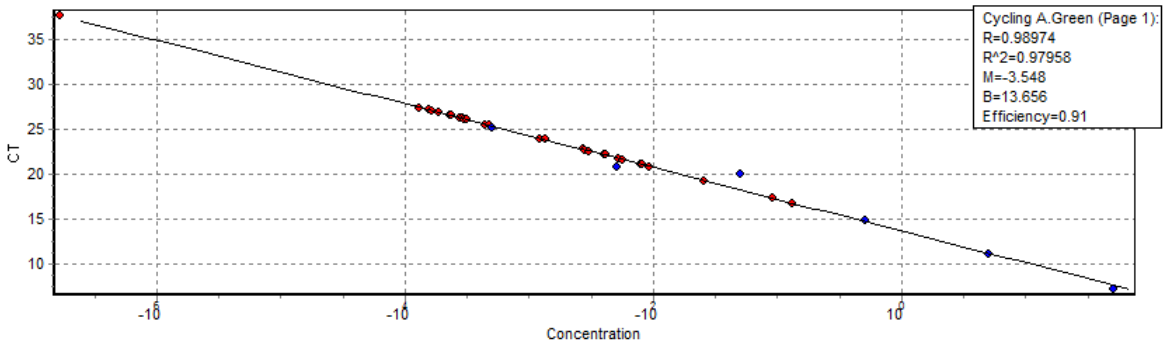

Figure A-1: Standard curve computer generated from known qPCR reactions

$$4861.8 \times e^{-0.668Ct}$$

$$4.86.8 \times e^{-0.668 \times 20.11} = 0.00712\ fg$$

$$number\ of\ copies\ per\ fg = \frac{fg \times 6.022 \times 10^{23}}{660 \times 5900 \times 10^{15}}$$

$$number\ of\ genomes = \frac{0.00712 \times 6.022 \times 10^{23}}{660 \times 5900 \times 10^{15}} = 2.20 \times 10^{3}\ VG/fg$$

Dilution factor = $Starting \frac{volume}{starting\ volume+DNase\ mix+EDTA+Pok\ mix+water} \times \frac{1}{5} \times dilution\ before\ qPCR \times 2\ \mu L$

$$Dilution\ factor = \frac{10 + 90 + 6 + 120}{10} \times \frac{1}{5} \times 0.1 \times 2 = 0.00177$$

$$\frac{VG}{\mu L} = \frac{2.20 \times 10^3}{0.00177} = 1.24 \times 10^6\ VG/\mu L$$

$$1.24 \times 10^6 VG/\mu L \times 1000\ \mu L/mL = 1.24 \times 10^9\ VG/mL$$

A melt of the multiplied DNA was also completed to ensure only a single product was produced. Figure A-2 shows an example of one of these melts.

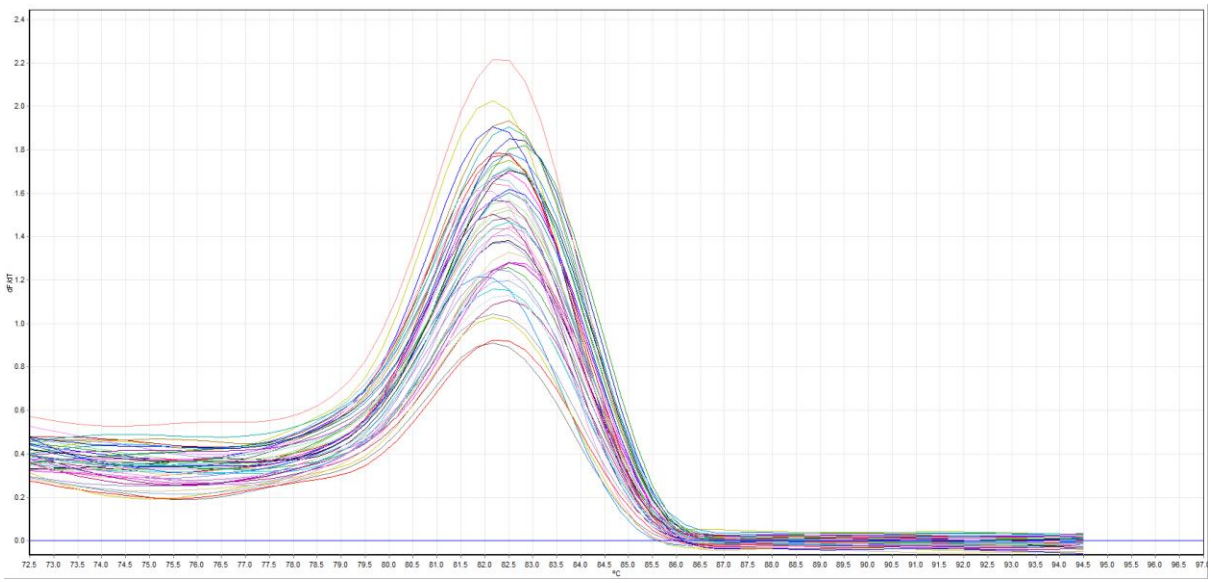

Figure A-2: qPCR melt curve showing single melt peak

Peak analyses from RTD

The peaks from RTD graphs were analyzed to determine both A_s and HETP values. Figure A-3 shows an example normalized peak with guidelines showing how it was dissected to determine correct values to be used for determining HETP and A_s. Explanation of these values can be found in Section 6.1.4.

A_s

$$b/a$$

$$\frac{1.34 - 1}{1 - 0.76} = 1.42$$

HETP

$$N = \frac{\mu_f^2}{\sigma^2} \cong \frac{1}{5.54} \times \left(\frac{w_h}{V_R}\right)^2$$

$$\frac{1}{5.54} \times \left(\frac{1}{0.33}\right)^2 = 50.4$$

$$HETP = \frac{L}{N}$$

$$\frac{10\ cm}{50.4} = 0.19\ cm$$

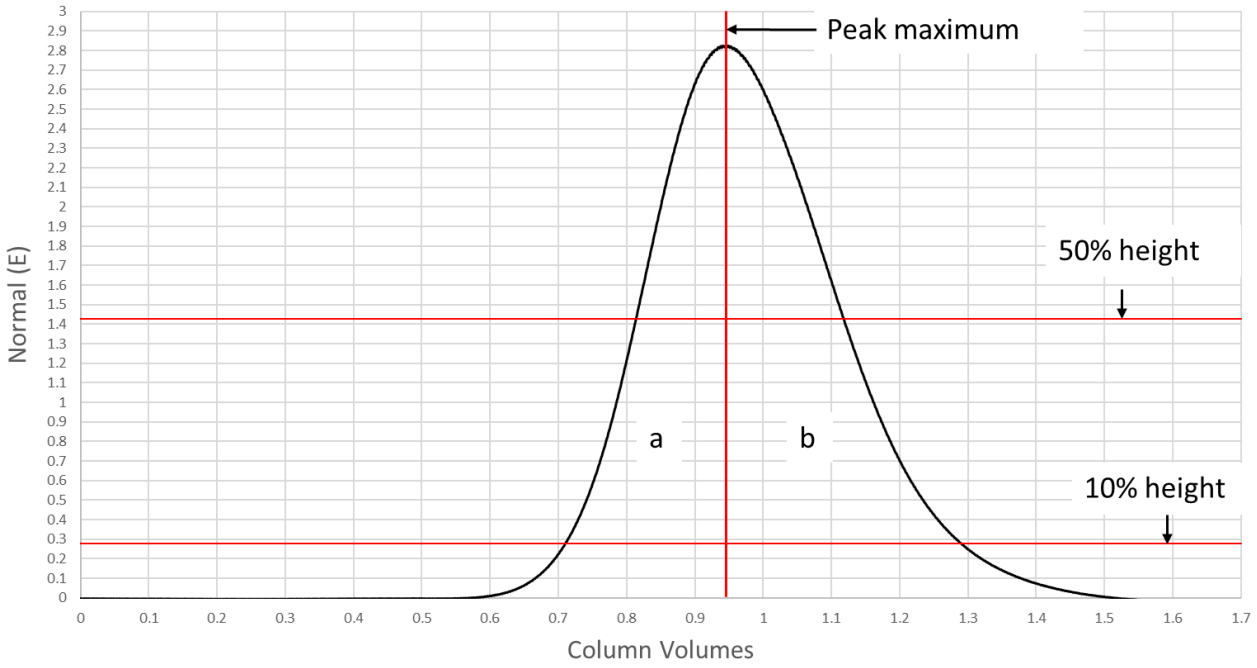

Figure A-3: Example image of a normalized peak dissected to determine w_h, V_R, a and b values.